

Aminoanthracene Appended Unsymmetrical Squaraine Derivatives: Synthesis and Ultrafast Time-Resolved Photophysical Characterization for NIR Photodetectors

By

GURUPRASAD M. S.

10CC14A39004

A thesis submitted to the
Academy of Scientific and Innovative Research
for the award of the degree of
DOCTOR OF PHILOSOPHY
in
SCIENCE

Under the supervision of
Dr. V. KARUNAKARAN



**CSIR-National Institute for Interdisciplinary
Science and Technology (CSIR-NIIST),
Thiruvananthapuram - 695 019**



Academy of Scientific and Innovative Research
AcSIR Headquarters, CSIR-HRDC campus
Sector 19, Kamla Nehru Nagar,
Ghaziabad, U.P. - 201 002, India

January-2022

सी एस आई आर- राष्ट्रीय अंतर्विषयी विज्ञान तथा प्रौद्योगिकी संस्थान

वैज्ञानिक तथा औद्योगिक अनुसंधान परिषद्
फोटो साइंस और फोटोनिक्स अनुभाग, रसायन विज्ञान तथा प्रौद्योगिकी प्रभाग
इंडस्ट्रियल इस्टेट-डाक घर, तिरुवनंतपुरम, भारत 695 019

CSIR-NATIONAL INSTITUTE FOR INTERDISCIPLINARY SCIENCE & TECHNOLOGY

Council of Scientific and Industrial Research
Photosciences and Photonic Section, Chemical Sciences and Technology Division
Industrial Estate P.O., Thiruvananthapuram, INDIA 695 019

डॉ. वी. करुणाकरण
प्रधान वैज्ञानिक




Dr. V. Karunakaran
Principal Scientist

January 7th, 2022
Thiruvananthapuram

CERTIFICATE

This is to certify that the work incorporated in this Ph.D. thesis entitled, "*Aminoanthracene Appended Unsymmetrical Squaraine Derivatives: Synthesis and Ultrafast Time-Resolved Photophysical Characterization for NIR Photodetectors*", submitted by Mr. Guruprasad M. S., to the Academy of Scientific and Innovative Research (AcSIR) in fulfillment of the requirements for the award of the Degree of *Doctor of Philosophy in Science*, embodies original research work carried out by the student. We further certify that this work has not been submitted to any other University or Institution in part or full for the award of any degree or diploma. Research materials obtained from other sources and used in this research work has been duly acknowledged in the thesis. Images, illustrations, figures, tables etc., used in the thesis from other sources, have also been duly cited and acknowledged.


Guruprasad M. S. 07/01/2022

 07/01/2022
Dr. V. Karunakaran

(Thesis Supervisor)

STATEMENTS OF ACADEMIC INTEGRITY

I, Guruprasad M. S., a Ph.D. student of the Academy of Scientific and Innovative Research (AcSIR) with Registration No. 10CC14A39004 hereby undertake that, the thesis entitled "*Aminoanthracene Appended Unsymmetrical Squaraine Derivatives: Synthesis and Ultrafast Time-Resolved Photophysical Characterization for NIR Photodetectors*" has been prepared by me and that the document reports original work carried out by me and is free of any plagiarism in compliance with the UGC Regulations on "*Promotion of Academic Integrity and Prevention of Plagiarism in Higher Educational Institutions (2018)*" and the CSIR Guidelines for "*Ethics in Research and in Governance (2020)*".



Guruprasad M. S. 07/01/2022

January 7th, 2022

Thiruvananthapuram

It is hereby certified that the work done by the student, under my supervision, is plagiarism-free in accordance with the UGC Regulations on "*Promotion of Academic Integrity and Prevention of Plagiarism in Higher Educational Institutions (2018)*" and the CSIR Guidelines for "*Ethics in Research and in Governance (2020)*".



Dr. V. Karunakaran


January 7th, 2022

Thiruvananthapuram

DECLARATION

I, Guruprasad M. S., bearing AcSIR Registration No. 10CC14A39004 declare: that my thesis entitled, "*Aminoanthracene Appended Unsymmetrical Squaraine Derivatives: Synthesis and Ultrafast Time-Resolved Photophysical Characterization for NIR Photodetectors*" is plagiarism free in accordance with the UGC Regulations on "*Promotion of Academic Integrity and Prevention of Plagiarism in Higher Educational Institutions (2018)*" and the CSIR Guidelines for "*Ethics in Research and in Governance (2020)*".

I would be solely held responsible if any plagiarised content in my thesis is detected, which is violative of the UGC regulations 2018.


Guruprasad M S. 07/01/2022

January 7th, 2022

Thiruvananthapuram

ACKNOWLEDGMENTS

I have great pleasure in expressing my deep sense of gratitude to Dr. V. Karunakaran, my thesis supervisor, for suggesting the research problem and for his constant guidance, support, motivation and encouragement, leading to the successful completion of this work.

I thank Dr. A. Ajayaghosh, Director CSIR–National Institute for Interdisciplinary Science and Technology (CSIR–NIIST), Thiruvananthapuram for his constant support and inspiration and for providing the necessary facilities for carrying out this work.

I thank Dr. Suresh Das (former Director) for his support, motivation and the fruitful discussion in completion of the work and Dr. Gangan Pratap (former acting Director) of CSIR–NIIST, Thiruvananthapuram, for providing the necessary facilities for carrying out this work.

My sincere thanks to,

Dr. K. N. Narayanan Unni, Dr. Vijayakumar C. Nair and Dr. E Bhoje Gowd, Doctoral Advisory Committee (DAC) members for their valuable comments and suggestions to improve the quality of my work.

Dr. C. H. Suresh, Dr. Luxmi Varma, and Dr. Mangalam S. Nair former AcSIR coordinators.

Dr. K. R. Gopidas, Dr. P. Sujatha Devi, Dr. Biswapriya Deb, Dr. Joshy Joseph, Dr. Praveen V. K, Dr. Suraj Soman, Dr. Sreejith Shankar P, Dr. Ishita Neogi and Dr. Adarsh Asok scientists of the Photosciences and Photonics Section, Chemical Sciences and Technology Division for their help and support.

Dr. Manoj A. G. Namboothiry, Mr. Vijith K. P, IISER, Thiruvananthapuram and Dr. Narayanan Unni. K. N. and Ms. Kavya Rajeev, CSIR–NIIST for photodetector characterization.

Mrs. Viji S and Mrs. Soumini Mathew for HRMS and NMR analysis respectively.

Mr. Robert Philip for general help.

Mr. Merin Santhosh and Ms. Aswathi C. S., for their helps in completing AcSIR procedures.

Dr Chinju Govind M. V., Ms. Sumitha Paul, Mrs. Tessy T. D., Mr. Hasim Fayiz P. N., Mrs. Megha Paul, Ms. Ranimol and Mrs. Afeefah, present and former group members.

Dr. Deepak D. Prabhu, Dr. Rahul. M. Ongungal and Dr. Aneesh P. S., former lab members for their valuable help and support in organic synthesis.

M. Sc. project student Ms. Hima Sundar for her hard work and support.

Dr. Chinnadhurai M., Mr. Lingamoorthy S, Mr. Shahansha Mohammed and Mr. Thejas K. K. friends at CSIR–NIIST for their care and support.

All my teachers and friends for their care and support.

My parents for their endless caring, love, and support.

CSIR for the fellowship.

Guruprasad M. S.

TABLE OF CONTENTS		Page No.
Certificate		i
Statements of academic integrity		ii
Declaration		iii
Acknowledgment		iv
Table of contents		vi
List of abbreviations		x
Preface		xiv
References		xvi
CHAPTER 1	An overview and Development of Squaraine Dyes in Organic Photodetector Applications	1–32
1.1	Abstract	1
1.2	Introduction	2
1.3	Squaraines and their Optical Properties	3
1.4	Overview of Organic Photodetectors	6
1.4.1	Mechanism of Organic Photodetectors	8
1.4.2	Performance Metrics of Organic Photodetectors	9
1.5	Near–Infrared Organic Photodetectors	11
1.5.1	Small Molecule–Based Near–Infrared Organic Photodetectors	12
1.5.2	Squaraine–Based Organic Photodetectors	18
1.6	Objectives of the Thesis	26
1.7	References	27
CHAPTER 2	Efficient Near–Infrared Organic Photodetector Using Pyrrole Linked Aryl Hydrazine–Based Unsymmetrical Squaraine Derivatives	33–84
2.1	Abstract	33

2.2	Introduction	34
2.3	Results and Discussions	36
2.3.1	Synthesis of APSQ Derivatives	36
2.3.2	Steady–State Photophysical Characterization	37
2.3.2.1	Solution State	37
2.3.2.2	Film State	44
2.3.2.3	Electrochemical Properties of APSQ Derivatives	46
2.3.2.4	Interaction of APSQs with PCBM	46
2.4	Time–Resolved Photophysical Characterization	50
2.4.1	Femtosecond Transient Absorption Spectra of APSQ derivatives	50
2.4.2	Analysis of the Transient Absorption Spectra of APSQ derivatives	56
2.5	Characterization of Photodetector	64
2.6	Summary	70
2.7	Experimental Section	71
2.7.1	Materials and Methods	71
2.8	Synthesis and Characterization of APSQ Derivatives	74
2.9	References	79
CHAPTER 3	Ultrafast Intermolecular Interaction Dynamics Between NIR–Absorbing Unsymmetrical Squaraines and PCBM: Effects of Halogen Substitution	85–141
3.1	Abstract	85
3.2	Introduction	86
3.3	Results and Discussions	88
3.3.1	Synthesis of ABSQ Derivatives	88

3.3.2	Steady–State Photophysical Characterization	88
3.3.2.1	Solution State	88
3.3.2.2	Film State	94
3.3.2.3	Electrochemical Properties of ABSQ Derivatives	101
3.3.2.4	Interaction of ABSQs with PCBM	101
3.4	Time–Resolved Photophysical Characterization	105
3.4.1	Femtosecond Transient Absorption Spectra of ABSQ derivatives	105
3.4.2	Analysis of the Transient Absorption Spectra of ABSQ derivatives	121
3.5	Characterization of Photodetector	129
3.6	Summary	131
3.7	Experimental Section	131
3.7.1	Materials and Methods	131
3.8	Synthesis and Characterization of ABSQ Derivatives	133
3.9	References	136
CHAPTER 4	Excited–State Relaxation Dynamics of Indolium –Based Unsymmetrical Squaraine Derivatives	142–176
4.1	Abstract	142
4.2	Introduction	143
4.3	Results and Discussions	145
4.3.1	Synthesis of AISQ Derivatives	145
4.3.2	Steady–State Photophysical Characterization	146
4.3.2.1	Solution State	146
4.3.2.2	Film State	152
4.3.2.3	Electrochemical Properties of AISQ Derivatives	154
4.3.2.4	Interaction of AISQs with PCBM	154

4.4	Time-Resolved Photophysical Characterization	158
4.4.1	Femtosecond Transient Absorption Spectra of AIQ derivatives	158
4.4.2	Analysis of the Transient Absorption Spectra of AIQ derivatives	165
4.5	Characterization of Photodetector	168
4.6	Summary	170
4.7	Experimental Section	170
4.7.1	Materials and Methods	170
4.8	Synthesis and Characterization of AIQ Derivatives	171
4.9	References	173
	Abstract of the Thesis	177
	List of Publications	178
	List of Posters Presented at Conferences	178
	Attachment of Photocopy of Publications	

List of Abbreviations

SQs	Squaraine dyes
USQ	Unsymmetrical squaraine dyes
PDs	Photodetectors
OPDs	Organic photodetectors
NIR	Near-infrared
NIR-OPDs	Near-infrared organic photodetectors
OPVs	Organic photovoltaics
BHJ	Bulk heterojunction
PHJ	Planar heterojunction
PM-HJ	Planar-mixed molecular heterojunction
D-A-D'	Donor-Acceptor-Donor'
ICT	Intramolecular charge transfer
EEL	Electron extraction layer
HEL	Hole extraction layer
HTL	Hole transport layer
ETL	Electron transport layer
PCE	Power conversion efficiency
EQE	External quantum efficiency
NEP	Noise equivalent power
D*	Specific detectivity
J-V	Current density-voltage
J_{sc}	Short-circuit current density
V_{oc}	Open-circuit voltage
J_{ph}	Photo-induced or photo-generated current density
J_d	Dark current density
V	Voltage
R	Photoresponsivity
IPCE	Incident photon-to-current efficiency
i_{noise}	Noise current

B	Detection bandwidth.
A	Device area
q	Charge of an electron
TPV	Transient photovoltage
TPC	Transient photocurrent
PPD	Picosecond photon detection module
TMS	Tetramethylsilane
ClAlPc	Chloroaluminium phthalocyanine
PbPc	Lead phthalocyanine
Bphen	Bathophenanthroline
CuI	Copper(I) iodide
F	Fluorine
Cl	Chlorine
Br	Bromine
C ₆₀	Buckminsterfullerene–C ₆₀
C ₇₀	Buckminsterfullerene–C ₇₀
PCBM	Phenyl-C ₆₁ -butyric acid methyl ester
BF ₄ ⁻	Tetrafluoroborate
TPFB ⁻	Tetrakis(pentafluorophenyl)borate
MEH-PPV	Poly[2-methoxy-5-(2-ethylhexyloxy)-1,4-phenylenevinylene]
Fc/Fc ⁺	Ferrocene/ferrocenium
AgCl	Silver chloride
TBAPF ₆	Tetrabutylammonium hexafluorophosphate
<i>E_{ox}</i>	Oxidation potential
ITO	Indium tin oxide
ZnO	Zinc oxide
MoO ₃	Molybdenum trioxide
Zn	Zinc
Al	Aluminium
Ag	Silver
°C	Degree Celsius
CaF ₂	Calcium fluoride

DADS	Decay associated difference spectra
SADS	Species associated difference spectra
DMSO	Dimethyl sulfoxide
Tol	Toluene
CHL	Chloroform
THF	Tetrahydrofuran
MEOH	Methanol
ACN	Acetonitrile
DMF	Dimethyl formamide
HCl	Hydrochloric acid
NaH	Sodium hydride
et al.	et alia
FRET	Förster resonance energy transfer
fs	Femtosecond
ps	Picosecond
ns	Nanosecond
<i>J</i>	Coupling constant
OUCs	Organic upconversion devices
OLED	Organic light-emitting diode
SWIR	Short wave infrared
FWHM	Full width at half maximum
GSB	Ground state bleach
ESA	Excited-state absorption
SE	Stimulated emission
HOMO	Highest occupied molecular orbital
LUMO	Lowest unoccupied molecular orbital
Hz	Hertz
MHz	Megahertz
IRF	Instrument response function
K_{sv}	Stern–Volmer quenching constant
k_q	Bimolecular quenching rate constant
mM	Millimolar

mA	Milliampere
W	Watt
nm	Nanometer
eV	Electron volt
h	Hour
min	Minutes
PDT	Photodynamic therapy
NMR	Nuclear magnetic resonance
HRMS–EI	High–resolution mass spectrometry–Electron Ionization
OD	Optical density
SVD	Singular value decomposition
fs–TAS	Femtosecond transient absorption spectra
TCSPC	Time–correlated single–photon counting
TOPAS	Travelling optical parametric amplification system
CV	Cyclic voltammogram
UV–vis	Ultraviolet–visible
ΔA	Change in absorbance
$\Delta \nu$	Stokes shift
λ	Wavelength
λ_{exctn}	Excitation wavelength
λ_{probe}	Probing wavelength
τ_f	Fluorescence lifetime
ϵ	Molar extinction coefficient
Φ	Quantum yield
K_r	Radiative rate constant
K_{nr}	Non–radiative rate constant

PREFACE

The structure–property relationship of the sensitizers plays a pivotal role in designing the suitable materials for optoelectronic devices. However, in the bulk heterojunction (BHJ)–based organic photodetectors (OPDs) devices using phenyl-C₆₁-butyric acid methyl ester (PCBM) as an electron acceptor, the ultrafast processes of photoinduced charge–transfer, charge carrier generation and their recombination control the efficiency of the devices.¹ Though a large number of steady–state and time–resolved photophysical properties of squaraine derivatives (SQs) were widely reported,^{2–6} the intermolecular interaction dynamics of unsymmetrical squaraine derivatives (USQ) with PCBM have not been investigated in detail. In this regard, herein, we report the design and synthesis of various USQ derivatives containing *N,N*–dimethyl aminoanthracene and other the aromatic donors such as pyrrole appended phenyl hydrazine, benzothiazolium and indolium moieties, which can extend the spectral window of OPDs to the near–infrared (NIR) region. The steady–state and mainly excited–state relaxation dynamics of USQ derivatives with and without PCBM were characterized using femtosecond pump–probe spectroscopy.

In **Chapter 1**, the overview of SQs, their optical properties and the fundamentals of OPDs were discussed. A detailed literature survey on the development of SQs used as donor materials in BHJ–based OPDs is also provided.

In **Chapter 2**, the USQ derivatives consisting of *N,N*–dimethyl aminoanthracene and pyrrole appended aryl hydrazine with variable alkyl chain length [ethyl (**APSQ–et**), hexyl (**APSQ–hex**), and hexenyl (**APSQ–hexen**)] attached to the pyrrolic nitrogen were synthesized. Femtosecond transient absorption and TCSPC measurements were carried out to

get insight into the intermolecular charge-transfer dynamics between the **APSQs** and PCBM. NIR-OPDs were fabricated using **APSQs** as an electron donor in BHJ mode. The NIR-OPDs showed a broadband response that extends to ~950 nm. The optimized NIR-OPDs exhibited a photocurrent value of 1.3 mA/cm² in the presence of light, which is almost 3–5 orders of magnitude larger than the dark current (~50 nA/cm²) at -1 V bias condition. The external quantum efficiency (EQE) increased from ~4% at short circuit condition to ~12% at -1 V in the NIR region, with the peak EQE at ~840 nm. At a reverse bias of -1 V, the device with an **APSQ-et** exhibited a maximum shot-noise-limited specific detectivity of $6 \times 10^{11} \text{ cm Hz}^{1/2} \text{ W}^{-1}$ (Jones) at a working wavelength of 840 nm.

In **Chapter 3**, the USQ derivatives (**ABSQs**) with donor-acceptor-donor (D-A-D') architectures having *N,N*-dimethyl aminoanthracene and benzothiazole (**ABSQ-H**) halogenated with fluoride (**ABSQ-F**), chloride (**ABSQ-Cl**) and bromide (**ABSQ-Br**) were synthesized to understand the effect of halogen on the photophysical properties and intermolecular interaction dynamics with PCBM widely used as an electron acceptor in BHJ-based devices. Interestingly, upon halogen substitution, red shift in the absorption spectra with an increase in molar absorptivity was observed ($\epsilon \sim 8.59 \times 10^4 \text{ M}^{-1} \text{ cm}^{-1}$) which is beneficial for NIR light harvesting. Upon addition of PCBM, the fluorescence intensity and dynamics of halogenated **ABSQs** were quenched, reflecting the occurrence of intermolecular charge transfer dynamics between the **ABSQs** and PCBM. These results will help for the development of efficient USQ derivatives for optoelectronic devices.

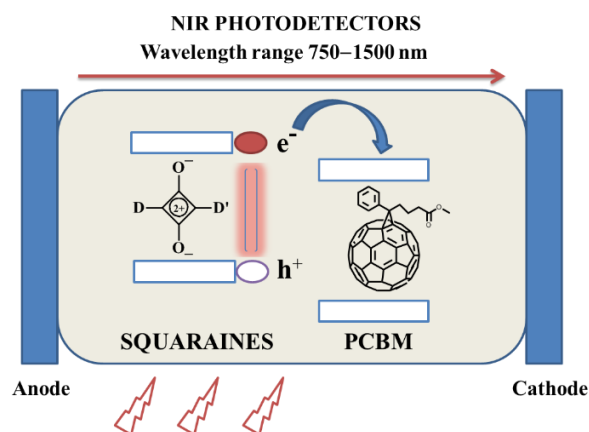
In **Chapter 4**, the USQ derivatives comprising *N,N*-dimethyl aminoanthracene and various *N*-alkylated indolium [ethyl (**AISQ-et**), hexyl (**AISQ-hex**) and

hexenyl (**AISQ–hexen**)] were synthesized. The absorption spectra of the **AISQ–et** exhibited intense absorption maximum at ~676 nm in toluene with high extinction coefficient, $\sim 8.0 \times 10^4 \text{ M}^{-1} \text{ cm}^{-1}$. The absorption spectra showed a negative solvatochromic shift with an increase in solvent polarity. When compared to the neat solvents, the absorption spectra in thin film exhibited broad in nature covering a wide range of wavelength starting from 500–800 nm due to the formation of aggregations. The femtosecond transient absorption spectra of **AISQ** derivatives were measured in nonpolar (toluene) and polar (acetonitrile, ACN) solvents to determine the effect of solvent polarity on the excited–state relaxation dynamics. It revealed that polarity of the solvent controlled the excited–state relaxation dynamics. The **AISQ** derivatives were finally applied to the OPD devices and showed sensitivity in the NIR region.

References

1. Rana, A.; Sharma, C.; Prabhu, D. D.; Kumar, M.; Karuvath, Y.; Das, S.; Chand, S.; Singh, R. K., Revealing Charge Carrier Dynamics in Squaraine:[6, 6]-Phenyl-C 71-Butyric Acid Methyl Ester Based Organic Solar Cells. *AIP Adv.* **2018**, *8*, 045302.
2. de Miguel, G.; Marchena, M.; Ziółek, M.; Pandey, S. S.; Hayase, S.; Douhal, A., Femto-to Millisecond Photophysical Characterization of Indole-Based Squaraines Adsorbed on TiO₂ Nanoparticle Thin Films. *J. Phys. Chem. C* **2012**, *116*, 12137-12148.
3. Singh, A. K.; Mele Kavungathodi, M. F.; Nithyanandhan, J., Alkyl-Group-Wrapped Unsymmetrical Squaraine Dyes for Dye-Sensitized Solar Cells: Branched Alkyl Chains Modulate the Aggregation of Dyes and Charge Recombination Processes. *ACS Appl. Energy Mater.* **2020**, *12*, 2555-2565.
4. Schreck, M. H.; Breitschwerdt, L.; Marciniak, H.; Holzapfel, M.; Schmidt, D.; Würthner, F.; Lambert, C., Fs–Ps Exciton Dynamics in a Stretched Tetraphenylsquaraine Polymer. *Phys. Chem. Chem. Phys.* **2019**, *21*, 15346-15355.
5. Marciniak, H.; Auerhammer, N.; Ricker, S.; Schmiedel, A.; Holzapfel, M.; Lambert, C., Reduction of the Fluorescence Transition Dipole Moment by Excitation Localization in a Vibronically Coupled Squaraine Dimer. *J. Phys. Chem. C* **2019**, *123*, 3426-3432.
6. Lambert, C.; Hoche, J.; Schreck, M. H.; Holzapfel, M.; Schmiedel, A.; Selby, J.; Turkin, A.; Mitric, R., Ultrafast Energy Transfer Dynamics in a Squaraine Heterotriad. *J. Phys. Chem. A* **2021**, *125*, 2504-2511.

An Overview and Development of Squaraine Dyes in Organic Photodetector Applications



1.1 Abstract

Organic light-absorbing materials with excellent semiconducting properties are of vital significance for applications in optoelectronic devices such as photodetectors. These materials are synthetically diverse, spectrally tunable, mechanically flexible, lightweight and can be processable even at temperatures (<100–150 °C). This thesis encompasses the molecular design and synthesis of novel unsymmetrical squaraine dyes (USQ) and the possibilities to extend the photoresponse of organic photodetectors (OPDs) to the near-infrared (NIR) regime. Since only a few organic and inorganic chromophores and polymers were reported for NIR sensitivity, this work for OPDs was based on potential small organic molecules. This Chapter provides an overview of the squaraine dyes (SQs), their optical properties and fundamentals of OPDs with the working mechanism. The recent advances in OPDs and their performance in the devices are also presented. In addition, the advances in the development of small molecule-based OPDs and the importance of USQ sensitizers are also discussed.

1.2 Introduction

The detection of light, one of the essential technologies, has extensive applications in industry and our daily life, e.g., communications, environmental monitoring, surveillance, advanced diagnosis and image sensors. Organic based semiconductors have become a promising class of materials, with several applications being developed at the research and development and industrial level, supported by a continued research effort. One of the several applications to which organic semiconductors have been applied is photodetection.¹⁻² In fact, in the region from UV to the NIR, the spectral sensitivity can be made panchromatic or particularly tuned to specific wavelengths. Photodetectors (PDs) that convert incident photons into electrical signals have extensive use in photodetection applications and an essential component in electronic devices that are used for a wide range of applications. Currently available commercial PDs are mainly based on inorganic semiconducting materials such as crystalline silicon, germanium, and indium gallium arsenide as the active layer.³ However, the processing of highly ordered crystalline inorganic materials needs high temperature, high vacuum, and complex lithography, which are expensive for device fabrication. Also, inorganic materials are fragile and hard to implement in flexible devices, preventing their application to some extent.⁴ Owing to the material tunability, inexpensive, solution processing, distinctive structure–property relationships, and high mechanical flexibility, OPDs emerged as a potential candidate for optoelectronics, mainly witnessed increasing research effort, particularly for extending their response from the visible spectrum into the NIR spectrum, leading to novel OPDs with improved NIR sensitivity and broadband activity within the past decade. In particular dyes with strong and desirable optical properties in the NIR region have made significant contributions to many fields, among which SQs have attracted specific research interests as one of the most promising materials candidates for OPDs because of

their intense absorption and emission in the visible to NIR region, as well as exceptional photochemical stability.⁵ SQs bear a π -conjugated Donor–Acceptor–Donor (D-A-D') zwitterionic molecular framework with the electron-deficient central four-membered cyclobutadione ring where the charge is delocalized over the whole molecule. **Figure 1.1** shows the simple aniline-based SQs with the corresponding zwitterionic structures.

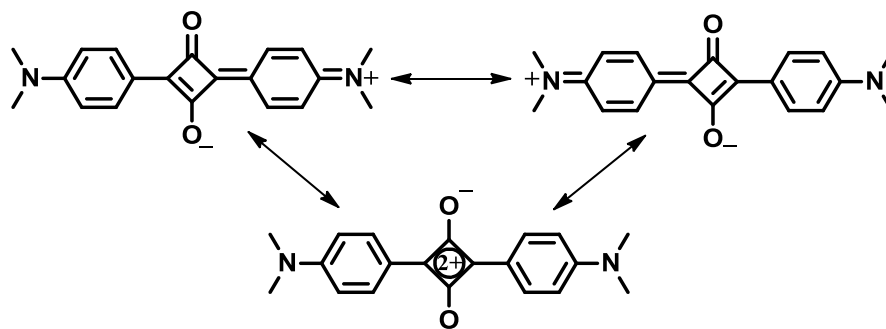


Figure 1.1 The π -conjugated zwitterionic structures of a SQs.

The first debut of SQs was synthesized in 1965 by Triebs and Jacob, obtained by the condensation reaction between pyrrole and squaric acid.⁶ Since then, many SQs have progressively reported and majority of them were prepared by the condensation between squaric acid and a variety of electron-rich aromatic/heterocyclic moieties such as *N,N*-dialkylamines, indolenines, phenols, and benzothiazoles.

1.3 Squaraines and their optical properties

According to the structures of SQs, they can be categorized into symmetrical and USQ dyes. Symmetrical SQs have the same electron-donating groups on either sides of the four membered ring, so the synthesis requires two equivalents of electron-rich aromatic/heterocyclic compounds and an equivalent of squaric acid. Upon refluxing in butanol/benzene mixture, symmetrical SQs can be obtained with high yields (~63%).⁷ The USQ dyes, have different

electron-donating groups on both sides, therefore the synthesis is complicated. In general, the synthesis and isolation of the semi-squaraine is essential and crucial in order to obtain USQ dyes. Based on the type of the terminal donors, USQ dyes can be categorized into three types, (i) Aromatic/heteroaromatic USQ dyes: cyclobutadione ring connected to two different aromatic/heteroaromatic donors, (ii) Heterocyclic USQ dyes: squaryl ring connected to two different heterocycles through reactive methylene group (iii) Mixed USQ dyes: squaryl ring connected with an aromatic/heterocyclic donor. The general structures of these USQ dyes are shown in **Figure 1.2**. Other derivatives such as core substituted SQs,⁸ polysquaraines,⁹ π -extended SQs and squaraine rotaxanes¹⁰⁻¹¹ have also been reported and used in various biological and technological applications.

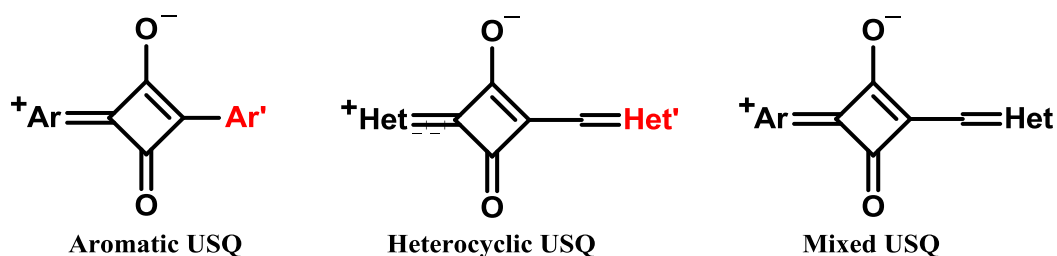


Figure 1.2 General structures of USQ dyes.

The general method employed to synthesize symmetrical SQs is the condensation of squaric acid with nucleophiles. During the reaction, water obtained by the condensation is regularly removed with a Dean-Stark apparatus,¹² leaving a solution of SQs behind. The synthesis of USQs, requires the squaric acid derivatives, such as esters of squaric acid or squarylium chloride, as the starting materials, which are much less reactive than squaric acid. As a result, the condensations result in semisquaric acid esters/squarylium chlorides. Both of the products can be converted into semisquaric acids after treatment with bases and/or acids. The condensation of

semisquaraine with another nucleophile yields USQ dyes.

The USQ dyes are more promising class of materials than symmetrical SQs and constitute an enormous portion of SQs chemistry due to their flexibility for synthetic modification. The structural manipulation of USQ dyes can be obtained by modification at terminal aromatic/heterocyclic donors leading to tunable photophysical and electronic properties, which encompasses their applicability for various technologically relevant applications. They generally exhibit redshift in absorption and emission and high molar extinction coefficient compared to symmetrical SQs due to more intramolecular charge-transfer (ICT) characteristics of D–A–D' type molecular structure,¹³ and also due to unidirectional flow of electrons from one donor to another through central acceptor.¹⁴ The optical bandgap of these dyes can be tuned through the choice of electron-rich aromatic/heterocyclic components and the linear extension of the cyclobutene core. Despite the photophysical properties of SQs not changing much in solution as the length of the alkyl group increases, their photophysical properties in the film state is highly influenced by the length of alkyl group due to the formation of various aggregates. The broadening and shifting of absorption and emission spectra are varied by the formation of various degrees of aggregates controlled by different side groups. The formation of aggregates of SQs is crucial to optoelectronic devices because it will affect their performance, such as the thermal stability, film morphology, excited-state lifetime and exciton diffusion length. It has been reported that aggregation could enhance exciton diffusion length through improved crystalline order and exciton mobility.¹⁵⁻¹⁶ This formation of aggregation is due to the self-association of SQs resulting from the strong intermolecular force between the molecules. They can be classified into two types based on the observation of a redshift or blue-shift absorption compared with the monomer band. The

aggregates that exhibit bathochromically shifted (redshifted) bands in absorption spectra are called J-aggregates, while others that exhibit hypsochromically shifted (blueshifted) bands are called H-aggregates. Such two different shifted absorption bands of aggregates have been explained in terms of molecular exciton coupling theory, which describes the coupling of transition moments of aggregated molecules.¹⁷

1.4 Overview of Organic Photodetectors

In OPDs, the light is detected upon absorption of incident photons with energy equal to or greater than the optical bandgap of the photoactive material. Due to the larger absorption coefficients of organic materials ($\sim 10^5 \text{ M}^{-1}\text{cm}^{-1}$) compared to Si ($\sim 50\text{--}100 \text{ M}^{-1} \text{ cm}^{-1}$), thin active layers ($\sim 100 \text{ nm}$) are adequate to absorb up to 60% of the incident light¹⁸ making them useful for photovoltaics and PDs. However, due to the lower relative permittivity ($\epsilon_r \sim 3\text{--}4$) of organic relative to inorganic semiconductors, light absorption leads to photogenerated excitons with a comparatively high binding energy of $\sim 0.35\text{--}0.5 \text{ eV}$,¹⁹ rather than free electrons and holes. Thus, like many organic photovoltaics (OPVs) devices, the active layer of OPDs is often based on a bulk heterojunction (BHJ) architecture²⁰ that comprises finely intermixed penetrating networks between the electron-donor and acceptor interface, in which their large interface area facilitates exciton dissociation and charge transport to the relevant electrodes. The **Figure 1.3a** represents the typical OPD configuration comprising a BHJ layer sandwiched between electron and hole extraction layers.²¹ The **Figure 1.3b** represents the OPD energetic band diagram under reverse bias. Photogenerated excitons separated into free charge carriers at the donor-acceptor interface then drifts to the respective electrodes due to the applied electric field.

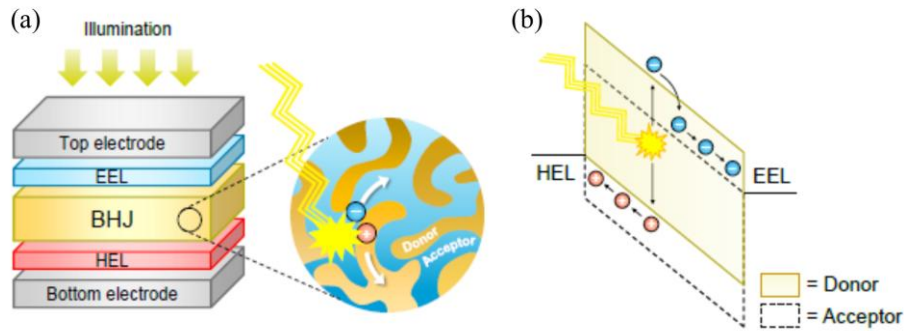


Figure 1.3 OPD architecture consisting of a BHJ layer inserted between hole and electron extraction layers (HEL and EEL) respectively (a) Energy band diagram of OPD under reverse bias (b). The Figure is copied from ref 21.

OPDs are similar to OPVs concerning their working mechanism and device structure.²²⁻²⁴ Both require diode architecture with BHJ configuration containing donor–acceptor materials.²⁵⁻²⁶ Both will operate with an external bias applied between the electrodes of the diode. However, the aim of OPVs is to obtain electrical energy from light energy, whereas that of OPDs is to convert light signals into electrical signals. To facilitate the power extraction from the devices, OPVs will operate in forward bias whereas OPDs will operate in reverse bias, which interns favorable for the light detection.²⁷ **Figure 1.4** represent the current density-voltage ($J-V$) characteristics of OPDs in linear and semilogarithmic representation respectively under dark and under illumination. The figure of merit parameter of OPVs is its power conversion efficiency (PCE). To increase the PCE of OPVs, the devices must convert as much light energy as possible from the entire solar spectrum into an electric current while instantaneously balancing the open circuit voltage and fill factor. However, the spectral response range of OPDs should be tuned according to the specific application, in contrast to OPVs, which are intended to absorb the entire solar spectrum. In addition to the spectral response, other performance factors of OPDs responsivity (R), External Quantum

efficiency (EQE), Noise Equivalent Power (NEP) and specific detectivity (D^*) are particularly essential. The simultaneous optimization of the above parameters decides the efficiency of OPD devices.²⁸⁻³⁰ Furthermore, applying a reverse bias to OPDs can improve their performance. Therefore, the OPDs can work in the third quadrant whereas the OPVs only work in the fourth quadrant.

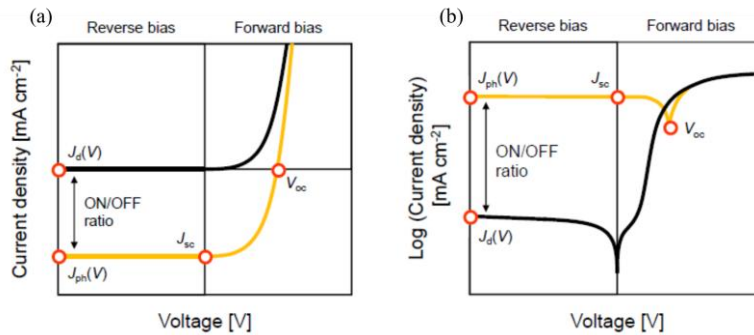


Figure 1.4 Typical J - V characteristics of OPDs in a linear (a) and semilogarithmic (b) plot under dark (black) and illumination (yellow) conditions, showing short-circuit current density (J_{sc}), open-circuit voltage (V_{oc}), and reverse bias photocurrent density (J_{ph}) and dark current density (J_d) at a given applied voltage V . The Figure is copied from the thesis ‘Device physics and applications of organic photodiodes’ by Giulio Simone (2020), Eindhoven University of Technology

1.4.1 Mechanism of Organic Photodetectors

In OPDs, the optical signal is converted into the electrical signal and the fundamental working mechanism is shown in **Figure 1.5** and it comprises the following steps 1) the absorption of the incident photons by the organic photoactive material and creates singlet Frenkel excitons ($\sim 10^{-15}$ s), 2) exciton diffusion to the acceptor interface ($< 10^{-9}$ s), 3) exciton dissociation by electron-transfer to the electronegative acceptor molecules ($\sim 10^{-14}$ s) and separation of charge-transfer excitons into free charges at the donor/acceptor interface ($\sim 10^{-6}$ s), 4) charge carrier transport to the respective electrodes and (5) extraction of the charges at electrodes to generate photocurrent.

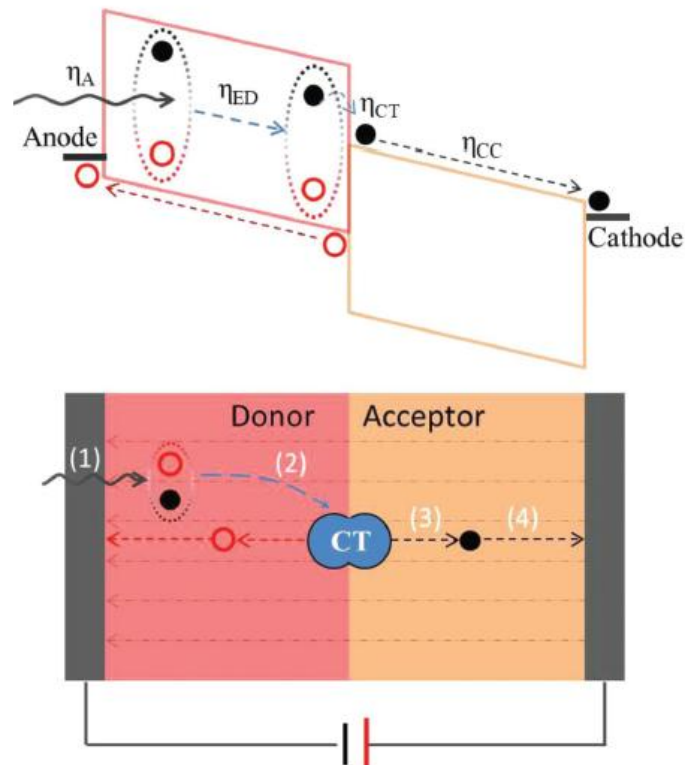


Figure 1.5 Working mechanism of OPDs from light absorption to photocurrent in a BHJ mode. Simplified energy diagram (top), from a kinetic point of view (bottom). The Figure is copied from ref. 21.

1.4.2 Performance metrics of Organic Photodetectors

(i) Photocurrent density and dark current density

The photocurrent density (J_i) and dark current density (J_d) are defined as the current density flowing through a device under illumination and in the dark, respectively. Dark current significantly increases the power consumption and complicates the signal readout. The difference between J_i and J_d is the photo-induced or photo-generated current density (J_{ph}), which depends on the photon absorption and charge transport process.

(ii) Photoresponsivity (R)

The R is defined as the ratio of photocurrent density to incident light power at a given wavelength. It describes how much current is generated by the OPD per incoming photon of a given energy. The R is thus measured in $A W^{-1}$. The R can be expressed as follows.

$$R(\lambda) = \frac{J(\lambda)_{ph}}{P(\lambda)_{in}} \quad (1)$$

Where J_{ph} is the photocurrent density, and P_{in} is the optical power density of the incident light.

(iii) External Quantum Efficiency (EQE)

EQE also referred as incident photon-to-current efficiency (IPCE), represents the number of charge carriers collected to the number of incident photons.³¹ In general, high EQE (and hence R) is desirable to ensure efficient photon flux detection. EQE is commonly represented in the more practical form R as follows.

$$EQE = \frac{R h \nu}{q} \quad (2)$$

Where q is the elementary charge and $h \nu$ is the photon energy. Thus, the EQE and R have the following relationship at a given wavelength, λ . EQE is unitless and often expressed as a percentage.

$$EQE(\lambda) = \frac{R(\lambda) 1240}{\lambda} 100\% \quad (3)$$

(iv) Noise Equivalent Power (NEP) and Specific Detectivity (D*)

NEP is a measure of the sensitivity of the PD. NEP is defined as the minimal detectable signal power, which is equivalent to the noise power yielding a signal-to-noise ratio (SNR) of 1.³¹ and it is expressed in $W Hz^{-1/2}$. The relation between i_{noise} and R as follows.

$$NEP = \frac{i_{noise}}{R} \quad (4)$$

NEP can be normalized to the bandwidth and obtain NEP_B

$$\text{NEP}_B = \frac{NEP}{\sqrt{B}} = \frac{i_{\text{noise}}}{R \sqrt{B}} \quad (5)$$

where i_{noise} is the noise current and B the detection bandwidth.

The inverse of the NEP_B is the detectivity (D) of the device, which can be normalized to the device area (A) and yield the D^* . The unit of D^* is $\text{cm Hz}^{1/2} \text{W}^{-1}$ (i.e., Jones).

$$D^* = \frac{\sqrt{A}}{\text{NEP}_B} = \frac{R\sqrt{AB}}{i_{\text{noise}}} \quad (6)$$

Even though the determination of noise current is essential for the accurate measurement of D^* , it is not always performed due to its challenging experimental techniques. Instead, the dark current (i_d) is often assumed to be the dominant contribution to noise current. Hence it is reasonable to simplify the equation as follows.

$$D^* = \frac{R(\lambda)\sqrt{AB}}{i_{\text{noise}}} = \frac{R(\lambda)\sqrt{A}}{\sqrt{2q}i_d} = \frac{R(\lambda)}{\sqrt{2q}J_d} \quad (7)$$

where $R(\lambda)$, A and B represent R , area and dark current density of the device respectively. i_{noise} , i_d and J_d represent the noise current, dark current and dark current density respectively, whereas q represents the charge of an electron.

1.5 Near-infrared Organic Photodetectors

The NIR light usually corresponds to the region of electromagnetic radiation with wavelength ranging from about 750–1400 nm.³² NIR compounds are defined as the substances that absorb or emit the NIR light, namely the absorption, emission, reflection of NIR light, or become NIR-absorbing, emitting, and reflecting under or after external stimulation, such as photoexcitation, electric fields, and chemical reactions. Despite being invisible to human visual perception, NIR sensing finds applications in several technologies, including medical monitoring,³³ quality inspection,³⁴ machine vision,³⁵ and bioimaging,³⁶ (tissue transparent

window, 700–1000 nm), telecommunications. Low bandgap organic semiconductors that absorb NIR light have attracted increasing attention for OPD applications. To construct OPDs with a NIR response, NIR–absorbing chromophores with a narrow bandgap are essential.³⁷ Both small molecule and polymer based OPDs have been widely investigated for different PDs applications. For polymers, the bandgap can be reduced by increasing the conjugation length of the material.³⁸⁻³⁹ For an example of small molecules and oligomers, NIR–absorbing phthalocyanines,⁴⁰⁻⁴¹ heptamethine salts,⁴² porphyrins,⁴³ and SQs⁴⁴⁻⁴⁵ have been applied in NIR OPDs. However, few examples of OPDs with satisfactory efficiency in the NIR can be found in literature.⁴⁶⁻⁴⁷ This is due to issues regarding synthetic accessibility, expensive, chemical stability, difficulty in processing or fabrication and solubility of low bandgap compounds.⁴⁸ Small molecules are materials of great interest due to their interesting intrinsic properties like well-defined molecular structure,⁴⁹⁻⁵⁰ high degree of purity without batch–to–batch variations,⁵¹⁻⁵² high carrier mobility⁵³ as well as increased environmental stability.⁵⁴ Moreover fabrication flexibility like better reproducibility, simple synthesis,⁵⁵ highly controllable film formation⁵⁶⁻⁵⁷ and tenability of thickness of the active layer on nanometer scale⁵⁸ make these materials interesting candidate for fabricating OPDs.

1.5.1 Small molecule–based NIR-OPDs

This chapter provides the recent advances in small molecule based materials applied to OPDs and their chemical structures are provided in **Figure 1.6**. Regarding small molecules, phthalocyanines were employed as classical materials widely used for NIR–OPDs to their characteristic absorption peak in the 600–700 nm range. In 2014 Li et al.⁵⁹ demonstrated lead phthalocyanine/C₆₀–based planar heterojunction (PHJ) mode NIR–PD, where it showed a

broad–band response extending to ~1100 nm. The performance of the NIR–OPDs was enhanced by using CuI and Bphen as anode and cathode buffer layers, respectively (**Figure 1.7a**). The optimized device exhibited an EQE and D^* of 18% and 2.34×10^{11} Jones, respectively at zero bias. When the applied reverse voltage was increased to –6 V, its EQE reached 33.2% (**Figure 1.7b**) with D^* of 6.63×10^{10} Jones.

In 2015 the same group showed enhanced OPD performance with PbPc/ C_{70} PHJ and PbPc/PbPc/ C_{70} hybrid planar–mixed molecular heterojunction (PM–HJ) structure. Both configurations showed the spectral response that covered wavelengths from 300 to 1100 nm as in the previous case. The enhancement of EQE and D^* in the NIR region was improved in the PM–HJ device. The optimized device showed EQE about 30.2% at 890 nm with 5% PbPc-doped C_{70} layers as shown in **Figure 1.8**. The enhancement is due to increased absorption efficiency, improved exciton dissociation caused by the formation of triclinic PbPc in the PbPc: C_{70} mixed film when it was deposited on a pristine PbPc layer, and high hole mobility of the PbPc-doped C_{70} layer. This results indicated that the slight modification in device structure led to improved OPD performance.⁶⁰

In 2020 Wong et al.⁶¹ fabricated the BHJ mode NIR–OPDs consisting of chloroaluminium phthalocyanine and C_{70} by varying the thickness (20, 40, 60 and 80 nm) in the ratio of 1:3. They used TAPC: 10% MoO_3 and BPhen as hole and electron transport layers respectively. Their results showed the device with 80 nm thick active layer provided enhanced performance with EQE 74.6% at 730 nm. The optimized devices exhibited the R value of ~0.439 A/W at 0 V bias (**Figure 1.9a**), while the D^* of $\sim 4.14 \times 10^{13}$ Jones at 0 V bias (**Figure 1.9b**). Their device performance suggested to use as a receiver in optical communication systems.

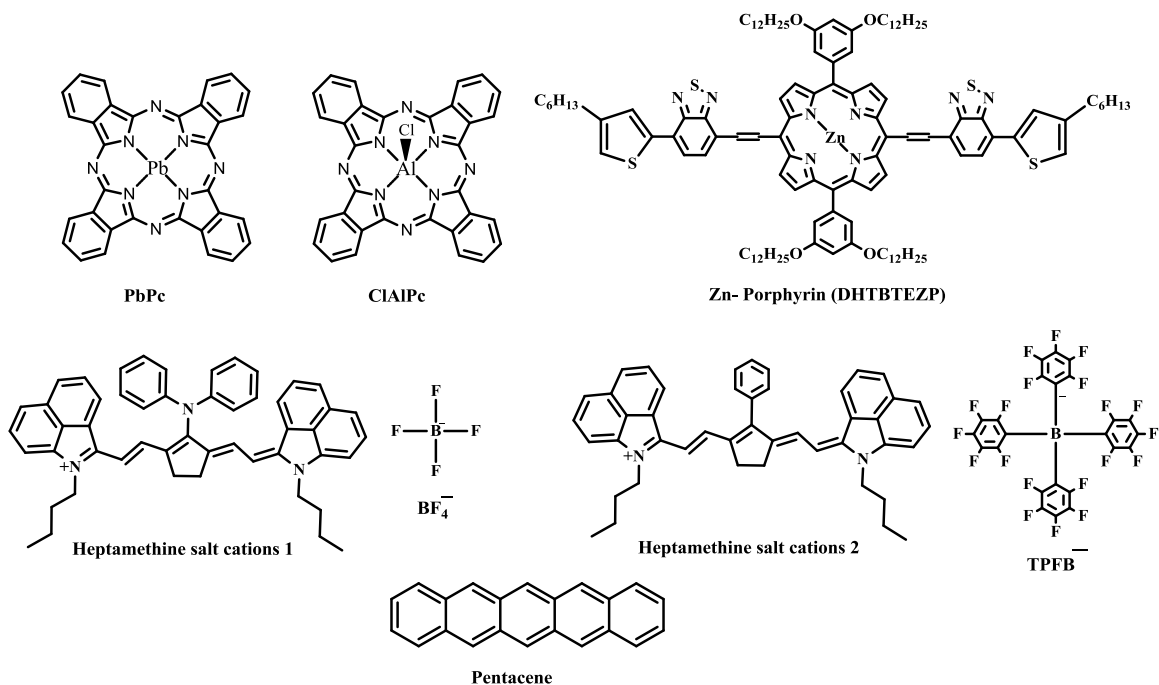


Figure 1.6 Chemical structures of lead phthalocyanine (PbPc), chloroaluminium phthalocyanine (ClAlPc), Zn–Porphyrin, heptamethine salt cation 1 and 2 with counter ions BF₄⁻ and TPFB⁻ and pentacene.

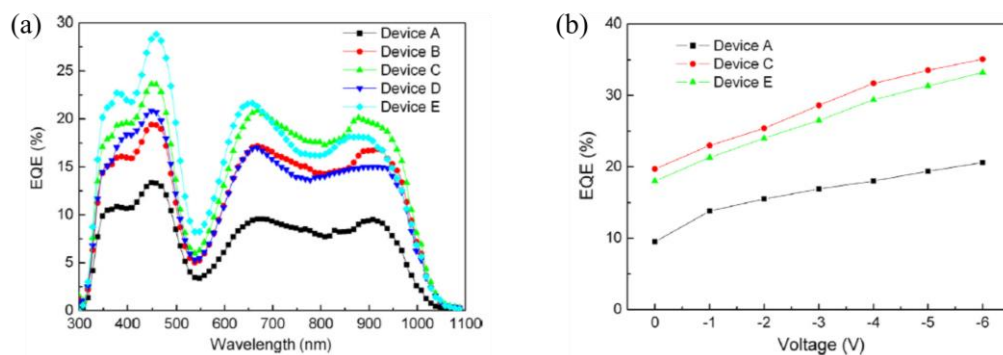


Figure 1.7 EQE spectra of the devices with CuI thickness of 0, 2, 4 and 6 nm corresponding to device A, B, C and D respectively, and Bphen thickness 10 nm for the device E at zero bias (a). EQE at 900 nm of ITO/PbPc (60 nm)/C₆₀ (60 nm)/Al (device A), ITO/CuI (4 nm)/PbPc (60 nm)/C₆₀ (60 nm)/Al (Device C), and ITO/CuI (4 nm)/PbPc (60 nm)/C₆₀ (60 nm)/Bphen (10 nm)/Al (device E) as a function of applied reverse voltage (b). The Figure is copied from ref.59.

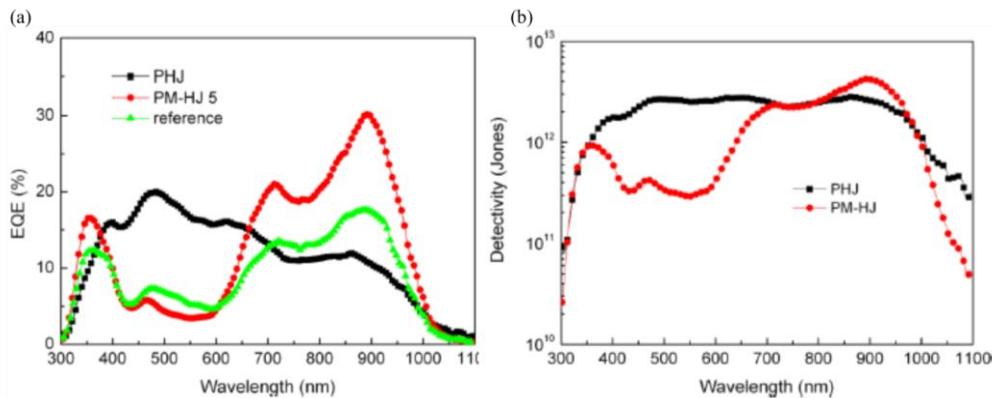


Figure 1.8 EQE spectra of the PHJ, PM–HJ 5 and reference device (a) D^* of PHJ and PM–HJ 5 device (b). The Figure is copied from ref.60.

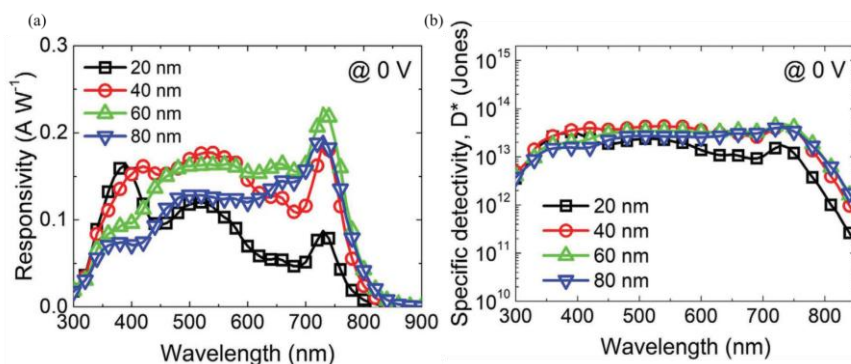


Figure 1.9 R (a) and D^* (b) of the OPD device with various active layer thicknesses by applying the zero bias voltage. The Figure is copied from ref.61.

Porphyrin–based compounds are another class of representative materials used for NIR–OPDs because the extension of π -conjugation leads to longer wavelength absorption. In 2014, Peng et al.⁴³ fabricated solution–processed NIR–OPDs based on Zn porphyrin/PC₆₁BM heterojunction. The device exhibited a broad spectral response from 380 to 960 nm with EQE around 20% in the NIR region at 0V bias (**Figure 1.10a**). The optimized devices showed a low dark current density 3.44 nA/cm² and a high photo to dark current density ratio 10^5 with D^* over 10^{12} Jones in the entire region from 380 to 930 nm (**Figure 1.10b**).

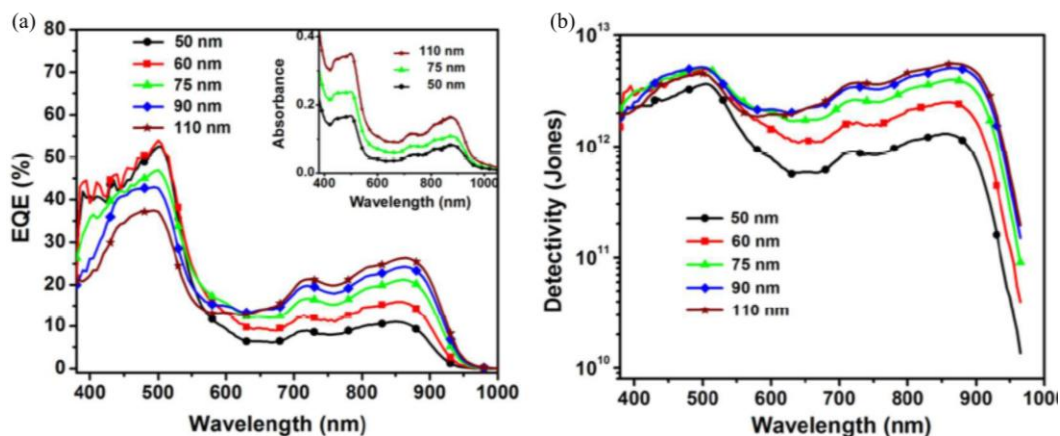


Figure 1.10 EQE of the devices with varied thicknesses of active layers under bias of 0 V. The inset displays the absorption spectra with different film thickness (a). D^* at bias of 0 V for the devices with different thickness of active layers (b). The Figure is copied from ref.43.

Cyanines are another class of functional dyes with a rigid framework, push-pull electronic structure, and extended conjugation, making their absorption and emission wavelength longer than other fluorescent dyes under the same conditions. Among various types of the length of their methine chain, heptamethine cyanine dyes are well suited for NIR-OPD applications. In 2016 Lunt et al.⁴² demonstrated the OPDs based on heptamethine dyes/ C_{60} heterojunction by exchanging counterions from heptamethine salts to BF_4^- and $TPFB^-$. The effect of counterion on the material properties of the dye was discussed. Their results showed counterion exchange shown to extend the photoresponse up to 1600 nm and increased EQE (**Figure 1.11a**). Exchange of the anion from $1-BF_4$ to $1-TPFB$ leads to increase the D^* by one order of magnitude from 3.7×10^9 to 5.3×10^{10} Jones (**Figure 1.11b**). The excellent performance is ascribed to an increase in interface gap, modest exciton binding energy (~ 0.4 – 0.55 eV) and decreased noise current for the device with the $TPFB^-$ anion.

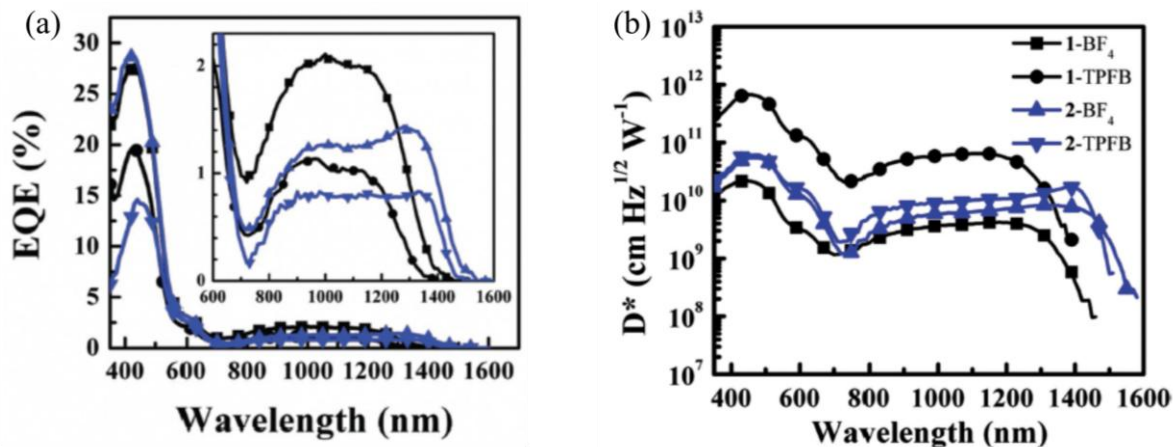


Figure 1.11 EQE spectra of the devices with salts of 12 nm thickness. The inset represents the EQE in the NIR region (a). D^* spectra for devices made with each salt donor (b). The Figure is copied from ref.43.

Polycyclic aromatic hydrocarbons such as pentacene are also employed in the photodetection in the NIR region. In 2020 Roy et al.⁶² fabricated pentacene/ C_{60} bilayer heterojunction OPD using thermal evaporation. They investigated the surface morphology of pentacene/ C_{60} heterojunction by the influence of thermal annealing. Their devices showed a broad response from 400 to 700 nm with improved device performance on thermal annealing. The R of the devices has increased from 0.0028 to 0.025 A/W (650 nm) at thermal annealing at 90 °C. The EQE and D^* of the devices were found to be 5% (**Figure 1.12a**) and 2×10^{10} Jones at 650 nm (**Figure 1.12b**). The increase of R on thermal treatment is due to the development of small grain size of the active layer materials favoring charge transport in the heterojunction.

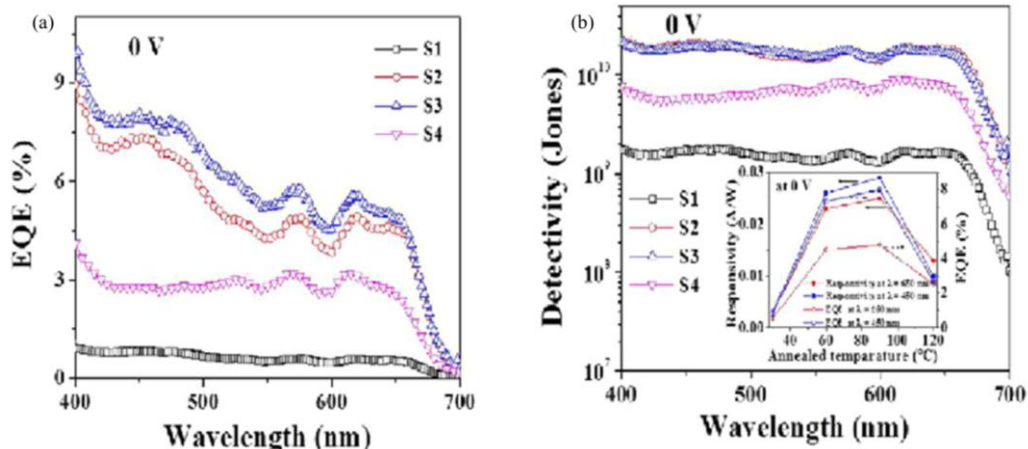


Figure 1.12 EQE (a). D^* (b) spectra for S1, S2, S3 and S4 devices at 0 bias. The inset shows EQE and R at 0 bias versus annealing temperature at 450 nm and 650 nm. The Figure is copied from ref.62.

1.5.2 Squaraine-Based OPDs

Recently there has been a great interest in using functional SQs for NIR-OPD applications due to their extensive material library. The suitable choice of the donor and acceptor moieties allows for tuning the optical and electronic properties of the dyes. The combination of strong donors with strong acceptors as well as a high degree of extended conjugation leads to a redshift of the absorption band. **Figure 1.13** displays the molecular structure of various SQs employed in OPD applications. In 2009, Binda et al.⁶³ developed fast and air stable NIR-OPDs based on pyrrole appended hydrazine symmetric SQs with alkyl and glycolic functionalized substituents. Both the dyes exhibited an intense absorption in the NIR region (**Figure 1.14a**). The optimized devices showed an EQE of 3.5% at 670 nm for 1:3 blend film of Gly SQ:PC₆₁BM as shown in **Figure 1.14b**. The efficiency, speed and stability of the optimized device were improved by tailoring the SQs substitution pattern and by tuning the blend composition. By such modification,

they achieved the smooth morphology in the optimized blend, which enables long-term air stability without further encapsulation. In addition, a good balance in charge carrier transport leads to a high EQE of 3.5% with a fast response speed in the range of few hundreds of nanoseconds.

In 2011 the same group⁶⁴ fabricated 1:3 blend film Gly SQ:PCBM (phenyl-C₆₁-butyric acid methyl ester) showed a high detectivity 3.4×10^{12} Jones with an EQE of about 15% at a wavelength of 700 nm (**Figure 1.15**). The enhanced R of the devices was due to the reduction of the dark current with simultaneously maintaining its EQE, as high as 15% at 700 nm. This was achieved by selecting the suitable hole transport layer (HTL) MEH-PPV, exploited to suppress electron injection from the device anode into the 1:3 blend film of GlySQ:PCBM, thus dropping the dark currents by a factor of 30, to the enormously low value of 2 nA/cm². In addition, the detector bandwidth (~1MHz) has a negligible effect on the R with the MEH-PPV.⁶⁵

In 2015 Zhang et al.⁶⁶ demonstrated a single crystalline aniline-based symmetric SQs nanowire and crystalline silicon heterojunction by a drop-casting method. Their devices showed a panchromatic spectral response from visible to NIR region due to the complementary absorption spectrum of SQs nanowire with silicon (**Figure 1.16a**). In addition, the devices are ultrahigh sensitive, fast responsive with excellent stability due to the high built-in field and the effective reduction of dark current. The R and D* of the devices are found to be 1.0 A/W and 6×10^9 Jones respectively from 254 to 980 nm (**Figure 1.16b**).

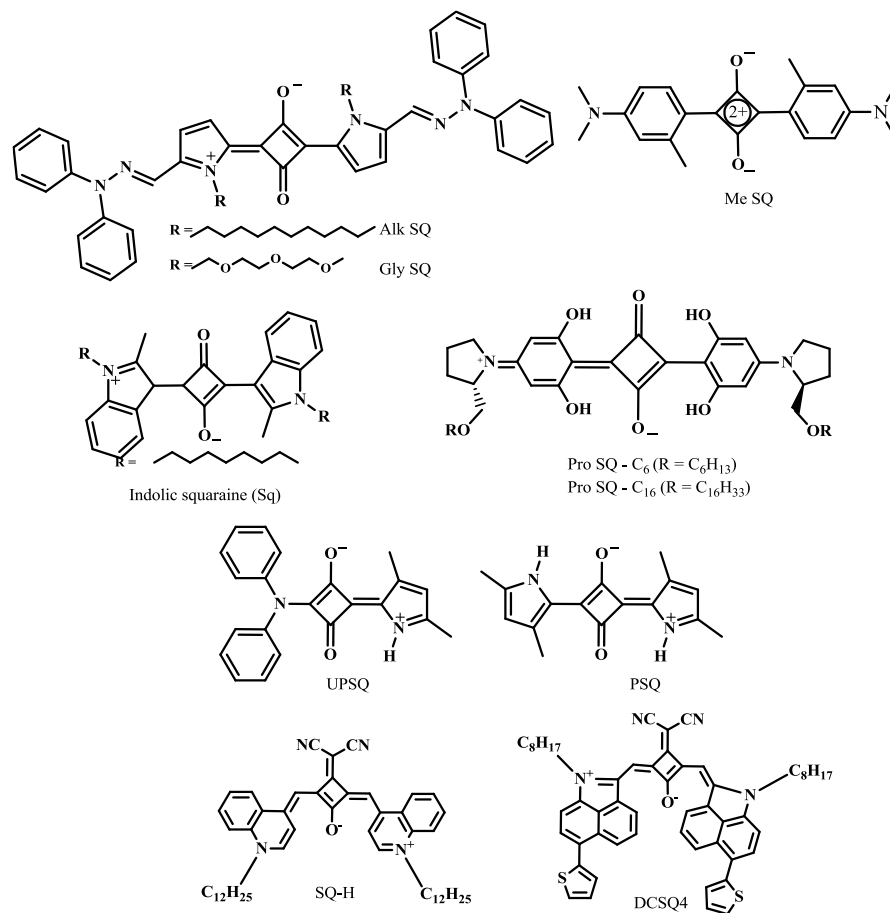


Figure 1.13 Chemical structures of SQs reported for OPDs.

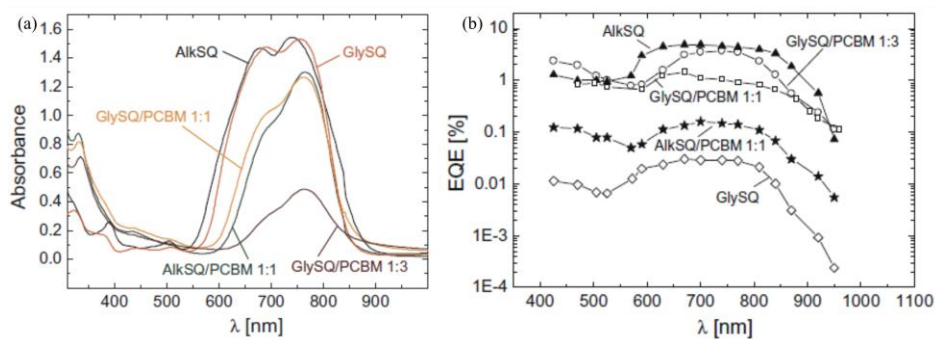


Figure 1.14 Solid-state absorption spectra of films based on pristine and blended SQs Alk SQ and Gly SQ (a). EQE of the devices on pristine Alk SQ, Alk SQ/PCBM blend with 1:1 by weight ratio, pristine Gly SQ, Gly SQ/PCBM blend with 1:1 by weight ratio and Gly SQ/PCBM blend with 1:3 by weight ratio upon light irradiation with 500 μs long light pulses (b). The Figure is copied from ref. 63.

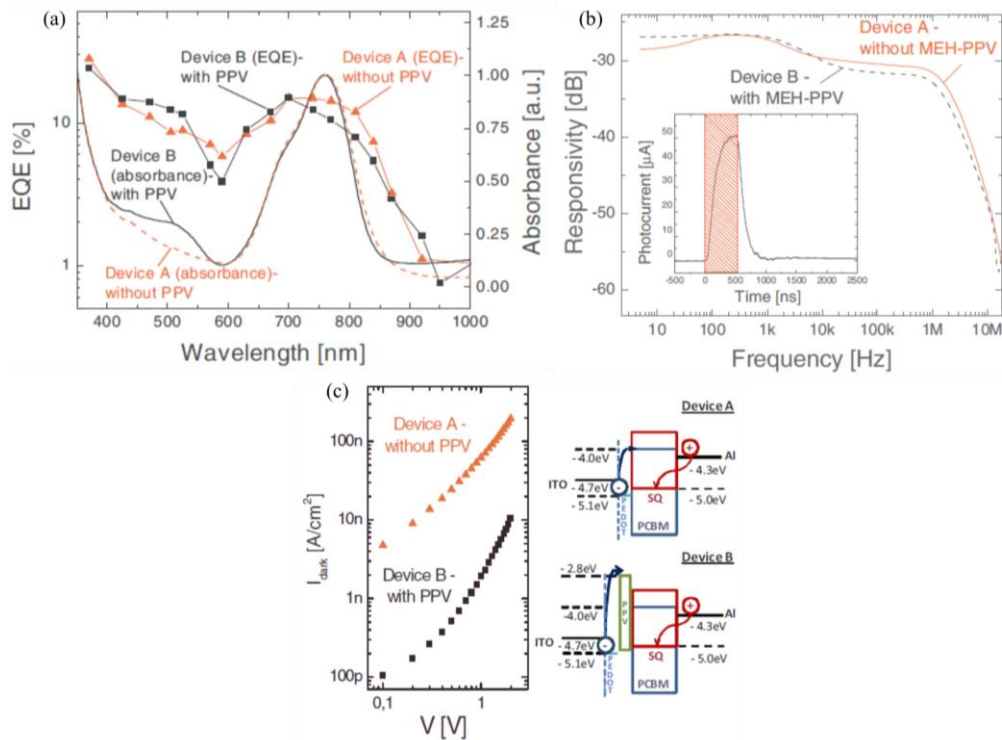


Figure 1.15 EQE of SQ: PC₆₁BM based OPDs with (squares–device B) and without (triangles –device A) the MEH–PPV layer. Solid and dashed lines show the normalized absorption spectra of devices B and A respectively (a). Normalized R as a function of frequency for the devices with (dashed line–device B) and without (solid line–device A) (b). Dark current densities for the devices with and without MEH–PPV blocking layer. On the right, a sketch of the expected energy level alignment for devices A and B (c). The Figure is copied from ref. 64.

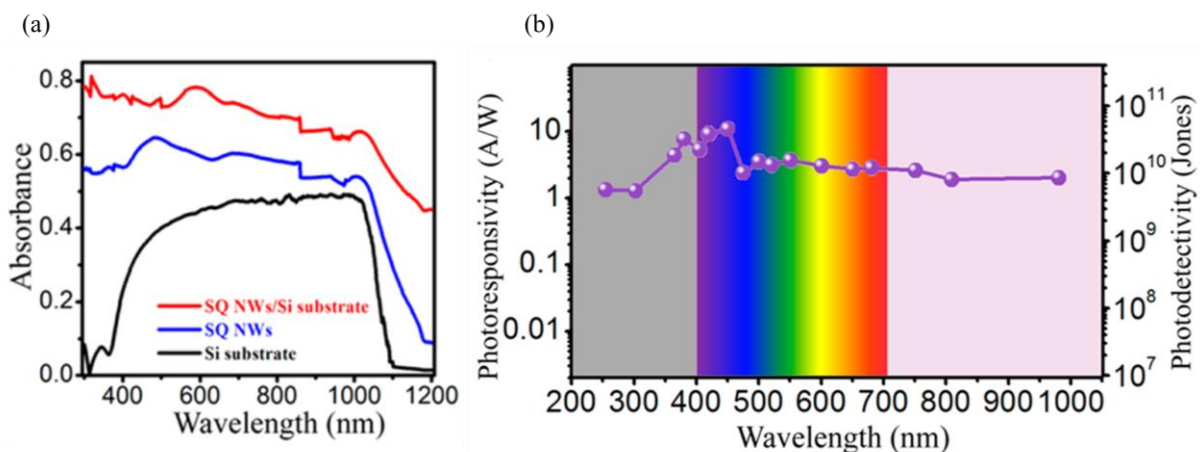


Figure 1.16 Absorption spectra of SQs nanowires on Si substrate and quartz substrate (a). R and D* of the SQs nanowire/c-Si-p-n junction at –3 V (b). The Figure is copied from ref. 66.

In 2015 Bellani et al.⁶⁷ developed PDs based on indolic symmetric SQs/PCBM heterojunction device structure (**Figure 1.17a**). The dye exhibited an absorption from 550 to 750 nm. The optimized blend showed the EQE as high as 12% at -1 V at the working wavelength of 590 nm (**Figure 1.17b**). The J–V curve of the device in the dark biased between 0.5 and 2 V, showed a photodiode-like behavior similar to previously reported SQs OPD devices.⁶⁸ The charge carrier transport of the devices was characterized by the admittance spectroscopy, which enabled the direct determination of the charge carrier mobility and recombination mechanism on the working devices. At low applied voltages (≤ 2 V), charge carrier transport is dominated by holes with an electric field-dependent mobility value of 10^{-5} to 10^{-4} $\text{cm}^2 \text{V}^{-1} \text{s}^{-1}$ suggesting the occurrence of a unipolar regime. At higher applied voltages (≥ 2 V) the device is operating in the bipolar regime suggesting the trap-mediated carrier recombination mechanism.

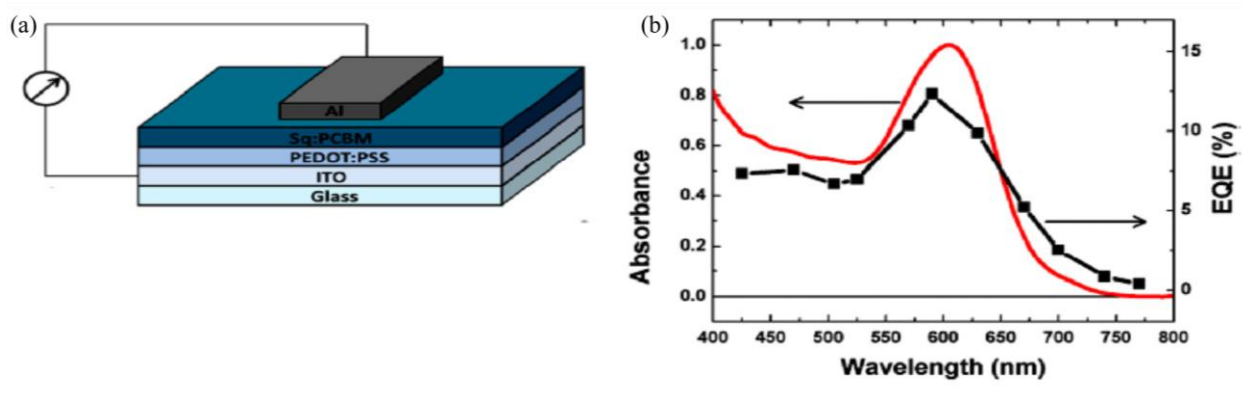


Figure 1.17 Schematic of vertical geometry of the monolithic PD device (a). Optical absorbance (red line) of the indolic SQs with PC₆₁BM as active material and EQE (black squares) spectrum of the OPD (b). The Figure is copied from ref. 67.

In 2017 Schiek et al.⁴⁴ fabricated OPDs based on circular dichroic active material homochiral L-Proline derived SQs/fullerene blend films. The neat and blended film showed H- and J-aggregate behavior with large splitting. The blend performance was recorded by varying

the active material's blend ratio and layer thickness. The J–V measurements exhibited light intensity dependant characteristics (**Figure 1.18a**). The optimized devices showed an EQE of 45% at 550 nm under modest reverse bias conditions for ProSQ–C₆₀: PCBM. The EQE exceeded 100% at 300 nm to 450 nm region in PCBM–rich devices (**Figure 1.18b**).

In 2021 Dond et al.⁶⁹ fabricated narrowband responsive OPDs based on diphenylamine and pyrrole bearing USQ dye and the absorption spectrum in solution and film state is depicted in **Figure 1.19a**. Their devices showed light selectivity with a peak at 500 nm and the absorption width of the film was significantly reduced due to the steric hindrance effect of the diphenylamine group. The EQE of the optimized devices reached 16% at –3 V in the working wavelength of 500 nm with a narrow responsive spectrum whose FWHM is ~90 nm, as shown in **Figure 1.19b**. The D* of the optimized devices was found to be 1×10^{11} Jones (**Figure 1.19c**). Their results indicated that the steric hindrance effect is pivotal in fabricating narrow–band green selective OPDs.

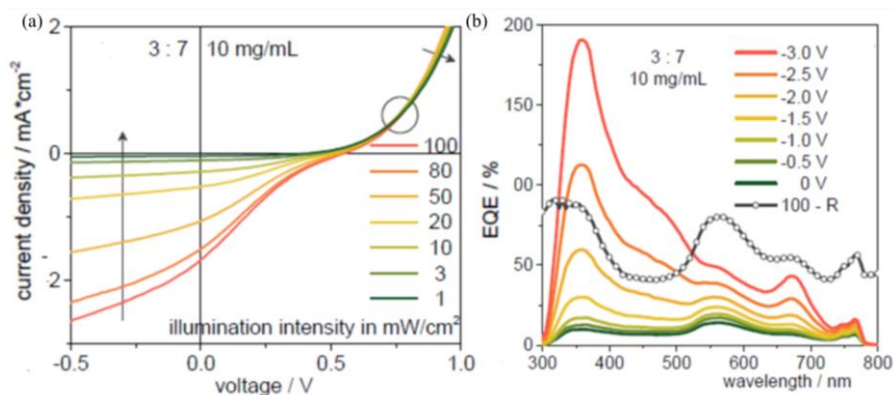


Figure 1.18 J–V characteristics with varying illumination intensity of 3:7, 10 mg/mL ProSQ–C₆₀: PCBM active layer blend (a). EQE (solid lines) and absorption (open circles) calculated from reflection measurements of 3:7 10 mg/mL ProSQ–C₆₀: PCBM photodiodes (b). The Figure is copied from ref. 44.

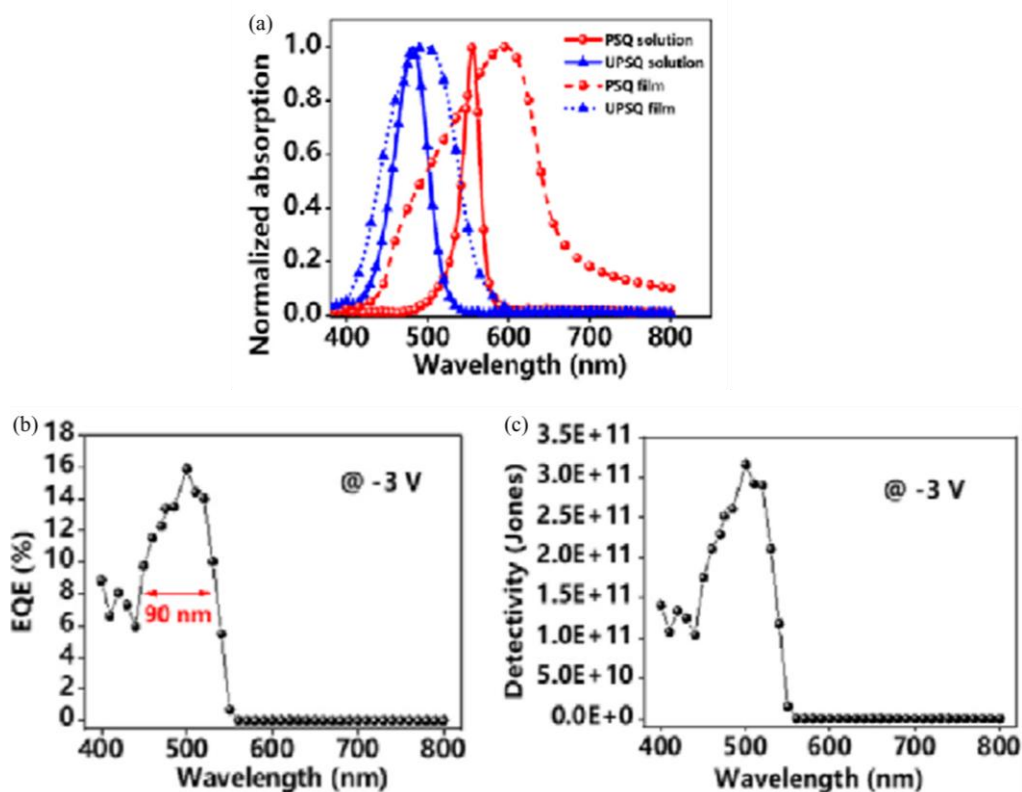


Figure 1.19 Absorption spectra of PSQ and UPSQ in DCM and thin film (a). The EQE of the UPSQ-based OPD at -3 V (b). D^* of the device at -3 V (c). The Figure is copied from ref. 69.

In 2021 Wurthner et al.⁴⁶ fabricated a short wave infrared (SWIR, $\lambda > 1000$ nm) organic photodiode using a dicyanovinyl functionalized squaraine dye (SQ-H) with PC₆₁BM. It showed a redshift and sharp absorption band at 1040 nm (**Figure 1.20a**) with an improved charge carrier mobility. The enhanced OPD showed an EQE of 12.3% and a full-width half-maximum of 85 nm (815 cm⁻¹) at 1050 nm under 0 V (**Figure 1.20b**). Photoplethysmography application for heart rate monitoring was constructed on flexible substrates at 0 bias voltage.

In 2021 Strassel et al.⁴⁷ fabricated benzindole capped SWIR SQs-based devices. In the solid-state the absorbance in the thin film extended considerably beyond 1100 nm. The optimized

devices exhibited an EQE over 30% at the working wavelength of 1100 nm at -8V (**Figure 1.21**).

Then they combined the OPD with a fluorescent organic light-emitting diode (OLED) and fabricated a highly stable organic upconversion device (OUCs) extending to beyond 1200 nm.

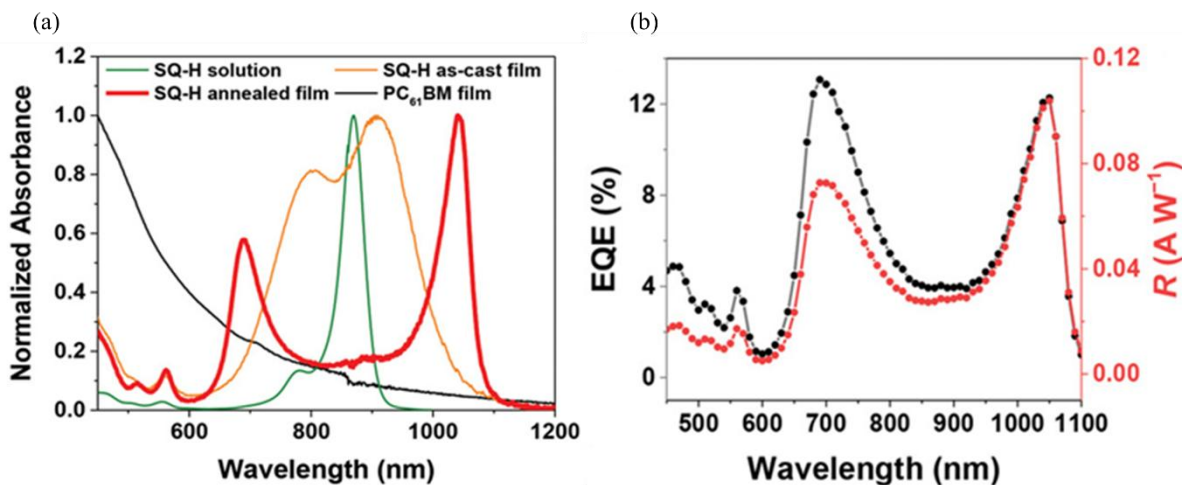


Figure 1.20 Absorption spectra of the SQ-H in DCM solution (solid green line) and thin film (solid orange line: as-cast; solid red line: after annealing at $130\text{ }^{\circ}\text{C}$ for 15 min) and of the PC₆₁BM in thin-film (solid black line) on quartz window (a) EQE (black) and R (red) of OPDs under unbiased condition (b). The Figure is copied from ref. 46.

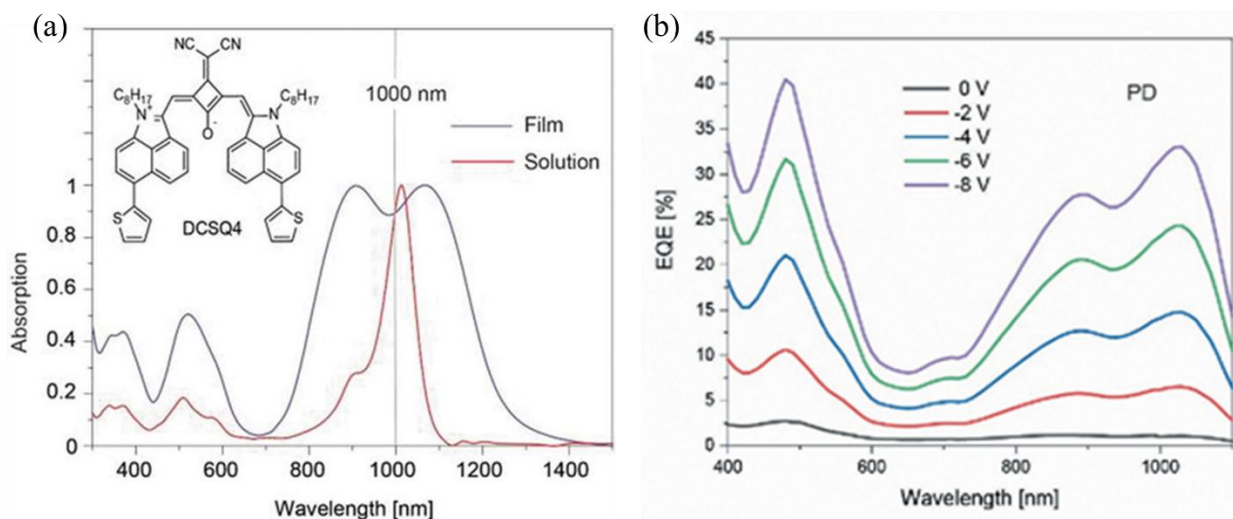


Figure 1.21 Absorbance spectra of DCSQ 4 in thin film and solution (a). EQE of the OPD as function of voltage bias (b). The Figure is copied from ref. 47.

1.6 Objectives of the Thesis

The primary objectives of the thesis are to design and synthesis of *N,N*-dimethyl amino anthracene based USQ derivatives by covalently linking the aromatic donors such as pyrrole appended phenylhydrazine, benzothiazolium and indolium moieties to obtain the spectral sensitivity of OPDs to the NIR regime. Since the ultrafast processes of photoinduced charge-transfer, charge carrier generation and their recombination control the efficiency of the devices, the excited-state relaxation dynamics of USQ derivatives with and without PCBM have been characterized using femtosecond pump-probe spectroscopy. Finally, all the USQ derivatives were applied to the optoelectronic devices. The details of the objectives and results of each chapter are provided below.

Chapter 2 particularly describes the design and synthesis of the USQ derivatives consisting of *N,N*-dimethyl aminoanthracene and pyrrole appended aryl hydrazine with various alkyl chain lengths attached to the pyrrolic nitrogen (**APSQs**). The steady-state and time-resolved photophysical studies are carried out in detail. The occurrence of intermolecular charge-transfer dynamics between **APSQs** and PCBM are corroborated by TCSPC and femtosecond pump-probe spectroscopy. The **APSQ** derivatives were used as donor molecule in BHJ-based OPDs with PCBM as the acceptor. The NIR-OPDs showed a broadband response that extends to ~950 nm.

Chapter 3 discusses the design and synthesis of the USQ derivatives (**ABSQs**) comprising *N,N*-dimethyl aminoanthracene and benzothiazole (**ABSQ-H**) halogenated with fluoride (**ABSQ-F**), chloride (**ABSQ-Cl**) and bromide (**ABSQ-Br**). The steady-state and time-resolved photophysical properties of **ABSQs** derivatives were investigated to understand the effect of halogen on the photophysical properties and intermolecular interaction dynamics with PCBM. It

is found that upon halogenation of **ABSQs**, the absorption spectra showed a red shift with an increase of molar absorptivity and interacted firmly with the PCBM. The **ABSQ-H** and **ABSQ-Cl** derivatives were applied to the OPDs and showed sensitivity in the NIR region.

Chapter 4 describes the design and synthesis of the USQ derivatives consisting of *N,N*-dimethyl aminoanthracene and *N*-alkylated indolium (**AISQs**). The steady-state and time-resolved photophysical studies are carried out in detail. The femtosecond transient absorption spectra of **AISQs** derivatives were measured in toluene and ACN solvents upon excitation at 600 nm using femtosecond pump-probe spectroscopy. It revealed that the polarity of the solvent controlled the excited state relaxation dynamics. The quenching of fluorescence intensity and lifetime upon the addition of PCBM reflected the occurrence of intermolecular charge-transfer dynamics between the **AISQs** and PCBM. The **AISQ-et** derivative was applied to the OPDs and showed sensitivity in the NIR region.

1.7 References

1. Simone, G.; Dyson, M. J.; Meskers, S. C. J.; Janssen, R. A. J.; Gelinck, G. H., Organic Photodetectors and Their Application in Large Area and Flexible Image Sensors: The Role of Dark Current. *Adv. Funct. Mater.* **2020**, *30*, 1904205.
2. Jansen-van Vuuren, R. D.; Armin, A.; Pandey, A. K.; Burn, P. L.; Meredith, P., Organic Photodiodes: The Future of Full Color Detection and Image Sensing. *Adv. Mater.* **2016**, *28*, 4766-4802.
3. Michel, J.; Liu, J.; Kimerling, L. C., High-Performance Ge-on-Si Photodetectors. *Nat. Photonics*, **2010**, *4*, 527-534.
4. Manders, J. R.; Lai, T.-H.; An, Y.; Xu, W.; Lee, J.; Kim, D. Y.; Bosman, G.; So, F., Low-Noise Multispectral Photodetectors Made from All Solution-Processed Inorganic Semiconductors. *Adv. Funct. Mater.* **2014**, *24*, 7205-7210.
5. Khopkar, S.; Shankarling, G., Synthesis, Photophysical Properties and Applications of Nir Absorbing Unsymmetrical Squaraines: A Review. *Dyes Pigm.* **2019**, *170*, 107645.
6. Treibs, A.; Jacob, K., Cyclotrimethine Dyes Derived from Squaric Acid. *Angew. Chem.* **1965**, *4*, 694-694.
7. Beverina, L.; Salice, P., Squaraine Compounds: Tailored Design and Synthesis Towards a

- Variety of Material Science Applications. *Eur. J. Org. Chem.* **2010**, 2010, 1207-1225.
8. Wu, J.; Yang, D.; Wang, Q.; Yang, L.; Sasabe, H.; Sano, T.; Kido, J.; Lu, Z.; Huang, Y., Central Dicyanomethylene-Substituted Unsymmetrical Squaraines and Their Application in Organic Solar Cells. *J. Mater. Chem. A*, **2018**, 6, 5797-5806.
 9. Garbay, G.; Tailliez, T.; Pavlopoulou, E.; Oriou, J.; Bezirdjoglou, M.; Hadziioannou, G.; Cloutet, E.; Brochon, C., Triaryl-1,4-Diamine-Based Polysquaraines: Effect of Co-Solvent and Monomer Insertion on Optoelectronic Properties. *Polym. Chem.* **2018**, 9, 1288-1292.
 10. Cole, E. L.; Arunkumar, E.; Xiao, S.; Smith, B. A.; Smith, B. D., Water-Soluble, Deep-Red Fluorescent Squaraine Rotaxanes. *Org. Biomol. Chem.* **2012**, 10, 5769-5773.
 11. Jarvis, T. S.; Collins, C. G.; Dempsey, J. M.; Oliver, A. G.; Smith, B. D., Synthesis and Structure of 3,3-Dimethylindoline Squaraine Rotaxanes. *J. Org. Chem.* **2017**, 82, 5819-5825.
 12. Tatars, A.; Fedyunyaeva, I.; Terpetschnig, E.; Patsenker, L., Synthesis of Novel Squaraine Dyes and Their Intermediates. *Dyes Pigm.* **2005**, 64, 125-134.
 13. Barbero, N.; Magistris, C.; Park, J.; Saccone, D.; Quagliotto, P.; Buscaino, R.; Medana, C.; Barolo, C.; Viscardi, G., Microwave-Assisted Synthesis of near-Infrared Fluorescent Indole-Based Squaraines. *Org. Lett.* **2015**, 17, 3306-3309.
 14. Alex, S.; Santhosh, U.; Das, S., Dye Sensitization of Nanocrystalline TiO₂: Enhanced Efficiency of Unsymmetrical Versus Symmetrical Squaraine Dyes. *J. Photochem. Photobiol. A*, **2005**, 172, 63-71.
 15. Lunt, R. R.; Giebink, N. C.; Belak, A. A.; Benziger, J. B.; Forrest, S. R., Exciton Diffusion Lengths of Organic Semiconductor Thin Films Measured by Spectrally Resolved Photoluminescence Quenching. *J. Appl. Phys.* **2009**, 105, 053711.
 16. Lunt, R. R.; Benziger, J. B.; Forrest, S. R., Relationship between Crystalline Order and Exciton Diffusion Length in Molecular Organic Semiconductors. *Adv. Mater.* **2010**, 22, 1233-1236.
 17. Kasha, M.; Rawls, H. R.; El-Bayoumi, M. A., The Exciton Model in Molecular Spectroscopy. *Pure Appl. Chem.* **1965**, 11, 371-392.
 18. The Electronic Structure of Organic Semiconductors. In *Electronic Processes in Organic Semiconductors*, 2015; pp 1-86.
 19. Scharber, M. C.; Sariciftci, N. S., Efficiency of Bulk-Heterojunction Organic Solar Cells. *Prog. Polym. Sci.* **2013**, 38, 1929-1940.
 20. Huang, Y.; Kramer, E. J.; Heeger, A. J.; Bazan, G. C., Bulk Heterojunction Solar Cells: Morphology and Performance Relationships. *Chem. Rev.* **2014**, 114, 7006-7043.
 21. Yang, D.; Ma, D., Development of Organic Semiconductor Photodetectors: From Mechanism to Applications. *Adv. Opt. Mater.* **2019**, 7, 1800522.
 22. Armin, A.; Hamsch, M.; Kim, I. K.; Burn, P. L.; Meredith, P.; Namdas, E. B., Thick Junction Broadband Organic Photodiodes. *Laser Photonics Rev.* **2014**, 8, 924-932.
 23. Armin, A.; Jansen-van Vuuren, R. D.; Kopidakis, N.; Burn, P. L.; Meredith, P., Narrowband Light Detection Via Internal Quantum Efficiency Manipulation of Organic

Photodiodes. *Nat. Commun.* **2015**, *6*, 6343.

24. Pierre, A.; Gaikwad, A.; Arias, A. C., Charge-Integrating Organic Heterojunction Phototransistors for Wide-Dynamic-Range Image Sensors. *Nat. Photonics*, **2017**, *11*, 193-199.

25. Wadsworth, A.; Hamid, Z.; Kosco, J.; Gasparini, N.; McCulloch, I., The Bulk Heterojunction in Organic Photovoltaic, Photodetector, and Photocatalytic Applications. *Adv. Mater.* **2020**, *32*, 2001763.

26. Yu, G.; Gao, J.; Hummelen, J. C.; Wudl, F.; Heeger, A. J., Polymer Photovoltaic Cells: Enhanced Efficiencies Via a Network of Internal Donor-Acceptor Heterojunctions. *Science*, **1995**, *270*, 1789-1791.

27. Deibel, C.; Dyakonov, V., Polymer–Fullerene Bulk Heterojunction Solar Cells. *Rep. Prog. Phys.* **2010**, *73*, 096401.

28. Fang, Y.; Armin, A.; Meredith, P.; Huang, J., Accurate Characterization of Next-Generation Thin-Film Photodetectors. *Nat. Photonics*, **2019**, *13*, 1-4.

29. Zhu, T.; Yang, Y.; Zheng, L.; Liu, L.; Becker, M. L.; Gong, X., Solution-Processed Flexible Broadband Photodetectors with Solution-Processed Transparent Polymeric Electrode. *Adv. Funct. Mater.* **2020**, *30*, 1909487.

30. Simone, G.; Dyson, M. J.; Weijtens, C. H. L.; Meskers, S. C. J.; Coehoorn, R.; Janssen, R. A. J.; Gelinck, G. H., On the Origin of Dark Current in Organic Photodiodes. *Adv. Opt. Mater.* **2020**, *8*, 1901568.

31. Wang, J.; Zheng, Q., Enhancing the Performance of Photomultiplication-Type Organic Photodetectors Using Solution-Processed ZnO as an Interfacial Layer. *J. Mater. Chem. C*, **2019**, *7*, 1544-1550.

32. Byrnes, J., *Unexploded Ordnance Detection and Mitigation*, 1st ed. 2009. ed.; Springer Netherlands: Dordrecht, 2009.

33. Xu, H.; Liu, J.; Zhang, J.; Zhou, G.; Luo, N.; Zhao, N., Flexible Organic/Inorganic Hybrid near-Infrared Photoplethysmogram Sensor for Cardiovascular Monitoring. *Adv. Mater.* **2017**, *29*, 1700975.

34. Millán, M. S.; Escofet, J., Fabric Inspection by near-Infrared Machine Vision. *Opt. Lett.* **2004**, *29*, 1440-1442.

35. Jonsson, P.; Casselgren, J.; Thörnberg, B., Road Surface Status Classification Using Spectral Analysis of Nir Camera Images. *IEEE Sens. J.* **2015**, *15*, 1641-1656.

36. Weissleder, R., A Clearer Vision for in Vivo Imaging. *Nat. Biotechnol.* **2001**, *19*, 316-317.

37. Qi, J.; Qiao, W.; Wang, Z. Y., Advances in Organic near-Infrared Materials and Emerging Applications. *Chem. Rec.* **2016**, *16*, 1531-1548.

38. Xia, Y.; Wang, L.; Deng, X.; Li, D.; Zhu, X.; Cao, Y., Photocurrent Response Wavelength up to 1.1 μm from Photovoltaic Cells Based on Narrow-Band-Gap Conjugated Polymer and Fullerene Derivative. *Appl. Phys. Lett.* **2006**, *89*, 081106.

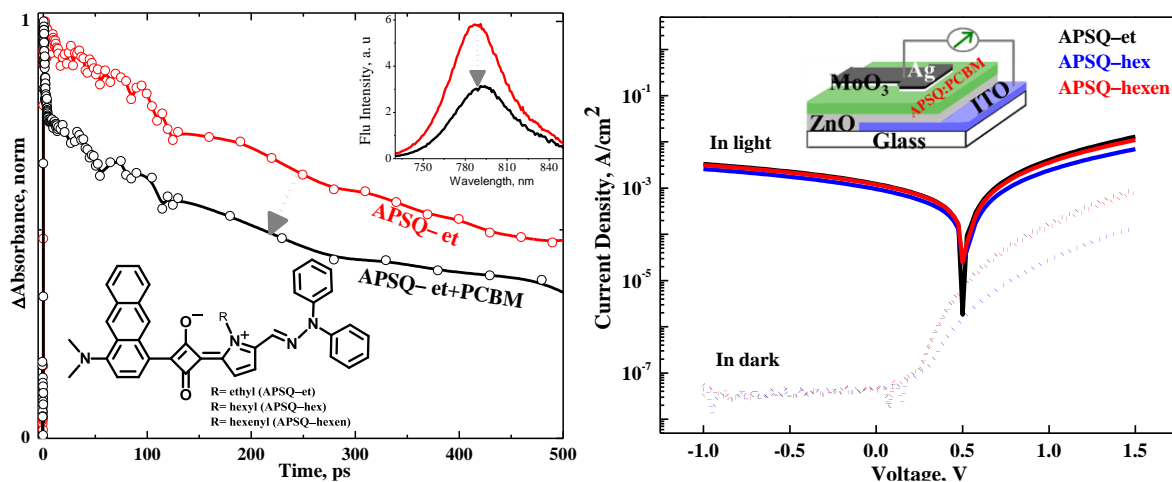
39. Liu, C.; Wang, K.; Gong, X.; Heeger, A. J., Low Bandgap Semiconducting Polymers for

- Polymeric Photovoltaics. *Chem. Soc. Rev.* **2016**, *45*, 4825-4846.
40. Abrahamse, H.; Houreld, N. N., Genetic Aberrations Associated with Photodynamic Therapy in Colorectal Cancer Cells. *Int. J. Mol. Sci.* **2019**, *20*, 3254.
41. Zink-Lorre, N.; Font-Sanchis, E.; Seetharaman, S.; Karr, P. A.; Sastre-Santos, Á.; D'Souza, F.; Fernández-Lázaro, F., Directly Linked Zinc Phthalocyanine–Perylenediimide Dyads and a Triad for Ultrafast Charge Separation. *Chem. Eur. J.* **2019**, *25*, 10123-10132.
42. Young, M.; Suddard-Bangsund, J.; Patrick, T. J.; Pajares, N.; Traverse, C. J.; Barr, M. C.; Lunt, S. Y.; Lunt, R. R., Organic Heptamethine Salts for Photovoltaics and Detectors with near-Infrared Photoresponse up to 1600 Nm. *Adv. Opt. Mater.* **2016**, *4*, 1028-1033.
43. Li, L.; Huang, Y.; Peng, J.; Cao, Y.; Peng, X., Highly Responsive Organic near-Infrared Photodetectors Based on a Porphyrin Small Molecule. *J. Mater. Chem. C*, **2014**, *2*, 1372-1375.
44. Schulz, M.; Mack, M.; Kolloge, O.; Lützen, A.; Schiek, M., Organic Photodiodes from Homochiral L-Proline Derived Squaraine Compounds with Strong Circular Dichroism. *Phys. Chem. Chem. Phys.* **2017**, *19*, 6996-7008.
45. Somashekharappa, G. M.; Govind, C.; Pulikodan, V.; Paul, M.; Namboothiry, M. A. G.; Das, S.; Karunakaran, V., Unsymmetrical Squaraine Dye-Based Organic Photodetector Exhibiting Enhanced near-Infrared Sensitivity. *J. Phys. Chem. C*, **2020**, *124*, 21730-21739.
46. Kim, J. H.; Liess, A.; Stolte, M.; Krause, A.-M.; Stepanenko, V.; Zhong, C.; Bialas, D.; Spano, F.; Würthner, F., An Efficient Narrowband near-Infrared at 1040 nm Organic Photodetector Realized by Intermolecular Charge Transfer Mediated Coupling Based on a Squaraine Dye. *Adv. Mater.* **2021**, *33*, 2100582.
47. Strassel, K., et al., Shortwave Infrared-Absorbing Squaraine Dyes for All-Organic Optical Upconversion Devices. *Sci. Technol. Adv. Mater.* **2021**, *22*, 194 - 204.
48. Kobayashi, A.; Sasa, M.; Suzuki, W.; Fujiwara, E.; Tanaka, H.; Tokumoto, M.; Okano, Y.; Fujiwara, H.; Kobayashi, H., Infrared Electronic Absorption in a Single-Component Molecular Metal. *J. Am. Chem. Soc.* **2004**, *126*, 426-427.
49. Liu, X.; Lin, Y.; Liao, Y.; Wu, J.; Zheng, Y., Recent Advances in Organic near-Infrared Photodiodes. *J. Mater. Chem. C*, **2018**, *6*, 3499-3513.
50. Wang, C.; Chen, X.; Chen, F.; Shao, J., Organic Photodetectors Based on Copper Phthalocyanine Films Prepared by a Multiple Drop Casting Method. *Org. Electron.* **2019**, *66*, 183-187.
51. Lin, Y.; Li, Y.; Zhan, X., Small Molecule Semiconductors for High-Efficiency Organic Photovoltaics. *Chem. Soc. Rev.* **2012**, *41*, 4245-4272.
52. Coughlin, J. E.; Henson, Z. B.; Welch, G. C.; Bazan, G. C., Design and Synthesis of Molecular Donors for Solution-Processed High-Efficiency Organic Solar Cells. *Acc. Chem. Res.* **2014**, *47*, 257-270.
53. Biber, M.; Aydoğan, Ş.; Çaldıran, Z.; Çakmak, B.; Karacalı, T.; Türüt, A., The Influence of Annealing Temperature and Time on the Efficiency of Pentacene: Ptdi Organic Solar Cells. *Results Phys.* **2017**, *7*, 3444-3448.

54. Zhao, Z.; Wang, J.; Miao, J.; Zhang, F., Photomultiplication Type Organic Photodetectors with Tunable Spectral Response Range. *Org. Electron.* **2019**, *69*, 354-360.
55. Joo, C. W.; Kim, J.; Moon, J.; Lee, K. M.; Pi, J.-E.; Kang, S.-Y.; Ahn, S.-D.; Park, Y.-S.; Chung, D. S., High-Performance Fab-Compatible Processed near-Infrared Organic Thin-Film Photodiode with 3.3×10^{12} Jones Detectivity and 80% External Quantum Efficiency. *Org. Electron.* **2019**, *70*, 101-106.
56. Würthner, F.; Meerholz, K., Systems Chemistry Approach in Organic Photovoltaics. *Chem. Eur. J.* **2010**, *16*, 9366-9373.
57. Lu, L.; Kelly, M. A.; You, W.; Yu, L., Status and Prospects for Ternary Organic Photovoltaics. *Nat. Photonics*, **2015**, *9*, 491-500.
58. Shafian, S.; Hwang, H.; Kim, K., Near Infrared Organic Photodetector Utilizing a Double Electron Blocking Layer. *Opt. Express*, **2016**, *24*, 25308-25316.
59. Wang, X., et al., Efficient Organic near-Infrared Photodetectors Based on Lead Phthalocyanine/C60 Heterojunction. *Org. Electron.* **2014**, *15*, 2367-2371.
60. Su, Z.; Hou, F.; Wang, X.; Gao, Y.; Jin, F.; Zhang, G.; Li, Y.; Zhang, L.; Chu, B.; Li, W., High-Performance Organic Small-Molecule Panchromatic Photodetectors. *ACS Appl. Mater. Interfaces*, **2015**, *7*, 2529-2534.
61. Lee, C.-C.; Estrada, R.; Li, Y.-Z.; Biring, S.; Amin, N. R. A.; Li, M.-Z.; Liu, S.-W.; Wong, K.-T., Vacuum-Processed Small Molecule Organic Photodetectors with Low Dark Current Density and Strong Response to near-Infrared Wavelength. *Advanced Optical Materials* **2020**, *8*, 2000519.
62. Nath, D.; Dey, P.; Joseph, A. M.; Rakshit, J. K.; Roy, J. N., Zero Bias High Responsive Visible Organic Photodetector Based on Pentacene and C60. *Opt Laser Technol*, **2020**, *131*, 106393.
63. Binda, M.; Agostinelli, T.; Caironi, M.; Natali, D.; Sampietro, M.; Beverina, L.; Ruffo, R.; Silvestri, F., Fast and Air Stable near-Infrared Organic Detector Based on Squaraine Dyes. *Org. Electron.* **2009**, *10*, 1314-1319.
64. Binda, M.; Iacchetti, A.; Natali, D.; Beverina, L.; Sassi, M.; Sampietro, M., High Detectivity Squaraine-Based near Infrared Photodetector with Na/cm^2 Dark Current. *Appl. Phys. Lett.* **2011**, *98*, 073303.
65. Binda, M.; Iacchetti, A.; Natali, D.; Beverina, L.; Sassi, M.; Sampietro, M., High Detectivity Squaraine-Based near Infrared Photodetector with Na/cm^2 Dark Current. *Applied Physics Letters* **2011**, *98*, 073303.
66. Deng, W.; Jie, J.; Shang, Q.; Wang, J.; Zhang, X.; Yao, S.; Zhang, Q.; Zhang, X., Organic Nanowire/Crystalline Silicon P-N Heterojunctions for High-Sensitivity, Broadband Photodetectors. *ACS Appl. Mater. Interfaces*, **2015**, *7*, 2039-2045.
67. Bellani, S.; Iacchetti, A.; Porro, M.; Beverina, L.; Antognazza, M. R.; Natali, D., Charge Transport Characterization in a Squaraine-Based Photodetector by Means of Admittance Spectroscopy. *Org. Electron.* **2015**, *22*, 56-61.

68. Iacchetti, A.; Binda, M.; Natali, D.; Giussani, M.; Beverina, L.; Fiorini, C.; Peloso, R.; Sampietro, M., Multi-Layer Organic Squaraine-Based Photodiode for Indirect X-Ray Detection. *IEEE Trans Nucl Sci IEEE T NUCL SC* **2012**, *59*, 1862-1867.
69. Guo, H.; Jiang, L.; Huang, K.; Wang, R.; Liu, S.; Li, Z.; Rong, X.; Dong, G., Unsymmetric Squaraine for Narrow Band Green-Selective Organic Photodetectors. *Org. Electron.* **2021**, *92*, 106122.

Efficient Near-Infrared Organic Photodetector Using Pyrrole Linked Aryl Hydrazine-Based Unsymmetrical Squaraine



2.1 Abstract

The USQ dyes are considered as promising candidates for BHJ-based NIR-OPDs due to their intense absorption as well as tunable spectroscopic and electrochemical properties. The USQ derivatives consisting of *N,N*-dimethyl aminoanthracene and pyrrole appended aryl hydrazine with variable alkyl chain length [ethyl (APSQ-et), hexyl (APSQ-hex), and hexenyl (APSQ-hexen)] attached to the pyrrolic nitrogen were synthesized and their steady and excited-state relaxation dynamics were studied. The absorption spectra of the derivatives showed a strong absorption maximum at around 760 nm with high molar extinction coefficient, $\sim 1.26 \times 10^5 \text{ M}^{-1} \text{ cm}^{-1}$. The LUMO energy levels of APSQs are higher in energy compared to that of the PCBM (-3.7 eV) and simultaneously the HOMO energy level of the PCBM (-6.1 eV) is lower compared to that of APSQs. Thus, the energy levels of all the derivatives are

appropriate to act as donor materials in the BHJ-based OPD with PCBM as an acceptor. Femtosecond transient absorption and TCSPC studies showed the quenching of time constants reflecting intermolecular charge-transfer dynamics between the APSQs and PCBM. NIR-OPDs were fabricated using APSQs as electron-donors in BHJ mode. The NIR-OPDs showed a broad-band response that extends to ~950 nm. The optimized NIR-OPDs exhibited a photocurrent value of 1.3 mA/cm² is observed under light illumination, which is almost 3–5 orders of magnitude greater than the dark current (~50 nA/cm²). at -1V bias condition. The NIR region, with the peak EQE at 840 nm. At a reverse bias of -1 V, the device with a APSQ-et displayed a maximum shot-noise-limited specific detectivity of $6 \times 10^{11} \text{ cm Hz}^{1/2} \text{ W}^{-1}$ (Jones) at 840 nm.

2.2 Introduction

The organic dyes with strong and desirable optical properties in the NIR region of 700–1500 nm are essential for the development of numerous optoelectronic devices used for a variety of applications, including photodynamic therapy (PDT),¹ bioimaging,² fluorescent labels,³⁻⁴ optical communications,⁵ remote monitoring⁶⁻⁷ and night vision.⁸ However, the organic detectors capable of sensing in the NIR range are limited due to the lack of advancement of their lightweight, large area, disposability, mechanical flexibility. Few classes of small molecules and oligomers of NIR absorbing dyes including cyanine dyes,⁹⁻¹² phthalocyanine,¹³⁻¹⁴ porphyrins,¹⁵ and SQs¹⁶⁻¹⁹ are feasible as sensitizers for the development of NIR-OPDs. Among other dyes, SQs comprising symmetrical D-A-D molecular architectures having electron-deficient central four-membered ring and two electron-donating chromophores exhibit intense light absorption ($\epsilon > 20000 \text{ M}^{-1}\text{cm}^{-1}$)²⁰ and emission ($\Phi \sim 0.8$)²¹ in the visible to NIR region. The optical and electrical properties of the symmetrical SQs can

be easily modified by changing the electron-donating capability of aromatic or heterocyclic peripheral substituents. However, USQ dyes are emerged as versatile sensitizers²²⁻²⁶ due to the unidirectional flow of electrons in the excited-states upon excitation yielding enhanced charge separation and leading to higher photocurrents, compared to the symmetrical derivatives.^{17, 27} Recently charge carrier and polaron dynamics have been investigated for the SQ and SQ:PC₇₁BM using ultrafast transient absorption spectroscopy resulting in the formation of polaron with a lifetime of 550 ps.²⁸ Binda et al.²⁹ developed fast and air-stable and efficient NIR planar OPD operating in the air without encapsulation of devices based on bulk heterojunction. It exhibited an EQE of 3.5% at 670 nm with a response speed of 240 ns. Recently Binda et al.³⁰ designed and fabricated OPD using hydrazine-based symmetric SQs with PCBM showed an EQE of 15% with D^* and dark current of $3.4 \times 10^{12} \text{ Hz}^{0.5} \text{ cm/W}$ at 700 nm and 2 nA/cm^2 respectively. Bellani et al.³¹ fabricated an OPD using indole-based SQs with PCBM acceptor showing the EQE of 12% at 590 nm and charge transport properties of the devices were characterized in the dark using admittance spectroscopy.

It is found that USQ dyes are more prospective molecules compared to symmetrical dyes due to the flexibility of synthetic manipulation, unidirectional flow of electrons and generating higher photocurrents compared to symmetric dyes.^{27, 32} Thus, the alteration of chromophores of terminal aromatic or heterocyclic donors of the USQ dyes provide the capability of tuning electronic and photophysical properties beneficial for the development of photoelectronic devices. Hence we have synthesized USQ dyes (**APSQs**) comprising the *N,N*-dimethyl aminoanthracene and aryl hydrazine with various alkyl chain length [ethyl (**APSQ-et**), hexyl (**APSQ-hex**) and hexenyl (**APSQ-hexen**)] attached to the pyrrolic nitrogen. (**Figure 2.1**). Interestingly the compounds showed intense NIR absorption ($\epsilon \sim 10^5 \text{ M}^{-1} \text{ cm}^{-1}$ at 760 nm) and the optical bandgap of the materials was estimated to be $\sim 1.52 \text{ eV}$,

which is appropriate for fullerene containing BHJ-based optoelectronic devices. Hence they were used as sensitizers for developing the NIR-OPDs. To explore the excited-state relaxation dynamics of APSQ derivatives, the femtosecond time-resolved transient absorption spectra (fs-TAS) in toluene and ACN were measured. The intermolecular charge-transfer dynamics between APSQs and PCBM in toluene were also investigated.

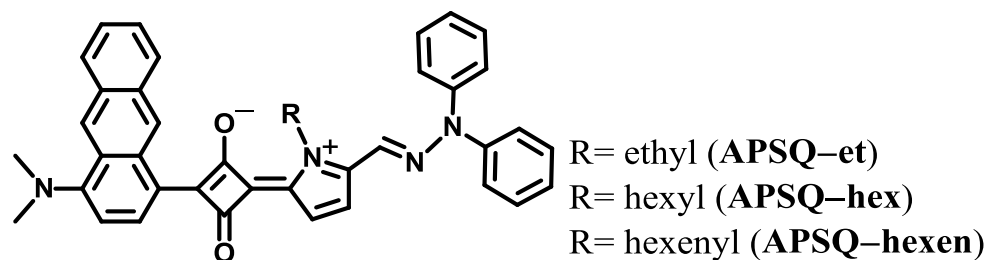
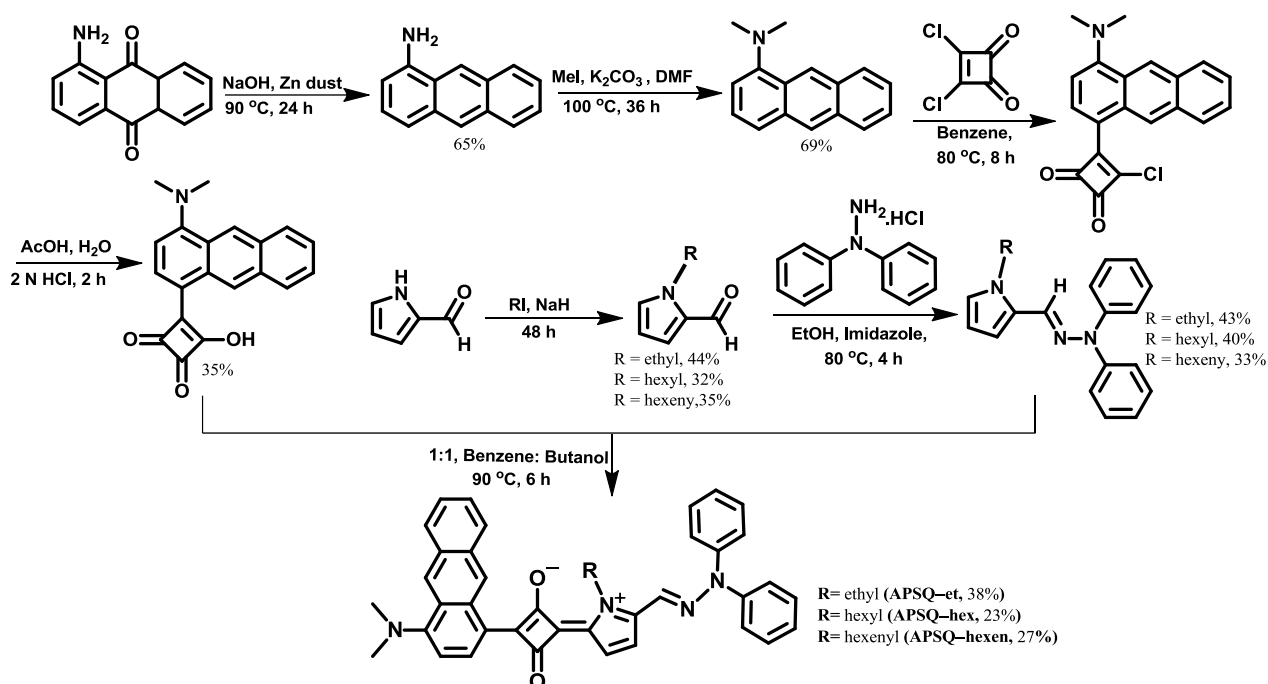


Figure 2.1 Chemical structure of APSQ derivatives.

2.3 Results and Discussion

2.3.1 Synthesis of APSQ Derivatives

The USQ derivatives (APSQs) comprising of *N,N*-dimethyl aminoanthracene and aryl hydrazine with various alkyl chain length [ethyl (APSQ-et), hexyl (APSQ-hex) and hexenyl (APSQ-hexen)] attached to the pyrrolic nitrogen were synthesized for NIR-OPDs applications. The APSQ derivatives were synthesized by modifying the previously reported procedures.³³⁻³⁵ The *N,N*-dimethyl aminoanthracene semisquaraine was prepared by the reduction and alkylation of 1-aminoanthroquinone and resulted *N,N*-dimethyl aminoanthracene treated with squarylium chloride. The alkyl and alkenylated pyrrole attached phenylhydrazine was refluxed with the *N,N*-dimethyl aminoanthracene semisquaraine in benzene: butanol azeotropic mixture (1:1) resulting the corresponding APSQ derivatives. The strategy adopted for synthesizing APSQ derivatives is shown in **Scheme 2.1**. The structure of the compounds was characterized by NMR spectroscopy and HRMS.



Scheme 2.1 Synthetic Scheme of APSQ Derivatives.

2.3.2 Steady-State Photophysical Characterization

2.3.2.1 Solution state

The steady-state absorption and emission spectra of **APSQ-et**, **APSQ-hex** and **APSQ-hexen** were measured in different solvents having various polarity and shown in **Figure 2.2–2.4** respectively. The **APSQ-et**, **APSQ-hex** and **APSQ-hexen** exhibited sharp and intense absorption maximum in the NIR region at around 762, 758 and 761 nm in toluene with the molar extinction coefficient of ~ 1.26 , 2.15 and $2.56 \times 10^5 \text{ M}^{-1} \text{ cm}^{-1}$ respectively. The intense absorption is due to combined π - π^* transition with intramolecular charge-transfer from *N,N*-dimethyl aminoanthracene and pyrrole appended arylhydrazine core.^{36–38} The **APSQ** derivatives having such high extinction coefficient will be used as an effective sensitizer in the form of thinner photoactive film in the optoelectronic devices.³⁹ The absorption maximum of the **APSQs** did not change considerably with the increase of polarity representing the negligible solvent reorganization during the electronic transition.^{40–41} The observation of similar spectral

features in the absorption and emission spectra of **APSQ** derivatives with small Stokes shift ($\sim 400\text{--}660\text{ cm}^{-1}$) reflect the comparable molecular configurations in the ground and excited-states.

The fluorescence dynamics of **APSQ** derivatives in different solvents was measured upon exciting at 670 nm and decay profiles are shown in **Figure 2.5**. The fluorescence lifetime (τ_f) of **APSQ-et**, **APSQ-hex** and **APSQ-hexen** in toluene were found to be around 830 ± 20 , 790 ± 15 and 790 ± 20 ps respectively. With the increase of solvent polarity, it was decreased to 150 ± 15 , 160 ± 15 and 100 ± 15 ps in acetonitrile. The absolute fluorescence quantum yield was also decreased with the increase of the solvent polarity. For example, the quantum yield of **APSQ-et**, 0.28 in toluene decreased to 0.02 in acetonitrile. The observation of the decrease of fluorescence quantum yield and lifetime reveals the participation of a non-radiative transition sensitive to the electronic redistribution in the excited **APSQ** derivatives and/or formation of the solute-solvent complexes with the increase of polarity.²⁴ The details of the absorption and emission maxima, Stokes shift, fluorescence lifetime and absolute quantum yield of **APSQ-et**, is given in **Table 2.1-2.3** respectively. The radiative and non-radiative rate constants were also calculated from fluorescence quantum yield (Φ) and lifetime (τ_f) using the following equations.

$$K_r = \frac{\Phi}{\tau_f} \quad \text{and} \quad K_{nr} = \frac{1}{\tau_f} - K_r \quad (1)$$

where k_r and k_{nr} represent the radiative and non-radiative rate constants, respectively.

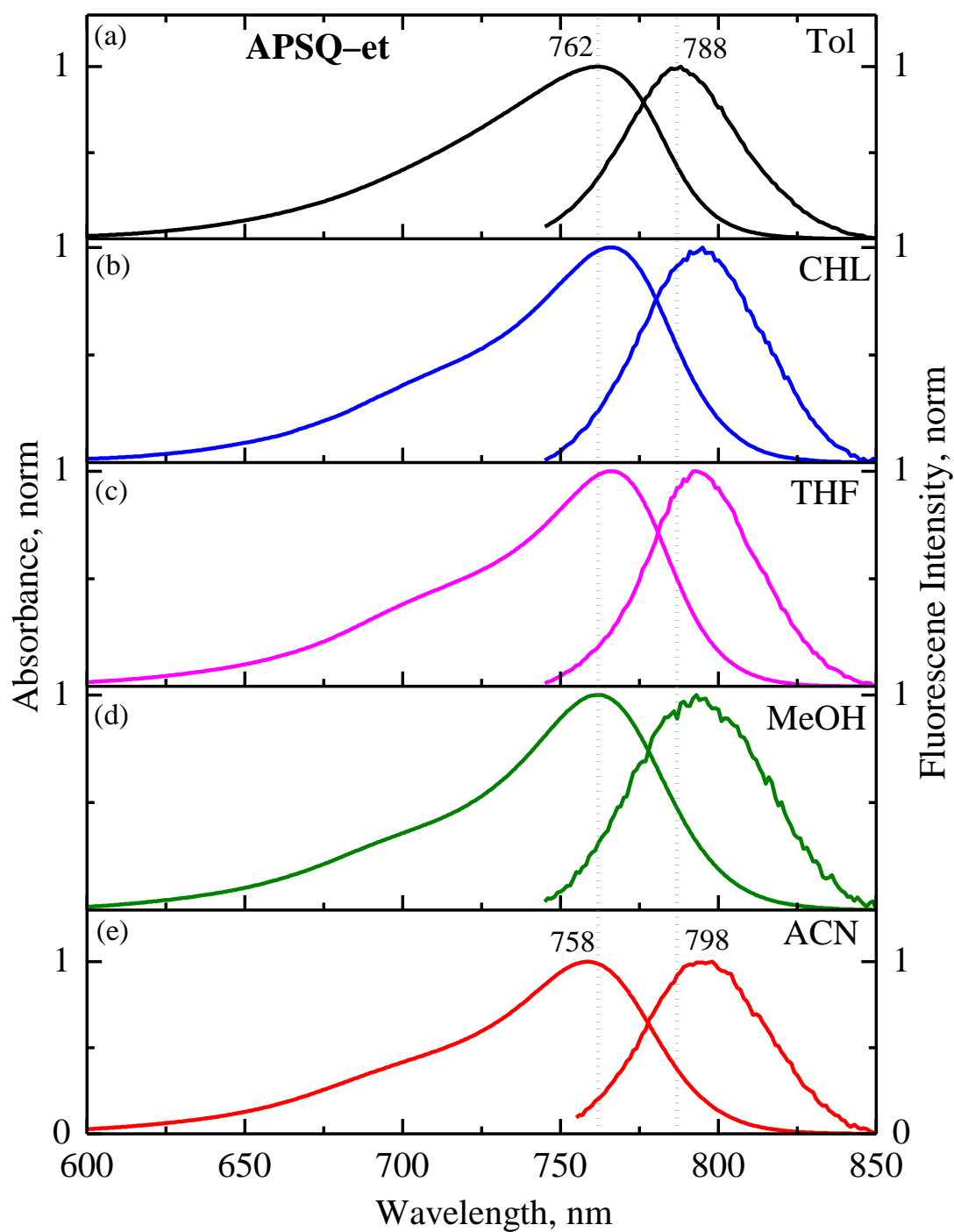


Figure 2.2 Steady-state absorption and emission spectra of APSQ-et in solvents of various polarities at room temperature.

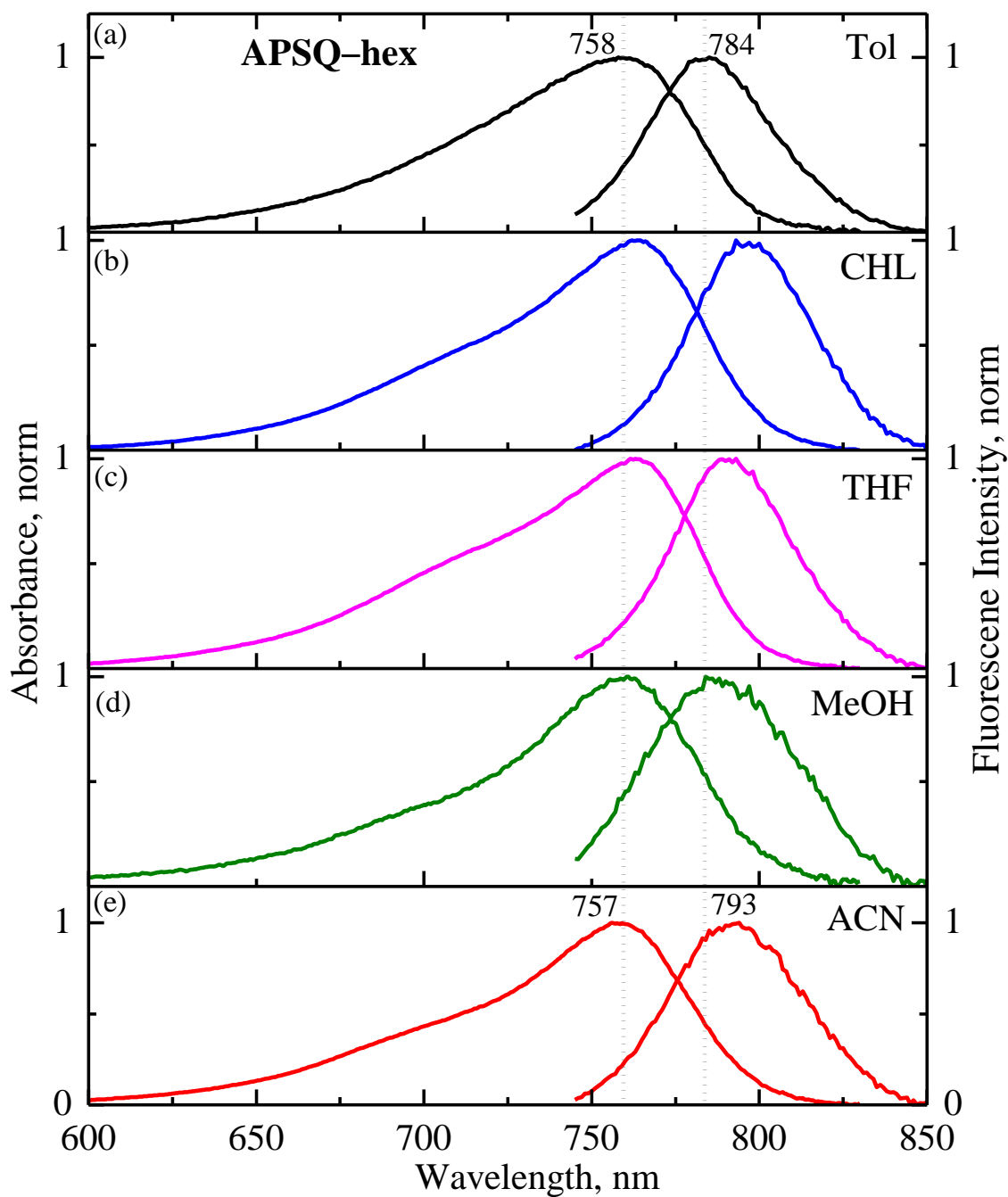


Figure 2.3 Steady-state absorption and emission spectra of APSQ-hex in solvents of various polarities at room temperature.

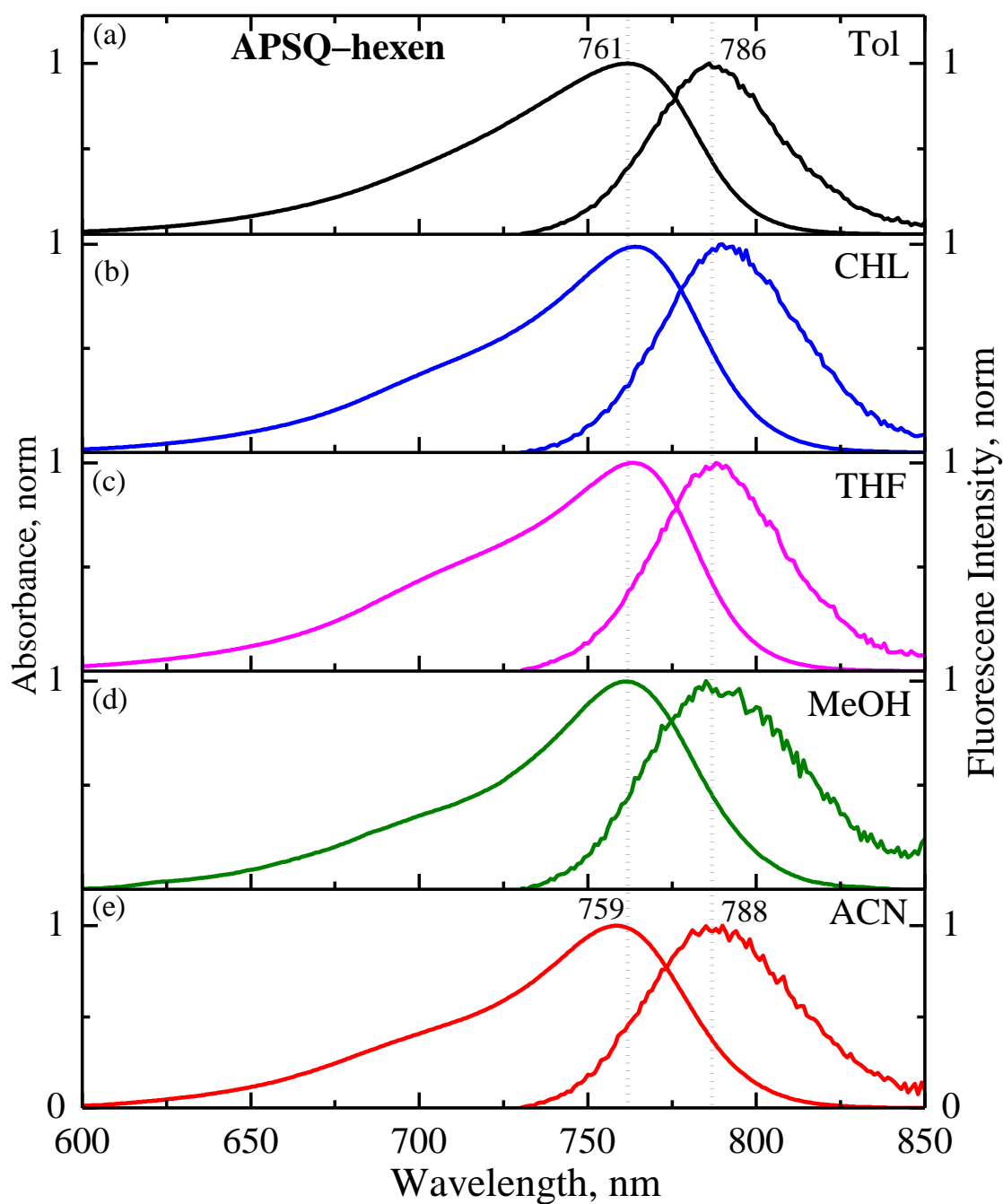


Figure 2.4 Steady-state absorption and emission spectra of APSQ-hexen in solvents of various polarities at room temperature.

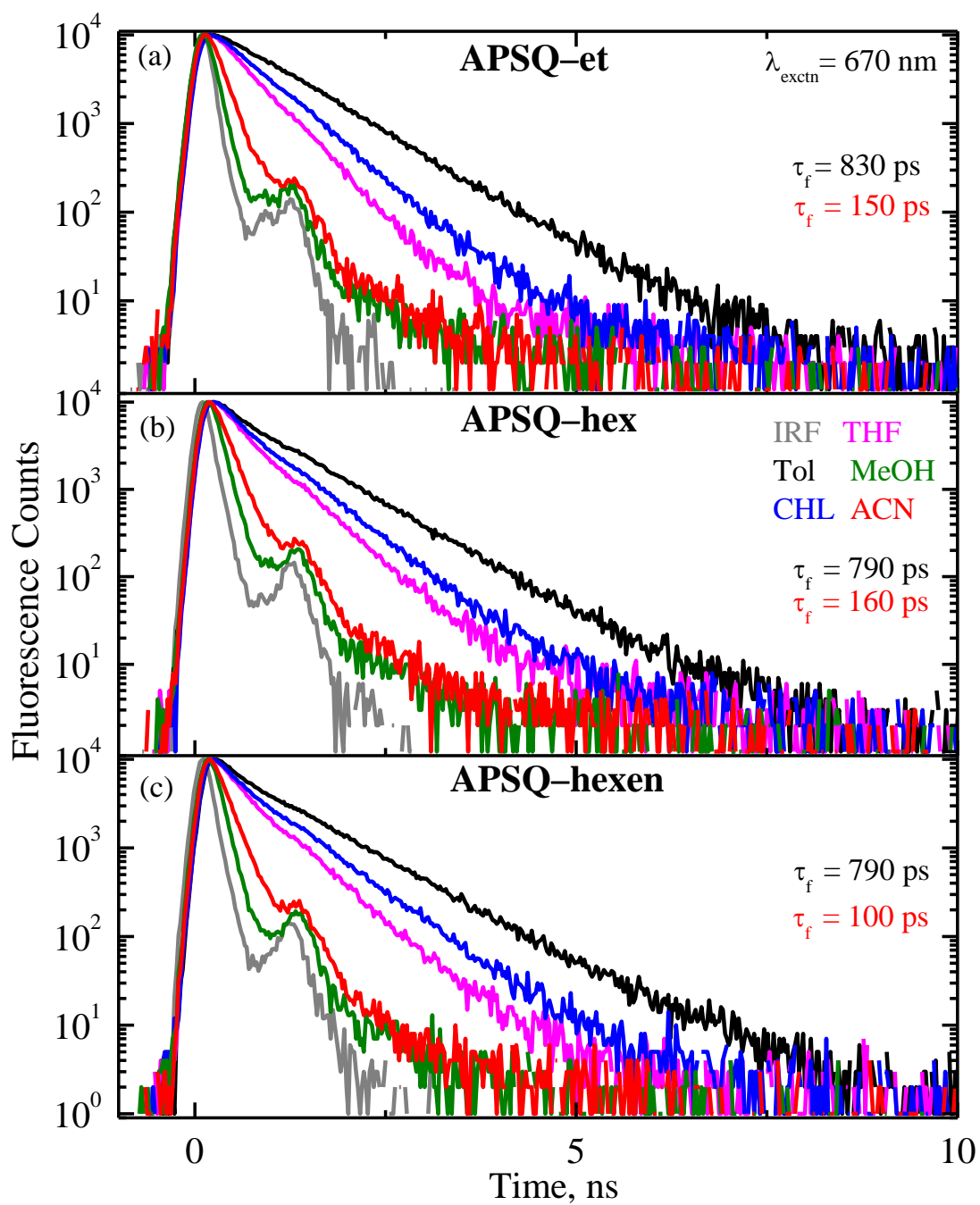


Figure 2.5 Fluorescence decay profiles of APSQ-et (a), APSQ-hex (b) and APSQ-hexen (c) in solvents of various polarities obtained upon excitation at 670 nm.

Table 2.1 Absorption and Fluorescence Maxima, Lifetime and Quantum Yield and of **APSQ-et** in Various Solvents

Solvents	Absorption max, nm (λ_{\max})	Fluorescence max, nm (λ_{\max})	Stokes shift, cm^{-1} ($\Delta\nu$)	Fluorescence quantum yield ^a (Φ_f)	Fluorescence lifetime ^b , ps (τ_f)	Radiative constant, $\times 10^7 \text{ s}^{-1}$ (K_r)	Non-radiative constant, $\times 10^7 \text{ s}^{-1}$ (K_{nr})
Toluene	762	788	433	0.28	830 ± 20	34	85
Chloroform	764	790	431	0.20	430 ± 20	48	184
THF	766	790	397	0.20	560 ± 15	37	141
MeOH	761	793	531	0.01	80 ± 20	15	1412
ACN	758	798	661	0.02	150 ± 15	19	695

^aAbsolute fluorescence quantum yield attained by exciting at emission maximum using an integrating sphere. ^bFluorescence lifetime was obtained upon excitation at 670 nm and the χ^2 value of fluorescence kinetics fit is between 1.0 and 1.2.

Table 2.2 Absorption, Fluorescence Maxima and Lifetime of **APSQ-hex** in Various Solvents

Solvents	Absorption max, nm (λ_{\max})	Fluorescence max, nm (λ_{\max})	Stokes shift, cm^{-1} ($\Delta\nu$)	Fluorescence lifetime ^a , ps (τ_f)
Toluene	758	784	437	790 ± 15
Chloroform	763	796	544	450 ± 20
THF	763	792	480	550 ± 20
MeOH	760	789	483	80 ± 20
ACN	757	793	600	160 ± 15

Table 2.3 Absorption and Fluorescence maxima and Lifetime of **APSQ-hexen** in Various Solvents

Solvents	Absorption max, nm (λ_{\max})	Fluorescence max, nm (λ_{\max})	Stokes shift, cm^{-1} ($\Delta\nu$)	Fluorescence lifetime ^a , ps (τ_f)
Toluene	761	786	418	790 ± 20
Chloroform	765	790	413	450 ± 15
THF	764	788	399	600 ± 20
MeOH	761	787	434	70 ± 15
ACN	759	788	485	100 ± 15

^aFluorescence lifetime was obtained upon excitation at 670 nm and the χ^2 value of fluorescence kinetics fit is between 1.0 and 1.2.

2.3.2.2 Film State

The normalized absorption spectra of **APSQ** derivatives in a thin film, obtained by drop-casting the **APSQs** (1.5 mM) in chloroform solution are shown in **Figure 2.6**. When

compared to the neat solvents, the absorption spectra in the thin film showed a broad in shape covering the wide wavelength range from 600–900 nm, revealing the formation of both H- and J-type aggregates by the strong intermolecular forces between the APSQ molecules.⁴²⁻⁴⁵ Such a broad range of wavelengths with high molar extinction coefficient will be significantly helpful for light harvesting.³⁹

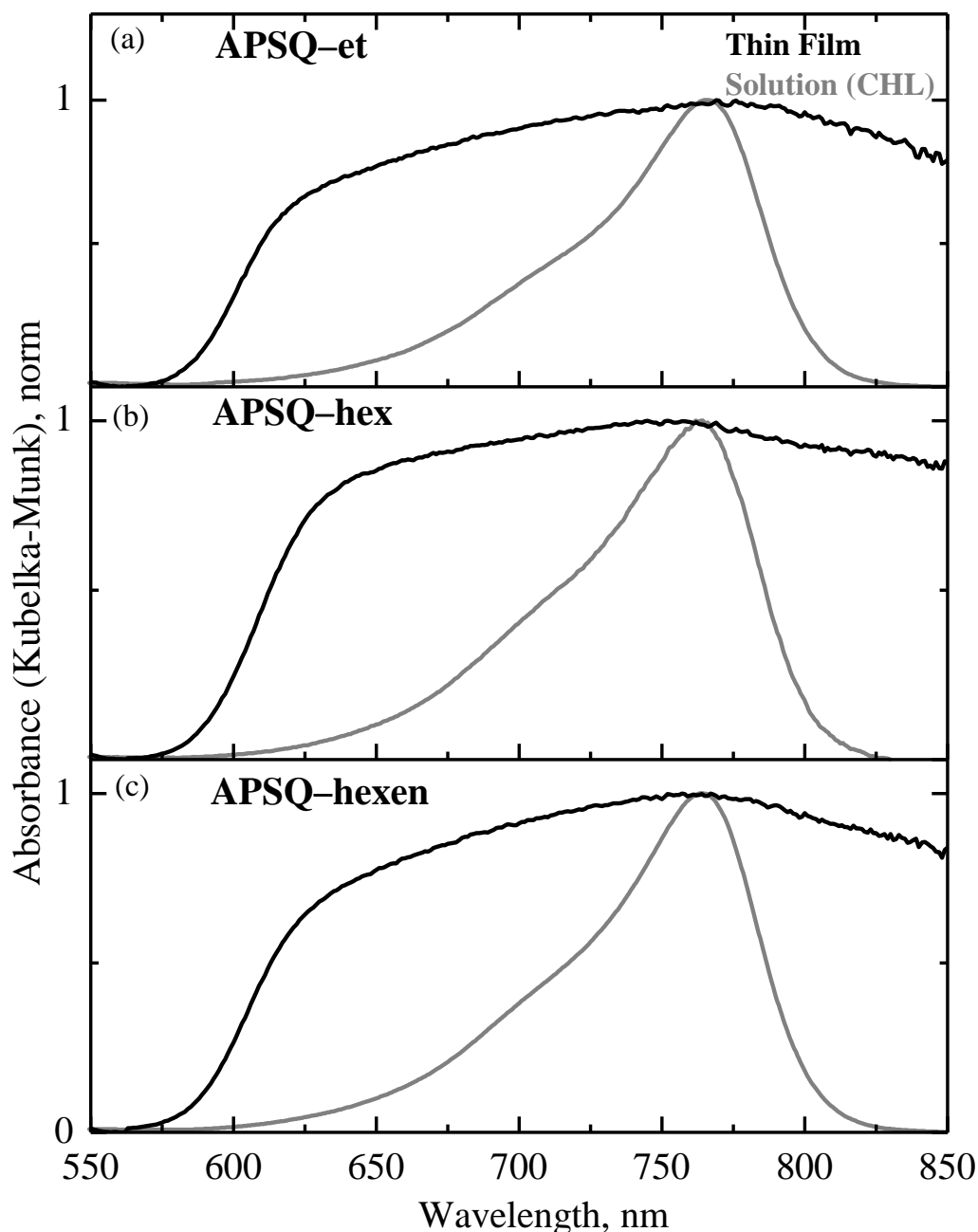


Figure 2.6 Normalized absorption spectra of APSQ-et (a), APSQ-hex (b) and APSQ-hexen (c) in a thin films and chloroform solution.

2.3.2.3 Electrochemical Properties of APSQ Derivatives

The redox potentials of the **APSQ** derivatives were determined using cyclic voltammetry in acetonitrile using ferrocene as standard and the corresponding voltammograms were given in **Figure 2.7a**. The highest occupied molecular orbital (HOMO) and lowest unoccupied molecular orbital (LUMO) energy levels of the **APSQ** derivatives in eV can be obtained from the following equation⁴⁶⁻⁴⁷ and given in **Table 2.4**.

$$\text{HOMO (APSQs)} = - [4.8 - E_{ox}(\text{Fc}/\text{Fc}^+ \text{ vs Ag}/\text{AgCl}) + E_{ox}(\text{APSQs vs Ag}/\text{AgCl})] \quad (2)$$

$$\text{LUMO (APSQs)} = E_{\text{HOMO}} + E_{00} \quad (3)$$

Where $E_{00} = 1242 / \lambda_{\text{onset}}$.

The HOMO energy levels of **APSQ-et**, **APSQ-hex** and **APSQ-hexen** are found to be -4.79, -4.82 and -4.81 eV respectively and the LUMO energy levels of **APSQ-et**, **APSQ-hex** and **APSQ-hexen** are found to be -3.26, -3.29 and -3.28 eV respectively. It is interesting to note from the **Figure 2.7b** that the LUMO energy levels of all the derivatives are higher in energy compared to that of the PCBM (-3.7 eV) and simultaneously the HOMO energy level of the PCBM (-6.1 eV) is lower compared to that of **APSQ** derivatives, which is the important requirement of the sensitizer to be used in the BHJ-based optoelectronic devices for the efficient intermolecular charge-transfer in the excited-state. Thus the energy levels of all the derivatives are appropriate to act as donor materials in the BHJ-based OPD with PCBM as an acceptor. The electrochemical data of **APSQ** derivatives are summarised in **Table 2.4**.

2.3.2.4 Interaction of APSQs with PCBM

The absorption and fluorescence spectra of **APSQ-et**, **APSQ-hex** and **APSQ-hexen** upon addition of various concentrations of PCBM (1.5 to 13.5 mM) in toluene were measured. With the increase in concentration of PCBM, no notable changes in the absorption spectra of **APSQ** derivatives were observed. Whereas the fluorescence intensity of all the **APSQ**

derivatives are decreased with the increase of concentration of PCBM as shown in **Figure 2.8**. This observation reflects the excited–state interaction between **APSQ** derivatives and PCBM. The fluorescence lifetime of **APSQ** derivatives with PCBM was measured upon exciting at 670 nm (left insets of **Figure 2.8**). In the presence of the PCBM (13.5 mM), the fluorescence lifetime is decreased from 750 ± 15 , 770 ± 20 and 790 ± 20 ps to 660 ± 15 , 710 ± 20 and 720 ± 20 ps for **APSQ–et**, **APSQ–hex** and **APSQ–hexen** respectively. The decrease of fluorescence intensity and lifetime deduces the occurrence of intermolecular charge–transfer from **APSQs** to PCBM.

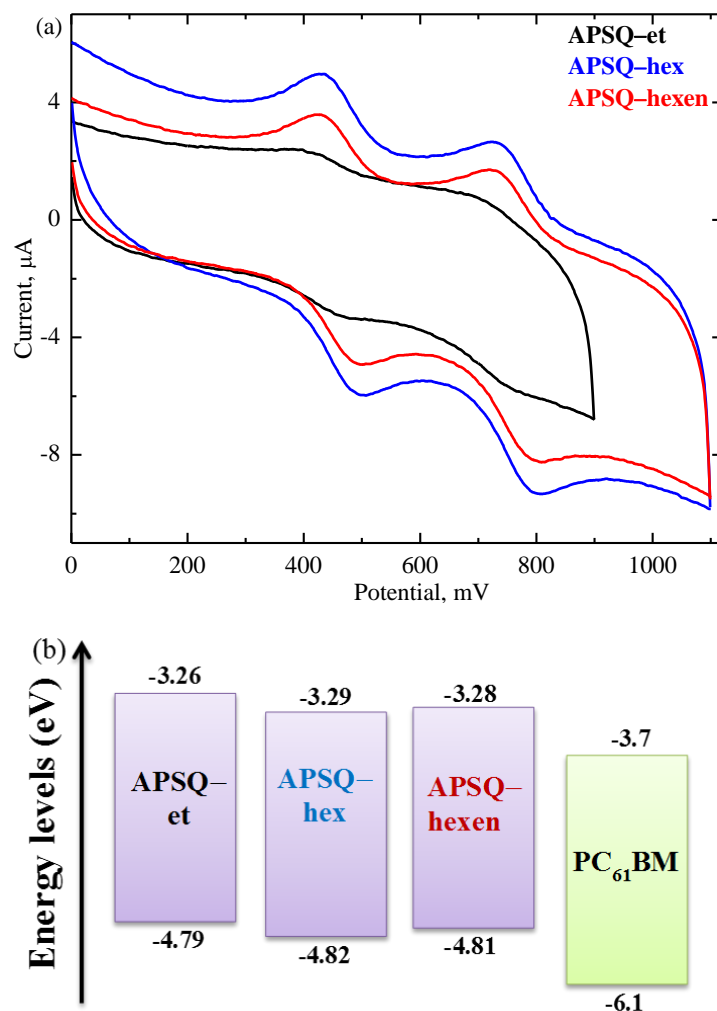


Figure 2.7 Cyclic voltammogram of **APSQ–et**, **APSQ–hex** and **APSQ–hexen** in ACN using tetrabutylammonium hexafluorophosphate as supporting electrolyte at a scanning rate of 50 mV/sec (a). HOMO and LUMO levels of **APSQ–et**, **APSQ–hex** and **APSQ–hexen** vs PCBM (b).

Table 2.4 Electrochemical data of **APSQ** derivatives from cyclic voltammetry in ACN

APSQs	λ_{00} , nm	E_{00} , eV	E_{ox} vs. Ag/AgCl, V	HOMO, eV	LUMO, eV
APSQ-et	810	1.53	0.43	-4.79	-3.26
APSQ-hex	807	1.53	0.46	-4.82	-3.29
APSQ-hexen	811	1.53	0.45	-4.81	-3.28

The Stern–Volmer plot (right insets of **Figure 2.8**) for fluorescence quenching of **APSQs** with the increase of concentration of PCBM showed linear behaviour suggesting the occurrence of dynamic quenching mechanism in the excited–state deactivation. The bimolecular quenching rate constant, k_q ($k_q = K_{SV}/\tau_0$) and Stern–Volmer quenching constant, K_{SV} ($\tau_0/\tau = 1 + K_{SV} \times [\text{PCBM}]$) were calculated and constants are provided in **Table 2.5**. Where τ_0/τ is the ratio of the fluorescence lifetime of **APSQs** in the absence and presence of PCBM. The k_q and K_{SV} for the **APSQ-et**, **APSQ-hex** and **APSQ-hexen** are found to be 13.74, 8.28 and $9.13 \times 10^9 \text{ M}^{-1} \text{ s}^{-1}$) and 10.30, 6.38 and $7.22 \text{ (M}^{-1})$ respectively. These constants are an order of magnitude larger⁴⁸ than that of normal diffusion controlled bimolecular reaction constant ($2 \times 10^9 \text{ M}^{-1} \text{ s}^{-1}$).⁴⁸ Overall upon addition of PCBM, the quenching of fluorescence intensity and a lifetime of **APSQ** derivatives reveal the occurrence of the intermolecular charge–transfer from the **APSQs** to the PCBM.¹⁸

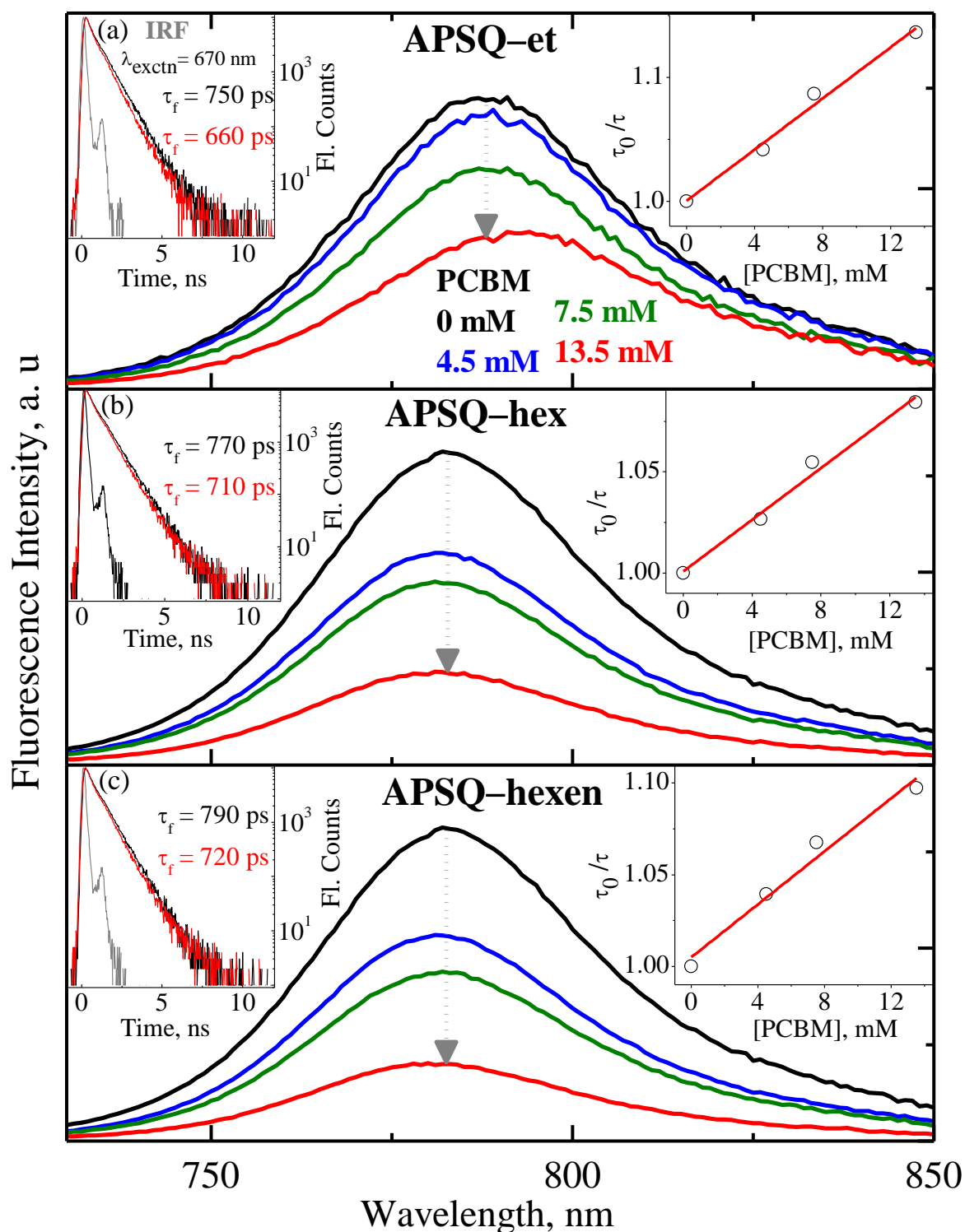


Figure 2.8 Fluorescence spectra of APSQ-et (a), APSQ-hex (b) and APSQ-hexen (c) with different concentrations of PCBM in toluene. Insets: Fluorescence decay profiles obtained upon excitation at 670 nm (left) and plot of τ_0/τ versus [PCBM] (right).

Table 2.5 The Stern–Volmer quenching constant (K_{SV}) and bimolecular quenching rate constant (k_q) of APSQ derivatives.

APSQs	K_{SV} , M^{-1}	τ_0 , ps	τ , ps	k_q , $\times 10^9 M^{-1} s^{-1}$
APSQ–et	10.30	750 ± 15	660 ± 15	13.74
APSQ–hex	6.38	770 ± 20	710 ± 20	8.28
APSQ–hexen	7.22	790 ± 20	720 ± 20	9.13

2.4 Time–Resolved Photophysical Characterization

2.4.1 Femtosecond Transient Absorption Spectra of APSQ derivatives:

To understand the role of solvent polarity on the excited–state relaxation dynamics of the APSQs, femtosecond time–resolved transient absorption spectra were measured in toluene and ACN upon excitation at 670 nm using femtosecond pump–probe spectroscopy. Transient absorption spectra of **APSQ–et**, **APSQ–hex** and **APSQ–hexen** in toluene covering the wavelength range of ~345–585 nm are shown in **Figure 2.9**. In **Figure 2.9**, panel a shows the spectral evolution of **APSQ–et** recorded from 900 fs to 1.47 ns. At early time scales, two transient absorption bands positioned at ~421 and 525 nm are observed. The intensity of both the bands gradually decreases with the increase of delay time. The panels b and c of **Figure 2.9** showed the spectral evolution of **APSQ–hex** and **APSQ–hexen** in toluene from 900 fs to 1.47 ns respectively. The transient absorption spectral features of all the APSQs are found to be similar to each other. As the decay profile of the peaks at ~525 and 420 nm is found to be the same, the positive bands are due to the excited state absorption (ESA) of the dyes ($S_n \leftarrow S_1$ transition).⁴⁹⁻⁵³ The transient absorption spectra extending the longer wavelength region (~585–785 nm) upon excitation at 670 nm were also measured and shown in **Figure 2.10**. In **Figure 2.10**, panel a shows the spectral evolution of **APSQ–et** recorded

from 50 fs to 1.47 ns. With the increase of delay time, the negative transient absorption peak at ~765 nm evolving to attain the steady-state emission maximum at ~780 nm, corresponds to the stimulated emission (SE). The spectral behaviours of APSQ-hex and APSQ-hexen shown in panel b and c of **Figure 2.10** respectively are similar to that of the APSQ-et.

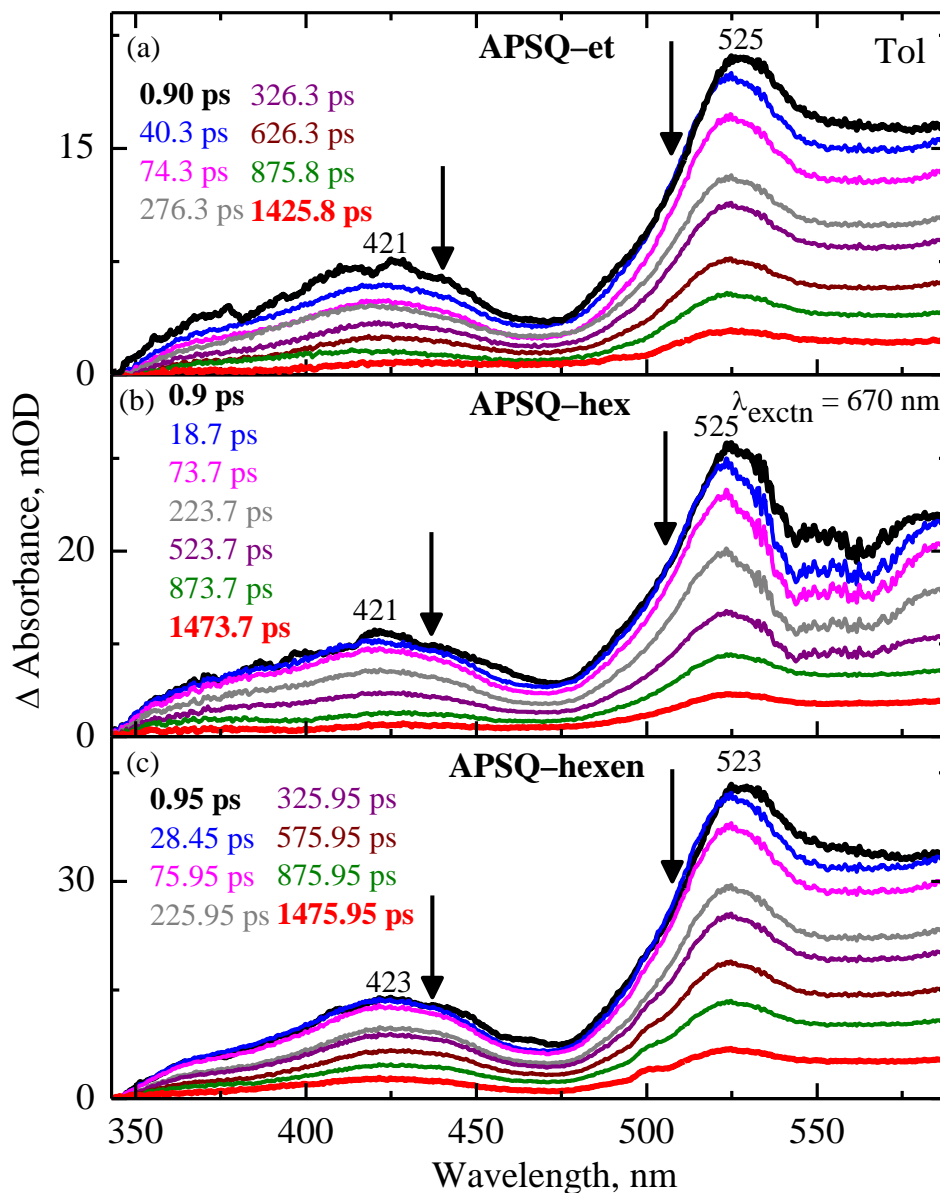


Figure 2.9 Femtosecond transient absorption spectra of APSQ-et (a), APSQ-hex (b) and APSQ-hexen (c) in toluene upon excitation at 670 nm in the shorter wavelength region at different delay times.

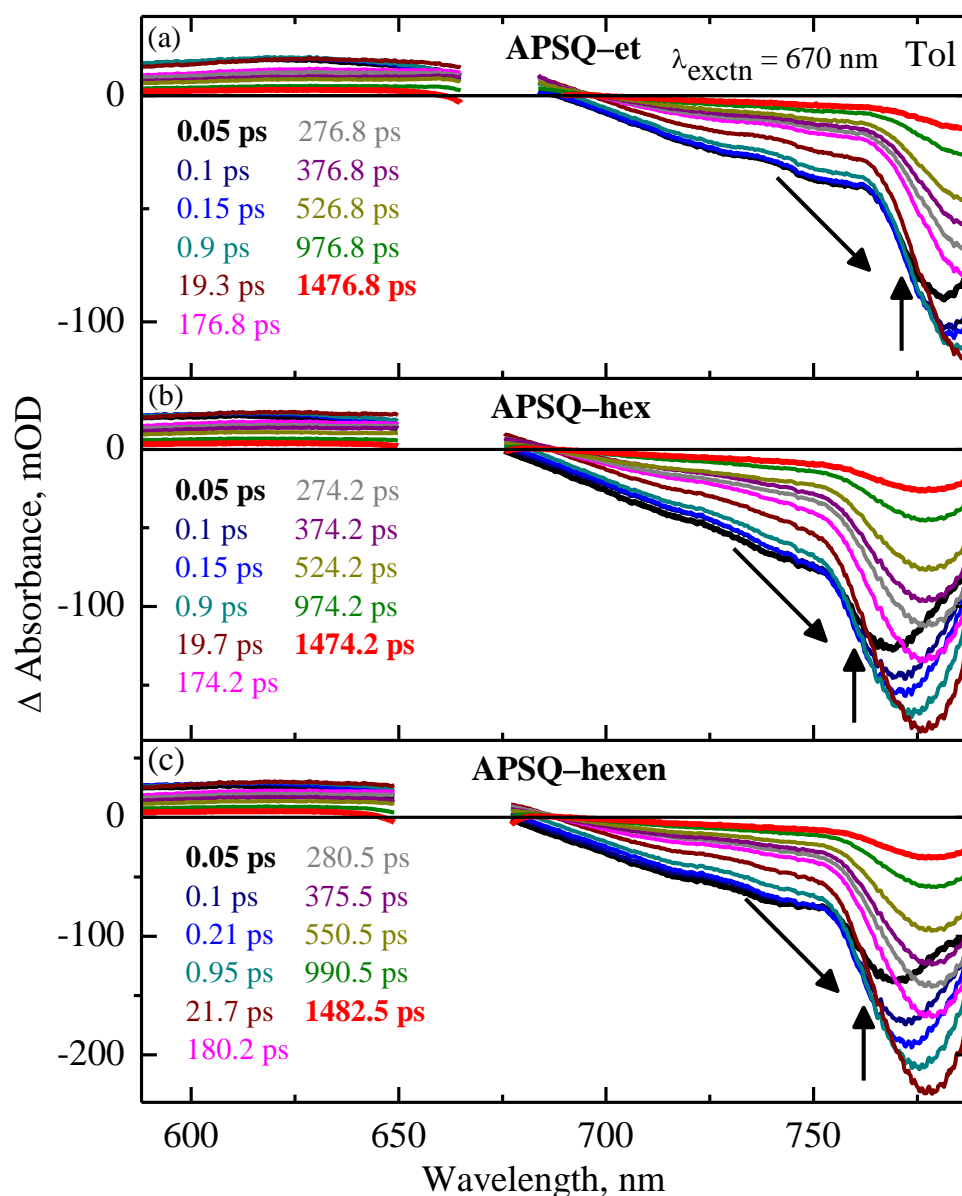


Figure 2.10 Femtosecond transient absorption spectra of **APSQ-et** (a), **APSQ-hex** (b) and **APSQ-hexen** (c) in toluene upon excitation at 670 nm in the longer wavelength region at different delay times.

The transient absorption spectra of **APSQ-et**, **APSQ-hex** and **APSQ-hexen** in ACN obtained upon exciting at 670 nm in the shorter and longer wavelength region are shown in **Figure 2.11** and **Figure 2.12** respectively. In **Figure 2.11** (panel a), the transient absorption spectra of **APSQ-et** showed two positive bands at around 415 and 514 nm in the early time scales. The intensity of both the bands decreased with the increase of delay time as shown in

Figure 2.11. The transient absorption spectra of APSQ–et in ACN (**Figure 2.12**, panel a) shown for the longer wavelength region exhibiting the negative band at ~738 nm reflects the characteristic feature of SE by shifting to the red region at ~771 nm with the increase of delay time. Overall the transient absorption spectral features of all the APSQ derivatives in ACN appeared to be similar to toluene. However, the excited–state relaxation dynamics of APSQs are faster in ACN when compared to toluene (**Figure 2.13**) due to the change in the solvation relaxation processes.⁵⁴⁻⁵⁸

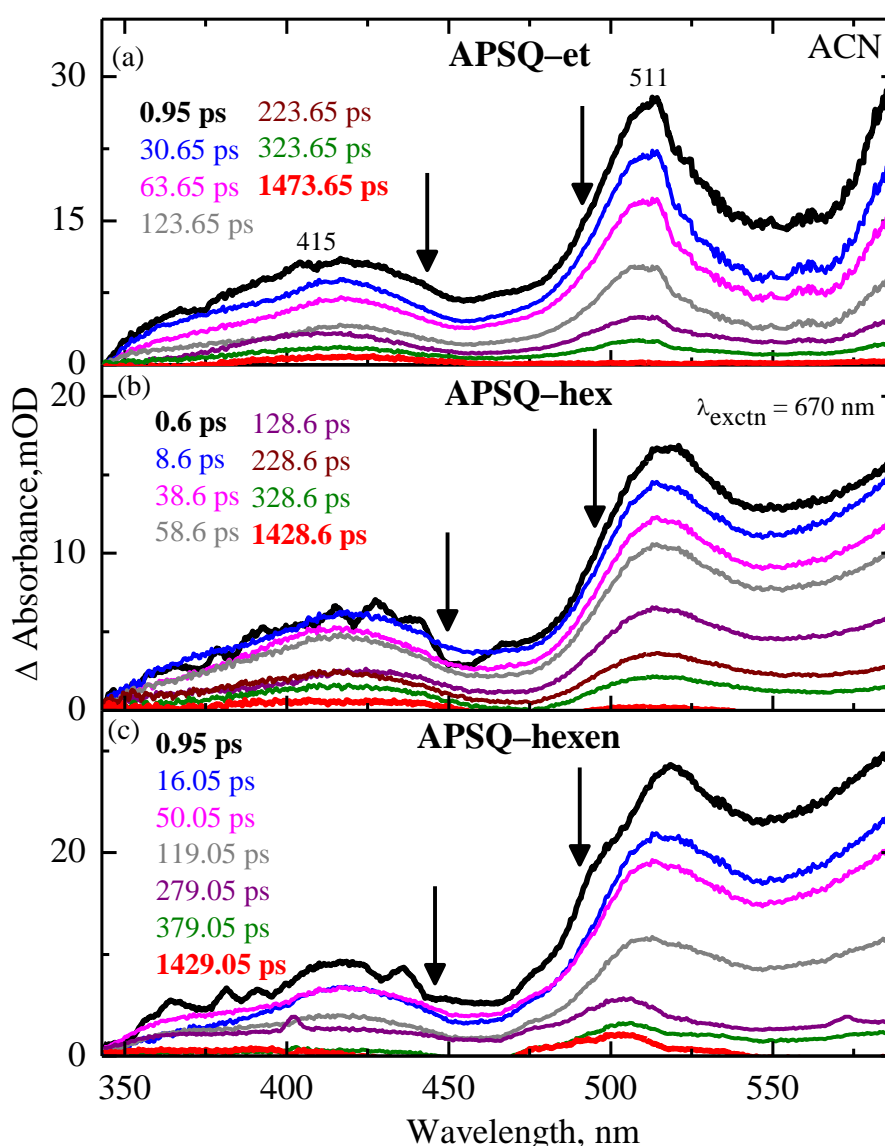


Figure 2.11 Femtosecond transient absorption spectra of APSQ–et (a), APSQ–hex (b) and APSQ–hexen (c) in ACN upon excitation at 670 nm in the shorter wavelength region at different delay times.

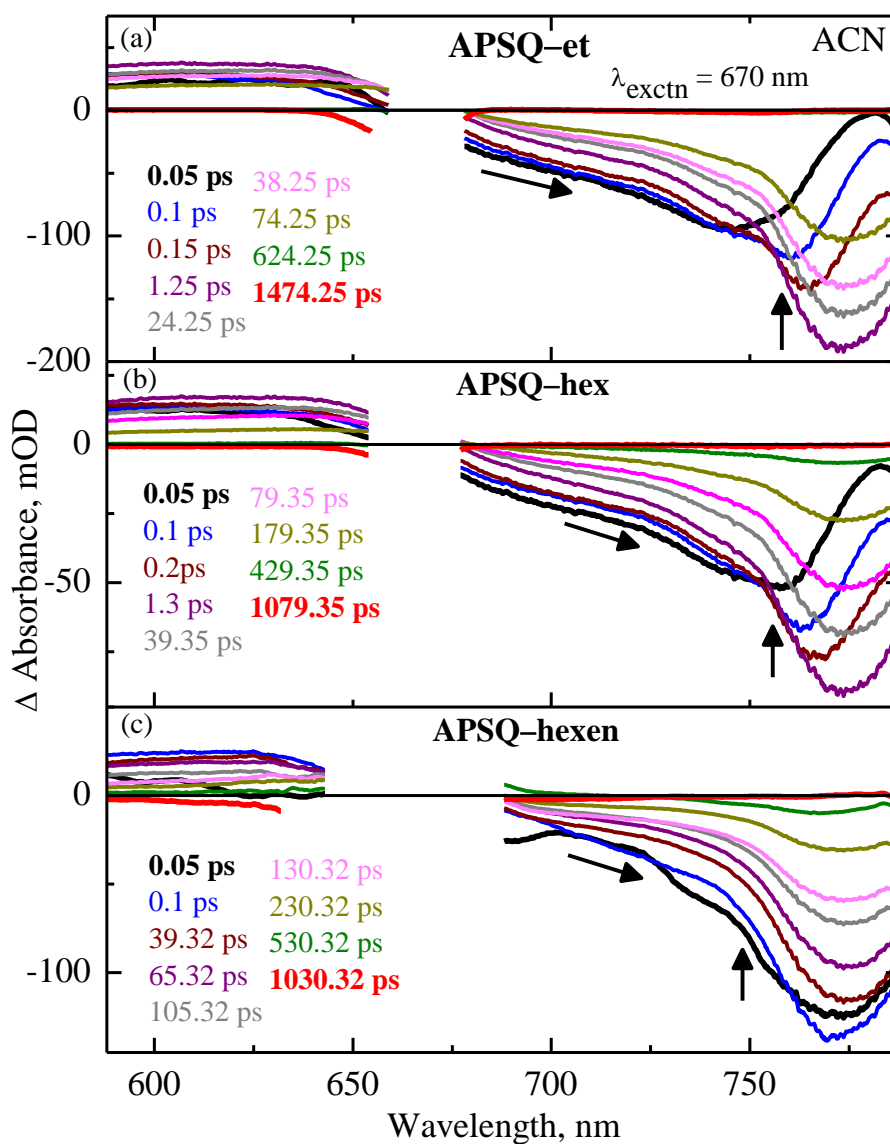


Figure 2.12 Femtosecond transient absorption spectra of **APSQ-et** (a), **APSQ-hex** (b) and **APSQ-hexen** (c) in ACN upon excitation at 670 nm in the longer wavelength region at different delay times.

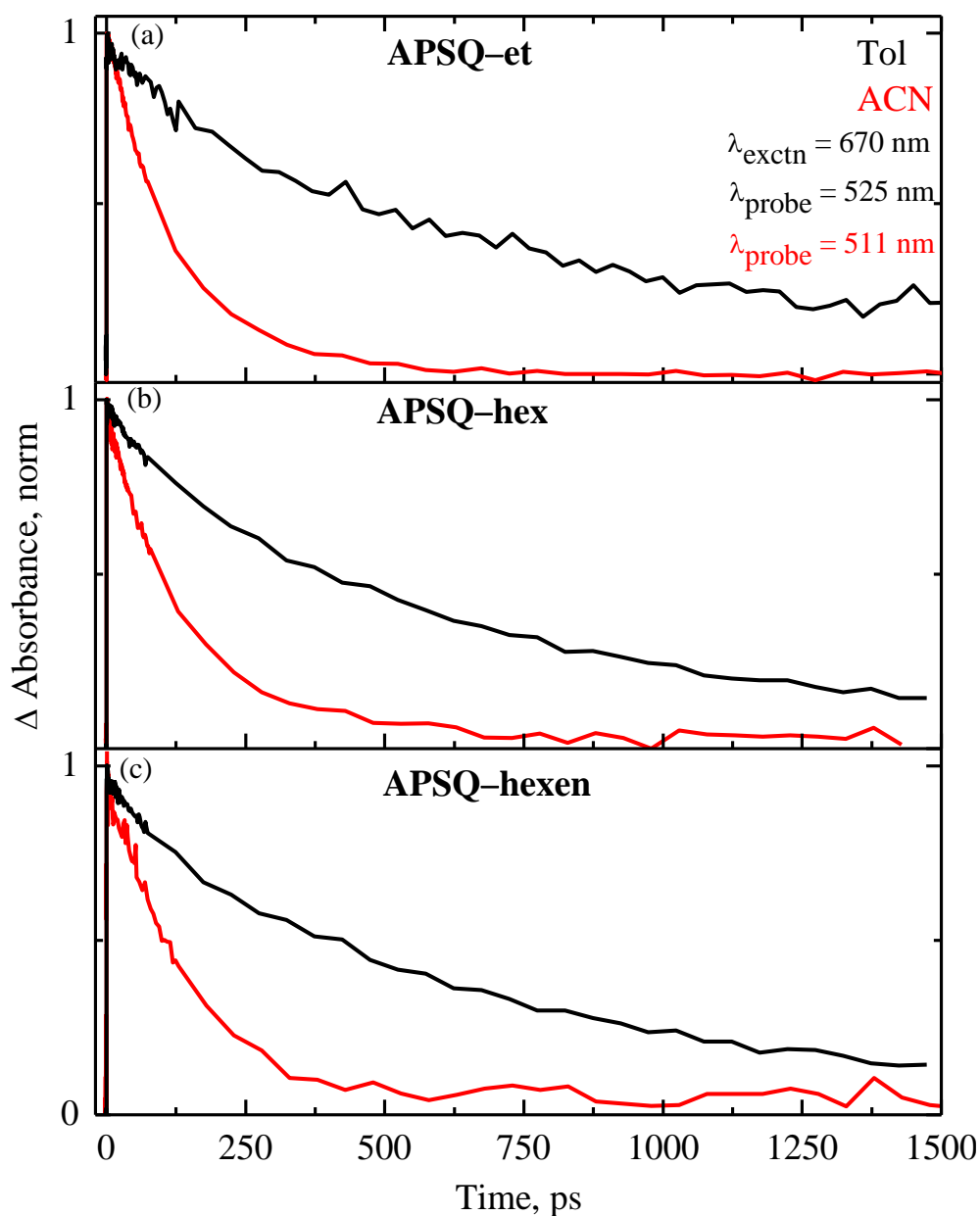


Figure 2.13 Femtosecond transient absorption decay **APSQ-et** (a), **APSQ-hex** (b) and **APSQ-hexen** (c) in toluene and acetonitrile upon excitation at 670 nm.

To understand the relationship between the efficiency of the devices and dynamics of the photogenerated charges, excited-state interaction dynamics between **APSQs** and PCBM were studied by measuring the fs-TAS of **APSQs** and PCBM mixture upon excitation at 670 nm. The transient absorption spectral behaviour of the mixture (**Figure 2.14–2.15**) is found to

be the same when compared to the **APSQs** alone in toluene. It is to be noted that we have used a PCBM concentration of 13.5 mM, having high OD in the region below 390 nm. Since all the probe light was absorbed well below 390 nm, we could not observe any changes in the absorbance. In addition, there is an artifact raised due to the strong and narrow absorption of PCBM at ~433 nm. However, the decay profile of **APSQ–et**, **APSQ–hex** and **APSQ–hexen** with PCBM mixture probed at 525 and 760 nm in toluene (**Figure 2.16 and 2.17**) respectively showed quenching of the dynamics when compared to the **APSQs** alone.

2.4.2 Analysis of the Transient Absorption Spectra of APSQ Derivatives

The femtosecond transient absorption spectra were analyzed globally with the sequential model using Glotaran.⁵⁹ Three exponential components were optimally obtained to completely describe the relaxation dynamics of **APSQs** in toluene and ACN as well as with PCBM mixture in toluene. The obtained time constants are provided in **Table 2.6** and the corresponding decay-associated difference spectra (DADS) are shown for comparison in **Figure 2.18 to 2.20**. There are no substantial changes in the excited-state relaxation dynamics of **APSQs** by changing the alkyl and alkenyl substituents attached to pyrrolic nitrogen (**Figure 2.13, 2.16–2.17**). Hence the time constants obtained for **APSQ–et** are considered for discussion and those are $\tau_1 = 412$ fs, $\tau_2 = 10.78$ ps, and $\tau_3 = 122$ ps in ACN and $\tau_1 = 2.5$ ps, $\tau_2 = 114.81$ ps and $\tau_3 = 747.84$ ps in toluene. Based on the observation of the characteristic feature of the redshift of SE (~763 nm) with the increase in delay time, the fast component ($\tau_1 = 412$ fs in ACN and $\tau_1 = 2.50$ ps in toluene) attributed to the solvation relaxation processes from Franck–Condon state to solvent stabilized local excited-state based on the observation of dynamic redshift of SE with the increase of delay time,⁶⁰⁻⁶¹ The time constant τ_2 , 10.78 and 114.81 ps for ACN and toluene respectively, could be attributed to the dark state, resulting from the conformational changes of **APSQs**, having the charge–transfer character stabilizing

in the polar solvent. This state facilitates the non-radiative deactivation to the ground state and supports the observation of a decrease of fluorescence quantum yield and lifetime in ACN (Table 2.1). Finally, the longer time constant τ_3 , resulting from the global analysis, is consistent with the fluorescence lifetime obtained from the TCSPC in neat solvents (Table 2.1). Hence the time constant of 122 (747.84) ps is attributed to the lifetime of the excited singlet state of APSQ-et in ACN (toluene).

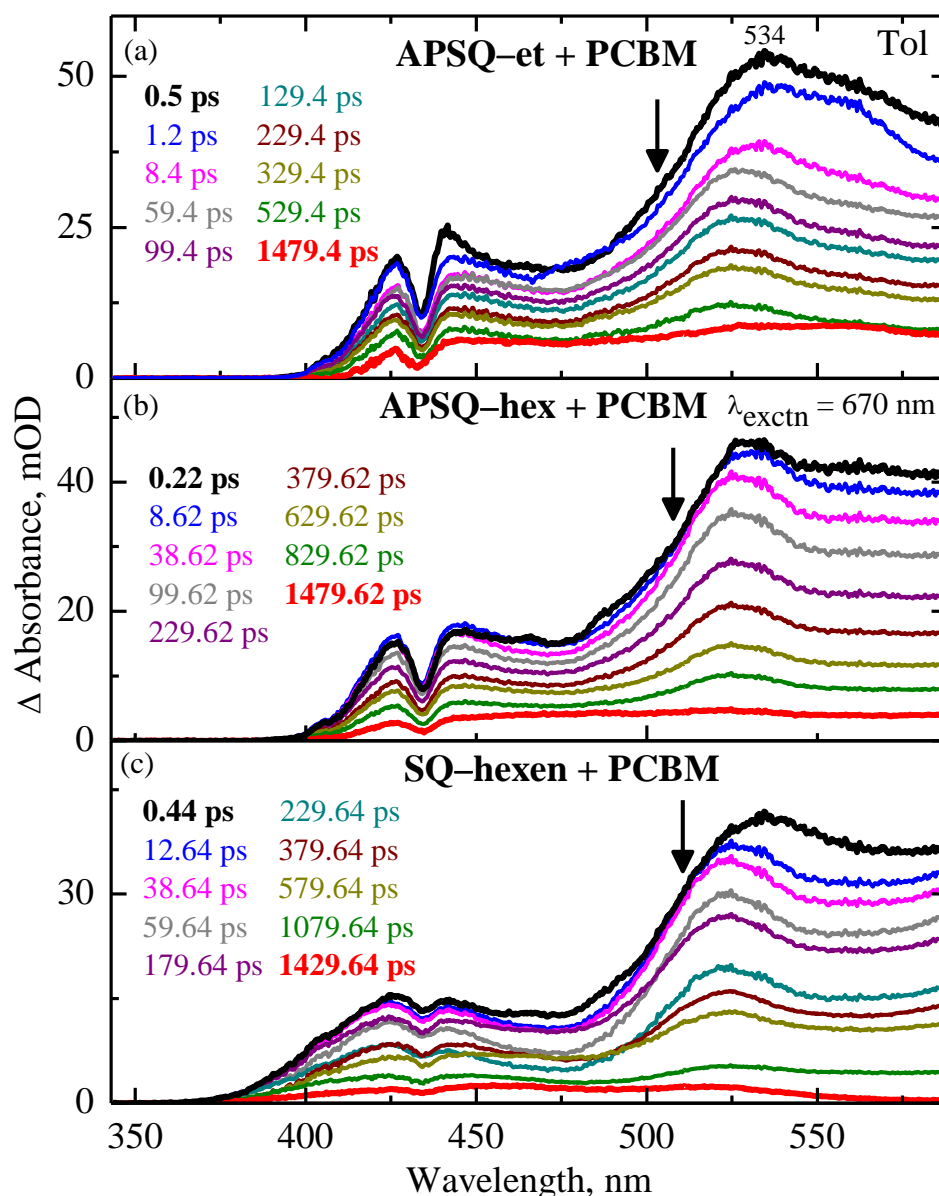


Figure 2.14 Femtosecond transient absorption spectra of APSQ-et (a), APSQ-hex (b) and APSQ-hexen (c) with PCBM in toluene upon excitation at 670 nm in the shorter wavelength region at different delay times.

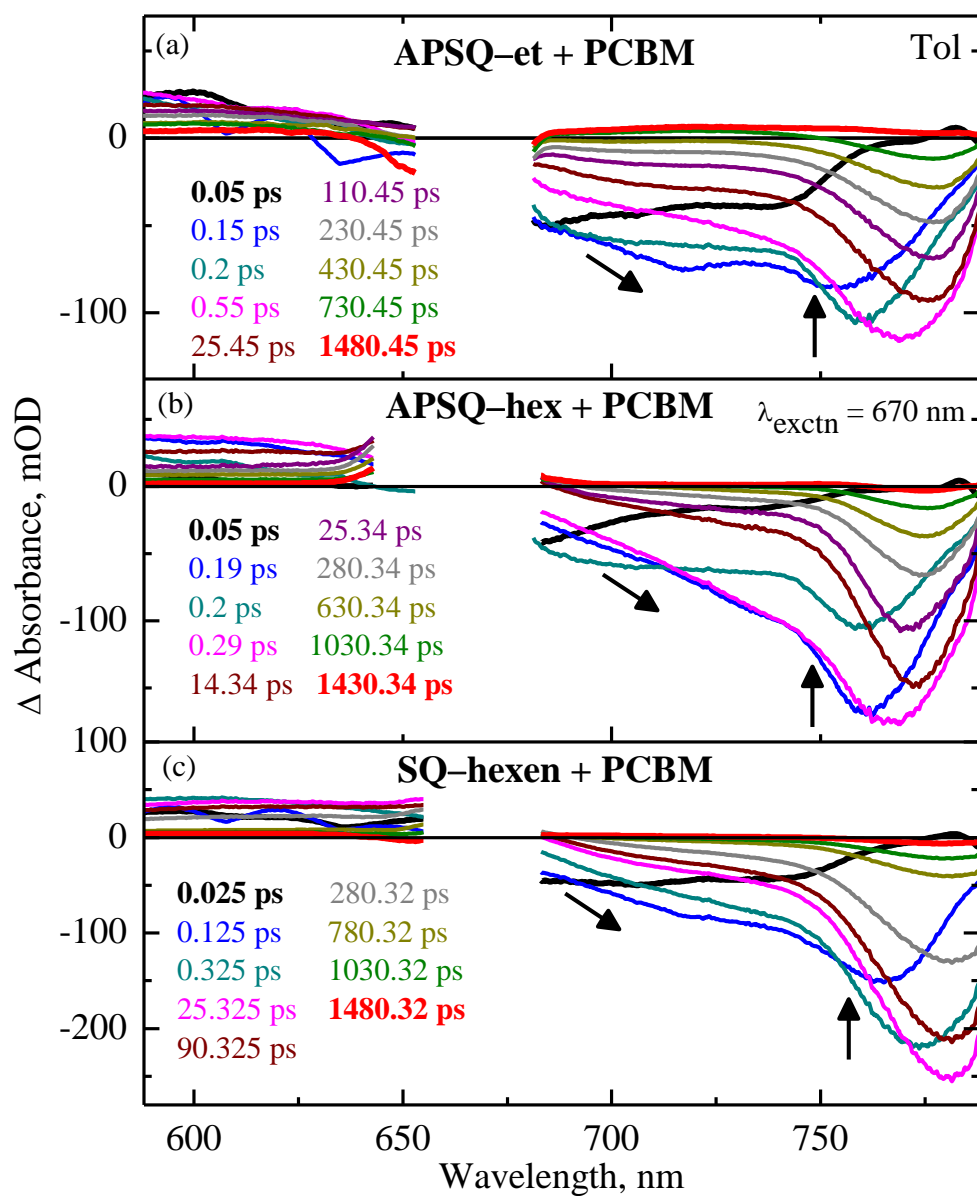


Figure 2.15 Femtosecond transient absorption spectra of APSQ-et (a), APSQ-hex (b) and APSQ-hexen (c) with PCBM in toluene upon excitation at 670 nm in the longer wavelength region at different delay times.

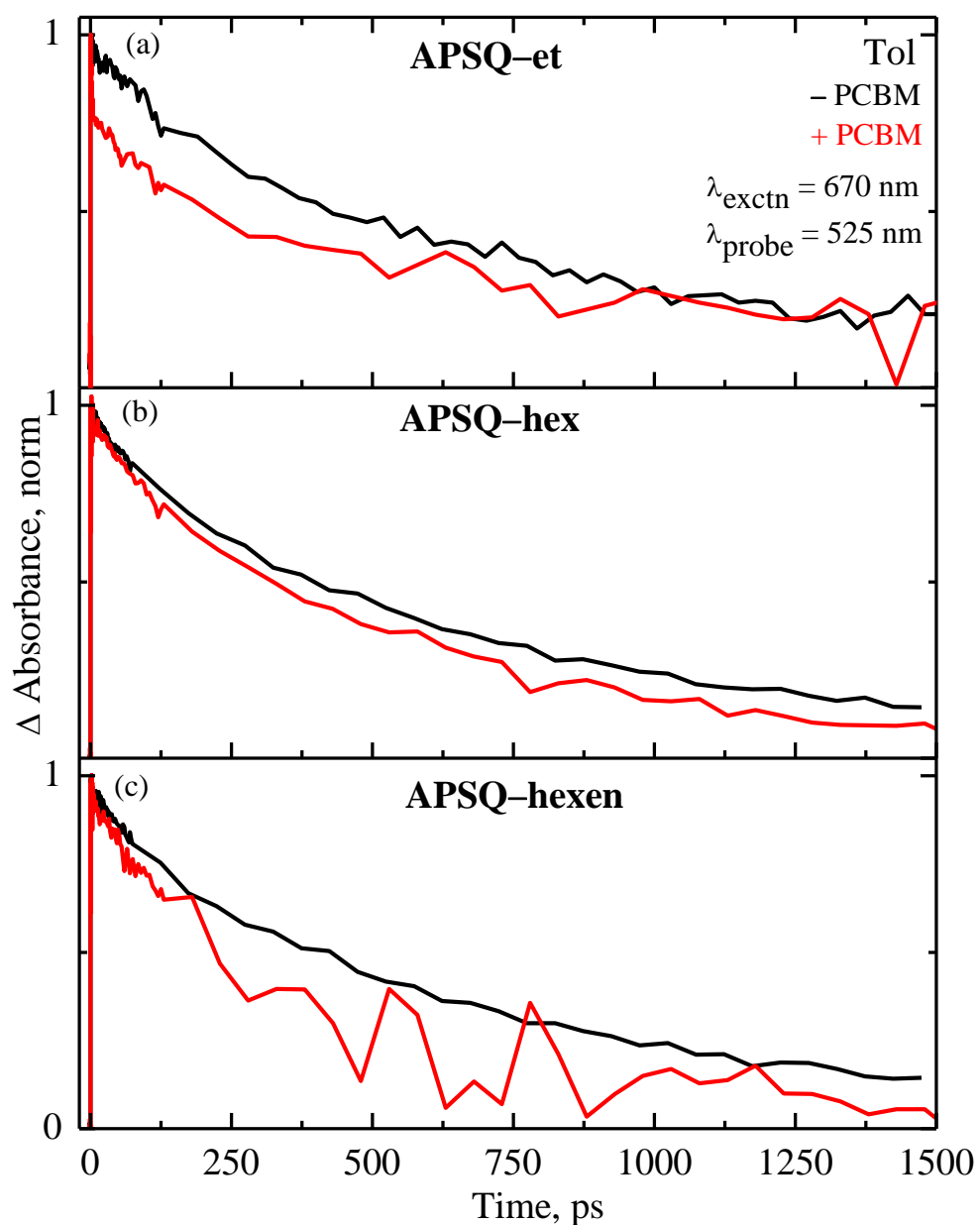


Figure 2.16 Femtosecond transient absorption decay of **APSQ-et** (a), **APSQ-hex** (b) and **APSQ-hexen** (c) with and without PCBM in toluene probed at 525 nm upon excitation at 670 nm.

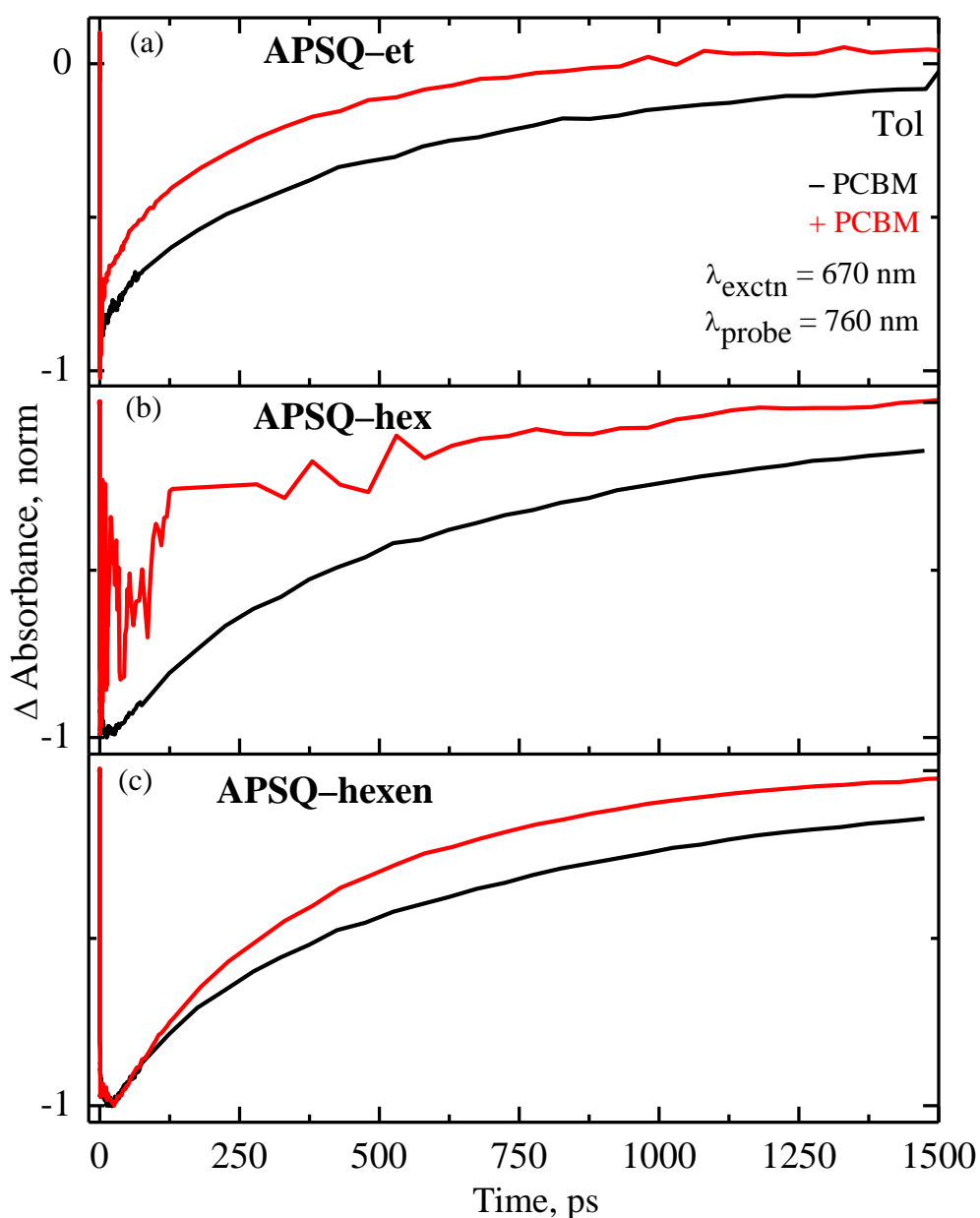


Figure 2.17 Femtosecond transient absorption decay **APSQ-et** (a), **APSQ-hex** (b) and **APSQ-hexen** (c) with and without PCBM in toluene probed at 760 nm upon excitation at 670 nm.

Interestingly upon addition of PCBM, quenching of all the time constants of **APSQ–et** was observed (1.50 ps (τ_1), 62.52 ps (τ_2) and 625 ps (τ_3)). The decrease of time constant, τ_3 is consistent with the fluorescence time constant observed in TCSPC in the presence of PCBM. Such a decrease of time constant could be due to the effect of the occurrence of the intermolecular charge–transfer between **APSQs** and PCBM.⁶²

Table 2.6 Time Constants Attained from Global Analysis Using Glotaran⁵⁹ for **APSQs** upon Excitation at 670 nm

APSQs	ACN	Toluene	
		– PCBM	+ PCBM
APSQ–et	$\tau_1 = 0.41 \pm 0.10$ ps	$\tau_1 = 2.50 \pm 0.20$ ps	$\tau_1 = 1.50 \pm 0.20$ ps
	$\tau_2 = 10.78 \pm 0.50$ ps	$\tau_2 = 114.81 \pm 2.20$ ps	$\tau_2 = 62.52 \pm 1.20$ ps
	$\tau_3 = 122 \pm 2$ ps	$\tau_3 = 747.84 \pm 6$ ps	$\tau_3 = 625 \pm 5$ ps
APSQ–hex	$\tau_1 = 0.45 \pm 0.15$ ps	$\tau_1 = 2.31 \pm 0.25$ ps	$\tau_1 = 2.11 \pm 0.20$ ps
	$\tau_2 = 15.32 \pm 0.60$ ps	$\tau_2 = 88.85 \pm 3.20$ ps	$\tau_2 = 35.41 \pm 1.25$ ps
	$\tau_3 = 154.87 \pm 2$ ps	$\tau_3 = 760.30 \pm 5$ ps	$\tau_3 = 668.55 \pm 5$ ps
APSQ–hexen	$\tau_1 = 0.44 \pm 0.12$ ps	$\tau_1 = 2.41 \pm 0.26$ ps	$\tau_1 = 2.30 \pm 0.23$ ps
	$\tau_2 = 19.51 \pm 1.00$ ps	$\tau_2 = 86.79 \pm 1.20$ ps	$\tau_2 = 54.83 \pm 1.30$ ps
	$\tau_3 = 172.65 \pm 3$ ps	$\tau_3 = 788.75 \pm 6$ ps	$\tau_3 = 680.27 \pm 5$ ps

Further to shed more light on the charge transfer dynamics, a global target analysis has been carried out to extract the time constant of charge–transfer and spectral signatures of each excited species. The rate constant of charge–transfer dynamics is obtained from the fraction of population conversion from one state to another divided by the associated time constant of the

state.⁶³⁻⁶⁶ The relative fraction of population is tested by multiplying the amplitude of each of the kinetic traces with the corresponding species associated spectrum and summing the result, leading to the observed transient absorption spectra within the experimental noise.⁶⁷ Thus, based on the target analysis, the charge-transfer proposed to occur from the solvent-stabilized local excited-state with the relative population of $\sim 89\%$ and the time constants of charge-transfer from APSQ-*et*, APSQ-*hex* and APSQ-*hexen* to PCBM were found to be ~ 70.42 , 39.84 and 61.72 ps respectively.

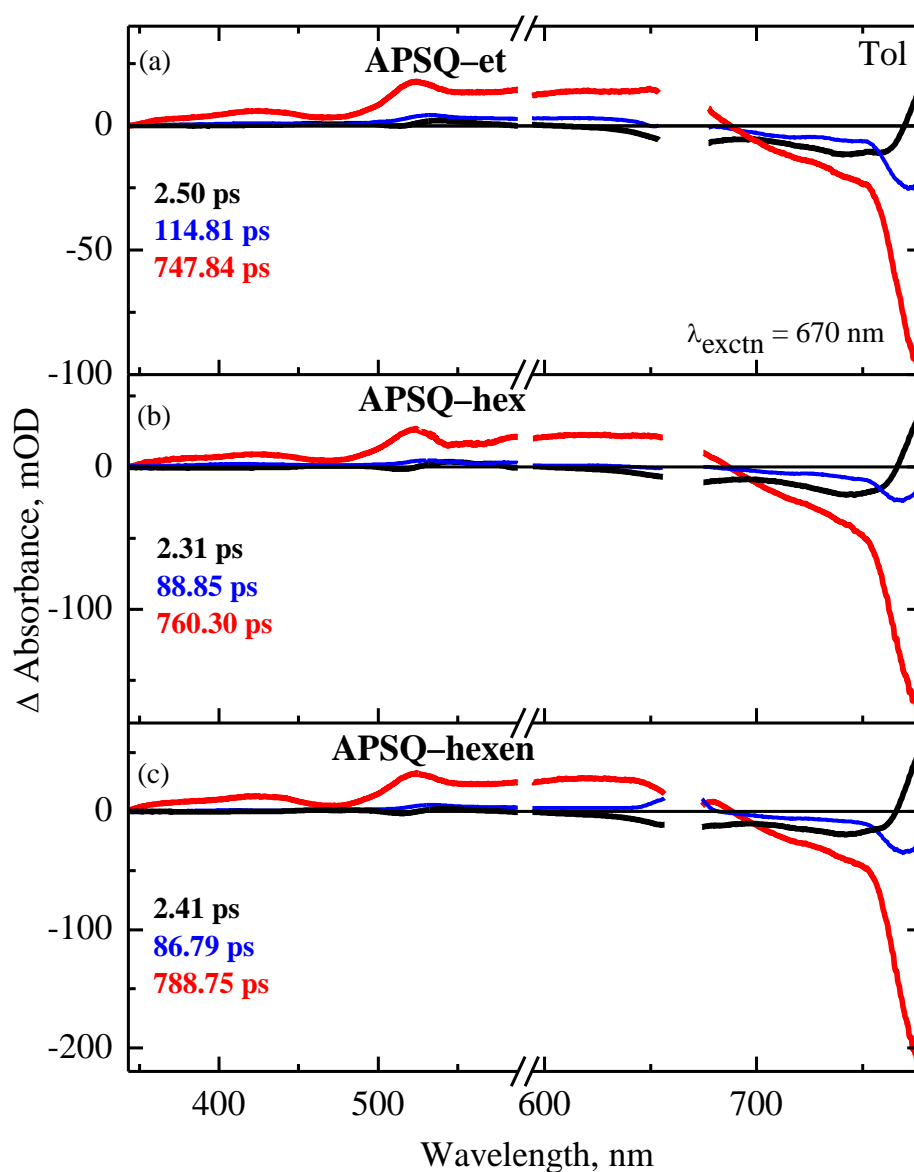


Figure 2.18 Decay associated difference spectra of APSQ-*et* (a), APSQ-*hex* (b) and APSQ-*hexen* (c) in toluene obtained by global analysis.

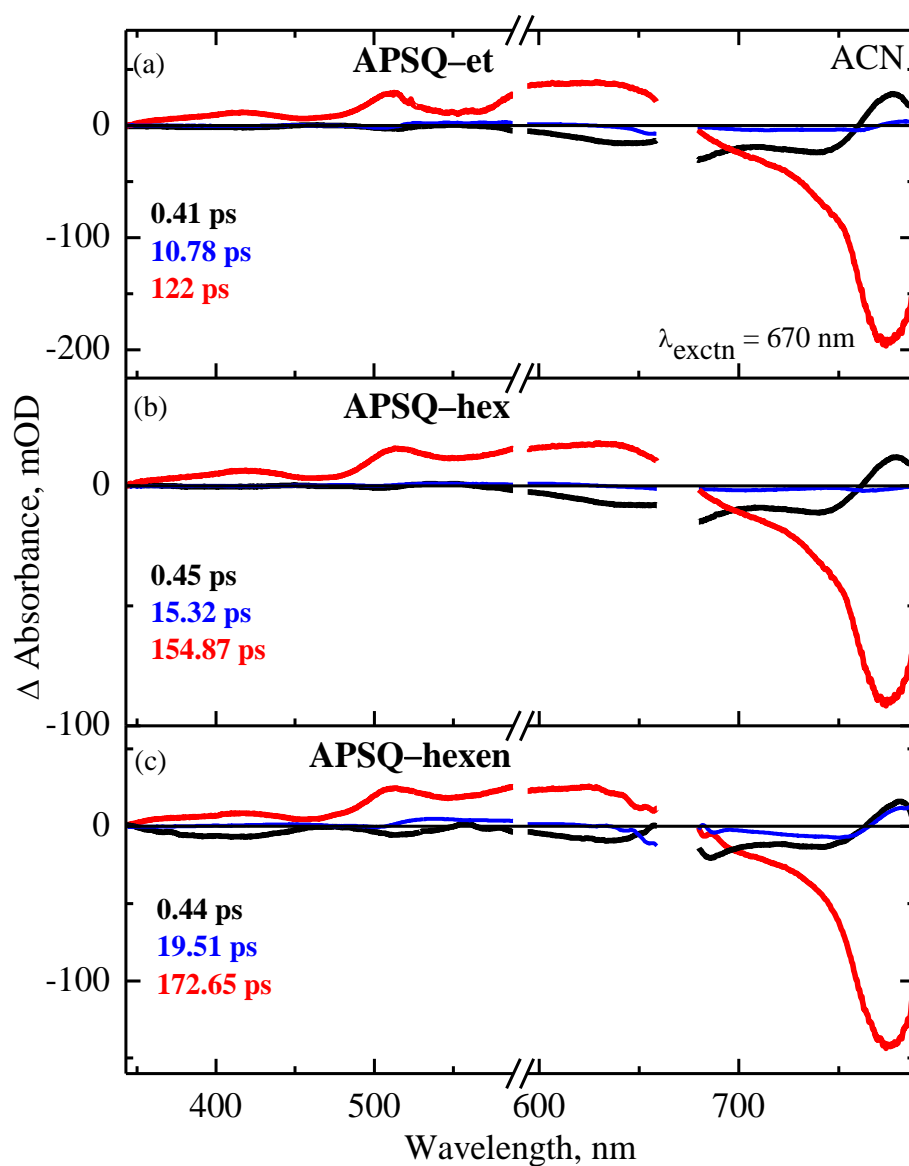


Figure 2.19 Decay associated difference spectra **APSQ-et** (a), **APSQ-hex** (b) and **APSQ-hexen** (c) in ACN obtained by global analysis.

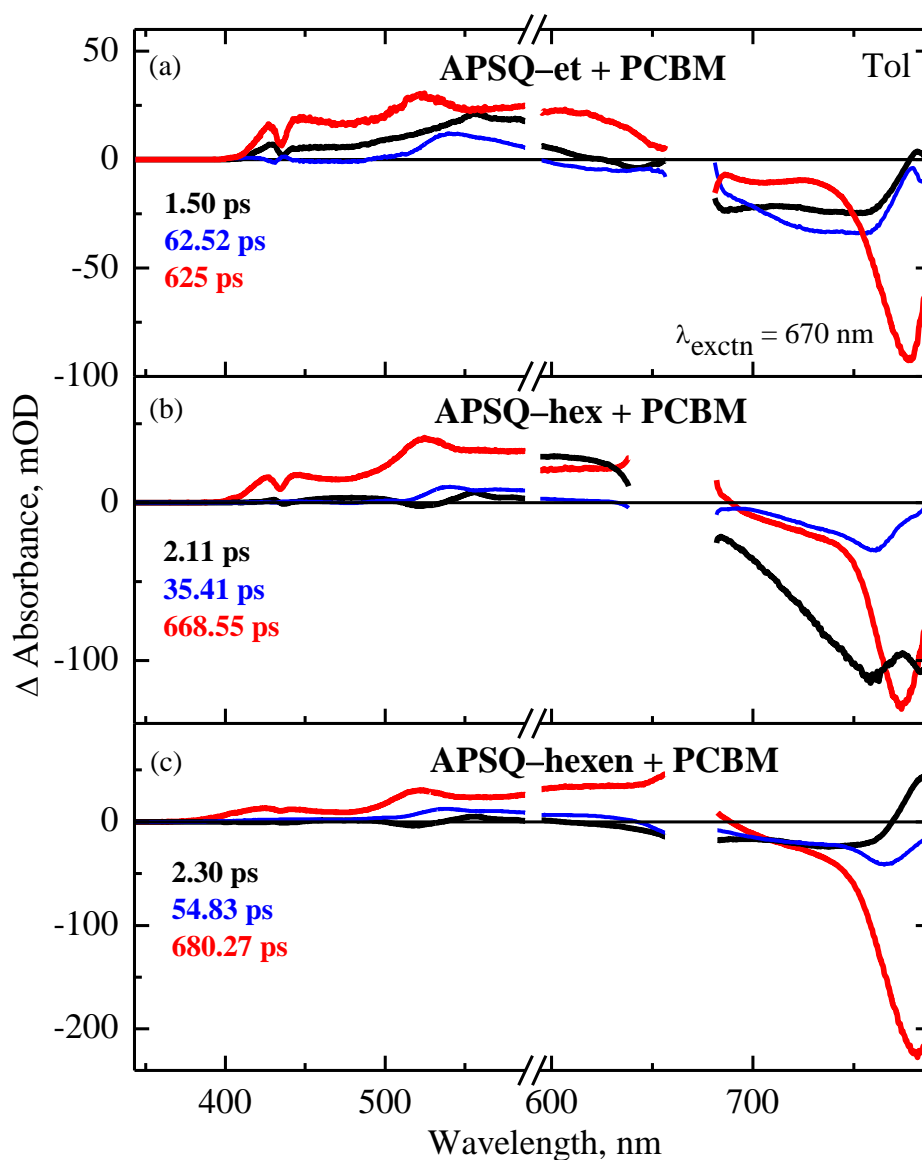


Figure 2.20 Decay associated difference spectra of APSQ-et (a), APSQ-hex (b) and APSQ-hexen (c) with PCBM in toluene obtained by global analysis.

2.5 Characterization of Photodetector

OPDs were fabricated using APSQs as sensitizers, and their device architecture and energy level diagram are shown in **Figure 2.21**. The J–V characteristics of the OPDs are shown in **Figure 2.22**. The asymmetric J–V features are due to the different hole–tunnelling injection barriers at the electrode/active layer interface. The hole–tunnelling injection from the Ag

electrode is much easier than the ITO electrode. Hence, the dark current in the reverse bias is much smaller than in the forward bias. The light current densities of the OPDs are significantly increased under light illumination compared to dark current. A current value of 1.3 mA/cm^2 is obtained under light illumination, which is nearly 3–5 orders of magnitude greater than the dark current ($\sim 50 \text{ nA/cm}^2$) at -1 V bias condition (with respect to ITO) of the OPD. In the presence of light, the current shows a steady increase with the increase of the reverse bias. This can be ascribed to improved charge extraction and a decrease of non-geminate losses in the presence of high electric field.⁶⁸

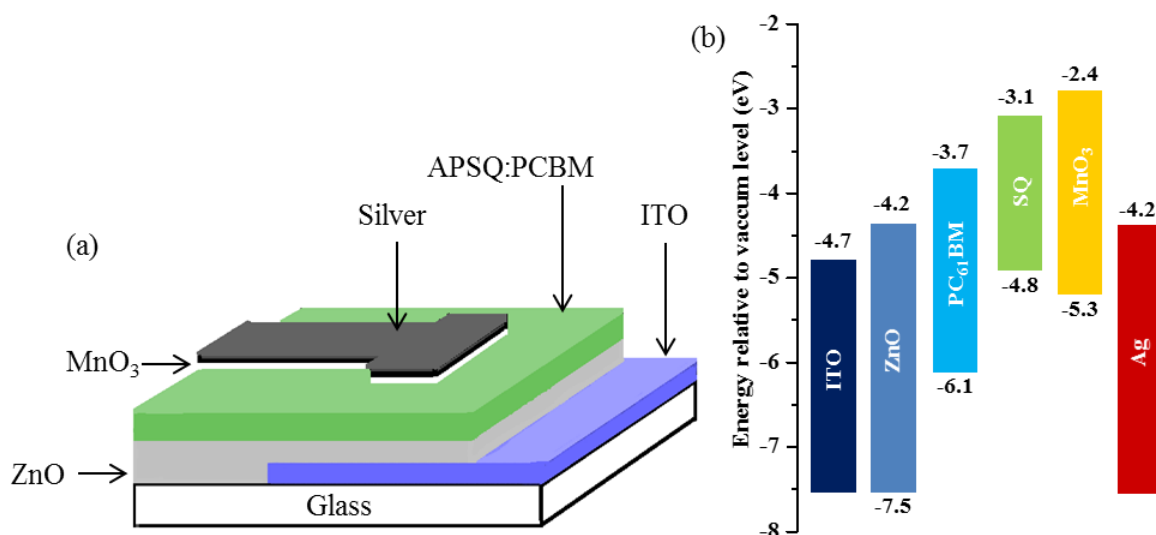


Figure 2.21 Fabricated OPD architecture (a) and Energy level diagram of the fabricated OPD (b).

The EQE of the OPDs under different bias conditions is shown in **Figure 2.23**. The EQE spectra follow the absorption spectra of the blend exhibited the features of PCBM and **APSQs**. EQE in the wavelength (λ) range $300 \text{ nm} < \lambda < 500 \text{ nm}$ is due to the PC₆₀BM and in the λ range, $600 \text{ nm} < \lambda < 950 \text{ nm}$ is ascribed to **APSQs**. The photocurrent is due to effective photogenerated exciton dissociation at the **APSQs/PCBM** interface and its transfer to the external circuit through the interface layers. It is found that the EQE increase with the

increasing reverse bias voltages. The devices exhibited an EQE increase from ~4% at short circuit conditions to ~12% at -1 V in the NIR region, with the peak EQE at ~840 nm for **APSQ-et**. Field-dependent dissociation of bound electron-hole pairs, the increased hole-transport velocity in the active layer with increasing electric field and increased hole-tunnelling injection can be the reason for such an enhancement in EQE.⁶⁹

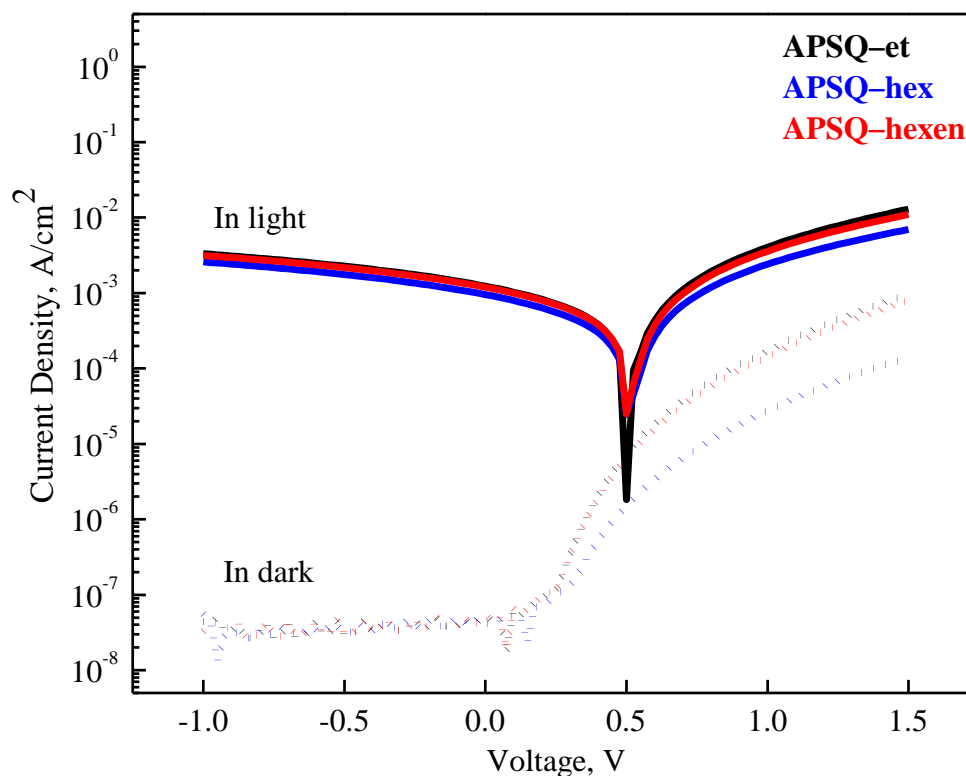


Figure 2.22 J–V characteristics of **APSQs** in dark and light in semi–logarithmic.

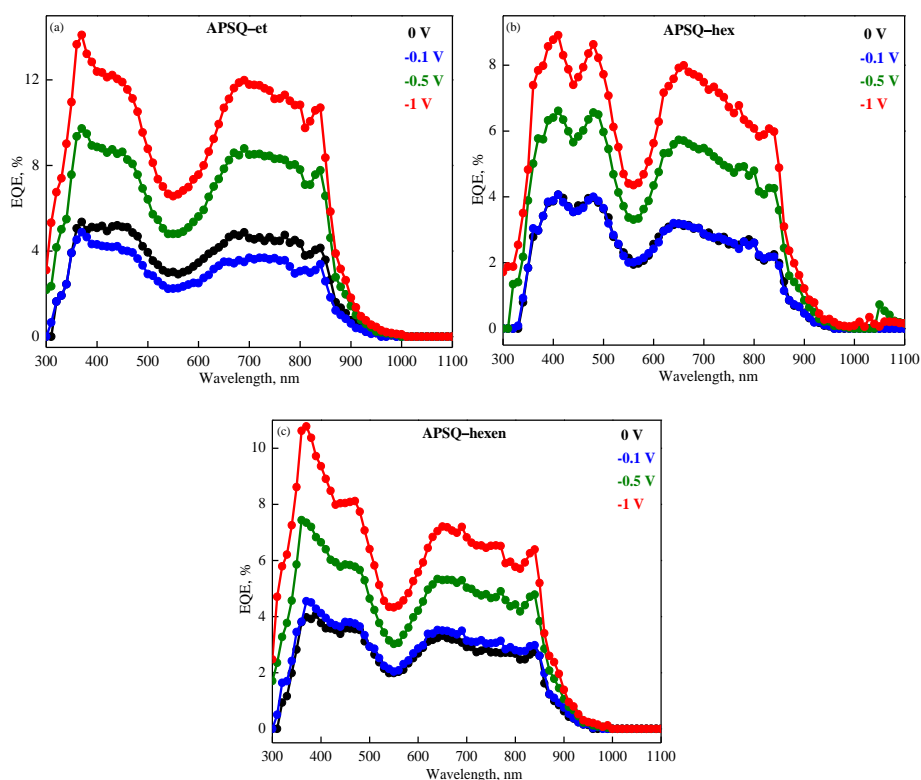


Figure 2.23 EQE spectra of devices using APSQ-et (a), APSQ-hex (b) and APSQ-hexen (c) at different bias conditions.

Figure 2.24 shows the R curve of the OPDs, which clearly shows a broad spectral response extending to $\lambda \sim 950$ nm. The spectral profile of R peaks around 700 nm and 840 nm. The R is 25 mA/W and 70 mA/W for unbiased and biased (-1 V) devices respectively at $\lambda \sim 840$ nm for APSQ-et. The R of the OPD is greatly enhanced with an increase in reverse bias, consistent with the increase in photocurrent with reverse bias. The combination of reduced dark current and improved EQE led to a dramatically enhanced D^* in the NIR region. At a reverse bias of -1 V, the device with an APSQ-et displayed a maximum D^* of 6×10^{11} cm Hz^{1/2} W⁻¹ (Jones) at 840 nm (**Figure 2.25b**). It is worth noting that D^* monotonically increases as the reverse bias increases for all the devices. The device performance data of APSQs at 840 nm are provided in **Table 2.7**.

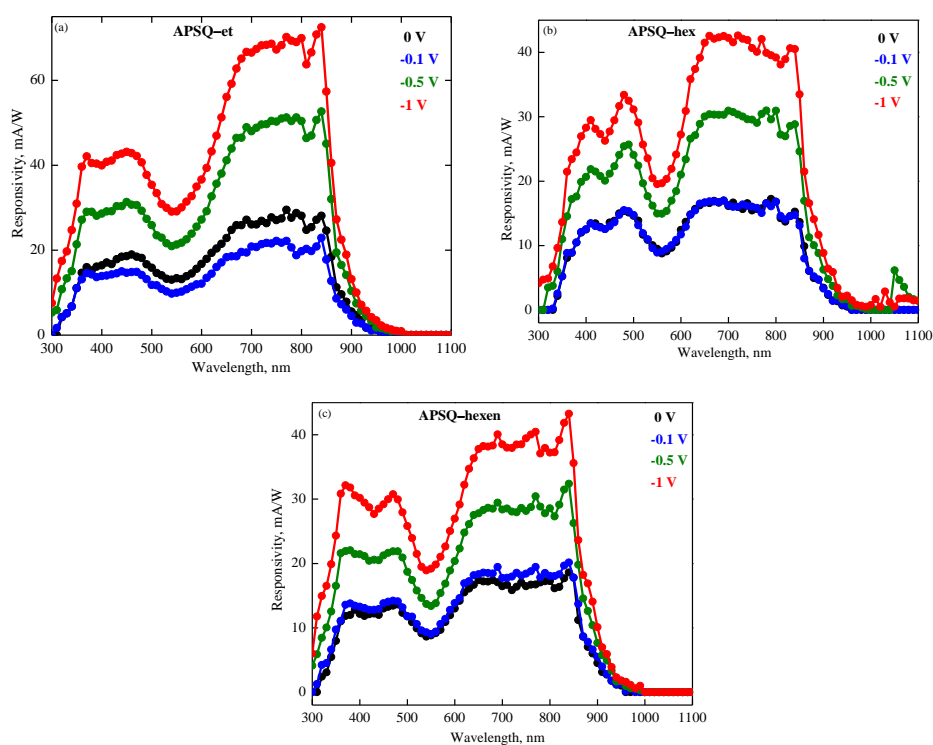


Figure 2.24 Spectral R of devices using APSQ-et (a), APSQ-hex (b) and APSQ-hexen (c) at different bias conditions.

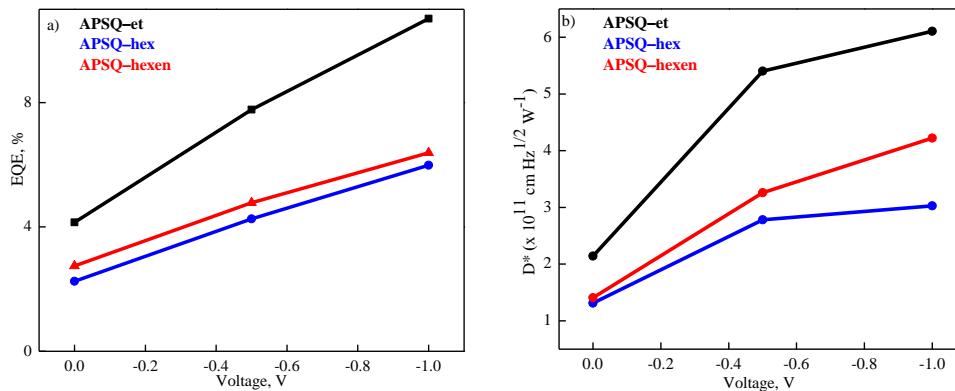


Figure 2.25 EQE (a) and D^* of APSQs devices at negative bias voltages (b).

Table 2.7 The Device Performance Data of **APSQs** at 840 nm

APSQs	EQE, %		R, mA/W		D*, × 10 ¹¹ Jones	
	0V	-1 V	0V	-1V	0V	-1V
APSQ-et	3.38	12.00	25.10	72.50	2.14	6.10
APSQ-hex	2.17	6.07	15.25	40.52	1.31	3.02
APSQ-hexen	2.80	6.38	18.60	43.30	1.40	4.22

The transient photovoltage (TPV) and transient photocurrent (TPC) measurements are well-known techniques for probing the charge carrier dynamics of OPD devices. TPC signal reveals the charge extraction dynamics, whereas the TPV signal is a good measure of the charge carrier density in the OPD. A combination of TPC and TPV studies shows insight into the recombination rate of the photogenerated charge.⁷⁰ **Figure 2.26** shows the TPC and TPV for the **APSQs** devices under 532 nm laser light pulses. A double exponential equation as shown below is used to fit the light OFF decay transient curve to determine the decay time constants.

$$y = A_1 e^{(-x/t_1)} + A_2 e^{(-x/t_2)} + y_0 \quad (4)$$

The response profile of both the TPC and TPV transients are similar. But the TPC decay time is typically 2–3 orders of magnitude shorter than the TPV time. The difference can be due to (i) TPV signal is measured at an approximately open circuit, so the decay primarily characterizes the charge recombination dynamics and (ii) TPC signal is recorded close to a short circuit, so the signal decay mainly represents the charge extraction (which occurs on a shorter timescale).⁷¹ All the transient measurements are measured in an unbiased condition. The devices showed a fast pulse response with short rise times and longer fall times. Hence the OPDs in the photovoltaic mode, displayed an ultrafast response in the range of ~15 ns.

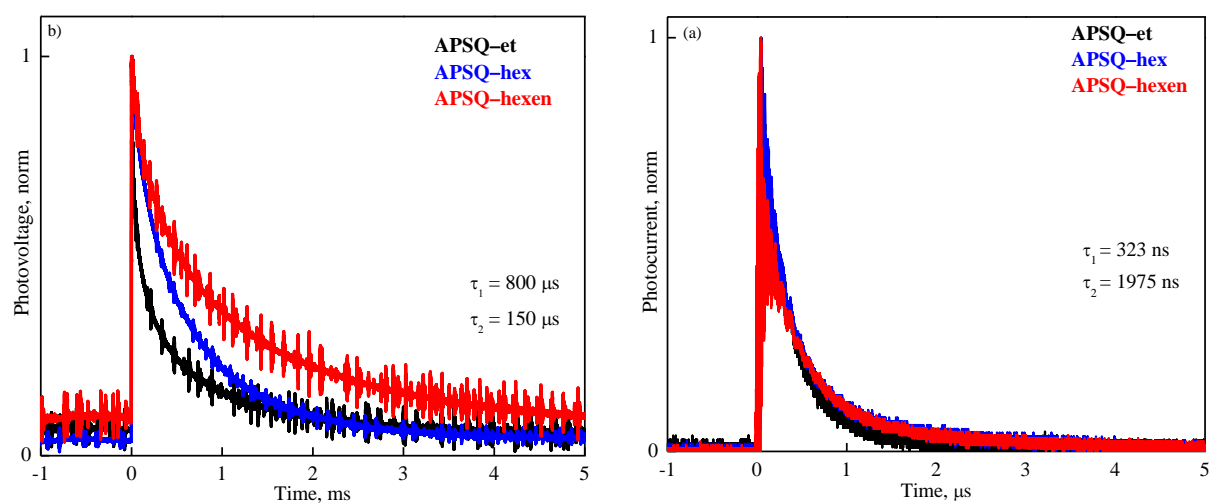


Figure 2.26 TPC (a) and TPV (b) decay response of APSQs detectors.

2.6 Summary

The USQ derivatives comprising *N,N*-dimethyl aminoanthracene and pyrrole appended phenylhydrazine (APSQs) were synthesized and their steady and time-resolved relaxation dynamics were recorded for the application of OPDs. The absorption spectra of APSQ derivatives showed a strong absorption maximum at around 760 nm with high extinction coefficient, $\sim 2.56 \times 10^5 \text{ M}^{-1}\text{cm}^{-1}$. Femtosecond transient absorption measurements revealed the quenching of time constants indicating the presence of the intermolecular charge-transfer dynamics between the APSQ derivatives and PCBM. OPDs were fabricated using APSQ derivatives as donor and PCBM as the acceptor working in the BHJ mode. OPDs showed a broad spectral response extending to $\lambda \sim 950 \text{ nm}$. A Photocurrent value of 1.3 mA/cm^2 was obtained under light illumination, which is almost 3–5 orders of magnitude greater than the dark current ($\sim 50 \text{ nA/cm}^2$) at -1 V bias condition of the OPD. The devices showed an EQE increase from $\sim 4 \%$ at 0 V to $\sim 12 \%$ at -1 V in the NIR region, with the peak EQE at $\sim 840 \text{ nm}$. At a reverse bias of -1 V , the device with a APSQ-et showed a maximum D^* of

$6 \times 10^{11} \text{ cm Hz}^{1/2} \text{ W}^{-1}$ (Jones) at 840 nm. The OPDs showed an ultrafast photoresponse in the range of ~ 15 ns. To the best of our knowledge, this will be the first OPDs with USQ dyes showed the ultrafast high detectivity in the NIR range of 760 nm.

2.7 Experimental Section

2.7.1 Materials and Methods

1 General Details: The chemicals and reagents used for synthesis were purchased from Sigma–Aldrich, Merck and TCI. Dry solvents were prepared by following the reported procedures.⁷² ^1H NMR spectra were measured using Bruker AMX 500 MHz spectrometer using tetramethylsilane (TMS) as the internal standard. High–resolution mass spectra of the derivatives were recorded using the Thermo Scientific Exactive LC–MS. The solvents used for the spectroscopic measurements were of HPLC grade (Merck) and used as received.

2 Steady–State Measurements: Absorption spectra were recorded using a UV–2600 (Shimadzu) UV–vis absorption spectrophotometer. Steady–state fluorescence experiments were performed with a Fluorolog–3 (Horiba) equipped with a 450W Xe arc lamp. The fluorescence quantum yields in different solvents were measured by using the integrating sphere (Quanta– ϕ , Horiba) following a reported procedure.⁷³

3 Electrochemical Measurements: Cyclic voltammetry experiments were performed using a BAS CV–50W voltammetric analyzer with three electrodes cell assemblies. Glassy carbon electrode, Ag/AgCl electrode and platinum wire were used as working, reference and counter electrodes respectively. The measurements were carried out in ACN with tetrabutylammonium hexafluorophosphate (TBAPF₆) as the supporting electrolyte at a scan rate of 50 mV s^{-1} . The ferrocene/ferrocenium (Fc/Fc⁺) redox couple was used as an external standard. The HOMO and LUMO energy values of PCBM are directly taken from the literature.^{74–75}

4 Time–Correlated Single–Photon Counting (TCSPC) Spectrometer: Fluorescence decays were measured using a picosecond single–photon counting system (Horiba, DeltaFlex) with the 670 nm LED as an excitation source and picosecond photon detection module (PPD–850) as a detector. The time resolution of TCSPC experimental setup is < 200 ps with 670 nm LED source. The instrument response function (IRF) was determined using a scattering solution of colloidal milk in deionized water. The fluorescence time constants are obtained by deconvoluting with the LED profile. The decay of the fluorescence intensity (I) with time (t) was fitted by a single exponential function:

$$I = A e^{-t/\tau} \quad (5)$$

where τ and A are the fluorescence lifetime and its amplitude of the compound respectively.

5 Femtosecond Transient Absorption Measurements: The instrument details for measuring the femtosecond transient absorption spectra have been discussed elsewhere.⁷⁶ It is a Ti:sapphire laser (MaiTai HP, Spectra Physics, USA) centered at 800 nm having 80 MHz repetition rate with a pulse width of < 100 fs. The amplified laser was split into two and the high energy beam was used as the pump (670 nm) for exciting the sample by using TOPAS (Prime, Light Conversion). The other part of the amplified beam (200 mW) focused on a 1 mm thick CaF₂ plate to generate a white light continuum (340–1000 nm) which further split into two beams (sample and reference probe beams). The sample cell (0.4 mm path length) was refreshed by rotating at a constant speed. Finally, the white light continuum was focused into a 100 μ m optical fiber coupled to imaging spectrometer after passing through the sample cell. The pump–probe spectrophotometer (ExciPro) setup was purchased from CDP Systems Corp, Russia. Normally transient absorption spectra were obtained by averaging about 2000 excitation pulses for each spectral delay. All the measurements were carried out at the magic angle (54.7°). All the transient absorption spectra obtained from the equipment is compensated

for the chirp of the white light by determining the time zero using coherent artefact observed in the solvent⁷⁷. The absorbance of the solution used was ~ 0.5 OD in 1 mm path length and the excitation energy was ~ 2 μJ for all the measurements. The laser fluence used for all the transient absorption measurements is ~ 3 $\mu\text{J}/\text{cm}^2$. The effective time resolution of the ultrafast spectrometer is determined to be about ≤ 120 fs. The concentration of **APSQs** used for transient absorption measurement was ~ 40 μM . The integrity of the sample is tested by measuring the absorption spectra of the sample before and after the experiments and found to be no significant changes in the absorption spectra.

6 Device Fabrication: PDs were fabricated in the device architecture, glass/ indium tin oxide (ITO)/ zinc oxide (ZnO)/ **APSQs:PCBM**/ molybdenum trioxide (MoO_3)/ silver (Ag). ITO coated glass plates were cleaned using detergent and deionized water. Further, the samples were ultrasonicated for 30 min in acetone, isopropanol and methanol respectively. Just before making devices, the ITO glass plate was dried in a vacuum oven for 1 h at 30 nm thick ZnO films are spin-coated on ITO by using a ZnO nanoparticle solution as mentioned previously.⁷⁸ **APSQs:PCBM** (1:6 ratio) blend in toluene (42 mg/ml) was spin-coated on top of ZnO to make a 100 nm thin active layer film. The hole transporting layer of 10 nm MoO_3 and back contact Ag of 100 nm were deposited by thermal evaporation. A shadow mask was used for thermal evaporation to make an active area of 3×3 mm.

7 Device Characterization: Current-voltage (J-V) characteristics of OPD were recorded in dark and light using a Keithley 6430 source measuring unit (Tektronix USA). Oriel class 3A solar simulator of intensity 100 mW/cm^2 with AM 1.5G filter was used as a light source for conducting light J-V measurements. EQE spectra of OPDs are measured using a lock-in technique. In this method, the photocurrent is measured with respect to wavelength

using a lock-in amplifier (Stanford Research SR830), which is locked at a non-harmonic light chopping frequency. A Xenon lamp coupled with a monochromator and order sorting filters was used as the light source (250 W Xenon lamp). All the measurements were calibrated with an NREL calibrated silicon solar cell. The D^* was calculated without measuring the noise current. Even though the determination of noise current is essential for the accurate measurement of D^* , it is not always performed due to its challenging experimental techniques. Instead, the dark current i_d is often assumed to be the dominant contribution to noise current.⁷⁹ Hence the $D^*(\lambda)$ of the OPDs were calculated using by simplifying the D^* (equation 6).⁸⁰

$$D^* = \frac{R(\lambda)\sqrt{AB}}{i_{noise}} = \frac{R(\lambda)\sqrt{A}}{\sqrt{2qi_d}} = \frac{R(\lambda)}{\sqrt{2qJ_d}} \quad (6)$$

Where $R(\lambda)$, A and B represent R, area and dark current density of the device respectively. i_{noise} , i_d and J_d represent the noise current, dark current and dark current density respectively, whereas q represents the charge of an electron. The response time of the OPDs was measured using photovoltage and photocurrent transient measurements. A 532 nm picosecond pulsed laser (Ekspla Nd:YAG laser delivering pulses of duration 100 ps) was used as an excitation pulse with a repetition rate of 10 Hz. Transient signals were measured using 1GHz, Tektronix MDO3104 oscilloscope. All the measurements were performed under ambient conditions without noticeable degradation of the devices.

2.8 Synthesis and Characterization of APSQ Derivatives

1 Synthesis of 1-Aminoanthracene

1-Aminoanthraquinone (5g) was stirred with 10% sodium hydroxide (60 ml) and zinc dust (5g) at room temperature for about 30 min. It was slowly heated to 85–90 °C. Zinc dust (5g) was then introduced into the reaction mixture in two equal proportions at 30 min each and heating was continued with constant stirring for 24 h, at 90 °C. After cooling, the solid material

from the reaction mixture was collected and washed several times with water. Soxhlet extraction with acetone and then recrystallization from ethanol gave 1-aminoanthracene (2.8 g, 65%).

^1H NMR (500 MHz, CDCl_3): δ 8.71 (s, 1H), 8.39 (s, 1H), 8.03-7.99 (t, 2H, $J = 1\text{Hz}$), 7.47-7.42 (m, 2H), 7.39-7.37 (d, 1H, $J = 8.5\text{ Hz}$), 6.76-6.74 (d, 1H, $J = 7\text{Hz}$), 7.37-7.24 (dd, 1H, $J = 7\text{ Hz}$); HRMS–EI: Calculated molecular weight for $\text{C}_{14}\text{H}_{11}\text{N}$ is 193.2438, found = 194.0962.

2 Synthesis of N, N-dimethylantracene-1-amine

1-Aminoanthracene (1.4 g, 7.24 mmol) and activated potassium carbonate (6.9 g, 50.68 mmol) was taken in a 250 ml round-bottomed flask. It was stirred in 20 ml of anhydrous *N,N*-dimethyl formamide (DMF). Then the pressure-equalizing funnel was connected between RB flask and condenser. To that 10 ml of DMF and methyl iodide (5.1g, 36.22 mmol) was added. Then this mixture was slowly added to the RB flask; it was stirred for about 1 h in room temperature. Then the reaction mixture was heated at 100 °C for about 36 h. After the reaction, the mixture is allowed to cool to room temperature and then transferred to a beaker containing ice. The organic phase was extracted with dichloromethane, washed several times with water, and dried over sodium sulfate. Then the solvent is removed under reduced pressure. The product was purified by column chromatography [silica gel, hexane: ethyl acetate (3:97)] to give a viscous green oil (1.1 g, 69%).

^1H NMR (500 MHz, CDCl_3): δ 8.79 (s,1H), 8.39 (s,1H), 8.06-8.04 (t,1H, $J = 4.5\text{ Hz}$), 7.99-7.97 (t,1H, $J = 4.5\text{ Hz}$), 7.46-7.44 (m,2H), 7.69-7.67 (d, 1H, $J = 8.5\text{Hz}$), 7.39-7.36 (dd, 1H, $J = 7\text{Hz}$), 7.02-7.01 (d, 1H, $J = 7\text{ Hz}$), 2.99(s,6H). HRMS–EI: Calculated molecular weight for $\text{C}_{16}\text{H}_{15}\text{N}$ is 221.2970, found = 222.0913.

3 Synthesis of 3-(4-(dimethylamino) anthracen-1-yl)-4-hydroxycyclobut-3ene1, 2 dione

3, 4-dichlorocyclobutene-1,2 dione (commonly called squarylium chloride, 0.73g, 4.9

mmol), and N, N- dimethylantracen-1-amine (1.1 g, 4.9 mmol), were dissolved in dry benzene (30ml) and refluxed for 8 h. After cooling the reaction mixture, the solvent was removed under reduced pressure and the crude product obtained was dissolved in a mixture of glacial acetic acid (15ml), distilled water (15ml) and 2N HCl (10 ml). The resulting mixture was then refluxed for 2 h at 120 °C. After cooling, the solution was added to crushed ice, the precipitated product thus obtained was isolated by filtration, washed with diethyl ether and dried. (0.85 g, 35%). The blackish–brown powder obtained was used without further purification. HRMS–EI: Calculated molecular weight for C₂₀H₁₅O₃ is 317.3380, found = 318.1131.

4 General procedure for the alkylation of pyrrole 2-carbaldehyde

A solution of pyrrole 2-carbaldehyde (1 equivalent) in anhydrous DMF (20ml) was added dropwise at 0 °C and under nitrogen to a suspension of sodium hydride (NaH, 60% suspension in mineral oil, 1.4 equivalent) in the same solvent. The resulting suspension was stirred at 0 °C for 30 min and a solution of ethyl iodide (1.4 equivalent) in anhydrous DMF (5ml) was added dropwise. The suspension was stirred for 48 h at room temperature, poured into brine and extracted with diethyl ether. The organic phase was washed with water, dried over anhydrous sodium sulfate and filtered. Thus, the crude product was purified by column chromatography (silica gel, hexane: ethyl acetate, 3:97) to give the desired product.

5 Characterization details of 1-ethyl-1H-pyrrole-2-carbaldehyde

¹H NMR (500 MHz, CDCl₃): δ 9.53 (s, 1H), 6.96 (s, 1H), 6.23-6.21 (dd, 1H, *J* = 2Hz), 6.93-6.92 (dd, 1H, *J* = 2Hz), 4.37-4.33 (q, 2H, *J* = 7.5 Hz), 1.40-1.37 (t, 3H).

1.4.2 Characterization details of 1-hexyl-1H-pyrrole-2-carbaldehyde

¹H NMR (500 MHz, CDCl₃): δ 9.58 (s, 1H), 7.00 (s, 1H), 6.27-6.25 (dd, 1H, *J* = 2Hz), 6.97-6.96 (dd, 1H, *J* = 2Hz), 4.37-4.33 (q, 2H), 1.75-1.71 (p, 2H), 1.33-1.30 (p, 2H), 1.27-1.23 (P, 2H), 1.20-0.97 (m, 2H), 0.90-0.87 (t, 3H).

6 Characterization details of 1-(hex-5-enyl)-1H-pyrrole-2-carbaldehyde

¹H NMR (500 MHz, CDCl₃): δ 9.55 (s, 1H), 6.98 (s, 1H), 6.28-6.26 (dd, 1H, *J* = 2Hz), 6.99-6.98 (dd, 1H, *J* = 2Hz), 5.82-5.79 (m, 1H), 5.02-5.00 (d, 2H), 4.37-4.33 (q, 2H), 2.19-2.15 (q, 2H), 1.75-1.71 (p, 2H), 1.33-1.30 (p, 2H).

7 General procedures for reaction between alkylated pyrrole-2-carbaldehyde and N, N-diphenylhydrazine hydrochloride

A mixture of N, N-diphenylhydrazine hydrochloride (1 equivalent), 1-ethyl-1H-pyrrole-2-carbaldehyde (1 equivalent) and imidazole (1 equivalent) was dissolved in anhydrous ethanol (30 ml), and refluxed for 4 h. After the reaction, the mixture is allowed to cool to room temperature. The solvent was removed under reduced pressure and the residue was purified by column chromatography (silica gel, hexane: ethyl acetate, 85:15) to give the desired product.

7.1 Characterization details of (E)-2-((2,2-diphenylhydrazono)methyl)-1-ethyl-1H-pyrrole

¹H NMR (500 MHz, CDCl₃): δ 6.72-6.71 (t, 1H, *J* = 2.5 Hz), 6.1-6.08 (dd, 1H, *J* = 3 Hz), 6.14-6.13 (dd, 1H, *J* = 2 Hz), 7.13-7.10 (m, 4H), 7.41-7.31 (m, 4H), 7.16-7.15 (m, 2H), 4.47-4.30 (q, 2H), 1.50-1.47 (t, 3H).

7.2 Characterization details of (E)-2-((2,2-diphenylhydrazono)methyl)-1-hexyl-1H-pyrrole

¹H NMR (500 MHz, CDCl₃): δ 6.77-6.75 (t, 1H, *J* = 2.5 Hz), 6.40-6.10 (dd, 1H, *J* = 3 Hz), 6.17-6.14 (dd, 1H, *J* = 2 Hz), 7.19-7.16 (m, 4H), 7.40-7.34 (m, 4H), 7.19-7.17 (m, 2H), 4.47-4.30 (q, 2H, *J* = 7.5 Hz), 1.77-1.73 (p, 2H), 1.36-1.33 (p, 2H), 1.30-1.27 (P, 2H), 1.22-0.99 (m, 2H), 0.92-0.89 (t, 3H)

7.3 Characterization details of (E)-2-((2,2-diphenylhydrazono)methyl)-1-(hex-5-enyl)-1H-pyrrole

¹H NMR (500 MHz, CDCl₃): δ 6.75-6.72 (t, 1H, *J* = 2.5 Hz), 6.30-6.28 (dd, 1H, *J* = 3 Hz), 6.17-6.14 (dd, 1H, *J* = 2 Hz), 7.23-7.20 (m, 4H), 7.43-7.38 (m, 4H), 7.19-7.15 (m, 2H), 5.82-

5.79 (m, 1H), 5.02-5.00 (d, 2H), 4.49-4.45 (q, 2H), 2.19-2.15 (q, 2H), 1.33-1.30 (p, 2H). 1.50-1.47 (t, 3H).

8 General procedure for the synthesis of APSQ–et, APSQ–hex and APSQ–hexen

A suspension of 3-(4-(dimethylamino) anthracen-1-yl)-4-hydroxycyclobut-3-ene-1,2-dione (1 equivalent), and the hydrazone precursor (1 equivalent) was dissolved in a 1:1 benzene: butanol azeotropic mixture (30 ml), and refluxed at 90 °C in a Dean–Stark apparatus for about 8 h. After the reaction, the mixture is allowed to cool to room temperature and the solvent is removed under reduced pressure. Then the residue was purified by column chromatography. (silica gel, hexane: ethyl acetate, 60:40), followed by recrystallization with chloroform.

8.1 Characterization details of APSQ–et [(E)-2-(3-(4-(dimethylamino) anthracen -1 yl) -2-hydroxy-4 oxocyclobut-2-en-1-ylidene)-5-((Z)-(2,2-diphenylhydrazono) methyl)-1-ethyl-2H-pyrrol-1 ium]

¹H NMR (500 MHz, CDCl₃): δ 9.34-9.33 (d, 1H, *J* = 8.5 Hz), 8.27-8.25 (d, 1H, *J* = 8.5 Hz), 8.03-8.02 (d, 1H, *J* = 4.5 Hz), 7.98-7.96 (d, 1H, *J* = 8.5 Hz), 7.55- 7.47 (m, 6H), 7.31-7.26 (m, 4H), 7.23-7.21 (m, 4H), 7.12 (s, 1H), 6.94-6.93 (d, 1H, *J* = 8.5 Hz), 6.86-6.85 (d, 1H, *J* = 4.5 Hz), 5.03-4.99 (q, 2H, *J* = 7Hz), 3.31 (s, 6H), 1.44-1.41 (t, 3H); HRMS–EI: Calculated molecular weight for C₃₉H₃₂N₄O₂ is 588.6970, found = 588.2530.

8.2 Characterization details of APSQ–hex [(E)-2-(4-(dimethylamino)anthracen-1-yl)-4-(5-((E)-(2,2-diphenylhydrazono)methyl)-1-hexyl-2H-pyrrol-2-ylidene)-3-oxocyclobut-1-enolate]

¹H NMR (500 MHz, CDCl₃): δ 9.38-9.36 (d, 1H, *J* = 8.5 Hz), 8.31-8.29 (d, 1H, *J* = 8.5 Hz), 8.09-8.06 (d, 1H, *J* = 4.5 Hz), 7.94-7.92 (d, 1H, *J* = 8.5 Hz), 7.51- 7.48 (m, 6H), 7.34-7.231 (m, 4H), 7.27-7.22 (m, 4H), 7.11 (s, 1H), 6.96-6.93 (d, 1H, *J* = 8.5 Hz), 6.85-6.83 (d, 1H, *J* = 4.5 Hz), 5.03-4.99 (q, 2H, *J* = 7Hz), 3.29 (s, 6H), 1.80-1.78 (p, 2H), 1.47-1.50 (p, 2H), 1.30-1.27 (p, 2H), 1.20-0.95 (m, 2H), 0.89-0.86 (t, 3H);

HRMS–EI: Calculated molecular weight for C₄₃H₄₀N₄O₂ is 644.8033, found = 644.2895.

8.3 Characterization details of APSQ–hexen [(E)-2-(4-(dimethylamino)anthracen-1-yl)-4-(5-((E)-(2,2-diphenylhydrazono)methyl)-1-(hex-5-enyl)-2H-pyrrolium-2-ylidene)-3-oxocyclobut-1-enolate]

¹H NMR (500 MHz, CDCl₃): δ 9.38-9.37 (d, 1H, *J* = 8.5 Hz), 8.25-8.23 (d, 1H, *J* = 8.5 Hz), 8.08-8.04 (d, 1H, *J* = 4.5 Hz), 7.95-7.93 (d, 1H, *J* = 8.5 Hz), 7.59- 7.44 (m, 6H), 7.34-7.29 (m, 2H), 7.22-7.18 (m, 4H), 7.15 (s, 1H), 6.98-6.96 (d, 1H, *J* = 8.5 Hz), 6.85-6.83 (d, 1H, *J* = 4.5 Hz), 5.85-5.79 (t, 1H), 5.05-5.01 (q, 2H), 4.98-4.96 (d, 2H), 3.29 (s, 6H), 2.2-1.9 (m, 6H), 1.30-1.27 (t, 2H); HRMS–EI: Calculated molecular weight for C₄₃H₃₈N₄O₂ is 642.7874, found = 642.3010.

2.9 References

1. Saneesh Babu, P. S., et al., Bis(3,5-Diiodo-2,4,6-Trihydroxyphenyl)Squaraine Photodynamic Therapy Disrupts Redox Homeostasis and Induce Mitochondria-Mediated Apoptosis in Human Breast Cancer Cells. *Sci. Rep.* **2017**, *7*, 42126.
2. Umezawa, K.; Citterio, D.; Suzuki, K., Water-Soluble Nir Fluorescent Probes Based on Squaraine and Their Application for Protein Labeling. *Anal Sci* **2008**, *24*, 213-217.
3. Chen, C.; Dong, H.; Chen, Y.; Guo, L.; Wang, Z.; Sun, J.-J.; Fu, N., Dual-Mode Unsymmetrical Squaraine-Based Sensor for Selective Detection of Hg²⁺ in Aqueous Media. *Org. Biomol. Chem.* **2011**, *9*, 8195-8201.
4. Butnarusu, C.; Barbero, N.; Barolo, C.; Visentin, S., Squaraine Dyes as Fluorescent Turn-on Sensors for the Detection of Porcine Gastric Mucin: A Spectroscopic and Kinetic Study. *J. Photochem. Photobiol. B, Biol.* **2020**, *205*, 111838.
5. Corredor, C. C.; Huang, Z.-L.; Belfield, K. D., Two-Photon 3d Optical Data Storage Via Fluorescence Modulation of an Efficient Fluorene Dye by a Photochromic Diarylethene. *Adv. Mater.* **2006**, *18*, 2910-2914.
6. Aragoni, M. C., et al., Monoreduced [M(R,R'Timdt)₂]– Dithiolenes (M = Ni, Pd, Pt; R,R'Timdt = Disubstituted Imidazolidine-2,4,5-Trithione): Solid State Photoconducting Properties in the Third Optical Fiber Window. *ChemComm* **2004**, 1882-1883.
7. Kobayashi, A.; Sasa, M.; Suzuki, W.; Fujiwara, E.; Tanaka, H.; Tokumoto, M.; Okano, Y.; Fujiwara, H.; Kobayashi, H., Infrared Electronic Absorption in a Single-Component Molecular Metal. *J. Am. Chem. Soc.* **2004**, *126*, 426-427.
8. Strassel, K., et al., Squaraine Dye for a Visibly Transparent All-Organic Optical Upconversion Device with Sensitivity at 1000 Nm. *ACS Appl. Mater. Interfaces* **2018**, *10*, 11063-11069.
9. Henary, M.; Paranjpe, S.; Owens Eric, A., Synthesis and Applications of Benzothiazole Containing Cyanine Dyes. In *Heterocycl. Commun.*, 2013; Vol. 19, p 1.
10. Duan, L.; Wang, L.; Zhang, C.; Yu, L.; Guo, F.; Sun, Z.; Xu, Y.; Yan, F., Role of near-Infrared Heptamethine Cyanine Dye Ir-783 in Diagnosis of Cervical Cancer and Its

- Mechanism. *Int J Clin Exp Pathol* **2019**, *12*, 2353-2362.
11. Li, P., et al., Ir-783 Inhibits Breast Cancer Cell Proliferation and Migration by Inducing Mitochondrial Fission. *Int J Oncol* **2019**, *55*, 415-424.
 12. Figueras, E., et al., Octreotide Conjugates for Tumor Targeting and Imaging. *Pharmaceutics* **2019**, *11*, 220.
 13. Zink-Lorre, N.; Font-Sanchis, E.; Seetharaman, S.; Karr, P. A.; Sastre-Santos, Á.; D'Souza, F.; Fernández-Lázaro, F., Directly Linked Zinc Phthalocyanine–Perylenediimide Dyads and a Triad for Ultrafast Charge Separation. *Chem.: Eur. J.* **2019**, *25*, 10123-10132.
 14. Abrahamse, H.; Houreld, N. N., Genetic Aberrations Associated with Photodynamic Therapy in Colorectal Cancer Cells. *Int. J. Mol. Sci.* **2019**, *20*, 3254.
 15. Li, L.; Huang, Y.; Peng, J.; Cao, Y.; Peng, X., Highly Responsive Organic near-Infrared Photodetectors Based on a Porphyrin Small Molecule. *J. Mater. Chem. C*, **2014**, *2*, 1372-1375.
 16. Schulz, M.; Mack, M.; Kolloge, O.; Lützen, A.; Schiek, M., Organic Photodiodes from Homochiral L-Proline Derived Squaraine Compounds with Strong Circular Dichroism. *Phys. Chem. Chem. Phys.* **2017**, *19*, 6996-7008.
 17. Kim, J. H.; Liess, A.; Stolte, M.; Krause, A.-M.; Stepanenko, V.; Zhong, C.; Bialas, D.; Spano, F.; Würthner, F., An Efficient Narrowband near-Infrared at 1040 nm Organic Photodetector Realized by Intermolecular Charge Transfer Mediated Coupling Based on a Squaraine Dye. *Adv. Mater.* **2021**, *33*, 2100582.
 18. Somashekharappa, G. M.; Govind, C.; Pulikodan, V.; Paul, M.; Namboothiry, M. A. G.; Das, S.; Karunakaran, V., Unsymmetrical Squaraine Dye-Based Organic Photodetector Exhibiting Enhanced near-Infrared Sensitivity. *J. Phys. Chem. C* **2020**, *124*, 21730-21739.
 19. Strassel, K., et al., Shortwave Infrared-Absorbing Squaraine Dyes for All-Organic Optical Upconversion Devices. *Sci. Technol. Adv. Mater.* **2021**, *22*, 194 - 204.
 20. Paternò, G. M.; Barbero, N.; Galliano, S.; Barolo, C.; Lanzani, G.; Scotognella, F.; Borrelli, R., Excited State Photophysics of Squaraine Dyes for Photovoltaic Applications: An Alternative Deactivation Scenario. *J. Mater. Chem. C*, **2018**, *6*, 2778-2785.
 21. Mayerhöffer, U.; Gsänger, M.; Stolte, M.; Fimmel, B.; Würthner, F., Synthesis and Molecular Properties of Acceptor-Substituted Squaraine Dyes. *Chem. Eur. J.* **2013**, *19*, 218-232.
 22. Khopkar, S.; Shankarling, G., Synthesis, Photophysical Properties and Applications of NIR Absorbing Unsymmetrical Squaraines: A Review. *Dyes Pigm.* **2019**, *170*, 107645.
 23. Yang, D.; Ma, D., Development of Organic Semiconductor Photodetectors: From Mechanism to Applications. *Adv. Opt. Mater.* **2019**, *7*, 1800522.
 24. Law, K. Y., Squaraine Chemistry: Effects of Structural Changes on the Absorption and Multiple Fluorescence Emission of Bis[4-(Dimethylamino)Phenyl]Squaraine and Its Derivatives. *J Phys Chem* **1987**, *91*, 5184-5193.
 25. Khopkar, S.; Shankarling, G., Synthesis, Photophysical Properties and Applications of NIR Absorbing Unsymmetrical Squaraines: A Review. *Dyes Pigm.* **2019**, *170*, 107645.
 26. Yang, D.; Yang, Q.; Yang, L.; Luo, Q.; Huang, Y.; Lu, Z.; Zhao, S., Novel High Performance Asymmetrical Squaraines for Small Molecule Organic Solar Cells with a High Open Circuit Voltage of 1.12 V. *ChemComm* **2013**, *49*, 10465-10467.
 27. Alex, S.; Santhosh, U.; Das, S., Dye Sensitization of Nanocrystalline TiO₂: Enhanced Efficiency of Unsymmetrical Versus Symmetrical Squaraine Dyes. *J. Photochem. Photobiol. A* **2005**, *172*, 63-71.
 28. Rana, A.; Sharma, C.; Prabhu, D. D.; Kumar, M.; Karuvath, Y.; Das, S.; Chand, S.; Singh, R. K., Revealing Charge Carrier Dynamics in Squaraine:[6, 6]-Phenyl-C 71-Butyric Acid Methyl Ester Based Organic Solar Cells. *AIP Adv.* **2018**, *8*, 045302.

29. Binda, M.; Agostinelli, T.; Caironi, M.; Natali, D.; Sampietro, M.; Beverina, L.; Ruffo, R.; Silvestri, F., Fast and Air Stable near-Infrared Organic Detector Based on Squaraine Dyes. *Org. Electron.* **2009**, *10*, 1314-1319.
30. Binda, M.; Iacchetti, A.; Natali, D.; Beverina, L.; Sassi, M.; Sampietro, M., High Detectivity Squaraine-Based near Infrared Photodetector with Na/Cm² Dark Current. *Appl. Phys. Lett.* **2011**, *98*, 073303.
31. Bellani, S.; Iacchetti, A.; Porro, M.; Beverina, L.; Antognazza, M. R.; Natali, D., Charge Transport Characterization in a Squaraine-Based Photodetector by Means of Admittance Spectroscopy. *Org. Electron.* **2015**, *22*, 56-61.
32. Kim, S.; Mor, G. K.; Paulose, M.; Varghese, O. K.; Baik, C.; Grimes, C. A., Molecular Design of near-Ir Harvesting Unsymmetrical Squaraine Dyes. *Langmuir* **2010**, *26*, 13486-13492.
33. Khan, R.; Ningombam, A.; Singh, K.; Singh, M., Stereoelectronic Effects in the Stereoselectivity of the Diels-Alder Reactions: Reactions of Aminoanthracenes with N-Phenylmaleimide. *J. Chem. Pharm. Res.* **2012**, *4*, 1532-1538.
34. Tatars, A.; Fedyunyaeva, I.; Terpetschnig, E.; Patsenker, L., Synthesis of Novel Squaraine Dyes and Their Intermediates. *Dyes Pigm.* **2005**, *64*, 125-134.
35. Inoue, T.; Pandey, S. S.; Fujikawa, N.; Yamaguchi, Y.; Hayase, S., Synthesis and Characterization of Squaric Acid Based NIR Dyes for Their Application Towards Dye-Sensitized Solar Cells. *J. Photochem. Photobiol. A* **2010**, *213*, 23-29.
36. Yum, J.-H.; Walter, P.; Huber, S.; Rentsch, D.; Geiger, T.; Nüesch, F.; De Angelis, F.; Grätzel, M.; Nazeeruddin, M. K., Efficient Far Red Sensitization of Nanocrystalline TiO₂ Films by an Unsymmetrical Squaraine Dye. *J. Am. Chem. Soc.* **2007**, *129*, 10320-10321.
37. So, S.; Choi, H.; Kim, C.; Cho, N.; Ko, H. M.; Lee, J. K.; Ko, J., Novel Symmetric Squaraine Chromophore Containing Triphenylamine for Solution Processed Small Molecule Bulk Heterojunction Solar Cells. *Sol. Energy Mater. Sol. Cells* **2011**, *95*, 3433-3441.
38. Della Pelle, A. M.; Homnick, P. J.; Bae, Y.; Lahti, P. M.; Thayumanavan, S., Effect of Substituents on Optical Properties and Charge-Carrier Polarity of Squaraine Dyes. *J. Phys. Chem. C* **2014**, *118*, 1793-1799.
39. Chen, G.; Sasabe, H.; Igarashi, T.; Hong, Z.; Kido, J., Squaraine Dyes for Organic Photovoltaic Cells. *J. Mater. Chem. A* **2015**, *3*, 14517-14534.
40. Beverina, L.; Salice, P., Squaraine Compounds: Tailored Design and Synthesis Towards a Variety of Material Science Applications. *Eur. J. Org. Chem.* **2010**, *2010*, 1207-1225.
41. Bigelow, R. W.; Freund, H.-J., An Mndo and Cndo / S(S + Des Ci) Study on the Structural and Electronic Properties of a Model Squaraine Dye and Related Cyanine. *Chem. Phys.* **1986**, *107*, 159-174.
42. Alex, S.; Basheer, M. C.; Arun, K. T.; Ramaiah, D.; Das, S., Aggregation Properties of Heavy Atom Substituted Squaraine Dyes: Evidence for the Formation of J-Type Dimer Aggregates in Aprotic Solvents. *J. Phys. Chem. A* **2007**, *111*, 3226-3230.
43. Gsänger, M.; Kirchner, E.; Stolte, M.; Burschka, C.; Stepanenko, V.; Pflaum, J.; Würthner, F., High-Performance Organic Thin-Film Transistors of J-Stacked Squaraine Dyes. *J. Am. Chem. Soc.* **2014**, *136*, 2351-2362.
44. Pandey, S. S.; Inoue, T.; Fujikawa, N.; Yamaguchi, Y.; Hayase, S., Alkyl and Fluoro-Alkyl Substituted Squaraine Dyes: A Prospective Approach Towards Development of Novel NIR Sensitizers. *Thin Solid Films* **2010**, *519*, 1066-1071.
45. Shafeekh, K. M.; Soumya, M. S.; Rahim, M. A.; Abraham, A.; Das, S., Synthesis and Characterization of near-Infrared Absorbing Water Soluble Squaraines and Study of Their

- Photodynamic Effects in D1a Live Cells. *Photochem. Photobiol.* **2014**, *90*, 585-595.
46. Duan, R.; Ye, L.; Guo, X.; Huang, Y.; Wang, P.; Zhang, S.; Zhang, J.; Huo, L.; Hou, J., Application of Two-Dimensional Conjugated Benzo[1,2-B:4,5-B']Dithiophene in Quinoxaline-Based Photovoltaic Polymers. *Macromolecules* **2012**, *45*, 3032-3038.
47. Vuk, D.; Radovanović-Perić, F.; Mandić, V.; Lovrinčević, V.; Rath, T.; Panžić, I.; Le-Cunff, J., Synthesis and Nanoarchitectonics of Novel Squaraine Derivatives for Organic Photovoltaic Devices. *Nanomaterials* **2022**, *12*, 1206.
48. Kabatc, J.; Kostrzewska, K.; Kozak, M.; Balcerak, A., Visible Light Photoinitiating Systems Based on Squaraine Dye: Kinetic, Mechanistic and Laser Flash Photolysis Studies. *RSC Adv.* **2016**, *6*, 103851-103863.
49. Chang, H.-J.; Bondar, M. V.; Liu, T.; Liu, X.; Singh, S.; Belfield, K. D.; Sheely, A.; Masunov, A. E.; Hagan, D. J.; Van Stryland, E. W., Electronic Nature of Neutral and Charged Two-Photon Absorbing Squaraines for Fluorescence Bioimaging Application. *ACS Omega* **2019**, *4*, 14669-14679.
50. Liu, T.; Bondar, M. V.; Belfield, K. D.; Anderson, D.; Masunov, A. E.; Hagan, D. J.; Stryland, E. W. V., Linear Photophysics and Femtosecond Nonlinear Spectroscopy of a Star-Shaped Squaraine Derivative with Efficient Two-Photon Absorption. *J. Phys. Chem. C* **2016**, *120*, 11099-11110.
51. Belfield, K. D.; Bondar, M. V.; Haniff, H. S.; Mikhailov, I. A.; Luchita, G.; Przhonska, O. V., Superfluorescent Squaraine with Efficient Two-Photon Absorption and High Photostability. *ChemPhysChem* **2013**, *14*, 3532-3542.
52. Webster, S., et al., Near-Unity Quantum Yields for Intersystem Crossing and Singlet Oxygen Generation in Polymethine-Like Molecules: Design and Experimental Realization. *J. Phys. Chem. Lett.* **2010**, *1*, 2354-2360.
53. Lambert, C.; Scherpf, T.; Ceymann, H.; Schmiedel, A.; Holzapfel, M., Coupled Oscillators for Tuning Fluorescence Properties of Squaraine Dyes. *J. Am. Chem. Soc.* **2015**, *137*, 3547-3557.
54. Horng, M. L.; Gardecki, J. A.; Papazyan, A.; Maroncelli, M., Subpicosecond Measurements of Polar Solvation Dynamics: Coumarin 153 Revisited. *J Phys Chem* **1995**, *99*, 17311-17337.
55. Kuang, Z.; He, G.; Song, H.; Wang, X.; Hu, Z.; Sun, H.; Wan, Y.; Guo, Q.; Xia, A., Conformational Relaxation and Thermally Activated Delayed Fluorescence in Anthraquinone-Based Intramolecular Charge-Transfer Compound. *J. Phys. Chem. C* **2018**, *122*, 3727-3737.
56. Eom, I.; Joo, T., Polar Solvation Dynamics of Coumarin 153 by Ultrafast Time-Resolved Fluorescence. *J. Chem. Phys.* **2009**, *131*, 244507.
57. Mohammed, O. F.; Vauthey, E., Excited-State Dynamics of Nitroperylene in Solution: Solvent and Excitation Wavelength Dependence. *J. Phys. Chem. A* **2008**, *112*, 3823-3830.
58. Martin, M. M.; Plaza, P.; Changenet-Barret, P.; Siemiarczuk, A., Uv Vis Subpicosecond Spectroscopy of 4-(9-Anthryl)-N,N -Dimethylaniline in Polar and Nonpolar Solvents: A Two-Dimensional View of the Photodynamic“. *J. Phys. Chem. A* **2002**, *106*, 2351-2358.
59. Snellenburg, J.; Liptonok, S.; Seger, R.; Mullen, K.; Van Stokkum, I., Glotaran: A Java-Based Graphical User Interface for the R Package Timp. *J. Stat. Softw.* **2012**, *49*, 1-22.
60. Zhu, H.; Li, M.; Hu, J.; Wang, X.; Jie, J.; Guo, Q.; Chen, C.; Xia, A., Ultrafast Investigation of Intramolecular Charge Transfer and Solvation Dynamics of Tetrahydro[5]-Helicene-Based Imide Derivatives. *Sci. Rep.* **2016**, *6*, 24313.
61. Neelambra, A. U.; Govind, C.; Devassia, T. T.; Somashekharappa, G. M.; Karunakaran, V., Direct Evidence of Solvent Polarity Governing the Intramolecular Charge and Energy Transfer: Ultrafast Relaxation Dynamics of Push–Pull Fluorene Derivatives. *Phys. Chem*

- Chem. Phys.* **2019**, *21*, 11087-11102.
62. Lee, S.; Lee, M.; An, J.; Ahme, H.; Im, C., Exciton Dynamics of P3ht:Pcbm Blend Films with Different Polymer Regioregularities Using Transient Absorption Spectroscopy. *Mol. Cryst. Liq. Cryst.* **2013**, *578*, 68-72.
63. Williams, R. M.; Van Anh, N.; van Stokkum, I. H. M., Triplet Formation by Charge Recombination in Thin Film Blends of Perylene Red and Pyrene: Developing a Target Model for the Photophysics of Organic Photovoltaic Materials. *J. Phys. Chem. B* **2013**, *117*, 11239-11248.
64. Ghosh, A.; Ghosh, S.; Ghosh, G.; Jana, B.; Patra, A., Revealing Complex Relaxation Processes of Collapsed Conjugated Polymer Nanoparticles in the Presence of Different Shapes of Gold Nanoparticles Using Global and Target Analysis. *J. Phys. Chem. C* **2020**, *124*, 26165-26173.
65. Lee, D., et al., Intrachain Delocalization Effect of Charge Carriers on the Charge-Transfer State Dynamics in Organic Solar Cells. *J. Phys. Chem. C* **2022**, *126*, 3171-3179.
66. van Stokkum, I. H. M.; Beekman, L. M. P.; Jones, M. R.; van Brederode, M. E.; van Grondelle, R., Primary Electron Transfer Kinetics in Membrane-Bound Rhodobacter Sphaeroides Reaction Centers: A Global and Target Analysis. *Biochemistry* **1997**, *36*, 11360-11368.
67. Karunakaran, V.; Perez Lustres, J. L.; Zhao, L.; Ernsting, N. P.; Seitz, O., Large Dynamic Stokes Shift of DNA Intercalation Dye Thiazole Orange Has Contribution from a High-Frequency Mode. *J. Am. Chem. Soc.* **2006**, *128*, 2954-2962.
68. Hahn, T., et al., Monomolecular and Bimolecular Recombination of Electron-Hole Pairs at the Interface of a Bilayer Organic Solar Cell. *Adv. Funct. Mater.* **2017**, *27*, 1604906.
69. Miao, J.; Zhang, F.; Du, M.; Wang, W.; Fang, Y., Photomultiplication Type Narrowband Organic Photodetectors Working at Forward and Reverse Bias. *Phys. Chem. Chem. Phys.* **2017**, *19*, 14424-14430.
70. Shuttle, C. G.; O'Regan, B.; Ballantyne, A. M.; Nelson, J.; Bradley, D. D. C.; Mello, J. d.; Durrant, J. R., Experimental Determination of the Rate Law for Charge Carrier Decay in a Polythiophene: Fullerene Solar Cell. *Appl. Phys. Lett.* **2008**, *92*, 093311.
71. Wood, S.; O'Connor, D.; Jones, C. W.; Claverley, J. D.; Blakesley, J. C.; Giusca, C.; Castro, F. A., Transient Photocurrent and Photovoltage Mapping for Characterisation of Defects in Organic Photovoltaics. *Sol. Energy Mater. Sol. Cells* **2017**, *161*, 89-95.
72. Armarego, W. L. F.; Chai, C., Chapter 4 - Purification of Organic Chemicals. In *Purification of Laboratory Chemicals (Seventh Edition)*, Armarego, W. L. F.; Chai, C., Eds. Butterworth-Heinemann: Boston, 2013; pp 103-554.
73. Palsson, L.-O.; Monkman, A. P., Measurements of Solid-State Photoluminescence Quantum Yields of Films Using a Fluorimeter. *Adv. Mater.* **2002**, *14*, 757-758.
74. Wang, Y.; Chen, J.; Kim, H.; Wang, B.; Iriguchi, R.; Ohkita, H., Ternary Blend Solar Cells Based on a Conjugated Polymer with Diketopyrrolopyrrole and Carbazole Units. *Front. Energy Res.* **2018**, *6*, 113.
75. Grollman, R.; Quist, N.; Robertson, A.; Rath, J.; Purushothaman, B.; Haley, M.; Anthony, J.; Ostroverkhova, O., Single-Molecule Level Insight into Nanoscale Environment-Dependent Photophysics in Blends. *J. Phys. Chem. C* **2017**, *121*.
76. Govind, C.; Karunakaran, V., Ultrafast Relaxation Dynamics of Photoexcited Heme Model Compounds: Observation of Multiple Electronic Spin States and Vibrational Cooling. *J. Phys. Chem. B* **2017**, *121*, 3111-3120.
77. Megerle, U.; Pugliesi, I.; Schrieffer, C.; Sailer, C. F.; Riedle, E., Sub-50 fs Broadband Absorption Spectroscopy with Tunable Excitation: Putting the Analysis of Ultrafast Molecular

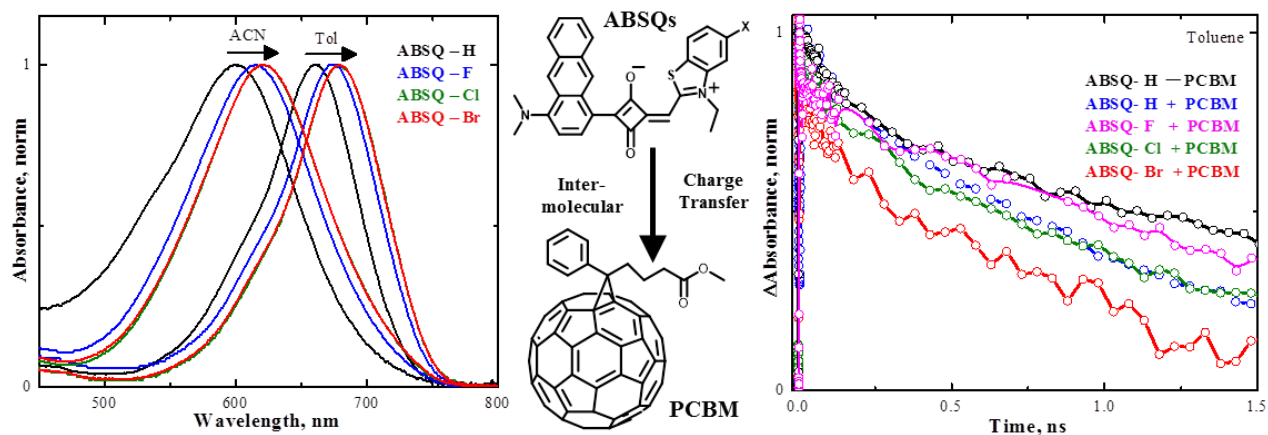
Dynamics On solid Ground. *Appl. Phys. B* **2009**, *96*, 215-231.

78. Mohan, M.; Nandal, V.; Paramadam, S.; Reddy, K. P.; Ramkumar, S.; Agarwal, S.; Gopinath, C. S.; Nair, P. R.; Namboothiry, M. A. G., Efficient Organic Photovoltaics with Improved Charge Extraction and High Short-Circuit Current. *J. Phys. Chem. C* **2017**, *121*, 5523-5530.

79. Simone, G.; Dyson, M. J.; Meskers, S. C. J.; Janssen, R. A. J.; Gelinck, G. H., Organic Photodetectors and Their Application in Large Area and Flexible Image Sensors: The Role of Dark Current. *Adv. Funct. Mater.* **2020**, *30*, 1904205.

80. Zhang, H.; Jenatsch, S.; De Jonghe, J.; Nüesch, F.; Steim, R.; Véron, A. C.; Hany, R., Transparent Organic Photodetector Using a near-Infrared Absorbing Cyanine Dye. *Scientific Reports* **2015**, *5*, 9439.

Ultrafast Intermolecular Interaction Dynamics between NIR-Absorbing Unsymmetrical Squaraines and PCBM: Effects of Halogen Substitution



3.1 Abstract

The NIR absorbing and emitting chromophores are essential for the applications of optoelectronic devices. Understanding the structure–property relationships will help in controlling the efficiency of such devices. Here USQ derivatives (ABSQs) with D–A–D' architectures having anthracene and halogenated benzothiazole (ABSQ–H) with fluoride (ABSQ–F), chloride (ABSQ–Cl) and bromide (ABSQ–Br) were synthesized to understand the effect of halogen on the photophysical properties and intermolecular interaction dynamics with PCBM widely used as an electron acceptor in BHJ–based devices. Interestingly the ABSQ–H exhibited intense absorption ($\epsilon \sim 6.72 \times 10^4 \text{ M}^{-1} \text{ cm}^{-1}$) spectra centered at $\sim 660 \text{ nm}$. Upon halogen substitution, a red shift in the absorption spectra with an increase of molar absorptivity was observed ($\epsilon = 8.59 \times 10^4 \text{ M}^{-1} \text{ cm}^{-1}$), which is beneficial for NIR light harvesting. The femtosecond

transient absorption spectra of **ABSQs** revealed that the polarity of the solvent controlled the excited state relaxation dynamics. Upon addition of **PCBM**, the fluorescence intensity and dynamics of halogenated **ABSQ** derivatives were quenched and the formation of a squaraine radical cation was observed, reflecting the occurrence of intermolecular charge transfer dynamics between the **ABSQs** and **PCBM**. Thus the observation of red shift with intense absorption and efficient charge-transfer upon halogenation of **ABSQ** derivatives provides a design strategy for developing derivatives for **BHJ**-based optoelectronic devices. The **ABSQ-H** and **ABSQ-Cl** were applied into the **OPD** devices and showed sensitivity in the **NIR** region.

3.2 Introduction

The **NIR** dyes are significantly used as sensitizers in various optoelectronic applications¹⁻² due to their efficient optical properties and high sensitivity in the 700–1500 nm range. Among the various **NIR** dyes, the **SQs** possessing **D-A-D'** architecture have been widely used in optoelectronic devices due to their strong absorption ($\epsilon > 10^5 \text{ M}^{-1} \text{ cm}^{-1}$)³ and high fluorescence ($\Phi = 0.8$)⁴ in the visible to **NIR** region and ease of synthesis with exceptional photostability.⁵⁻⁷ However, **USQ** dyes are emerged as versatile sensitizers⁸⁻¹⁰ due to the unidirectional flow of electron in the excited states upon excitation, yielding enhanced charge separation and leading to higher photocurrents, compared to the symmetrical derivatives.^{3, 11} Indeed, the **USQ** dyes have been widely used in various applications including organic photovoltaic cells,¹²⁻¹⁶ optical data storage,¹⁷ two-photon absorption,¹⁸ fluorescent labels¹⁹⁻²⁰ and photodynamic therapy.²¹ However, in the **BHJ**-based **OPD** devices using **PCBM** as an electron acceptor, the ultrafast processes of photoinduced charge transfer, charge carrier generation and their recombination controls the

efficiency of the devices. Though a large number of steady-state and time-resolved photophysical properties of SQs derivatives were widely reported²²⁻³⁰ the intermolecular interaction dynamics of USQ derivatives with PCBM have not been investigated in detail.

Indeed, the structure-property relationship of the sensitizers plays a significant role in designing suitable materials for optoelectronic devices. In this connection, Würthner et al.³¹ reported exceptional NIR photophysical properties of SQ derivatives upon halogen substitution, where a redshift of absorption with an increase of the extinction coefficient and improvement of the fluorescence quantum yield was observed from fluorine over chlorine and bromine to iodine substituted SQs derivatives. Here a series of USQ derivatives (**ABSQs**) having the D-A-D' architecture comprising *N,N*-dimethyl aminoanthracene and benzothiazole (**ABSQ-H**) halogenated with fluoride (**ABSQ-F**), chloride (**ABSQ-Cl**) and bromide (**ABSQ-Br**) were synthesized (**Figure 3.1**). The steady-state and time-resolved photophysical properties of **ABSQ** derivatives were investigated to understand the effect of halogen on the photophysical properties and intermolecular interaction dynamics with PCBM. It is found that upon halogenation of **ABSQs**, the absorption spectra showed a red shift with an increase of molar absorptivity and firm interaction with the PCBM.

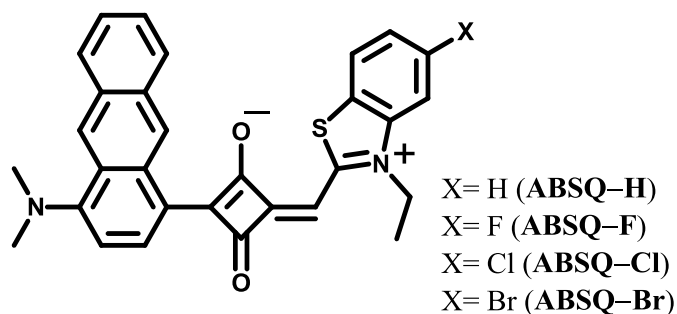


Figure 3.1 Chemical structure of **ABSQ** derivatives.

3.3 Results and Discussion

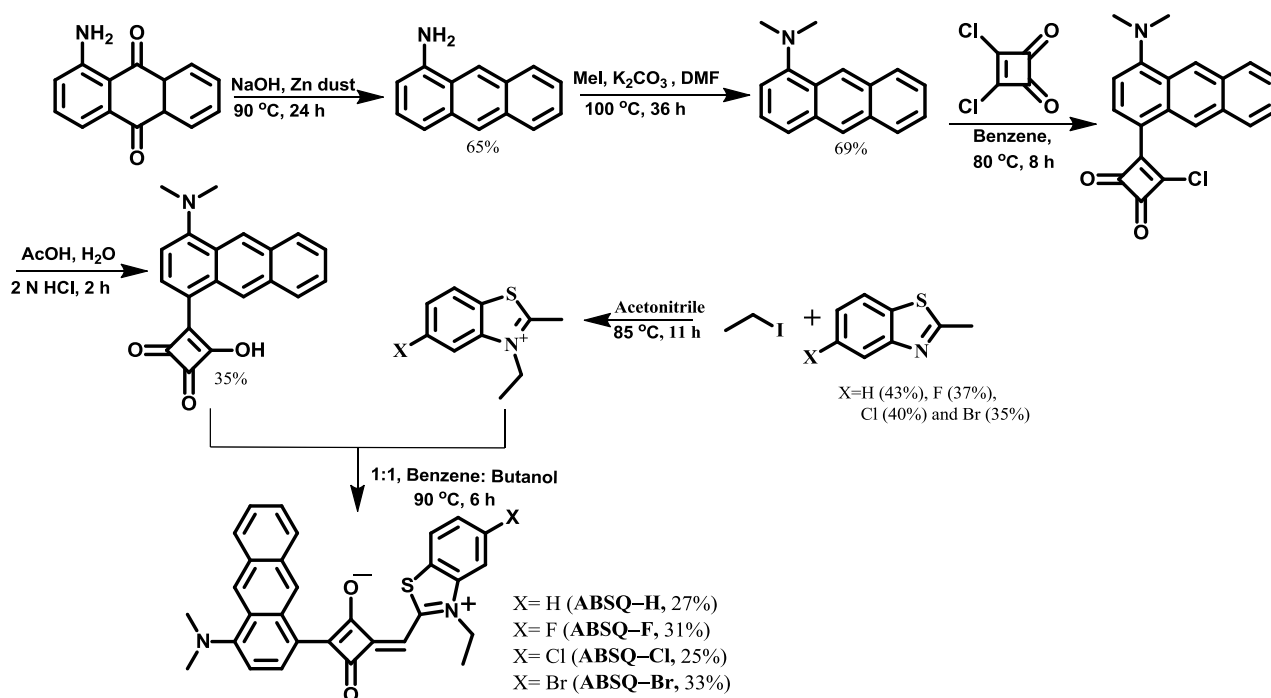
3.3.1 Synthesis of ABSQ derivatives

Here a series of USQ derivatives (**ABSQs**) having the D–A–D' architecture comprising *N,N*-dimethyl aminoanthracene and benzothiazole (**ABSQ–H**) halogenated with fluoride (**ABSQ–F**), chloride (**ABSQ–Cl**) and bromide (**ABSQ–Br**) were synthesized (**Scheme 3.1**). The unsymmetrical **ABSQ** derivatives were synthesized by modifying the reported procedures.³²⁻³⁴ *N,N*-dimethyl aminoanthracene semisquaraine was synthesized by the reduction and alkylation of 1-aminoanthroquinone and subsequent *N,N*-dimethyl aminoanthracene was reacted with squarylium chloride. Then the halogenated *N*-ethyl benzothiazolium salt was refluxed with the *N,N*-dimethyl aminoanthracene semisquaraine in benzene:butanol azeotropic mixture (1:1) resulting the **ABSQ** derivatives. The structure of the derivatives were characterized by ¹H and ¹³C NMR and HRMS.

3.3.2 Steady–State Photophysical Characterization

3.3.2.1 Solution State

The absorption and emission spectra of **ABSQ–H**, **ABSQ–F**, **ABSQ–Cl** and **ABSQ–Br** derivatives with an increase in solvent polarity were recorded and shown in **Figure 3.2–3.5** respectively. The **ABSQ–H**, **ABSQ–F**, **ABSQ–Cl** and **ABSQ–Br** exhibited an intense absorption maximum at ~660, 674, 678 and 679 nm in toluene with a molar extinction coefficient of ~6.72, 7.15, 8.59 and $7.96 \times 10^4 \text{ M}^{-1} \text{ cm}^{-1}$ respectively due to combined π – π^* transition with intramolecular charge transfer from *N,N*-dimethyl anthracene and benzothiazolium donors to the central squaraine core.³⁵⁻³⁷



Scheme 3.1 Synthetic Scheme of ABSQ Derivatives.

Interestingly it is found that upon substitution of halogen, the absorption maximum shifted to the red region (~19 nm) compared to **ABSQ-H** consistent with the previous report.³¹ Upon increasing the polarity of solvent (acetonitrile, ACN), the absorption maximum of **ABSQ** derivatives shifted to the blue region (~60 nm), negative solvatochromism, indicating more polarity of ground state compared to the excited state.³⁸ The fluorescence spectra of **ABSQ-H**, **ABSQ-F**, **ABSQ-Cl** and **ABSQ-Br** in toluene exhibited maximum at around 733, 741, 736 and 743 nm respectively and showed the red shift with increase of polarity of the solvent. When compared to other derivatives, there is a significant red shift of the emission spectra of **ABSQ-Cl** in ACN compared to toluene reflecting the stabilization of excited-state of the **ABSQ-Cl** in a highly polar solvent.

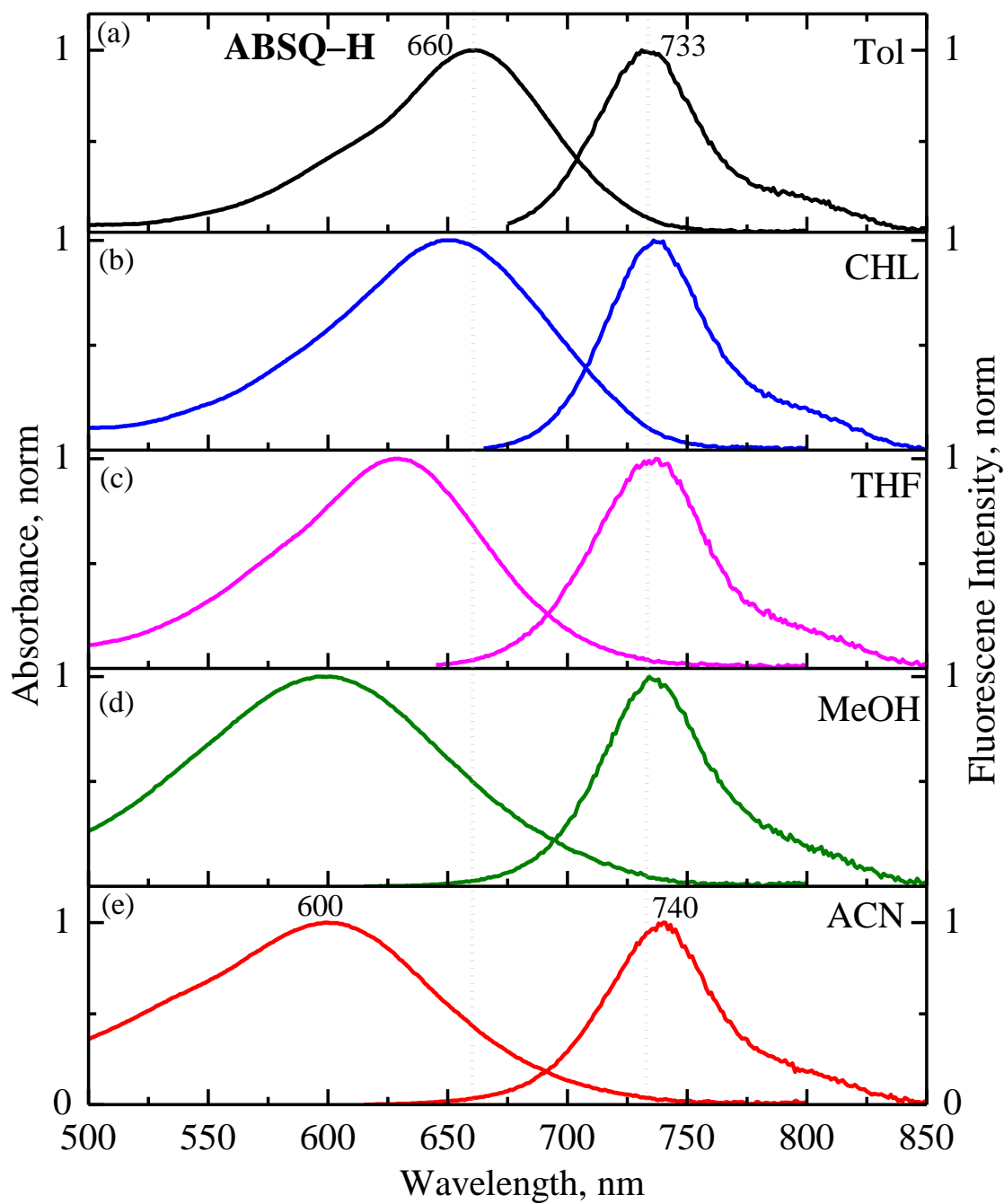


Figure 3.2 Steady-state absorption and emission spectra of **ABSQ-H** in solvents of various polarities at room temperature.

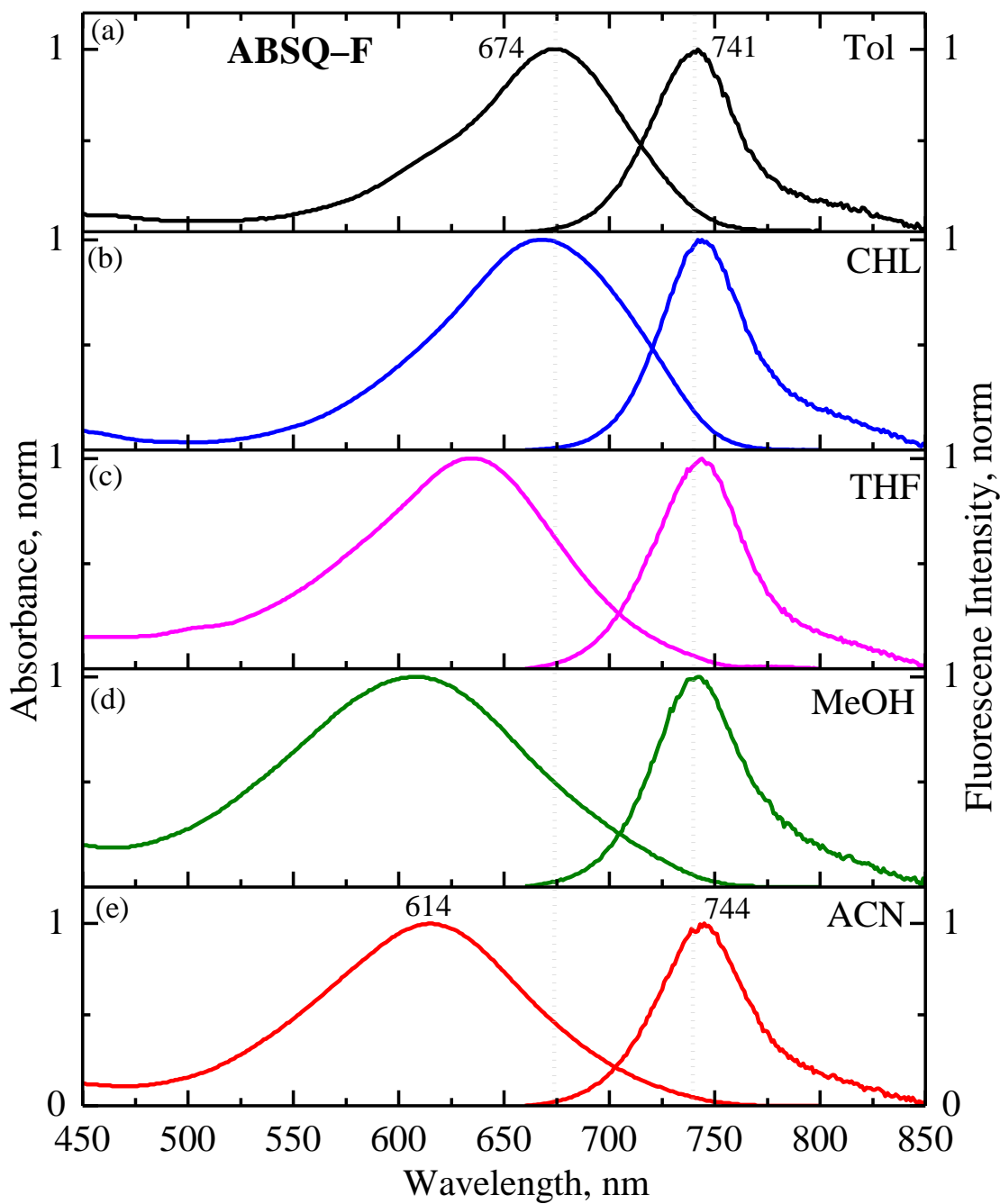


Figure 3.3 Steady-state absorption and emission spectra of **ABSQ-F** in solvents of various polarities at room temperature.

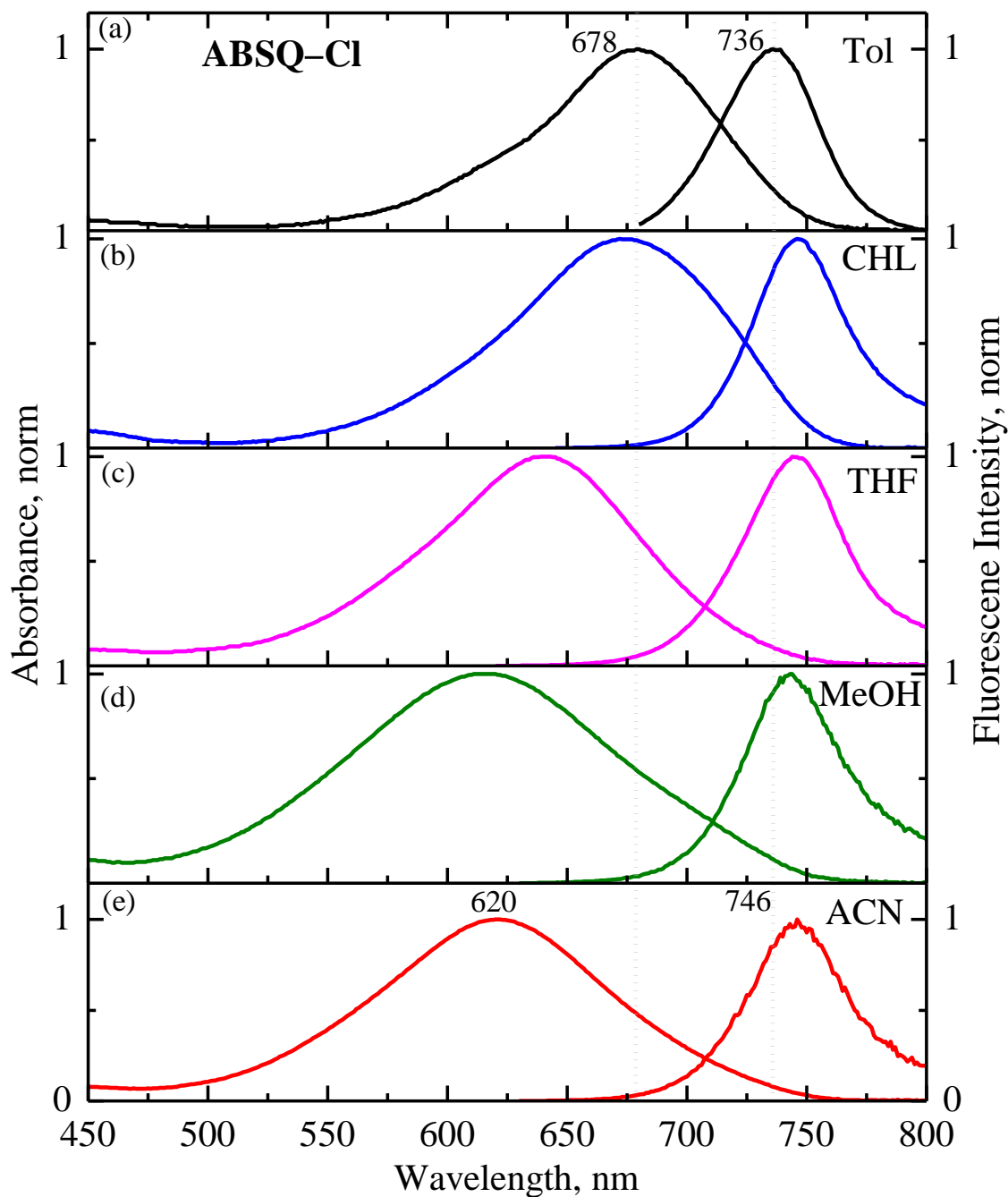


Figure 3.4 Steady-state absorption and emission spectra of ABSQ-Cl in solvents of various polarities at room temperature.

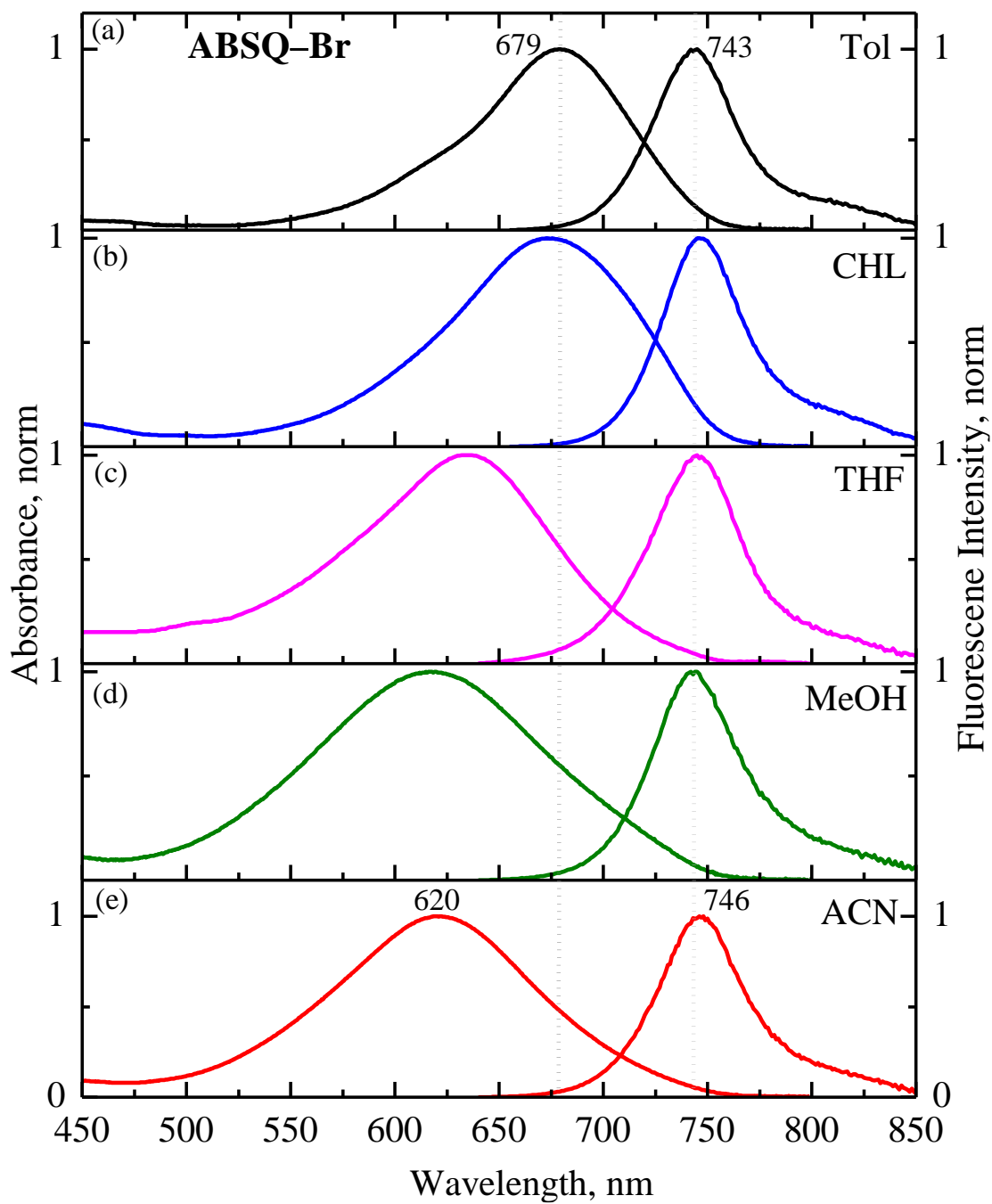


Figure 3.5 Steady-state absorption and emission spectra of ABSQ-Br in solvents of various polarities at room temperature.

The fluorescence dynamics of **ABSQ** derivatives were measured in various solvents upon excitation at 670 nm and the corresponding decay profiles are shown in **Figure 3.6**. The fluorescence lifetime (τ_f) of **ABSQ-H** in toluene was obtained as $\sim 2.27 \pm 0.20$ ns, and with an increase of solvent polarity, it decreased to $\sim 0.63 \pm 0.20$ ns in ACN. Though there are no significant changes in the fluorescence lifetime upon halogenation in toluene, a difference of ~ 0.32 ns in the fluorescence lifetime in the order of **ABSQ-H** (2.27 ns) < **ABSQ-F** (2.51 ns) < **ABSQ-Cl** (2.59 ns) \approx **ABSQ-Br** (2.58 ns) were observed. The absolute fluorescence quantum yield (Φ) of **ABSQ-H** in toluene was found to be ~ 0.46 , which was reduced to ~ 0.14 in ACN. Such a similar trend was observed for other derivatives revealing the contribution of a non-radiative transition sensitive to the electronic redistribution in the excited **ABSQ** derivatives and/or formation of the solute-solvent complexes with an increase of polarity.⁸ The photophysical characterization data of the absorption and emission maxima, Stokes shift, fluorescence lifetime and absolute quantum yield of **ABSQ-H**, **ABSQ-F**, **ABSQ-Cl** and **ABSQ-Br** are provided in **Table 3.1-3.4** respectively. The radiative (k_r) and non-radiative (k_{nr}) rate constants were also calculated using the equation 1 provided in the Chapter 2.

3.3.2.2 Film State

The absorption spectra of **ABSQ** derivatives were measured in the thin film state by drop-casting 1.5 mM of **ABSQs** in chloroform and shown in **Figure 3.7**. The absorption spectra in the thin film state showed a broad band covering the wide range of ~ 475 – 775 nm with a maximum at around 550 nm. When compared to the solution state, the appearance of absorption maximum at ~ 560 nm showed a broad band in nature and shifted to the blue region by ~ 100 nm,

suggesting the formation of H-aggregates by intermolecular π - π interaction³⁶ in the thin film. Indeed such a broad range of absorption wavelength with a high molar absorptivity will be advantageous for light harvesting for optoelectronic devices.⁵

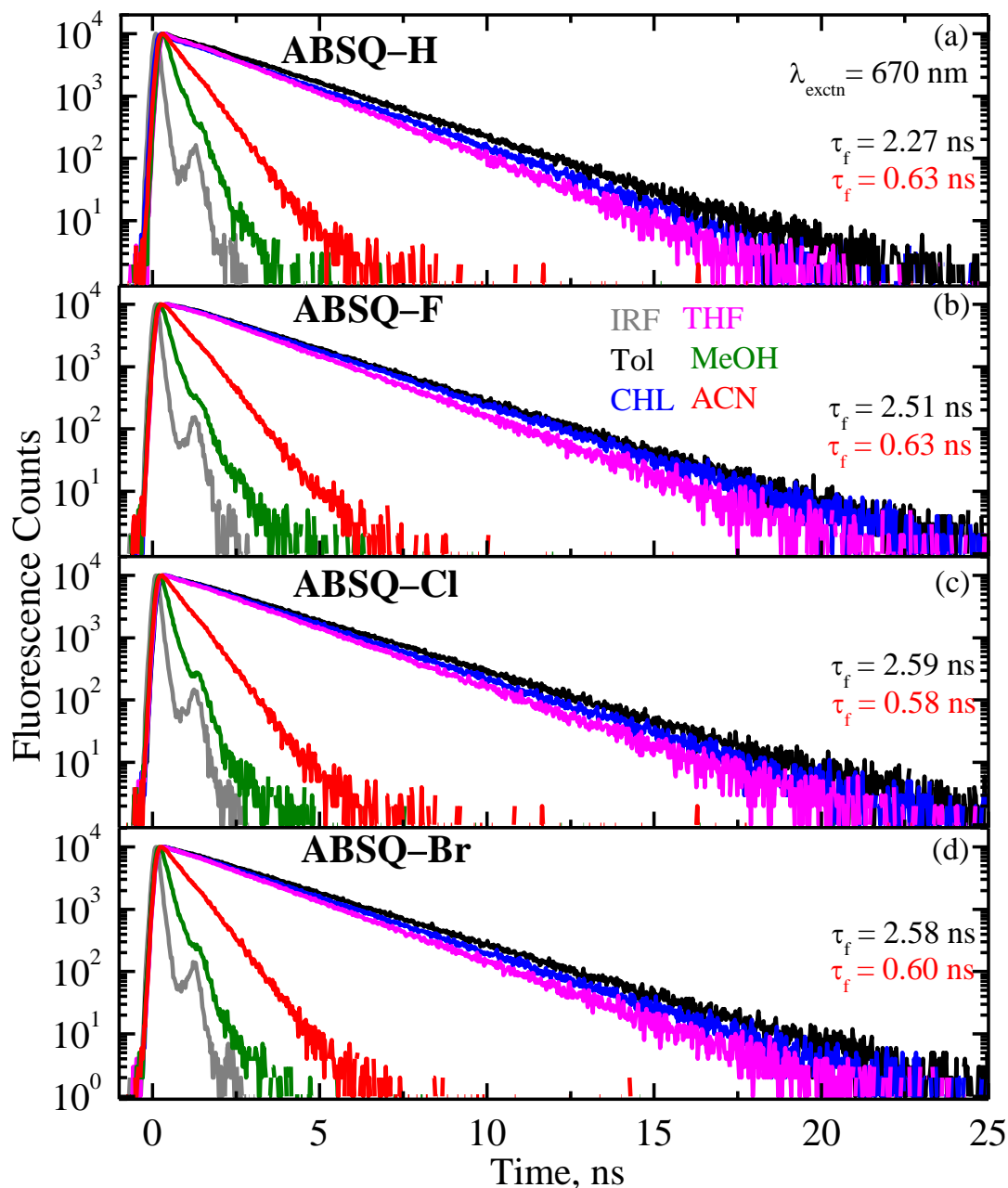


Figure 3.6 Fluorescence decay profiles of ABSQ-H (a), ABSQ-F (b), ABSQ-Cl (c) and ABSQ-Br (d) in solvents of varying polarities obtained upon excitation at 670 nm.

Table 3.1 Absorption and Fluorescence Maxima, Lifetime and Quantum Yield and of **ABSQ-H** in Different Solvents

Solvents	Absorption max, nm (λ_{\max})	Fluorescence max, nm (λ_{\max})	Stokes shift, cm^{-1} ($\Delta\nu$)	Fluorescence quantum yield ^a (Φ_f)	Fluorescence lifetime ^b , ns (τ_f)	Radiative constant, $\times 10^7 \text{ s}^{-1}$ (K_r)	Non-radiative constant, $\times 10^7 \text{ s}^{-1}$ (K_{nr})
Toluene	660	733	1509	0.46	2.27 ± 0.20	20.26	23
Chloroform	651	737	1792	0.44	2.48 ± 0.25	17.74	22
THF	629	736	2311	0.32	2.06 ± 0.25	15.53	33
MeOH	599	735	3089	0.06	0.23 ± 0.20	27.39	407
ACN	600	740	3153	0.14	0.63 ± 0.20	22.22	136

^aAbsolute fluorescence quantum yield attained by exciting at emission maximum using an integrating sphere. ^bFluorescence lifetime was obtained upon excitation at 670 nm and the χ^2 value of fluorescence kinetics fit is between 1.0 and 1.2.

Table 3.2 Absorption and Fluorescence Maxima, Lifetime and Quantum Yield and of **ABSQ-F** in Different Solvents

Solvents	Absorption max, nm (λ_{\max})	Fluorescence max, nm (λ_{\max})	Stokes shift, cm^{-1} ($\Delta\nu$)	Fluorescence quantum yield ^a (Φ_f)	Fluorescence lifetime ^b , ns (τ_f)	Radiative constant, $\times 10^7 \text{ s}^{-1}$ (K_r)	Non-radiative constant, $\times 10^7 \text{ s}^{-1}$ (K_{nr})
Toluene	674	741	1341	0.42	2.51 ± 0.20	16.73	23.10
Chloroform	669	743	1489	0.40	2.60 ± 0.25	15.38	23.07
THF	636	744	2282	0.36	2.11 ± 0.20	17.06	30.33
MeOH	609	745	2997	0.02	0.25 ± 0.20	8.80	391
ACN	614	744	2845	0.08	0.63 ± 0.25	12.85	145

^aAbsolute fluorescence quantum yield attained by exciting at emission maximum using an integrating sphere. ^bFluorescence lifetime was obtained upon excitation at 670 nm and the χ^2 value of fluorescence kinetics fit is between 1.0 and 1.2.

Table 3.3 Absorption and Fluorescence Maxima, Lifetime and Quantum Yield and of **ABSQ–Cl** in Different Solvents

Solvents	Absorption max, nm (λ_{\max})	Fluorescence max, nm (λ_{\max})	Stokes shift, cm^{-1} ($\Delta\nu$)	Fluorescence quantum yield ^a (Φ_f)	Fluorescence lifetime ^b , ns (τ_f)	Radiative constant, $\times 10^7 \text{ s}^{-1}$ (K_r)	Non-radiative constant, $\times 10^7 \text{ s}^{-1}$ (K_{nr})
Toluene	678	736	1162	0.42	2.59 ± 0.25	16.21	22.39
Chloroform	676	747	1406	0.37	2.45 ± 0.25	15.10	25.71
THF	641	746	2196	0.42	2.27 ± 0.20	18.50	25.51
MeOH	617	743	2749	0.003	0.11 ± 0.10	2.72	906
ACN	620	749	2778	0.07	0.58 ± 0.20	13.62	158

^aAbsolute fluorescence quantum yield attained by exciting at emission maximum using an integrating sphere. ^bFluorescence lifetime was obtained upon excitation at 670 nm and the χ^2 value of fluorescence kinetics fit is between 1.0 and 1.2.

Table 3.4 Absorption and Fluorescence Maxima, Lifetime and Quantum Yield and of **ABSQ-Br** in Different Solvents

Solvents	Absorption max, nm (λ_{\max})	Fluorescence max, nm (λ_{\max})	Stokes shift, cm^{-1} ($\Delta\nu$)	Fluorescence quantum yield ^a (Φ_f)	Fluorescence lifetime ^b , ns (τ)	Radiative constant, $\times 10^7 \text{ s}^{-1}$ (K_r)	Non-radiative constant, $\times 10^7 \text{ s}^{-1}$ (K_{nr})
Toluene	679	743	1269	0.42	2.58 ± 0.20	16.21	22.39
Chloroform	675	747	1428	0.37	2.41 ± 0.25	15.35	26.14
THF	636	746	2318	0.32	2.21 ± 0.20	14.48	30.76
MeOH	618	743	2722	0.02	0.18 ± 0.10	11.11	544
ACN	620	746	2724	0.06	0.60 ± 0.25	11.33	155

^aAbsolute fluorescence quantum yield attained by exciting at emission maximum using an integrating sphere. ^bFluorescence lifetime was obtained upon excitation at 670 nm and the χ^2 value of fluorescence kinetics fit is between 1.0 and 1.2.

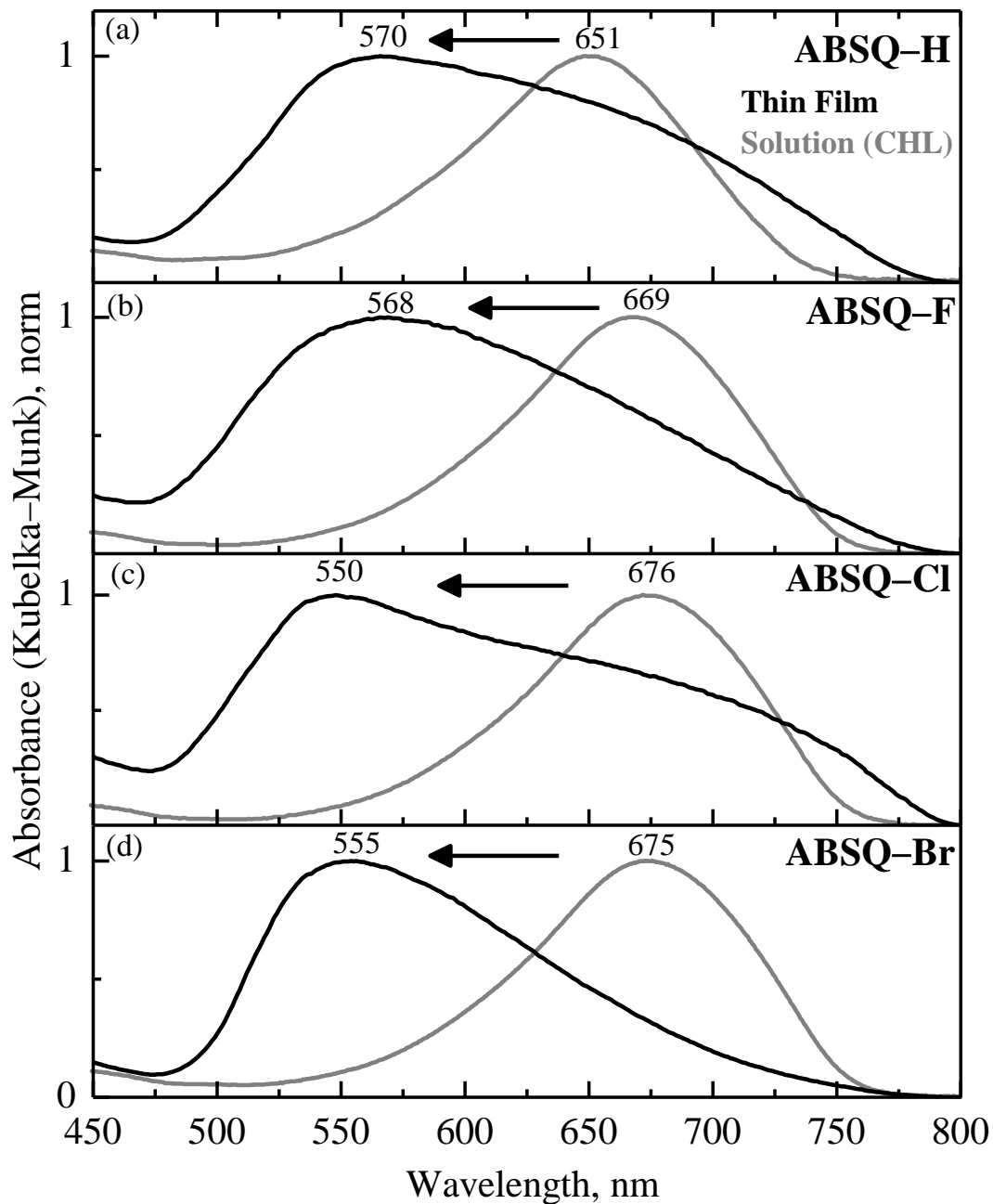


Figure 3.7 Normalized absorption spectra of **ABSQ-H** (a), **ABSQ-F** (b), **ABSQ-Cl** (c) and **ABSQ-Br** (d) in the thin film and chloroform solution.

3.3.2.3 Electrochemical Characterization

Likewise, in the previous Chapter, the redox potentials of the **ABSQ** derivatives were determined using cyclic voltammetry and the corresponding voltammograms are depicted in **Figure 3.8a**. The HOMO and LUMO energy levels of **ABSQ–H** were found to be -4.78 and -3.04 eV respectively. Though there are no significant changes in the HOMO energy levels of **ABSQ** derivatives, there is a remarkable reduction of LUMO energy levels and thus leading to the decrease of the energy band gap energy of **ABSQ** derivatives upon substitution of halogen. Interestingly HOMO and LUMO energy levels of **ABSQ** derivatives are higher than those of the PCBM (**Figure 3.8b**), which is an essential requirement of the sensitizer to be used in the BHJ-based optoelectronic devices with efficient intermolecular charge-transfer in the excited-state. Hence these **ABSQ** derivatives are highly suitable for optoelectronic devices. The electrochemical data of **ABSQ** derivatives are summarised in **Table 3.5**.

3.3.2.4 Interaction of ABSQs with PCBM

The absorption and fluorescence spectra of **ABSQ–H**, **ABSQ–F**, **ABSQ–Cl** and **ABSQ–Br** with an increase of concentration of PCBM (1.5 to 13.5 mM) in toluene were investigated. Though there were no notable changes in the absorption spectra of **ABSQ** derivatives, the decrease of fluorescence intensity of all the **ABSQ** derivatives upon the addition of PCBM was observed (**Figure 3.9**), indicating the excited **ABSQ** derivatives interacting with PCBM. Upon addition of PCBM, the fluorescence lifetime of **ABSQ** derivatives was recorded by the excitation at 670 nm (left insets of **Figure 3.9**). The fluorescence lifetime of **ABSQ–H**, **ABSQ–F**, **ABSQ–Cl** and **ABSQ–Br** upon addition of PCBM (13.5 mM) was decreased from $\sim 2.27 \pm 0.20$, 2.51 ± 0.20 , 2.59 ± 0.25 and 2.58 ± 0.20 ns to 2.08 ± 0.20 , 1.86 ± 0.20 , 1.81 ± 0.25 and 1.90 ± 0.20 ns respectively, indicating the occurrence of dynamic quenching (diffusion controlled) in the excited

state. It is important to note that the magnitude of quenching of fluorescence lifetime is higher in the halogenated derivatives (~ 780 ps, **ABSQ-Cl**) compared to the non-halogenated derivative (330 ps, **ABSQ-H**) upon the addition of PCBM.

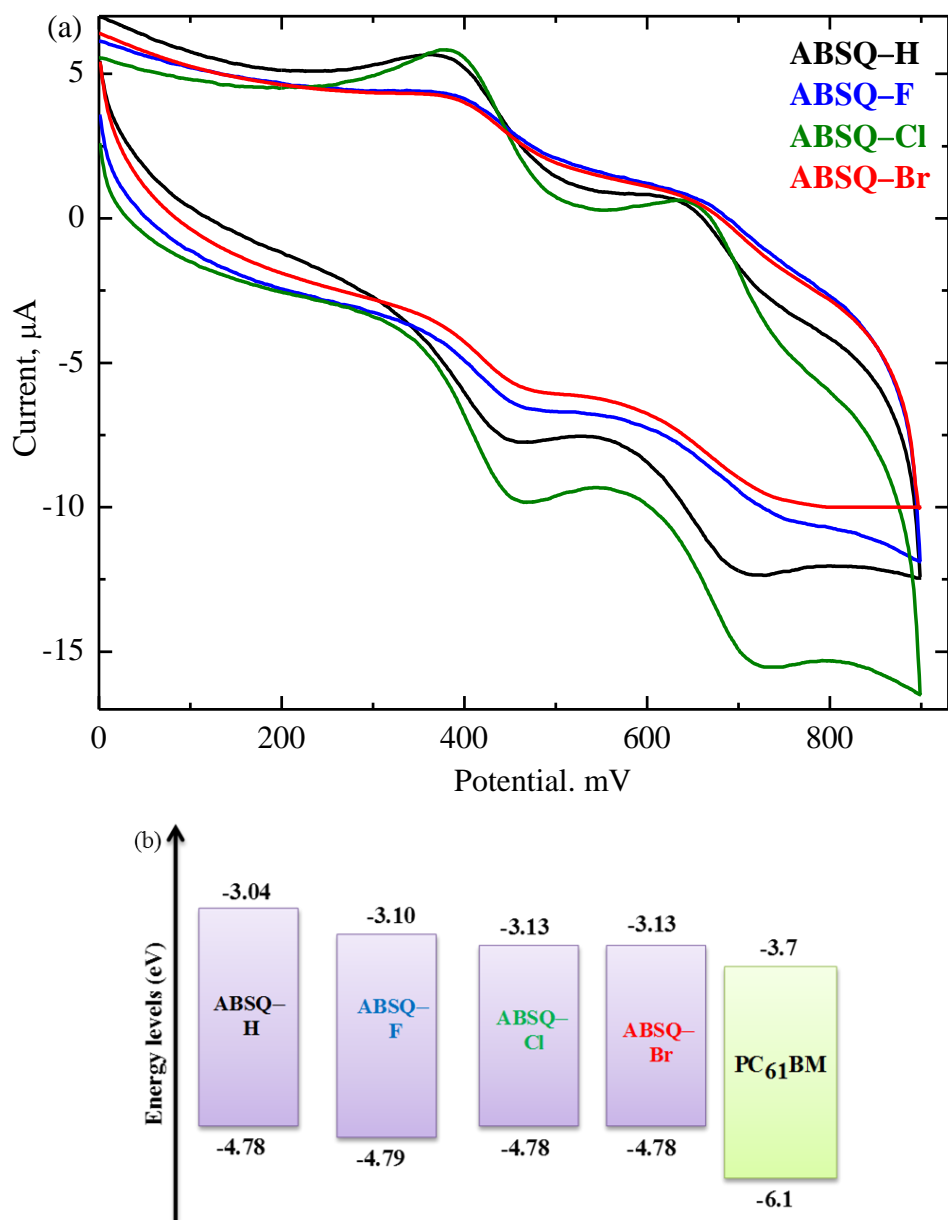


Figure 3.8 Cyclic voltammogram of **ABSQ-H**, **ABSQ-F**, **ABSQ-Cl** and **ABSQ-Br** in ACN using tetrabutylammonium hexafluorophosphate as supporting electrolyte at a scanning rate of 50 mV/sec (a) and HOMO and LUMO levels of **ABSQ-H**, **ABSQ-F**, **ABSQ-Cl** and **ABSQ-Br** vs PCBM (b).

Table 3.5 Electrochemical data of **ABSQ** derivatives from cyclic voltammetry in ACN.

ABSQs	λ_{00} , nm	E_{00} , eV	E_{ox} vs. Ag/AgCl, V	HOMO, eV	LUMO, eV
ABSQ–H	712	1.74	0.42	–4.78	–3.04
ABSQ–F	731	1.69	0.43	–4.79	–3.10
ABSQ–Cl	749	1.65	0.42	–4.78	–3.13
ABSQ–Br	749	1.65	0.42	–4.78	–3.13

The k_q ($k_q = K_{SV} / \tau_0$) and K_{SV} ($\tau_0 / \tau = 1 + K_{SV} \times [\text{PCBM}]$) were calculated and constants are provided in **Table 3.6**. Where τ_0 and τ are the fluorescence lifetime of **ABSQ** derivatives in the absence and presence of PCBM. The k_q and K_{SV} for the **ABSQ–H** are found to be $2.88 \times 10^9 \text{ M}^{-1} \text{ s}^{-1}$ and 6.54 M^{-1} respectively. These constants are increased upon halogen substitution (**ABSQ–Cl**: $1.24 \times 10^{10} \text{ M}^{-1} \text{ s}^{-1}$ and 32.10 M^{-1}), suggesting the occurrence of strong interaction between the halogenated **ABSQ** derivatives and PCBM compared to that of the **ABSQ–H** with PCBM. It is to be noted that the k_q of the halogen substituted **ABSQ** derivatives is an order of magnitude larger³⁹ than that of normal diffusion controlled bimolecular quenching constant ($2 \times 10^9 \text{ M}^{-1} \text{ s}^{-1}$).³⁹ However, **ABSQ–F** showed complete quenching of fluorescence intensity compared to other derivatives, whereas **ABSQ–Cl** showed fast decay time compared to other derivatives. Such an observation of difference in the photophysical properties could be due to the resultant competition between the electron-withdrawing (electronegativity) and electron-donating (mesomeric effect) characteristics of halogens in nature.³¹ Overall, upon addition of PCBM, the quenching of fluorescence intensity and a lifetime of **ABSQ** derivatives reveal the occurrence of

the intermolecular charge–transfer between the ABSQ derivatives and PCBM²² and consistent with their electrochemical data (Table 3.5).

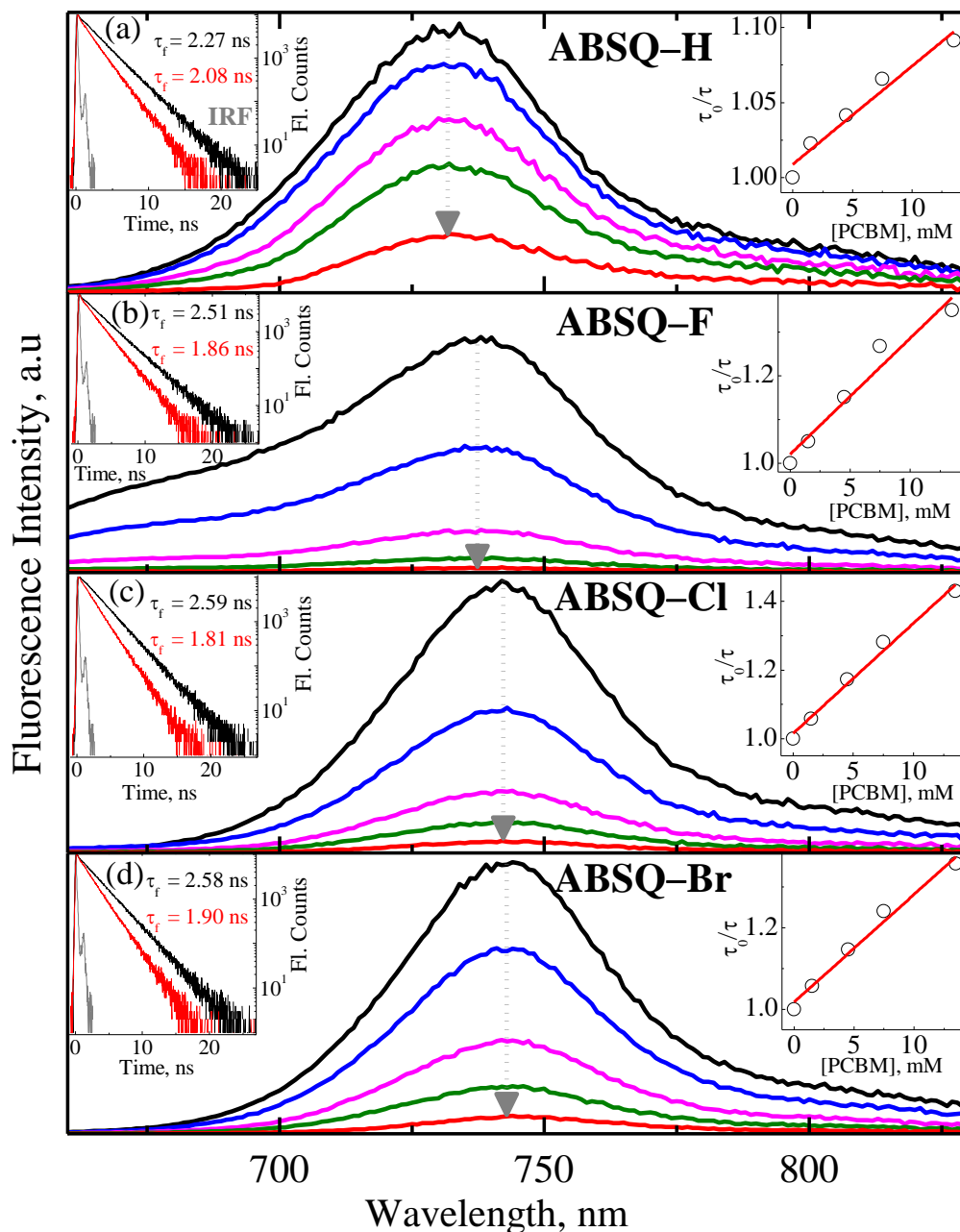


Figure 3.9 Fluorescence spectra of ABSQ-H (a), ABSQ-F (b), ABSQ-Cl (c) and ABSQ-Br (d) with different concentrations of PCBM in toluene 0 mM (black), 1.5 mM (blue), 4.5 mM (magenta), 7.5 mM (olive), 13.5 mM (red). Insets: Fluorescence decay profiles obtained upon excitation at 670 nm (left) and plot of τ_0/τ versus [PCBM] (right).

Table 3.6 The Stern–Volmer quenching constant (K_{SV}) and bimolecular quenching rate constant (k_q) of **ABSQ** derivatives.

ABSQs	K_{SV}, M^{-1}	τ_0, ns	τ, ns	$k_q, \times 10^9 M^{-1} s^{-1}$
ABSQ–H	6.54	2.27 ± 0.20	2.08 ± 0.20	2.88
ABSQ–F	26.50	2.51 ± 0.20	1.86 ± 0.20	10.55
ABSQ–Cl	32.10	2.59 ± 0.25	1.81 ± 0.25	12.39
ABSQ–Br	26.40	2.58 ± 0.20	1.90 ± 0.20	10.23

3.4 Time–Resolved Photophysical Characterization

3.4.1 Femtosecond Transient Absorption Spectra of ABSQ derivatives

To understand the influence of solvent polarity on the excited state relaxation dynamics of the **ABSQ** derivatives, femtosecond time–resolved transient absorption spectra were investigated in nonpolar (toluene) and polar (acetonitrile, ACN) upon excitation at 670 nm using femtosecond pump–probe spectroscopy. The transient absorption spectra of **ABSQ–H** in ACN are shown in **Figure 3.10**, where panel a shows the spectral evolution starting from 0.1 to 0.9 ps. At early time scale of 100 fs, it shows the broad positive band at ~500 nm and two negative absorption bands at around 630 and 730 nm. The positive band at 500 nm is due to the excited singlet state absorption (ESA, $S_n \leftarrow S_1$ transition) of the compound.^{40–44} With an increase of delay time, at 900 fs the negative band at 630 nm shifted to a blue region consistent with the ground–state bleaching (GSB) of the absorption spectra **ABSQ–H**. Whereas the negative transient absorption band at ~730 nm evolved to attain the steady–state emission maximum at ~740 nm, corresponding to the SE. In addition, peak formation at around 680 nm was observed. The panel b of **Figure 3.10** exhibits the

transient absorption spectra recorded from 1 ps to 1.47 ns, where the intensity of the ESA, GSB and SE bands decreased with the delay time increase.

The femtosecond transient absorption spectra of **ABSQ-H** in toluene are shown at representative delay time in **Figure 3.11**. The spectral evolution at early time scales shown in panel a of **Figure 3.11** exhibited dominant ESA at around 516 nm. Though the evolution of GSB is not observed evidently due to the scattering of laser excitation at 670 nm and superimposing of SE spectra, the evolution of SE was observed clearly at around 733 nm. In **Figure 3.11**, panel b shows the spectral evolution from 13.0 ps to 1.55 ns where the intensity of ESA, GSB and SE bands decreased with increase of the delay time. The femtosecond transient absorption spectra of **ABSQ-F**, **ABSQ-Cl** and **ABSQ-Br** in ACN and toluene are shown in **Figure 3.12-3.17** and the spectral behaviors of **ABSQ-F**, **ABSQ-Cl** and **ABSQ-Br** are observed to be similar to that of **ABSQ-H** in ACN and toluene respectively. Though the spectral features of ESA, SE and GSB of **ABSQ-H** in ACN resembled that of in toluene, the excited state relaxation dynamics are faster in ACN compared to that in toluene (**Figure 3.18**) due to the change in the solvation dynamics.⁴⁵⁻⁴⁸ Importantly to understand the intermolecular interaction dynamics between **ABSQs** and PCBM, the transient absorption spectra of **ABSQs** with PCBM in toluene were recorded by exciting at 670 nm are shown in **Figure 3.19-3.22**. Since the excitation wavelength of 670 nm is used to measure the transient absorption spectra of **ABSQs** upon addition of PCBM, where PCBM has a negligible absorbance and **ABSQs** derivatives have high extinction coefficient ($\sim 7.5 \times 10^4 \text{ M}^{-1} \text{ cm}^{-1}$), there will be negligible signal contribution arising from PCBM alone in the probe range of wavelength.

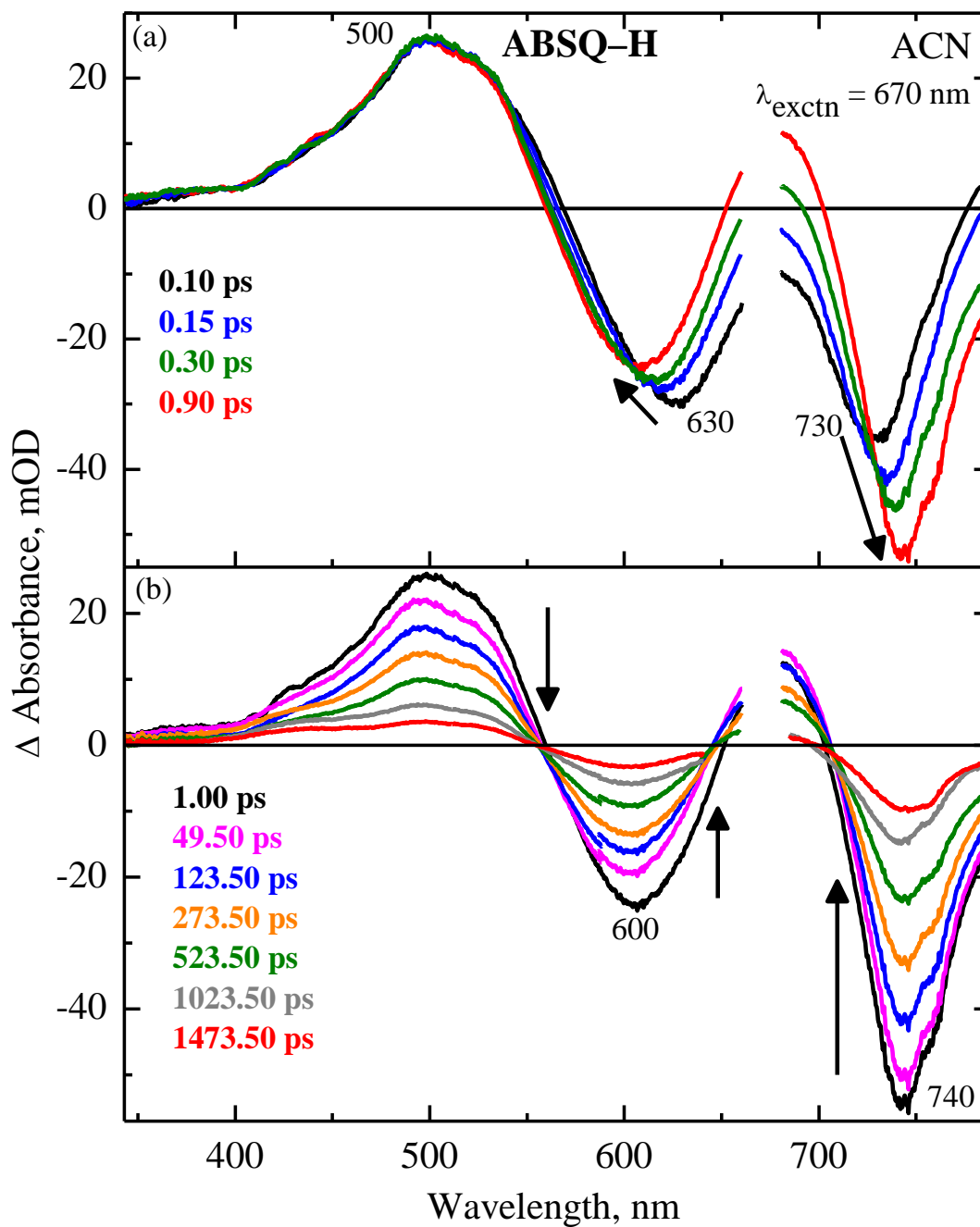


Figure 3.10 Femtosecond transient absorption spectra of ABSQ-H in ACN upon excitation at 670 nm at different delay times.

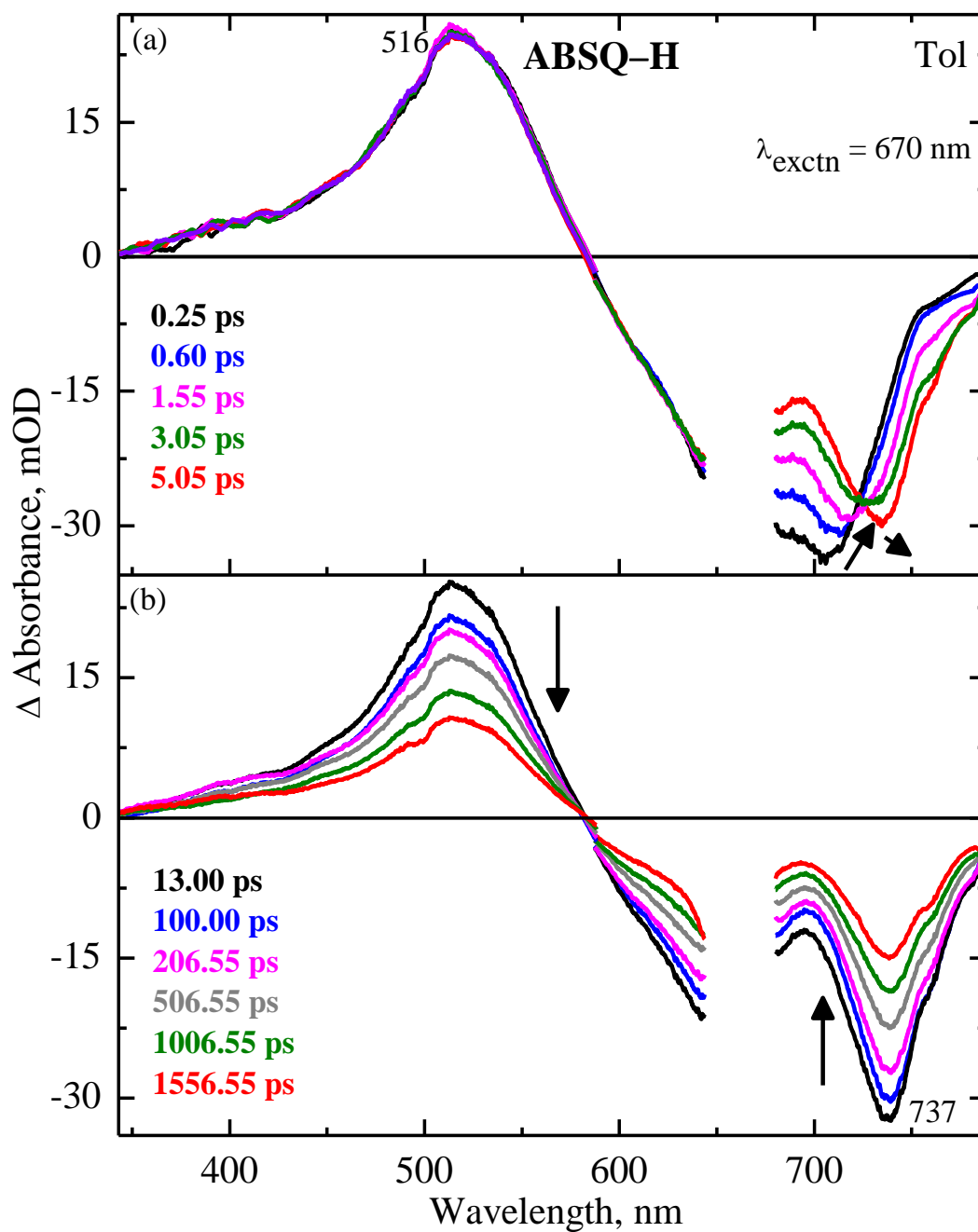


Figure 3.11 Femtosecond transient absorption spectra of ABSQ-H in toluene upon excitation at 670 nm at different delay times.

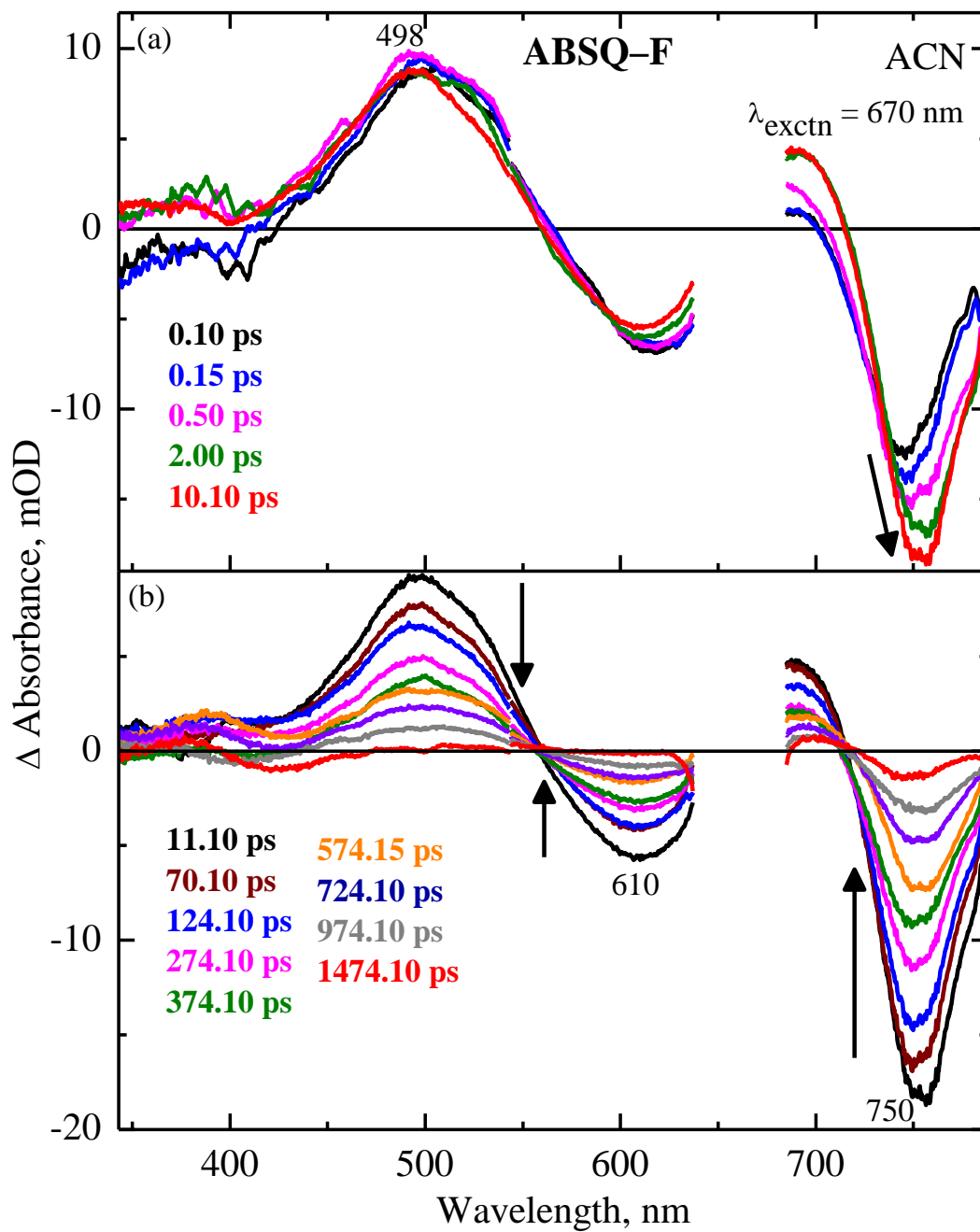


Figure 3.12 Femtosecond transient absorption spectra of ABSQ-F in ACN upon excitation at 670 nm at different delay times.

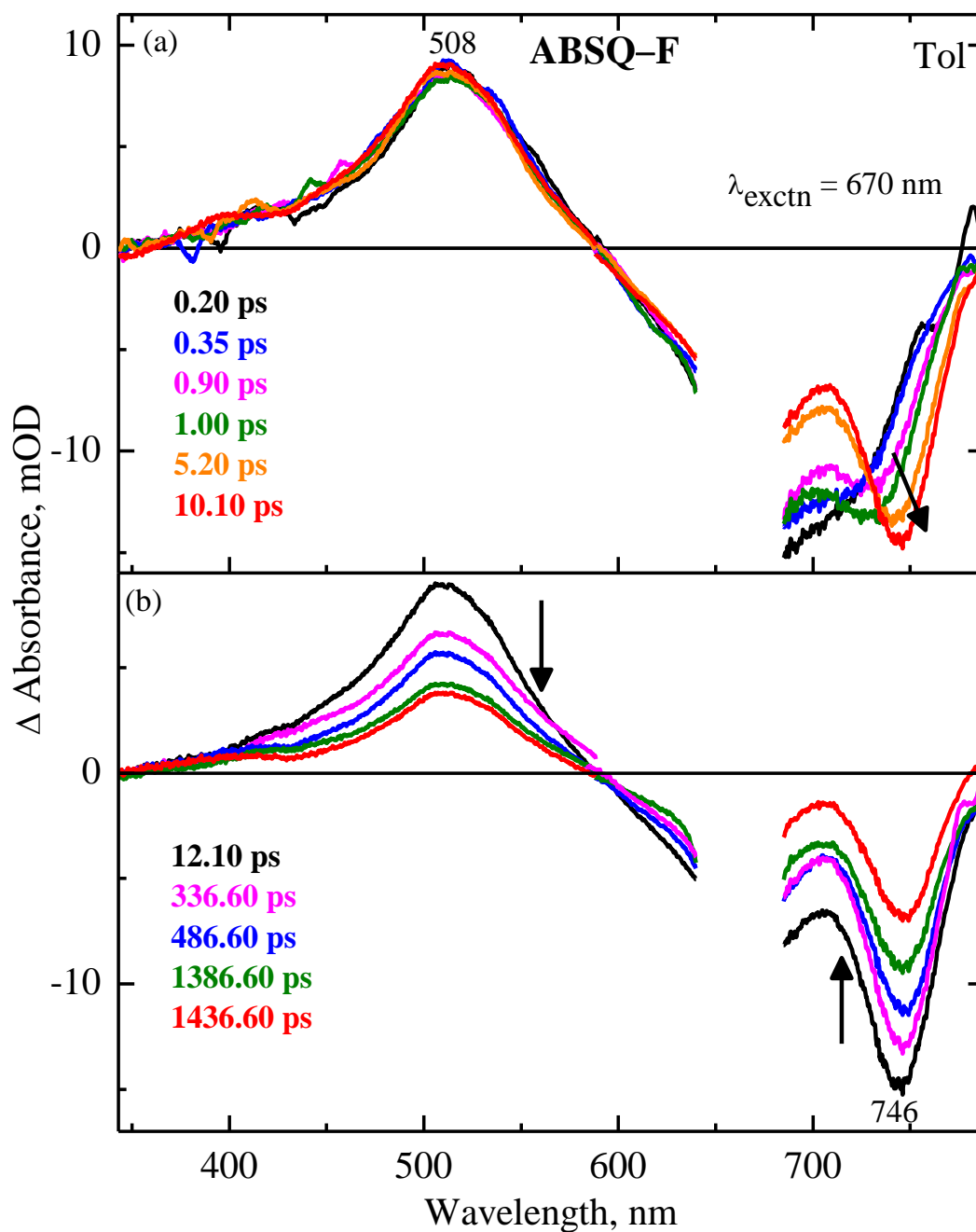


Figure 3.13 Femtosecond transient absorption spectra of ABSQ-F in toluene upon excitation at 670 nm at different delay times.

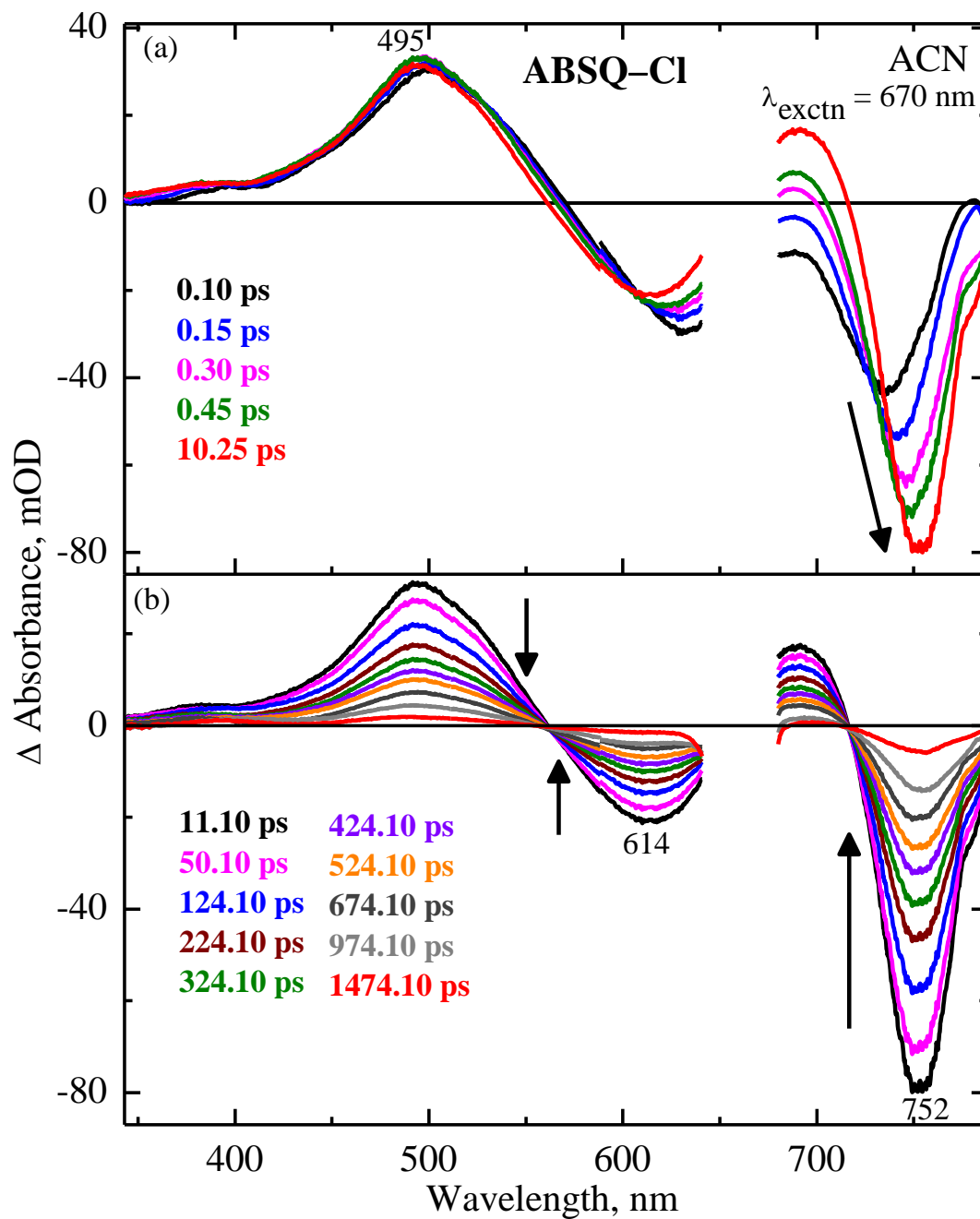


Figure 3.14 Femtosecond transient absorption spectra of ABSQ-Cl in ACN upon excitation at 670 nm at different delay times.

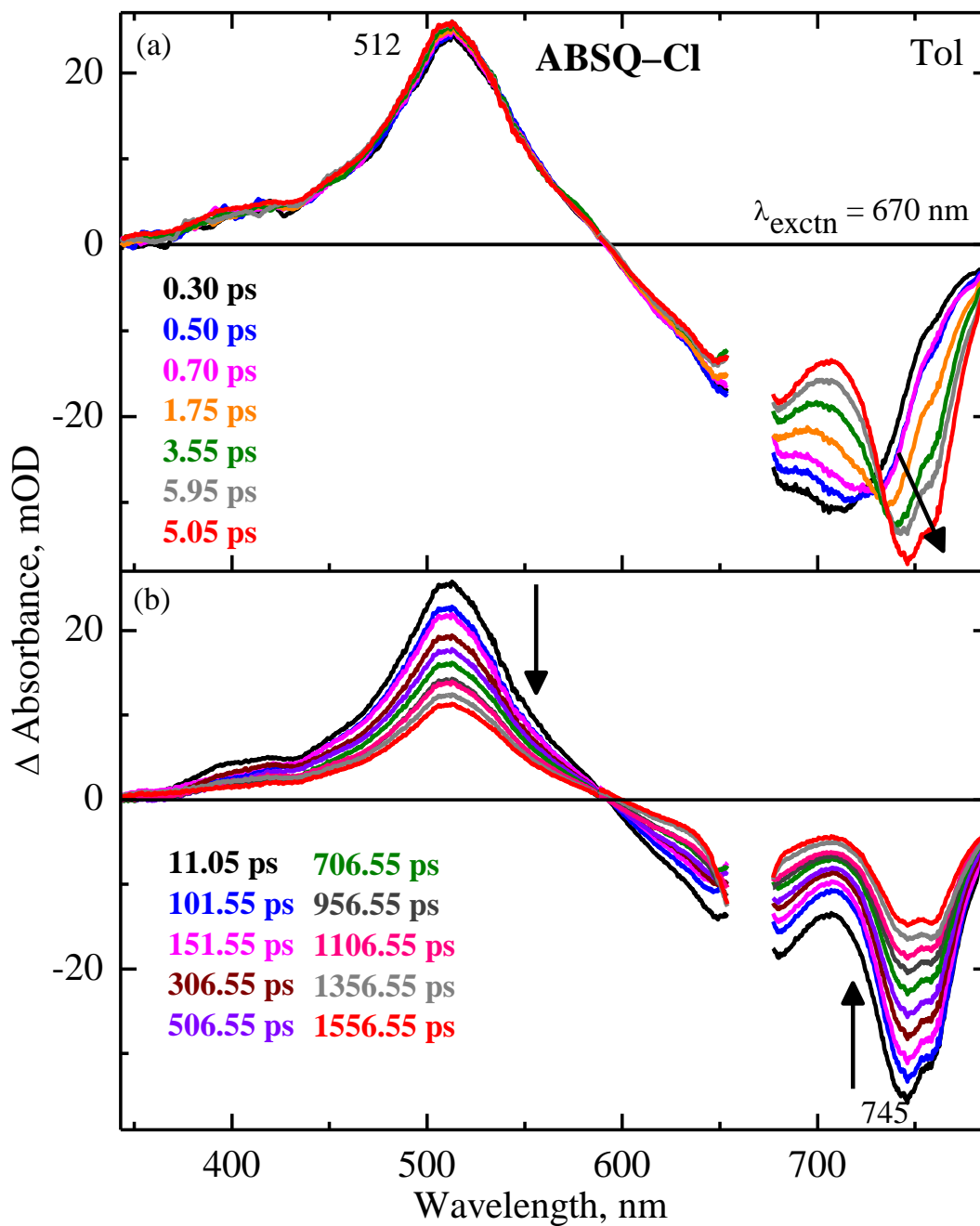


Figure 3.15 Femtosecond transient absorption spectra of ABSQ-Cl in toluene upon excitation at 670 nm at different delay times.

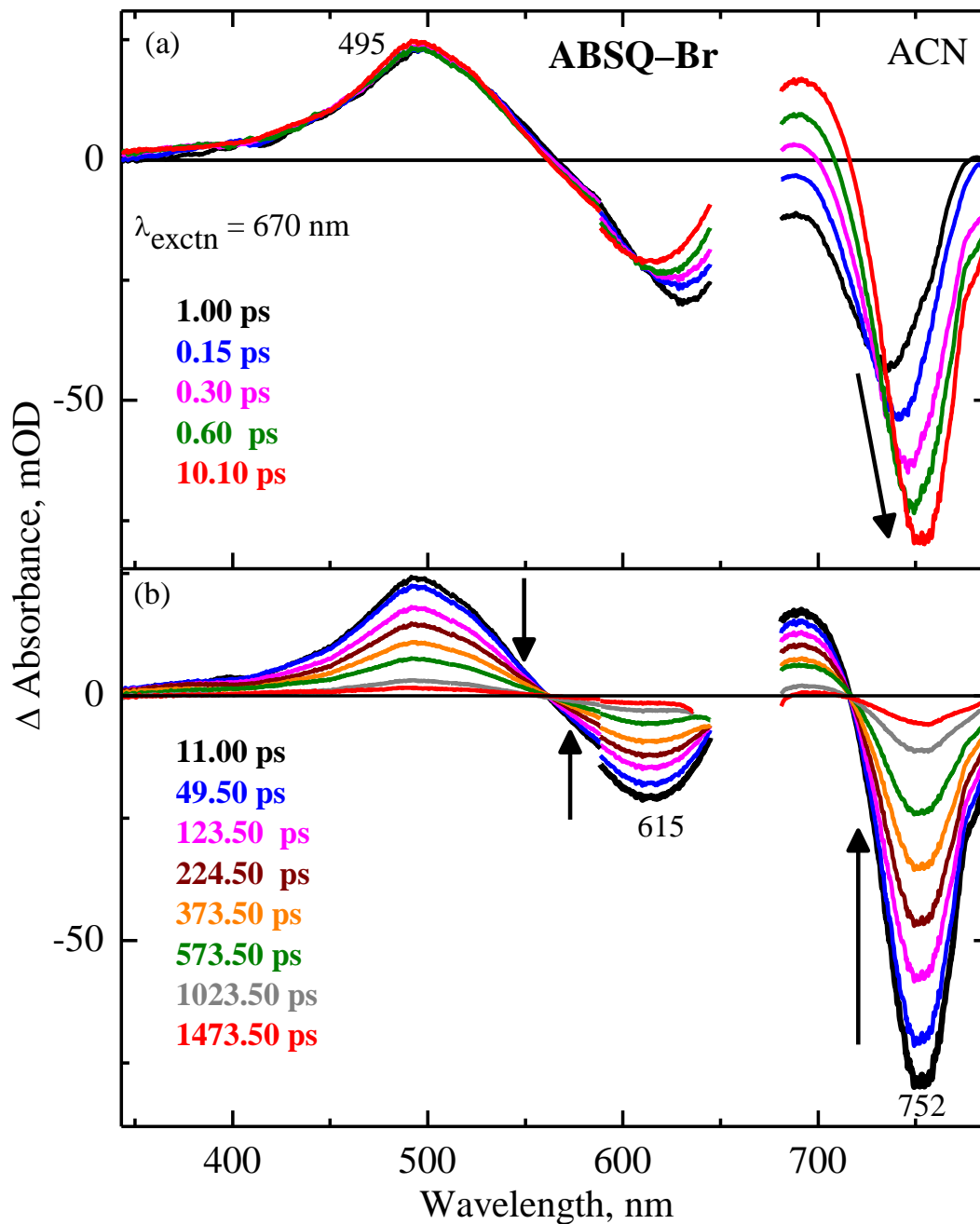


Figure 3.16 Femtosecond transient absorption spectra of ABSQ-Br in ACN upon excitation at 670 nm at different delay times.

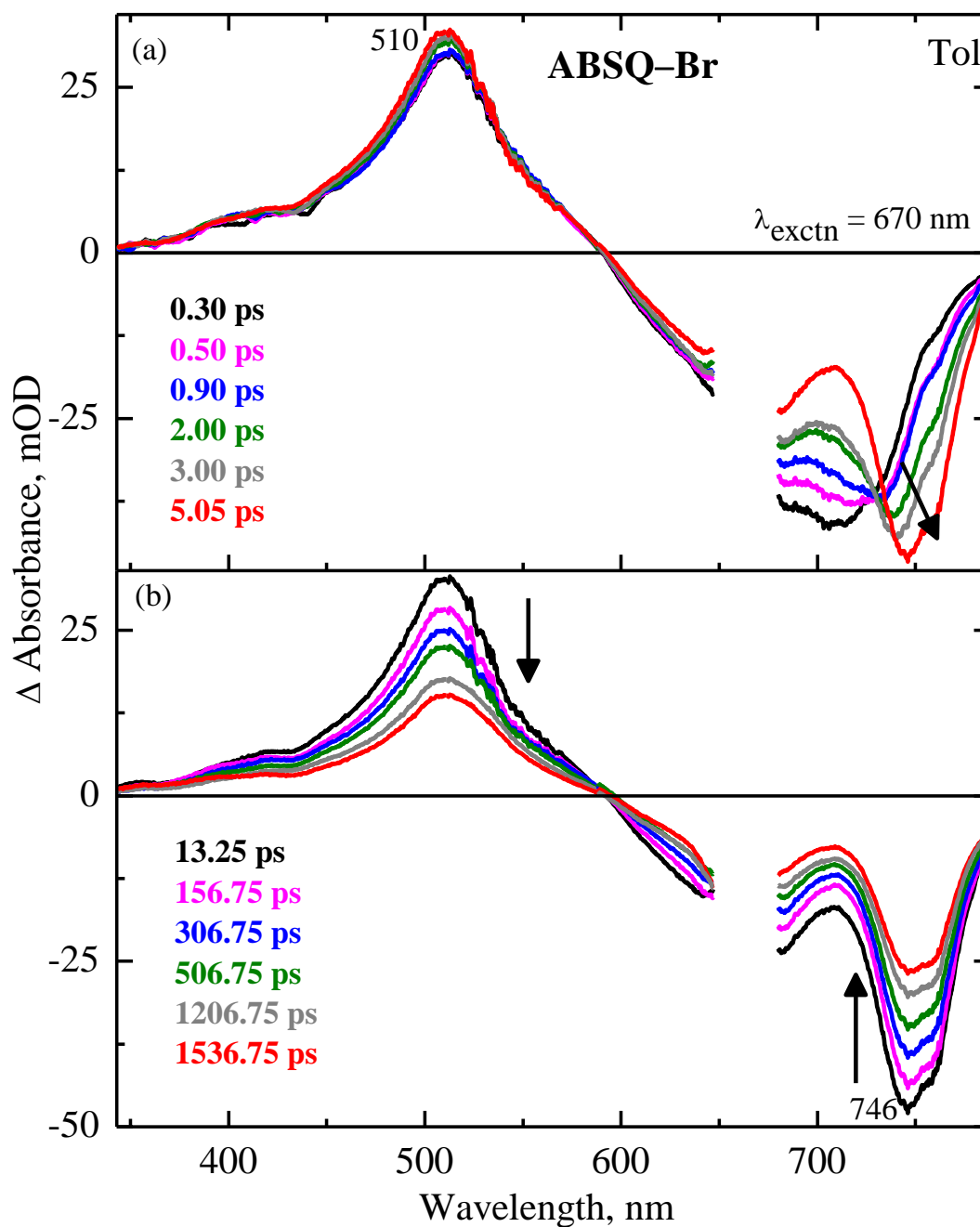


Figure 3.17 Femtosecond transient absorption spectra of **ABSQ-Br** in toluene upon excitation at 670 nm at different delay times.

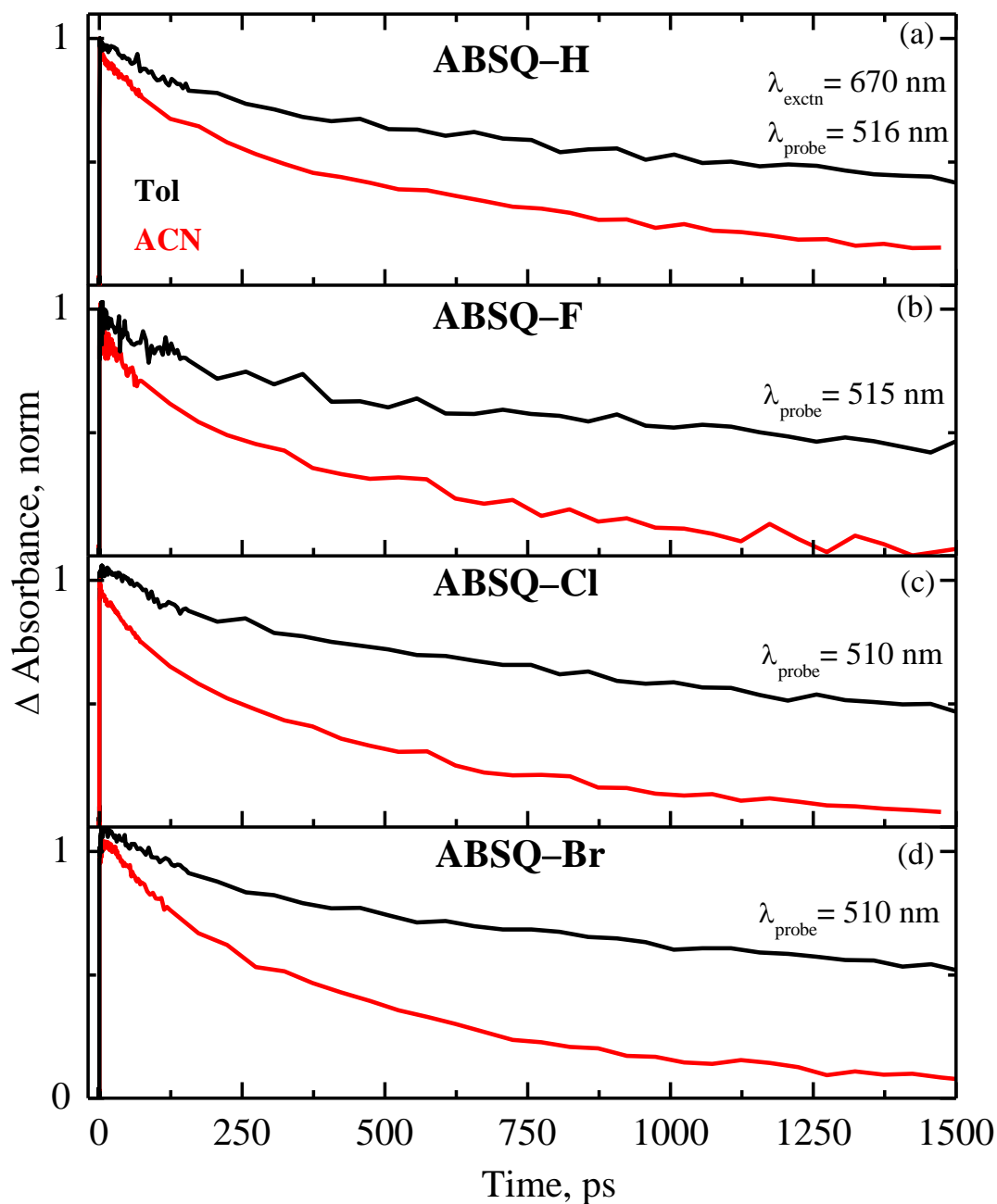


Figure 3.18 Femtosecond transient absorption decay of **ABSQ-H** (a), **ABSQ-F** (b), **ABSQ-Cl** (c) and **ABSQ-Br** (d) in toluene and acetonitrile upon excitation at 670 nm.

When compared to the **ABSQ–H**, the transient absorption spectra showed narrow absorption spectra at early dynamics (~500 fs) upon the addition of PCBM (**Figure 3.19**, right panel). With an increase of delay time, the transient absorption spectrum became broader and the increase of positive absorption in the red region at ~710 nm was observed at a longer time delay. The appearance of positive transient absorption at around 710 nm is attributed to the formation of radical cation of squaraine derivatives and consistent with the literature.^{23, 49-50} Similarly, for other derivatives, changes in the spectral width of transient absorption spectra were observed upon addition of PCBM. These observations could reflect the effect of intermolecular interaction between the **ABSQs** and PCBM. It is to be noted that the concentration of PCBM was 13.5 mM having high absorbance in the region of <390 nm. Since all the probe beam below 390 nm was completely absorbed by PCBM, we could not observe any changes in the optical density in this region. In addition, there is an artifact raised at ~433 nm due to the strong and narrow absorption of PCBM. The excited–state relaxation dynamics probed at ESA maximum were quenched upon addition of PCBM (**Figure 3.23**) as observed in the fluorescence dynamics (**Figure 3.9**). Nevertheless, only a small change between the transient absorption decay of **ABSQ–F** with and without PCBM was observed, despite significant quenching in the fluorescence data. This could be due to the resultant of competition between the characters of fluoride by the electron–withdrawing (electronegativity) and electron–donating (+ mesomeric effect) in nature.³¹

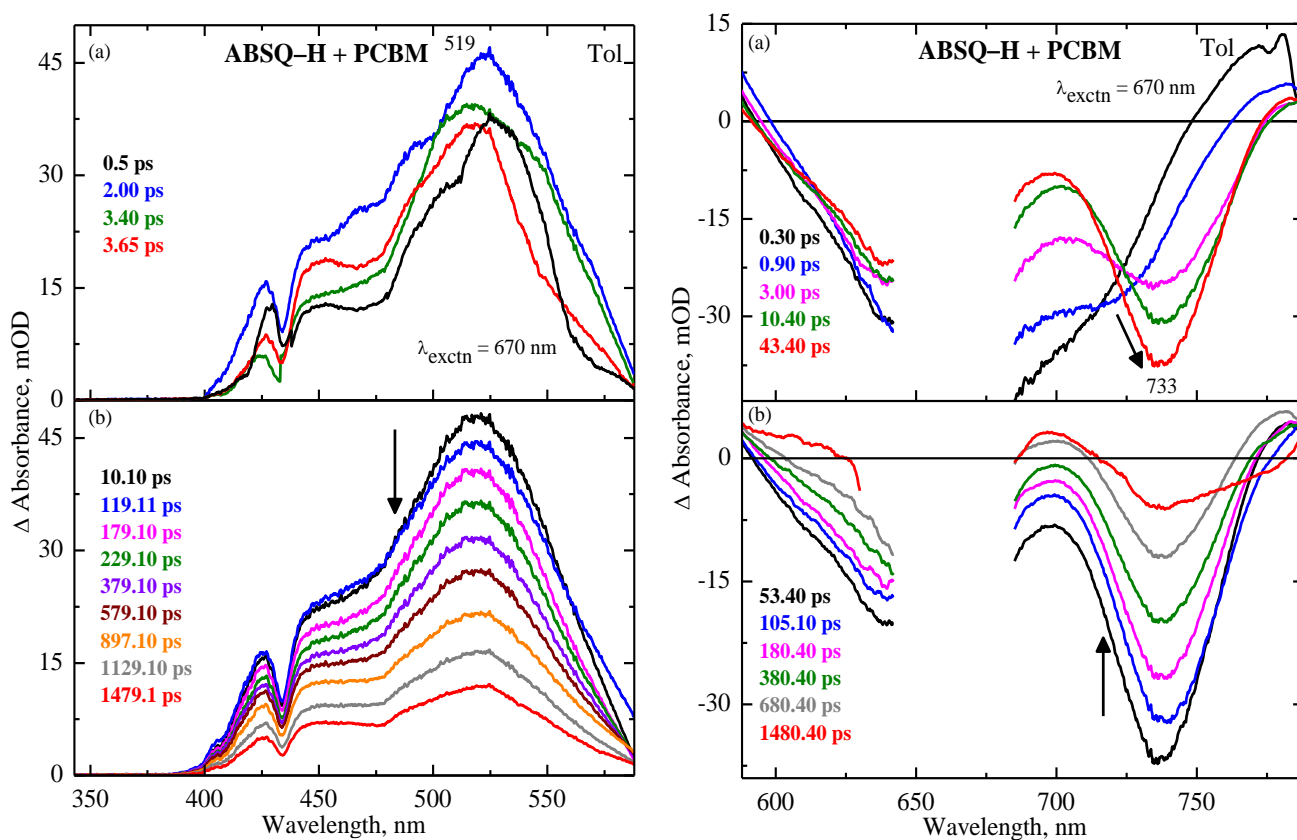


Figure 3.19 Femtosecond transient absorption spectra of **ABSQ-H** with **PCBM** in toluene upon excitation at 670 nm in the shorter wavelength (left) and longer wavelength (right) region at different delay times.

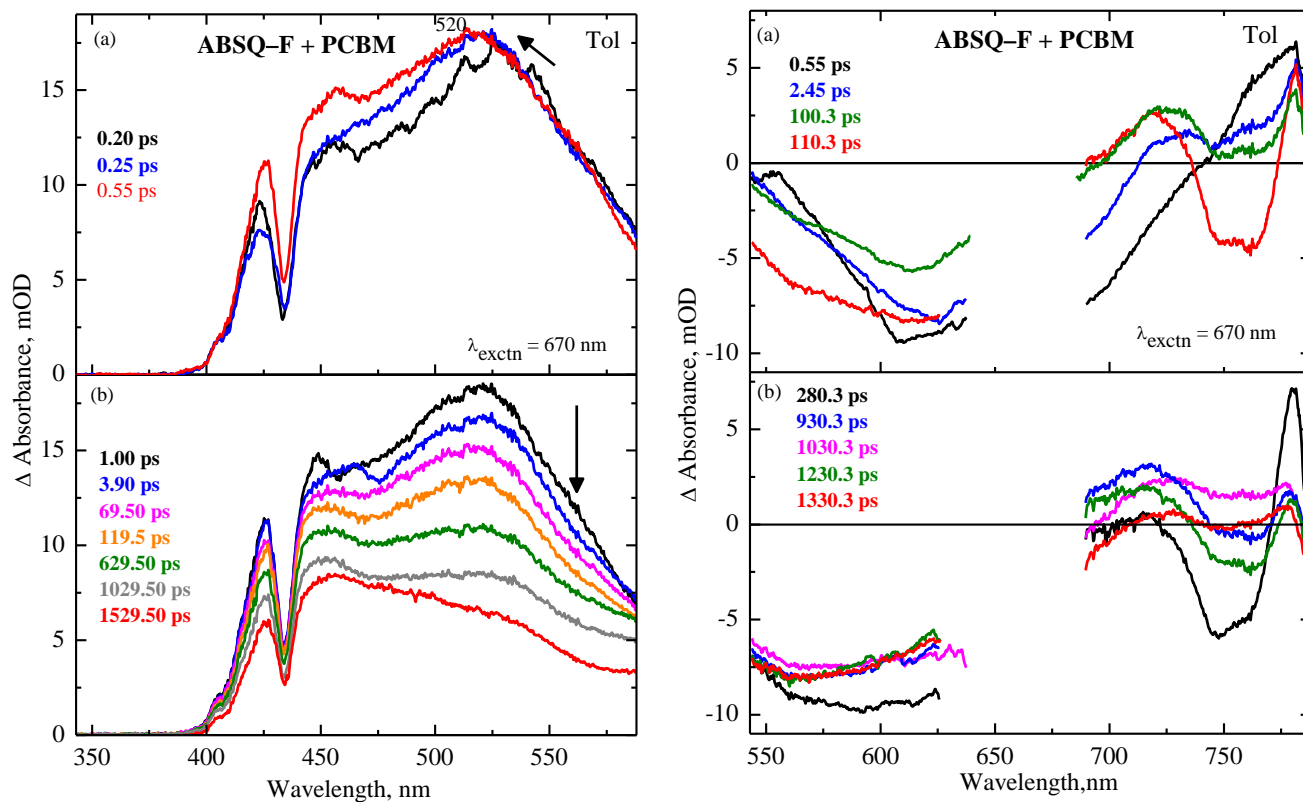


Figure 3.20 Femtosecond transient absorption spectra of **ABSQ-F** with **PCBM** in toluene upon excitation at 670 nm in the shorter wavelength (left) and longer wavelength (right) region at different delay times.

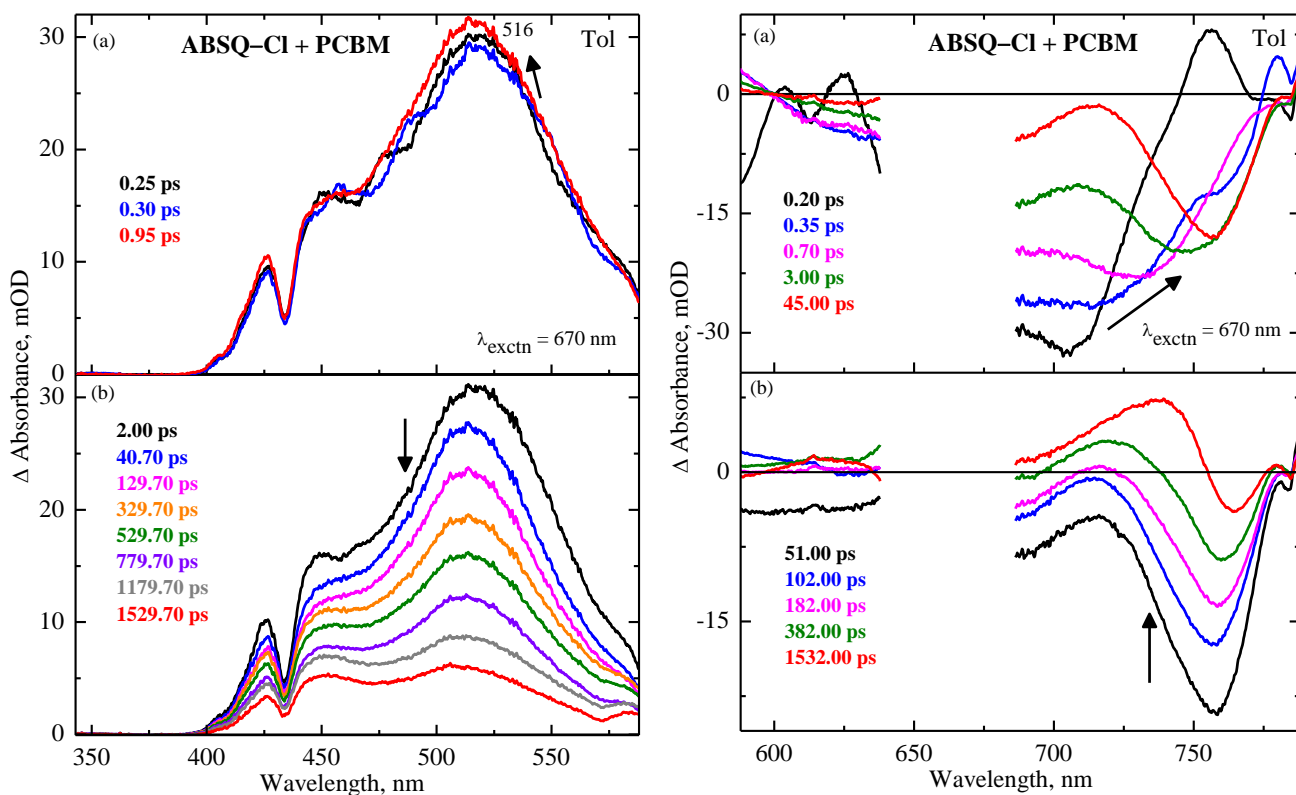


Figure 3.21 Femtosecond transient absorption spectra of ABSQ-Cl with PCBM in toluene upon excitation at 670 nm in the shorter wavelength (left) and longer wavelength (right) region at different delay times.

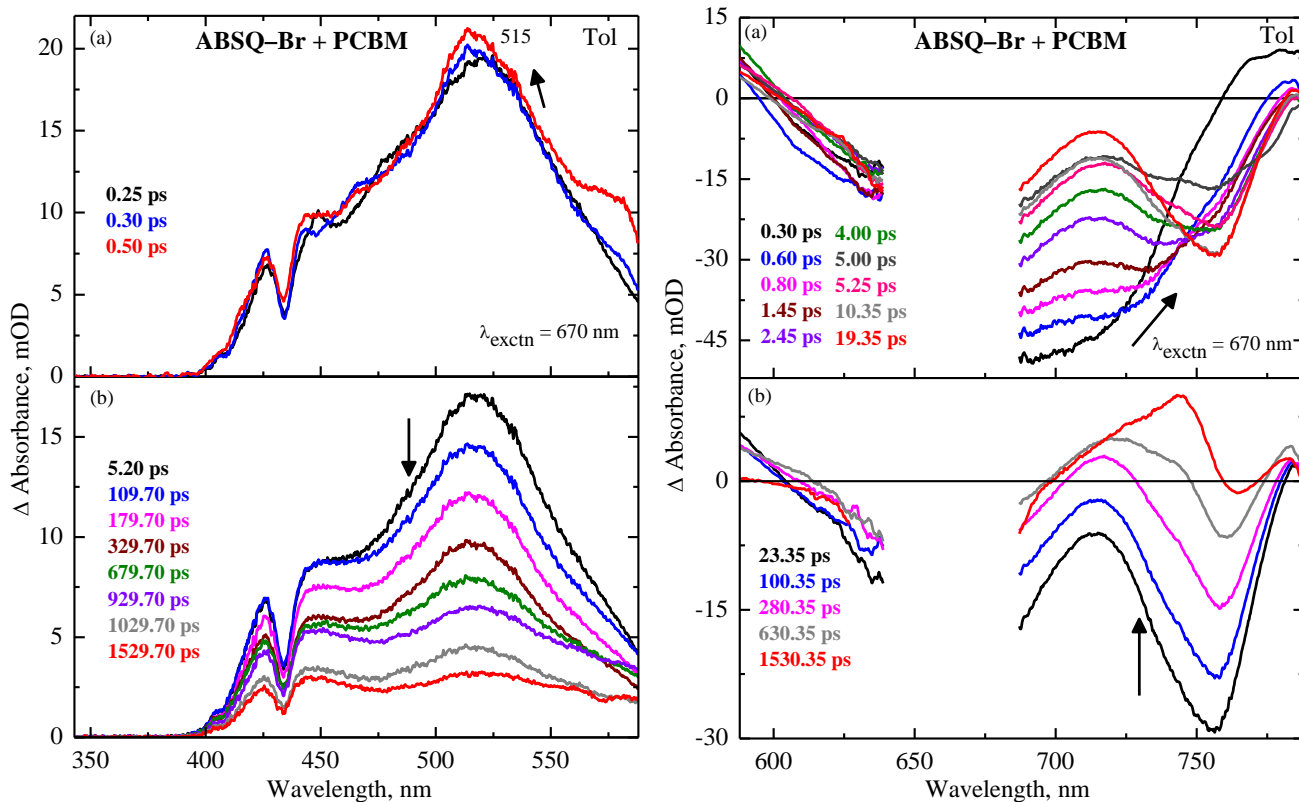


Figure 3.22 Femtosecond transient absorption spectra of **ABSQ-Br** with **PCBM** in toluene upon excitation at 670 nm in the shorter wavelength (left) and longer wavelength (right) region at different delay times.

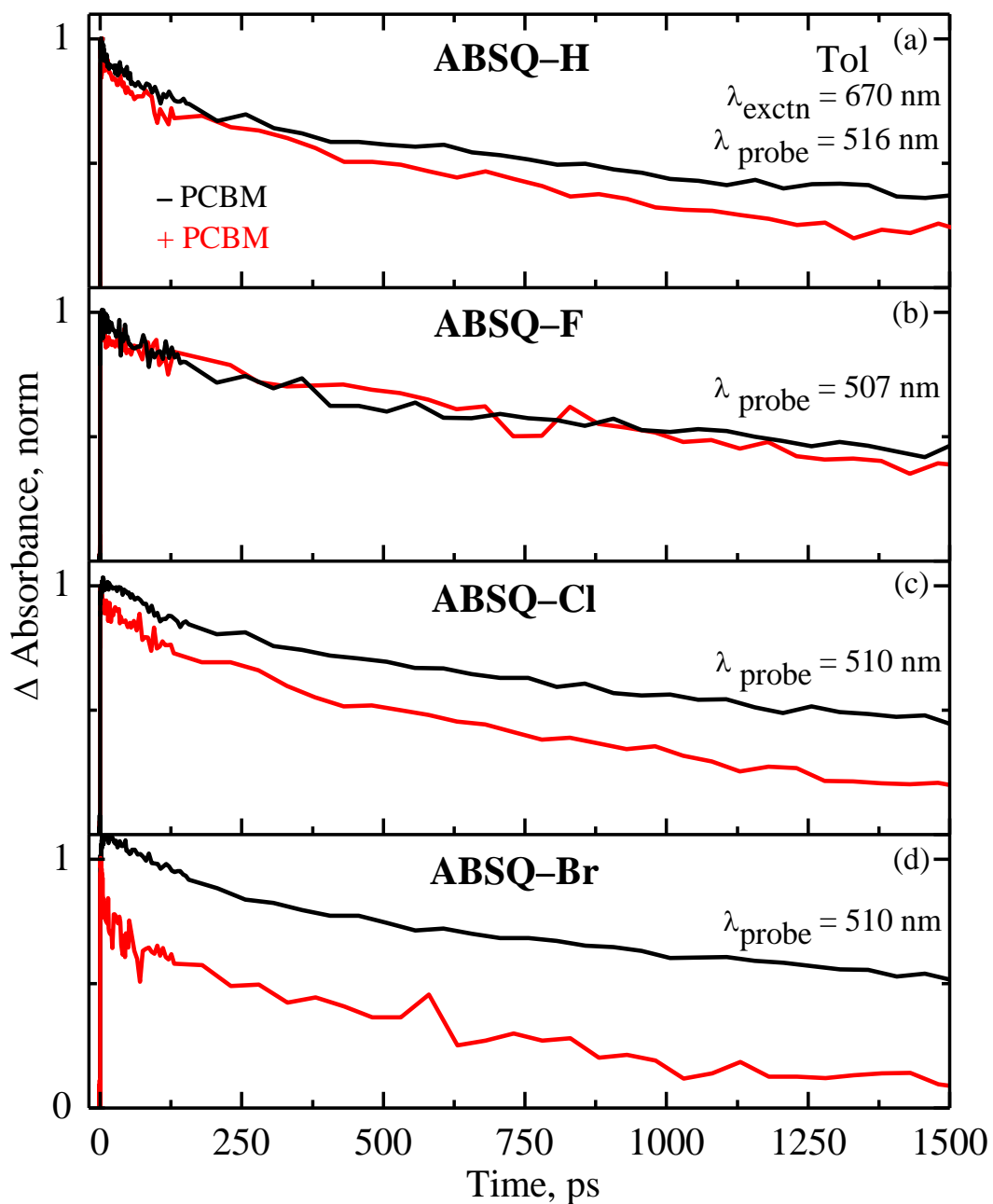


Figure 3.23 Femtosecond transient absorption decay of **ABSQ-H** (a), **ABSQ-F** (b), **ABSQ-Cl** (c) and **ABSQ-Br** (d) with and without PCBM in toluene upon excitation at 670 nm.

3.4.2 Analysis of the Transient Absorption Spectra of ABSQ Derivatives

The femtosecond transient absorption spectra were analyzed globally with the sequential

model using Glotaran.⁵¹ Three exponential time constants were ideally determined to completely describe the excited state relaxation dynamics of **ABSQ** derivatives in ACN and toluene and PCBM in toluene. The obtained time constants are provided in **Table 3.7** and their respective DADS are shown for comparison in Figure **3.24–3.27**. The DADS exhibited the amplitude of a particular decay time constant as a function of the corresponding wavelength and reflected the common features of transient absorption spectra.

The **ABSQ–H** is considered at first for the discussion of time constants obtained from the global analysis. The fast component ($\tau_1 = 445$ fs in ACN and $\tau_1 = 2.22$ ps in toluene) is attributed to the solvation relaxation processes from the Franck–Condon state to solvent stabilized local excited state based on the observation of dynamic redshift of SE with an increase of delay time.⁵²⁻
⁵⁴ The time constant τ_2 , 33.23 ps and 167 ps for ACN and toluene respectively, might be due to the formation of the dark state resulting from the conformational changes of **ABSQ–H**. This state enables the non–radiative deactivation to the ground state supporting the observation of a decrease of fluorescence quantum yield and lifetime in ACN (**Table 3.1–3.4**). Finally, the longer time constant τ_3 , obtained from the global analysis is equivalent with the fluorescence lifetime obtained from the TCSPC in a neat solvent (**Table 3.1–3.4**). Hence the time constant of 0.63 (2.50) ns is attributed to the lifetime of the excited singlet state of **ABSQ–H** in ACN (toluene). A similar excited state relaxation pathway is plausible to occur for other halogenated **ABSQ** derivatives. The DADS are shown for comparison in Figure **3.24** and **3.25**. The DADS exhibited the amplitude of a particular decay time constant as a function of the corresponding wavelength and reflected the common features of transient absorption spectra.

Interestingly the analysis of transient absorption measurements of all the derivatives upon

the addition of PCBM exhibited the quenching of all the time constants (**Table 3.7**). For example, the time constants of **ABSQ-H** were decreased from $\tau_1 = 2.22$ ps, $\tau_2 = 167$ ps and $\tau_3 = 2.50$ ns to $\tau_1 = 1.81$ ps, $\tau_2 = 76.92$ ps and $\tau_3 = 2$ ns upon addition of PCBM. Importantly the decrease of τ_3 for all the derivatives is consistent with the quenching of fluorescence dynamics observed in the TCSPC. Such a decrease of all the time constants further supports the existence of the intermolecular charge-transfer between **ABSQ** derivatives and PCBM.⁵⁵

Table 3.7 Time Constants Attained from Global Analysis Using Glotaran⁵¹ for **ABSQs** upon Excitation at 670 nm

ABSQs	ACN	Toluene	
		- PCBM	+ PCBM
ABSQ-H	$\tau_1 = 0.44 \pm 0.12$ ps	$\tau_1 = 2.22 \pm 0.12$ ps	$\tau_1 = 1.81 \pm 0.12$ ps
	$\tau_2 = 33.23 \pm 1.20$ ps	$\tau_2 = 167 \pm 5.5$ ps	$\tau_2 = 76.92 \pm 2.5$ ps
	$\tau_3 = 632 \pm 10$ ps	$\tau_3 = 2.50 \pm 0.25$ ns	$\tau_3 = 2 \pm 0.15$ ns
ABSQ-F	$\tau_1 = 0.43 \pm 0.12$ ps	$\tau_1 = 2.31 \pm 0.12$ ps	$\tau_1 = 1.89 \pm 0.12$ ps
	$\tau_2 = 41.84 \pm 1.50$ ps	$\tau_2 = 151.51 \pm 4.50$ ps	$\tau_2 = 83.34 \pm 2.35$ ps
	$\tau_3 = 629 \pm 10$ ps	$\tau_3 = 2.41 \pm 0.15$ ns	$\tau_3 = 1.96 \pm 0.10$ ns
ABSQ-Cl	$\tau_1 = 0.45 \pm 0.12$ ps	$\tau_1 = 2.25 \pm 0.15$ ps	$\tau_1 = 1.15 \pm 0.12$ ps
	$\tau_2 = 35 \pm 1.35$ ps	$\tau_2 = 140 \pm 3.25$ ps	$\tau_2 = 85.85 \pm 3.25$ ps
	$\tau_3 = 577 \pm 5$ ps	$\tau_3 = 2.62 \pm 0.10$ ns	$\tau_3 = 1.85 \pm 0.15$ ns
ABSQ-Br	$\tau_1 = 0.42 \pm 0.12$ ps	$\tau_1 = 2.39 \pm 0.15$ ps	$\tau_1 = 1.18 \pm 0.12$ ps
	$\tau_2 = 17.60 \pm 0.82$ ps	$\tau_2 = 134.90 \pm 3.15$ ps	$\tau_2 = 91.19 \pm 4.05$ ps
	$\tau_3 = 616 \pm 10$ ps	$\tau_3 = 2.60 \pm 0.10$ ns	$\tau_3 = 1.97 \pm 0.15$ ns

The occurrence of the charge-transfer dynamics is further confirmed by the formation of radical cations of squaraine derivatives exhibiting positive transient absorption at around 710 nm, consistent with the literature,^{23, 49-50} upon addition of PCBM at a longer time delay. Further to

shed more light on the charge–transfer dynamics, a global target analysis has been carried out to extract the time constant of charge–transfer and spectral signatures of each excited species. The species associated difference spectra (SADS) of **ABSQ** derivatives upon addition of PCBM are shown in **Figure 3.26** and **3.27**. The rate constant of a particular process can be obtained from the fraction of population conversion from one state to another divided by the associated time constant of the state.⁵⁶⁻⁵⁹ The relative fraction of population is tested by multiplying the amplitude of each of the kinetic traces with the corresponding species associated spectrum and summing the result, leading to the observed transient absorption spectra within the experimental noise.⁶⁰ Thus, based on the target analysis, the charge transfer proposed to occur from the solvent-stabilized local excited state with the relative population of ~89% and the time constants of charge transfer from **ABSQ–H**, **ABSQ–F**, **ABSQ–Cl** and **ABSQ–Br** to PCBM were found to be ~86.43, 93.72, 96.52, and 102.56 ps, respectively. The transient absorption spectra showing the anion radical of PCBM in the NIR region⁶¹⁻⁶² would be advantageous in supporting the occurrence of the intermolecular charge transfer process in the mixture. Thus, based on the spectral observations and kinetic analysis, the excited–state relaxation dynamics of the **ABSQs** are proposed in **Scheme 3.2** upon ultrafast laser excitation.

Thus upon halogenation of **ABSQ** derivatives, the red shift with an increase of molar absorptivity, high bimolecular quenching constant and efficient intermolecular charge transfer with PCBM were observed. These effects could be due to the transfer of electron density from the halogen substituents to the benzothiazole moiety core which increases with an increase of polarizability of the halogen substituents. This is consistent with the report of Frank Würthner et

al.³¹ that a redshift of absorption with an increase of the molar extinction coefficient and enhancement of the fluorescence quantum yield was observed from fluorine over chlorine and bromine to iodine substituted NIR-SQ derivatives.

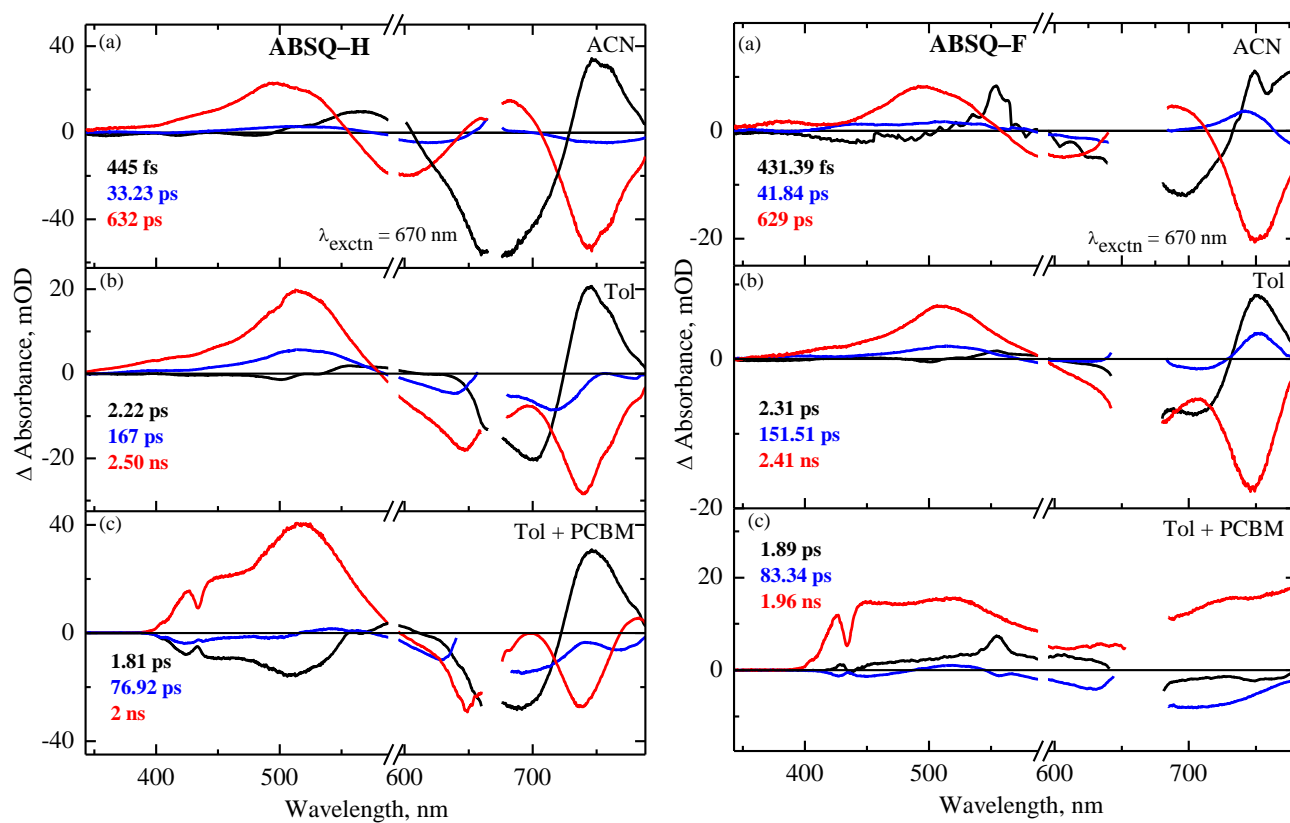


Figure 3.24 Decay associated difference spectra of **ABSQ-H** (left) and **ABSQ-F** (right) in ACN (a), toluene (b) and with PCBM (c) obtained by global analysis.

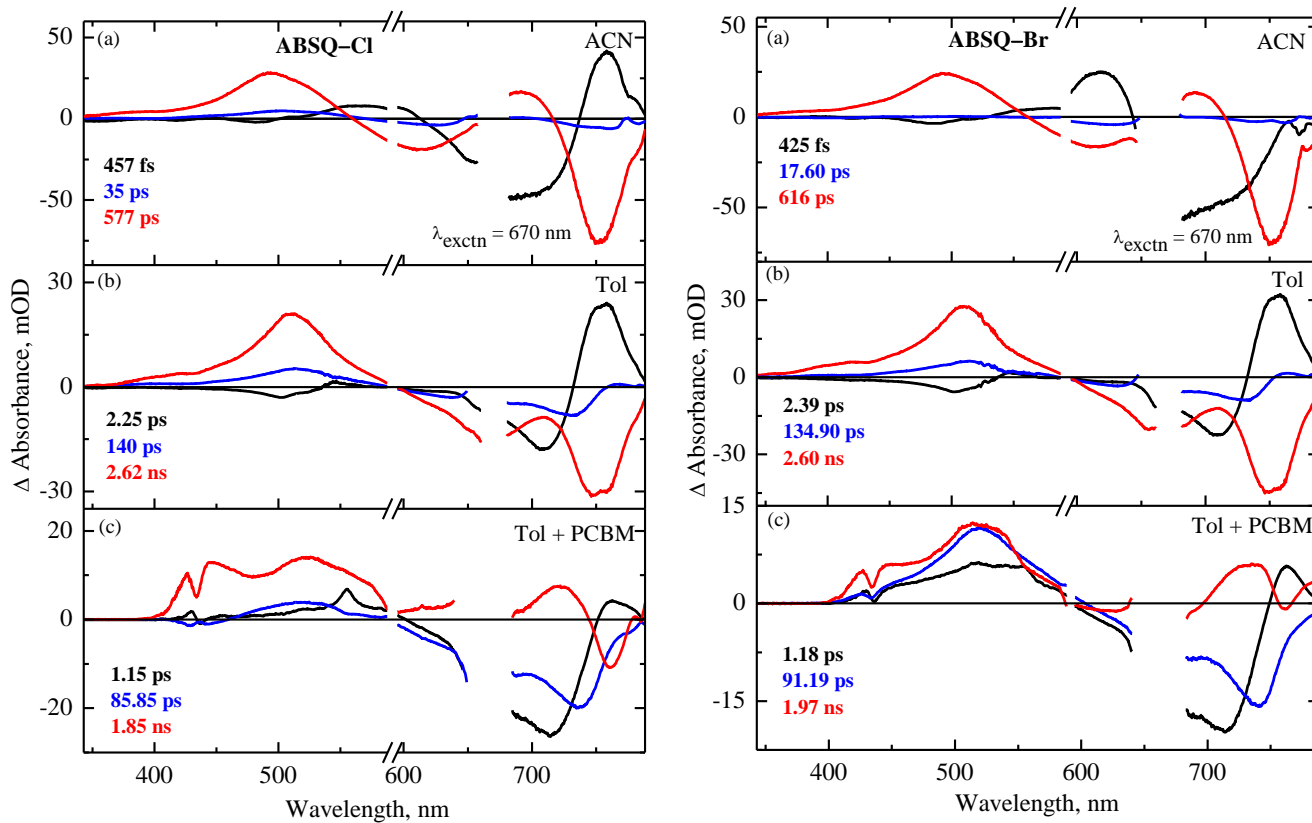


Figure 3.25 Decay associated difference spectra of **ABSQ-Cl** (left) and **ABSQ-Br** (right) in ACN (a), toluene (b) and with PCBM (c) obtained by global analysis.

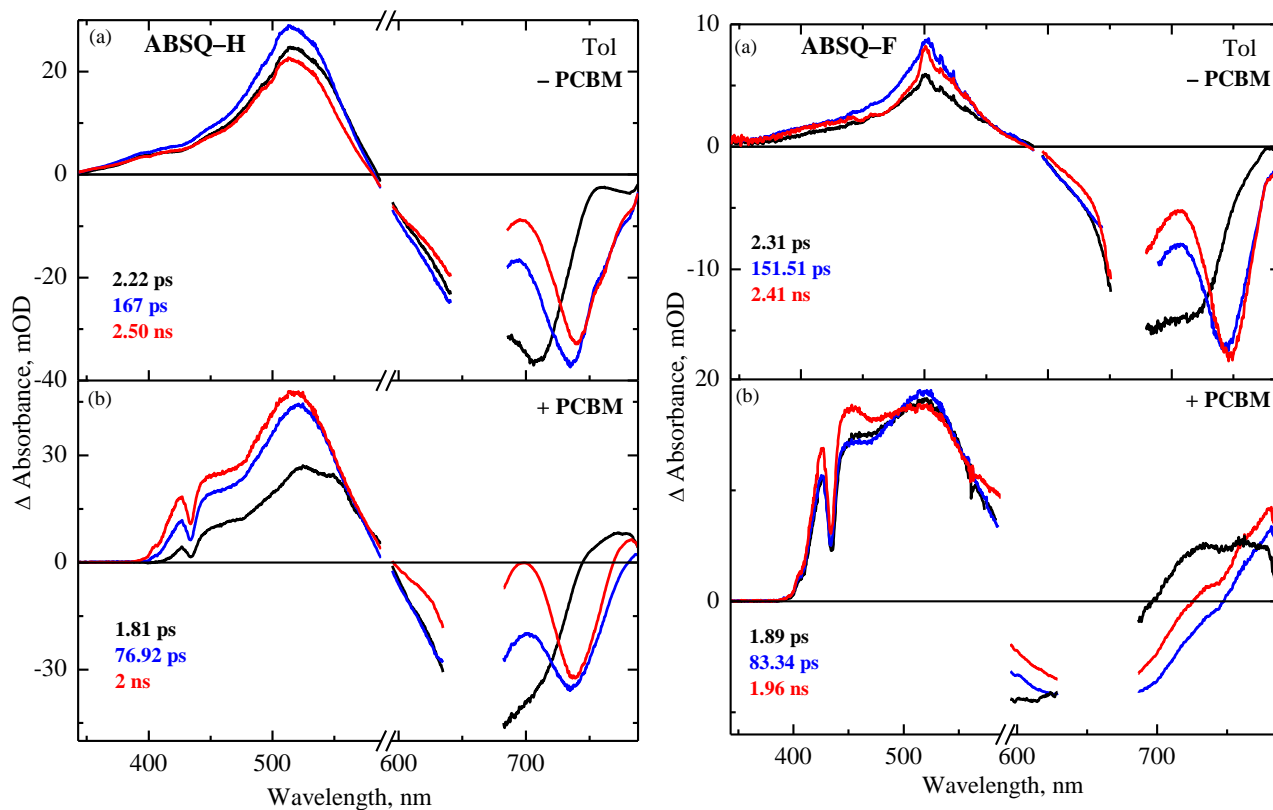


Figure 3.26 Species associated difference spectra of **ABSQ-H** (left) and **ABSQ-F** (right) alone (a) and with PCBM (b) in toluene obtained by global target analysis.

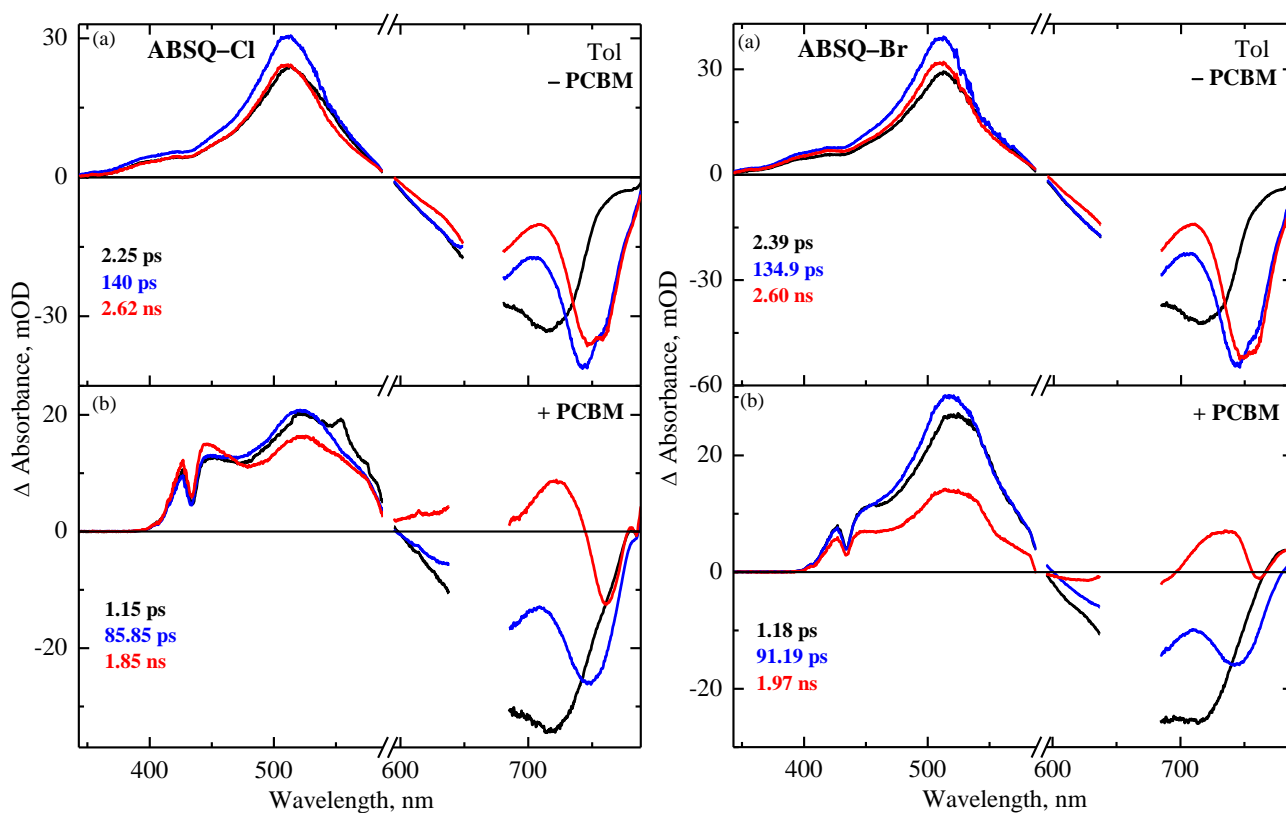
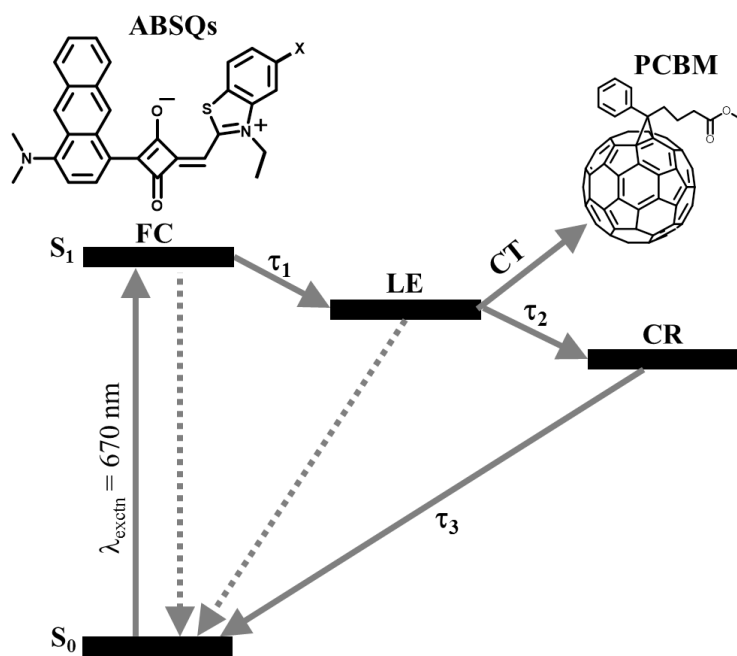


Figure 3.27 Species associated difference spectra of **ABSQ-Cl** (left) and **ABSQ-Br** (right) alone (a) and with PCBM (b) in toluene obtained by global target analysis.



Scheme 3.2 Proposed Excited-State Relaxation Dynamics of **ABSQ** Derivatives upon Ultrafast Excitation^a. ^aFC–Franck–Condon state, LE–Local Excited State, CR–Conformationally Relaxed State and CT–Charge–Transfer.

3.5 Characterization of Photodetector

The BHJ-based OPDs were fabricated using **ABSQ-H** and **ABSQ-Cl** derivatives as donor materials and its architecture and the corresponding energy level diagram are represented in **Figure 3.28**. In the device, molybdenum trioxide (MoO_3) and zinc oxide act as a hole and electron transporting layer respectively.

The results of preliminary characterization of the spectral response of the OPDs under unbiased conditions are shown in **Figure 3.29**. Interestingly, the devices showed sensitivity in the NIR region and needed further investigation.

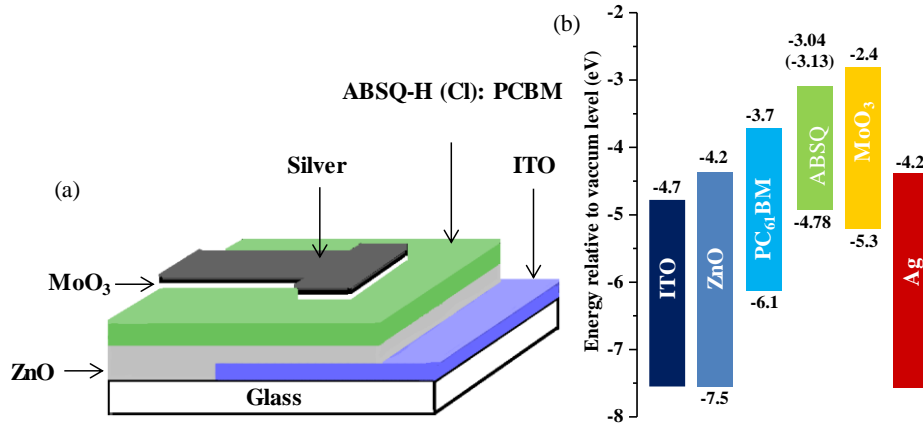


Figure 3.28 a) Fabricated OPD structure, b) band diagram for fabricated OPD.

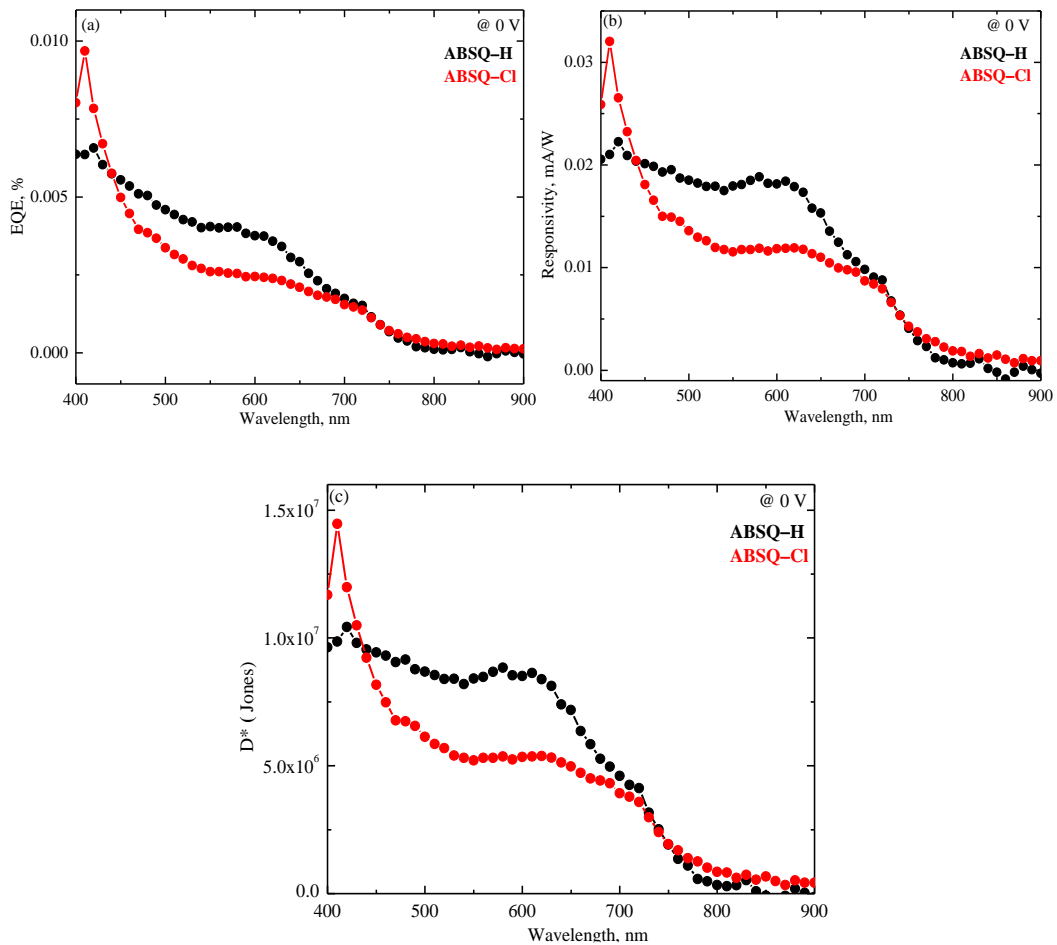


Figure 3.29 EQE (a), R (b) and D* (c) spectra of devices using ABSQ-H and ABSQ-Cl at short circuit condition.

3.6 Summary

The USQ derivatives consisting of *N,N*-dimethyl aminoanthracene and benzothiazole (**ABSQ-H**) halogenated with fluoride (**ABSQ-F**), chloride (**ABSQ-Cl**) and bromide (**ABSQ-Br**) were synthesized to understand the effect of halogen on the intermolecular interaction dynamics between the **ABSQ** derivatives and PCBM. Interestingly the **ABSQ-H** exhibited intense absorption ($\epsilon \sim 6.72 \times 10^4 \text{ M}^{-1} \text{ cm}^{-1}$) in the NIR region with maxima centered $\sim 660 \text{ nm}$. Upon halogen substitution, red shift in the absorption spectra with an increase in molar absorptivity was observed. The excited-state relaxation dynamics of **ABSQ** derivatives in acetonitrile are faster when compared to that in toluene due to the change in the solvation relaxation dynamics. The quenching of fluorescence intensity and lifetime of **ABSQs** upon addition of PCBM revealed the occurrence of intermolecular charge transfer between the **ABSQs** and PCBM. The **ABSQ-H** and **ABSQ-Cl** were applied to the OPD devices and showed sensitivity in the NIR region. These results will help for the development of efficient USQ derivatives for optoelectronic devices.

3.7 Experimental Section

3.7.1 Materials and Methods

1 General Details: The reagents and chemicals used for synthesis were purchased from Merck, Sigma-Aldrich, and TCI. Dry solvents were prepared by following the reported procedures.⁶³ The material characterization techniques, steady-state measurements, electrochemical measurements, TCSPC measurements, femtosecond transient absorption measurements details were provided in the experimental section of Chapter 2.

2. Device Fabrication: The OPDs were fabricated in the device architecture, glass/ indium tin oxide (ITO)/ zinc oxide (ZnO)/ **ABSQ–H (Cl): PCBM**/ molybdenum trioxide (MoO₃)/ silver (Ag). ITO –coated glass substrates (Kintec Company, Hong Kong) were cleaned in a liquid detergent solution (Alkanox) and subsequently sonicated in deionized water and 2-propanol. After drying, the substrates were UV–ozone–treated (Novascan). The ZnO solution was spin–coated onto the substrates and annealed for 30 minutes at 170⁰ C. The **ABSQ–H(Cl): PCBM** (1:6 ratio) blend in toluene (42 mg/mL) was spin–coated on top of ZnO, inside a N₂ filled glovebox system. A hole transporting layer of 10 nm MoO₃ and back contact Ag of 100 nm were deposited by thermal evaporation (Angstrom Inc.) The evaporation process was automatically controlled by Inficon software and thickness of films were optimized using Dektak XT stylus profilometer.

3 Device Characterization: The incident photon–to–current conversion efficiency (IPCE) measurements were carried out in DC mode using the constant light source as 350 W Xenon arc lamp (6258, Newport, lamp house S/N: 876). The Cornerstone TM 260 UV–vis monochromator is used to get the monochromatic light for the measurement, the reference is recorded using the detector (818–UV, S/N: 10878) calibrated and provided by Newport. The power meter (Model: 1918–R, S/N: 17953, Newport) is used for recording the measurement in each wavelength synchronized to the Cornerstone TM Monochromator using TracQ TM 6.5 data acquisition software provided by Newport. The measurement of the reference silicon solar cell (QE Solar Cell, Newport) is being carried out to verify the measurement conditions. The dark current was measured by using a Keithley 2400 source meter.

3.8 Synthesis and Characterization of ABSQ Derivatives

1. The synthetic procedure and characterization details of 1-Aminoanthracene, *N,N*-Dimethylantracene-1-amine and 3-(4-(dimethylamino) anthracen-1-yl)-4-hydroxycyclobutene-1, 2-dione were provided in the experimental section of Chapter 2.

2. Synthesis of 3-ethyl-2-methylbenzo[d]thiazol-3-ium

A mixture of 2-methylbenzo[d]thiazole (1.17 g, 3.3 mmol), and ethyl iodide (0.7g, 4.95 mmol) was taken in a pressure tube. To this 4 ml of dry acetonitrile was added and the mixture was heated at 80° C for 15 h. The solvent was removed under reduced pressure. The residue was washed several times with diethyl ether to give the desired product. (0.6 g, 43.16%).

¹H NMR (500 MHz, DMSO-*d*₆): δ 7.97-7.95 (d, 1H, *J*= 7.5 Hz), 7.85-7.62 (m, 3H), 4.51-4.46 (q, 2H, *J*=7.5 Hz), 2.82 (s, 3H), 1.46-1.43 (t, 3H, *J*= 7.5 Hz); HRMS–EI: Calculated molecular weight for C₁₀H₁₂SN⁺ is 178.2734, found=178.0693.

3 General procedure for the quaternization of 5-halo-2-methylbenzo[d]thiazole

A suspension of 5-halo-2-methylbenzo[d]thiazole (1 equivalent) and ethyl iodide (1.5 equivalent) was taken in a pressure tube. To this dry acetonitrile was added and the mixture was heated at 80° C for 15 h. The solvent was vacuum eliminated and the residue was washed several times with diethyl ether to give the desired product.

3.1 Characterization details of 3-ethyl-5-fluoro-2-methylbenzo[d]thiazol-3-ium

¹NMR (500 MHz, DMSO-*d*₆): δ 6.75 (s, 1H), 6.88-6.82 (d, 2H, *J*= 7.5 Hz), 4.49-4.43 (q, 2H, *J*= 7.5 Hz), 2.79 (s, 3H), 1.45-1.41 (t, 3H, *J*= 7.5 Hz). HRMS–EI: Calculated molecular weight for C₁₀H₁₁FSN⁺ is 196.2639, found = 196.0570.

3.2 Characterization details of 3-ethyl-5-chloro-2-methylbenzo[d]thiazol-3-ium

^1H NMR (500 MHz, $\text{DMSO}-d_6$): δ 7.23 (s, 1H), δ 7.12-6.98 (d, 2H, $J=7.5$ Hz), 4.50-4.44 (q, 2H, $J=7.5$ Hz), 2.85 (s, 3H), 1.47-1.43 (t, 3H, $J=7.5$ Hz); HRMS–EI: Calculated molecular weight for $\text{C}_{10}\text{H}_{11}\text{ClSN}^+$ is 212.7185, found = 212.0270.

3.3 Characterization details of 3-ethyl-5-bromo-2-methylbenzo[d]thiazol-3-ium

^1H NMR (500 MHz, $\text{DMSO}-d_6$): δ 7.51 (s, 1H), δ 7.37-7.34 (d, 2H, $J=7.5$ Hz), 4.47-4.41 (q, 2H, $J=7.5$ Hz), 2.80 (s, 3H), 1.42-1.39 (t, 3H, $J=7.5$ Hz); HRMS–EI: Calculated molecular weight for $\text{C}_{10}\text{H}_{11}\text{BrSN}^+$ is 257.1695, found = 257.9730.

4 Characterization details of ABSQ–H [(Z)-2-(4-(dimethylamino) anthracen-1-yl)-4-((3-ethylbenzo[d]thiazol-3-ium-2-yl) methylene)-3-oxocyclobut-1-enolate]

A mixture of 3-(4-(dimethylamino) anthracen-1-yl)-4-hydroxycyclobut-3-ene-1, 2-dione (0.17g, 0.56 mmol), and 3-ethyl-2-methylbenzo[d]thiazol-3-ium (0.1g, 0.56 mmol) was dissolved in a 1:1 benzene: butanol azeotropic mixture (30 ml) to that 1 or 2 drops of quinoline was added and refluxed at 90°C in a Dean–Stark apparatus for about 8 h. After the reaction, the mixture is allowed to cool to room temperature and then the solvent is removed under reduced pressure. Then the residue was purified by column chromatography. (Silica gel, Ethyl acetate,), followed by recrystallization with chloroform. (0.07 g, 26.92%).

^1H NMR (500 MHz, CDCl_3): 8.86-8.85 (d, 1H, $J=8$ Hz), 8.76 (s, 1H), 8.15-8.14 (d, 1H, $J=8$ Hz), 8.08-8.07 (d, 1H, $J=8.5$ Hz), 7.66-7.65 (d, 1H, $J=7.5$ Hz), 7.59-7.51 (m, 5H), 7.47-7.44 (dd, 1H, $J=6.5$ Hz), 7.11-7.09 (d, 1H, $J=8$ Hz), 6.49 (s, 1H), 4.51-4.46 (q, 2H), 3.17 (s, 6H), 1.56-1.53 (t, 3H); ^{13}C NMR (125 MHz, CDCl_3): δ 187.8, 172.5, 152.3, 143.3, 132.1, 127.8, 122.9, 113.6, 57.5, 46.2, 16;

HRMS–EI: Calculated molecular weight for C₃₀H₂₄N₂O₂S is 476.5888, found = 476.1574.

5 General procedures for the synthesis of ABSQ–F, ABSQ–Cl and ABSQ–Br

A suspension of 3-(4-(dimethylamino) anthracen-1-yl)-4-hydroxycyclobut-3-ene-1, 2-dione (1 equivalent), and 3-ethyl-2-methylbenzo[d]thiazol-3-ium (1 equivalent) was dissolved in a required amount 1:1 benzene: butanol azeotropic mixture, to that 1 or 2 drops of quinoline was added and refluxed at 90° C in a Dean–Stark apparatus for about 8 h. After the reaction, the mixture was allowed to cool to room temperature and the solvent was vacuum eliminated. Then the residue was purified by column chromatography. (Silica gel, Ethyl acetate) followed by recrystallization with chloroform.

5.1 Characterization details of ABSQ–F [(Z)-2-(4-(dimethylamino) anthracen-1-yl)-4-((3-ethyl-5- fluorobenzo[d]thiazol-3-ium-2-yl) methylene)-3-oxocyclobut-1-enolate]

¹H NMR (500 MHz, CDCl₃): δ 8.96-8.94 (d, 1H, *J* = 8Hz), 8.65 (s, 1H), 8.24-7.67 (m, 4H), 7.66-7.65 (d, 2H, *J* = 7.5 Hz), 7.52 (s, 1H), 7.49-7.46 (d, 2H, *J* = 7.5 Hz), 6.43 (s, 1H), 4.37-4.35 (q, 2H), 3.12 (s, 6H), 1.55-1.52 (t, 3H); ¹³C NMR (125 MHz, CDCl₃): δ 188.5, 173, 162.9, 152.6, 145.6, 131.3, 127.3, 122.5, 114, 56.7, 45.8, 17; HRMS–EI: Calculated molecular weight for C₃₀H₂₃FN₂O₂S is 494.5792, found = 494.1397.

5.2 Characterization details of ABSQ–Cl [(Z)-4-((5-chloro-3-ethylbenzo[d]thiazol-3-ium-2-yl) methylene)-2-(4-(dimethylamino) anthracen-1-yl)-3-oxocyclobut-1-enolate]

¹H NMR (500 MHz, CDCl₃): δ 8.92-8.90 (d, 1H, *J* = 8Hz), 8.63 (s, 1H), 7.48-7.47 (m, 4H), 7.22-7.21 (d, 2H, *J* = 7.5 Hz), 7.20 (s, 1H), 6.96-6.95 (d, 2H, *J* = 7.5 Hz), 6.41 (s, 1H), 4.33-4.28 (q, 2H), 3.12 (s, 6H), 1.51-1.48 (t, 3H); ¹³C NMR (125 MHz, CDCl₃): δ 191.1, 187.6, 172.5, 134.3, 131.1, 128.1, 123.6, 113, 57.5, 46.2, 15.9;

HRMS–EI: Calculated molecular weight for C₃₀H₂₃ClN₂O₂S is 511.0338, found = 510.1101.

5.3 Characterization details of ABSQ–Br [(Z)-4-((5-bromo-3-ethylbenzo[d]thiazol-3-ium-2-yl) methylene)-2-(4-(dimethylamino) anthracen-1-yl)-3-oxocyclobut-1-enolate]

¹H NMR (500 MHz, CDCl₃): δ 8.94-8.92 (d, 1H, *J* = 8Hz), 8.64 (s, 1H), 8.24-7.99 (m, 4H), 7.52-7.51 (d, 2H, *J* = 7.5 Hz), 7.50 (s, 1H), 7.40-7.38 (d, 2H, *J* = 7.5 Hz), 6.41 (s, 1H), 4.33-4.31 (q, 2H), 3.12 (s, 6H), 1.52-1.49 (t, 3H); ¹³C NMR (125 MHz, CDCl₃): δ 192, 188.5, 179, 131.6, 128.9, 125.6, 112.5, 56.8, 46.1, 14.9; HRMS–EI: Calculated molecular weight for C₃₀H₂₃BrN₂O₂S is 555.4848, found = 556.0659.

3.9 References

1. Aumaitre, C.; Rodriguez-Seco, C.; Jover, J.; Bardagot, O.; Caffy, F.; Kervella, Y.; López, N.; Palomares, E.; Demadrille, R., Visible and near-Infrared Organic Photosensitizers Comprising Isoindigo Derivatives as Chromophores: Synthesis, Optoelectronic Properties and Factors Limiting Their Efficiency in Dye Solar Cells. *J. Mater. Chem. A* **2018**, *6*, 10074-10084.
2. Sharma, V.; Kovida; Sahoo, D.; Varghese, N.; Mohanta, K.; Koner, A. L., Synthesis and Photovoltaic Application of Nir-Emitting Perylene-Monoimide Dyes with Large Stokes-Shift. *RSC Adv.* **2019**, *9*, 30448-30452.
3. Kim, S.; Mor, G. K.; Paulose, M.; Varghese, O. K.; Baik, C.; Grimes, C. A., Molecular Design of near-Ir Harvesting Unsymmetrical Squaraine Dyes. *Langmuir* **2010**, *26*, 13486-13492.
4. Mayerhöffer, U.; Gsänger, M.; Stolte, M.; Fimmel, B.; Würthner, F., Synthesis and Molecular Properties of Acceptor-Substituted Squaraine Dyes. *Chem. Eur. J.* **2013**, *19*, 218-232.
5. Chen, G.; Sasabe, H.; Igarashi, T.; Hong, Z.; Kido, J., Squaraine Dyes for Organic Photovoltaic Cells. *J. Mater. Chem. A* **2015**, *3*, 14517-14534.
6. Strassel, K., et al., Squaraine Dye for a Visibly Transparent All-Organic Optical Upconversion Device with Sensitivity at 1000 Nm. *ACS Appl. Mater. Interfaces* **2018**, *10*, 11063-11069.
7. Kim, J. H.; Liess, A.; Stolte, M.; Krause, A.-M.; Stepanenko, V.; Zhong, C.; Bialas, D.; Spano, F.; Würthner, F., An Efficient Narrowband near-Infrared at 1040 nm Organic Photodetector Realized by Intermolecular Charge Transfer Mediated Coupling Based on a Squaraine Dye. *Adv. Mater.* **2021**, *33*, 2100582.
8. Law, K. Y., Squaraine Chemistry: Effects of Structural Changes on the Absorption and Multiple Fluorescence Emission of Bis[4-(Dimethylamino)Phenyl]Squaraine and Its Derivatives. *J Phys Chem* **1987**, *91*, 5184-5193.

9. Khopkar, S.; Shankarling, G., Synthesis, Photophysical Properties and Applications of NIR Absorbing Unsymmetrical Squaraines: A Review. *Dyes Pigm.* **2019**, *170*, 107645.
10. Yang, D.; Yang, Q.; Yang, L.; Luo, Q.; Huang, Y.; Lu, Z.; Zhao, S., Novel High Performance Asymmetrical Squaraines for Small Molecule Organic Solar Cells with a High Open Circuit Voltage of 1.12 V. *ChemComm* **2013**, *49*, 10465-10467.
11. Alex, S.; Santhosh, U.; Das, S., Dye Sensitization of Nanocrystalline TiO₂: Enhanced Efficiency of Unsymmetrical Versus Symmetrical Squaraine Dyes. *J. Photochem. Photobiol. A* **2005**, *172*, 63-71.
12. Chen, Y.; Zhu, W.; Wu, J.; Huang, Y.; Facchetti, A.; Marks, T. J., Recent Advances in Squaraine Dyes for Bulk-Heterojunction Organic Solar Cells. *Org. Photonics Photovolt.* **2019**, *6*, 1-16.
13. Kublitski, J.; Fischer, A.; Xing, S.; Baisinger, L.; Bittrich, E.; Spoltore, D.; Benduhn, J.; Vandewal, K.; Leo, K., Enhancing Sub-Bandgap External Quantum Efficiency by Photomultiplication for Narrowband Organic near-Infrared Photodetectors. *Nat. Commun.* **2021**, *12*, 4259.
14. Maeda, T.; Nguyen, T. V.; Kuwano, Y.; Chen, X.; Miyanaga, K.; Nakazumi, H.; Yagi, S.; Soman, S.; Ajayaghosh, A., Intramolecular Exciton-Coupled Squaraine Dyes for Dye-Sensitized Solar Cells. *J. Phys. Chem. C* **2018**, *122*, 21745-21754.
15. Singh, A. K.; Veetil, A. N.; Nithyanandhan, J., D-a-D Based Complementary Unsymmetrical Squaraine Dyes for Co-Sensitized Solar Cells: Enhanced Photocurrent Generation and Suppressed Charge Recombination Processes by Controlled Aggregation. *ACS Appl. Energy Mater.* **2021**, *4*, 3182-3193.
16. Rao, G. H.; Rana, P. J. S.; Islam, A.; Singh, S. P., Synthesis of Multichromophoric Asymmetrical Squaraine Sensitizer Via C-H Arylation for See-through Photovoltaic. *ACS Appl. Energy Mater.* **2018**, *1*, 4786-4793.
17. Corredor, C. C.; Huang, Z.-L.; Belfield, K. D., Two-Photon 3d Optical Data Storage Via Fluorescence Modulation of an Efficient Fluorene Dye by a Photochromic Diarylethene. *Adv. Mater.* **2006**, *18*, 2910-2914.
18. Sun, C.-L.; Lv, S.-K.; Liu, Y.-P.; Liao, Q.; Zhang, H.-L.; Fu, H.; Yao, J., Benzoindolic Squaraine Dyes with a Large Two-Photon Absorption Cross-Section. *J. Mater. Chem. C* **2017**, *5*, 1224-1230.
19. Chen, C.; Dong, H.; Chen, Y.; Guo, L.; Wang, Z.; Sun, J.-J.; Fu, N., Dual-Mode Unsymmetrical Squaraine-Based Sensor for Selective Detection of Hg²⁺ in Aqueous Media. *Org. Biomol. Chem.* **2011**, *9*, 8195-8201.
20. Butnarusu, C.; Barbero, N.; Barolo, C.; Visentin, S., Squaraine Dyes as Fluorescent Turn-on Sensors for the Detection of Porcine Gastric Mucin: A Spectroscopic and Kinetic Study. *J. Photochem. Photobiol. B, Biol.* **2020**, *205*, 111838.
21. Saneesh Babu, P. S., et al., Bis(3,5-Diiodo-2,4,6-Trihydroxyphenyl)Squaraine Photodynamic Therapy Disrupts Redox Homeostasis and Induce Mitochondria-Mediated

- Apoptosis in Human Breast Cancer Cells. *Sci. Rep.* **2017**, *7*, 42126.
22. Somashekharappa, G. M.; Govind, C.; Pulikodan, V.; Paul, M.; Namboothiry, M. A. G.; Das, S.; Karunakaran, V., Unsymmetrical Squaraine Dye-Based Organic Photodetector Exhibiting Enhanced near-Infrared Sensitivity. *J. Phys. Chem. C* **2020**, *124*, 21730-21739.
23. de Miguel, G.; Marchena, M.; Ziółek, M.; Pandey, S. S.; Hayase, S.; Douhal, A., Femto-to Millisecond Photophysical Characterization of Indole-Based Squaraines Adsorbed on TiO₂ Nanoparticle Thin Films. *J. Phys. Chem. C* **2012**, *116*, 12137-12148.
24. Rana, A.; Sharma, C.; Prabhu, D. D.; Kumar, M.; Karuvath, Y.; Das, S.; Chand, S.; Singh, R. K., Revealing Charge Carrier Dynamics in Squaraine:[6, 6]-Phenyl-C 71-Butyric Acid Methyl Ester Based Organic Solar Cells. *AIP Adv.* **2018**, *8*, 045302.
25. Singh, A. K.; Mele Kavungathodi, M. F.; Nithyanandhan, J., Alkyl-Group-Wrapped Unsymmetrical Squaraine Dyes for Dye-Sensitized Solar Cells: Branched Alkyl Chains Modulate the Aggregation of Dyes and Charge Recombination Processes. *ACS Appl. Energy Mater.* **2020**, *12*, 2555-2565.
26. Lambert, C.; Koch, F.; Völker, S. F.; Schmiedel, A.; Holzapfel, M.; Humeniuk, A.; Röhr, M. I. S.; Mitric, R.; Brixner, T., Energy Transfer between Squaraine Polymer Sections: From Helix to Zigzag and All the Way Back. *J. Am. Chem. Soc.* **2015**, *137*, 7851-7861.
27. Auerhammer, N.; Schmiedel, A.; Holzapfel, M.; Lambert, C., Exciton Coupling Enhancement in the Relaxed Excited State. *J. Phys. Chem. C* **2018**, *122*, 11720-11729.
28. Schreck, M. H.; Breitschwerdt, L.; Marciniak, H.; Holzapfel, M.; Schmidt, D.; Würthner, F.; Lambert, C., Fs–Ps Exciton Dynamics in a Stretched Tetraphenylsquaraine Polymer. *Phys. Chem. Chem. Phys.* **2019**, *21*, 15346-15355.
29. Marciniak, H.; Auerhammer, N.; Ricker, S.; Schmiedel, A.; Holzapfel, M.; Lambert, C., Reduction of the Fluorescence Transition Dipole Moment by Excitation Localization in a Vibronically Coupled Squaraine Dimer. *J. Phys. Chem. C* **2019**, *123*, 3426-3432.
30. Lambert, C.; Hoche, J.; Schreck, M. H.; Holzapfel, M.; Schmiedel, A.; Selby, J.; Turkin, A.; Mitric, R., Ultrafast Energy Transfer Dynamics in a Squaraine Heterotriad. *J. Phys. Chem. A* **2021**, *125*, 2504-2511.
31. Mayerhöffer, U.; Fimmel, B.; Würthner, F., Bright near-Infrared Fluorophores Based on Squaraines by Unexpected Halogen Effects. *Angew. Chem. Int. Ed.* **2012**, *51*, 164-167.
32. Khan, R.; Ningombam, A.; Singh, K.; Singh, M., Stereoelectronic Effects in the Stereoselectivity of the Diels–Alder Reactions: Reactions of Aminoanthracenes with N-Phenylmaleimide. *J. Chem. Pharm. Res.* **2012**, *4*, 1532-1538.
33. Tatars, A.; Fedyunyaeva, I.; Terpetschnig, E.; Patsenker, L., Synthesis of Novel Squaraine Dyes and Their Intermediates. *Dyes Pigm.* **2005**, *64*, 125-134.
34. Inoue, T.; Pandey, S. S.; Fujikawa, N.; Yamaguchi, Y.; Hayase, S., Synthesis and Characterization of Squaric Acid Based Nir Dyes for Their Application Towards Dye-Sensitized

Solar Cells. *J. Photochem. Photobiol. A* **2010**, *213*, 23-29.

35. Yum, J.-H.; Walter, P.; Huber, S.; Rentsch, D.; Geiger, T.; Nüesch, F.; De Angelis, F.; Grätzel, M.; Nazeeruddin, M. K., Efficient Far Red Sensitization of Nanocrystalline TiO₂ Films by an Unsymmetrical Squaraine Dye. *J. Am. Chem. Soc.* **2007**, *129*, 10320-10321.

36. So, S.; Choi, H.; Kim, C.; Cho, N.; Ko, H. M.; Lee, J. K.; Ko, J., Novel Symmetric Squaraine Chromophore Containing Triphenylamine for Solution Processed Small Molecule Bulk Heterojunction Solar Cells. *Sol. Energy Mater. Sol. Cells* **2011**, *95*, 3433-3441.

37. Della Pelle, A. M.; Homnick, P. J.; Bae, Y.; Lahti, P. M.; Thayumanavan, S., Effect of Substituents on Optical Properties and Charge-Carrier Polarity of Squaraine Dyes. *J. Phys. Chem. C* **2014**, *118*, 1793-1799.

38. Park, J., et al., Symmetric Vs. Asymmetric Squaraines as Photosensitisers in Mesoscopic Injection Solar Cells: A Structure-Property Relationship Study. *ChemComm* **2012**, *48*, 2782-2784.

39. Kabatc, J.; Kostrzewska, K.; Kozak, M.; Balcerak, A., Visible Light Photoinitiating Systems Based on Squaraine Dye: Kinetic, Mechanistic and Laser Flash Photolysis Studies. *RSC Adv.* **2016**, *6*, 103851-103863.

40. Liu, T.; Bondar, M. V.; Belfield, K. D.; Anderson, D.; Masunov, A. E.; Hagan, D. J.; Stryland, E. W. V., Linear Photophysics and Femtosecond Nonlinear Spectroscopy of a Star-Shaped Squaraine Derivative with Efficient Two-Photon Absorption. *J. Phys. Chem. C* **2016**, *120*, 11099-11110.

41. Belfield, K. D.; Bondar, M. V.; Haniff, H. S.; Mikhailov, I. A.; Luchita, G.; Przhonska, O. V., Superfluorescent Squaraine with Efficient Two-Photon Absorption and High Photostability. *ChemPhysChem* **2013**, *14*, 3532-3542.

42. Webster, S., et al., Near-Unity Quantum Yields for Intersystem Crossing and Singlet Oxygen Generation in Polymethine-Like Molecules: Design and Experimental Realization. *J. Phys. Chem. Lett.* **2010**, *1*, 2354-2360.

43. Lambert, C.; Scherpf, T.; Ceymann, H.; Schmiedel, A.; Holzappel, M., Coupled Oscillators for Tuning Fluorescence Properties of Squaraine Dyes. *J. Am. Chem. Soc.* **2015**, *137*, 3547-3557.

44. Chang, H.-J.; Bondar, M. V.; Liu, T.; Liu, X.; Singh, S.; Belfield, K. D.; Sheely, A.; Masunov, A. E.; Hagan, D. J.; Van Stryland, E. W., Electronic Nature of Neutral and Charged Two-Photon Absorbing Squaraines for Fluorescence Bioimaging Application. *ACS Omega* **2019**, *4*, 14669-14679.

45. Martin, M. M.; Plaza, P.; Changenet-Barret, P.; Siemiarczuk, A., Uv Vis Subpicosecond Spectroscopy of 4-(9-Anthryl)-N,N -Dimethylaniline in Polar and Nonpolar Solvents: A Two-Dimensional View of the Photodynamic“. *J. Phys. Chem. A* **2002**, *106*, 2351-2358.

46. Mohammed, O. F.; Vauthey, E., Excited-State Dynamics of Nitroperylene in Solution: Solvent and Excitation Wavelength Dependence. *J. Phys. Chem. A* **2008**, *112*, 3823-3830.

47. Eom, I.; Joo, T., Polar Solvation Dynamics of Coumarin 153 by Ultrafast Time-Resolved

- Fluorescence. *J. Chem. Phys.* **2009**, *131*, 244507.
48. Kuang, Z.; He, G.; Song, H.; Wang, X.; Hu, Z.; Sun, H.; Wan, Y.; Guo, Q.; Xia, A., Conformational Relaxation and Thermally Activated Delayed Fluorescence in Anthraquinone-Based Intramolecular Charge-Transfer Compound. *J. Phys. Chem. C* **2018**, *122*, 3727-3737.
49. Sauve, G.; Kamat, P. V.; Thomas, K. G.; Thomas, K. J.; Das, S.; George, M. V., Photochemistry of Squaraine Dyes: Excited Triplet State and Redox Properties of Crown Ether Squaraines. *J. Phys. Chem.* **1996**, *100*, 2117-2124.
50. Marchena, M.; de Miguel Rojas, G.; Cohen, B.; Organero, J.; Pandey, S.; Hayase, S.; Douhal, A., Real-Time Photodynamics of Squaraine-Based Dye-Sensitized Solar Cells with Iodide and Cobalt Electrolytes. *J. Phys. Chem. C* **2013**, *117*, 11906-11919.
51. Snellenburg, J.; Laptinok, S.; Seger, R.; Mullen, K.; Van Stokkum, I., Glotaran: A Java-Based Graphical User Interface for the R Package Timp. *J. Stat. Softw.* **2012**, *49*, 1-22.
52. Horng, M. L.; Gardecki, J. A.; Papazyan, A.; Maroncelli, M., Subpicosecond Measurements of Polar Solvation Dynamics: Coumarin 153 Revisited. *J Phys Chem* **1995**, *99*, 17311-17337.
53. Neelambra, A. U.; Govind, C.; Devassia, T. T.; Somashekharappa, G. M.; Karunakaran, V., Direct Evidence of Solvent Polarity Governing the Intramolecular Charge and Energy Transfer: Ultrafast Relaxation Dynamics of Push–Pull Fluorene Derivatives. *Phys. Chem. Chem. Phys.* **2019**, *21*, 11087-11102.
54. Zhu, H.; Li, M.; Hu, J.; Wang, X.; Jie, J.; Guo, Q.; Chen, C.; Xia, A., Ultrafast Investigation of Intramolecular Charge Transfer and Solvation Dynamics of Tetrahydro[5]-Helicene-Based Imide Derivatives. *Sci. Rep.* **2016**, *6*, 24313.
55. Lee, S.; Lee, M.; An, J.; Ahme, H.; Im, C., Exciton Dynamics of P3ht:Pcbm Blend Films with Different Polymer Regioregularities Using Transient Absorption Spectroscopy. *Mol. Cryst. Liq. Cryst.* **2013**, *578*, 68-72.
56. Williams, R. M.; Vãn Anh, N.; van Stokkum, I. H. M., Triplet Formation by Charge Recombination in Thin Film Blends of Perylene Red and Pyrene: Developing a Target Model for the Photophysics of Organic Photovoltaic Materials. *J. Phys. Chem. B* **2013**, *117*, 11239-11248.
57. Ghosh, A.; Ghosh, S.; Ghosh, G.; Jana, B.; Patra, A., Revealing Complex Relaxation Processes of Collapsed Conjugated Polymer Nanoparticles in the Presence of Different Shapes of Gold Nanoparticles Using Global and Target Analysis. *J. Phys. Chem. C* **2020**, *124*, 26165-26173.
58. Lee, D., et al., Intrachain Delocalization Effect of Charge Carriers on the Charge-Transfer State Dynamics in Organic Solar Cells. *J. Phys. Chem. C* **2022**, *126*, 3171-3179.
59. van Stokkum, I. H. M.; Beekman, L. M. P.; Jones, M. R.; van Brederode, M. E.; van Grondelle, R., Primary Electron Transfer Kinetics in Membrane-Bound Rhodospirillum rubrum Reaction Centers: A Global and Target Analysis. *Biochemistry* **1997**, *36*, 11360-11368.
60. Karunakaran, V.; Pérez Lustres, J. L.; Zhao, L.; Ernstring, N. P.; Seitz, O., Large Dynamic Stokes Shift of DNA Intercalation Dye Thiazole Orange Has Contribution from a High-Frequency

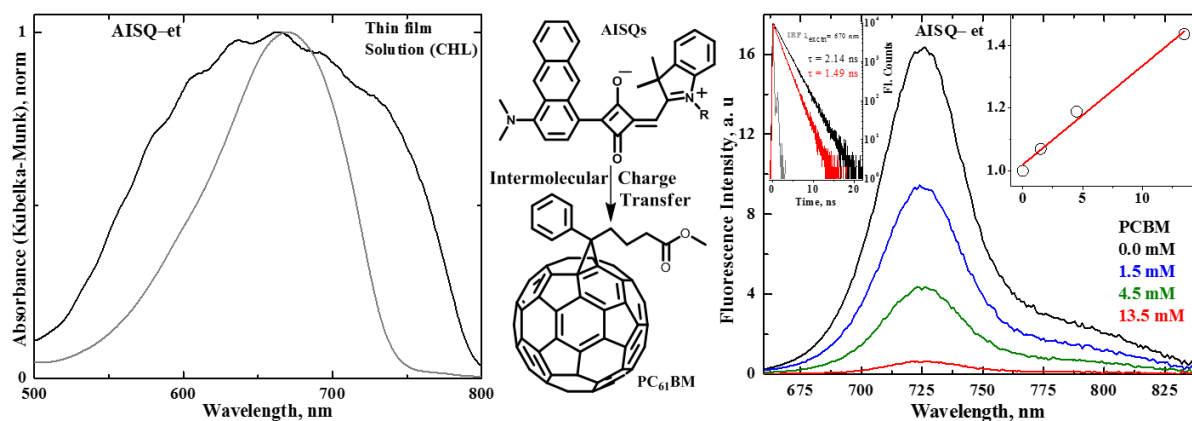
Mode. *J. Am. Chem. Soc.* **2006**, *128*, 2954-2962.

61. Guldi, D. M.; Prato, M., Excited-State Properties of C60 Fullerene Derivatives. *Acc. Chem. Res.* **2000**, *33*, 695-703.

62. Yamamoto, S.; Guo, J.; Ohkita, H.; Ito, S., Formation of Methanofullerene Cation in Bulk Heterojunction Polymer Solar Cells Studied by Transient Absorption Spectroscopy. *Adv. Funct. Mater.* **2008**, *18*, 2555-2562.

63. Armarego, W. L. F., Chapter 3 - Purification of Organic Chemicals. In *Purification of Laboratory Chemicals (Eighth Edition)*, Armarego, W. L. F., Ed. Butterworth-Heinemann: 2017; pp 95-634.

Excited State Relaxation Dynamics of Indolium–Based Unsymmetrical Squaraine Derivatives



4.1 Abstract

The distinctive optical features of symmetrical SQs exhibiting strong NIR absorption and emission are extensively used as a sensitizer for optoelectronic devices. However, the usage of USQ dyes towards OPDs are limited. In this connection, the USQ derivatives comprising of *N,N*-dimethyl aminoanthracene and various *N*-alkylated indolium [ethyl (AISQ-*et*), hexyl (AISQ-*hex*) and hexenyl (AISQ-*hexen*)] were synthesized and their steady and excited state relaxation dynamics were investigated. The absorption spectra of the AISQ-*et* exhibited an intense absorption maximum at ~ 676 nm in toluene with a high extinction coefficient, $\sim 8.0 \times 10^4 \text{ M}^{-1}\text{cm}^{-1}$. The absorption spectra showed a negative solvatochromic shift with an increase of solvent polarity. When compared to the neat solvents, the absorption spectra in the thin film exhibited broad in nature, covering a wide range of wavelength starting from 500–800 nm due to the formation of aggregations. Such a wide range

of wavelengths with high extinction coefficient will be significantly beneficial for optoelectronic devices. The femtosecond transient absorption spectra of AISQ derivatives were measured in nonpolar (toluene) and polar (acetonitrile, ACN) solvents upon excitation at 600 nm using femtosecond pump–probe spectroscopy. It revealed that the polarity of the solvent controlled the excited state relaxation dynamics. The observation of quenching of fluorescence intensity and fluorescence lifetime upon the addition of PCBM reflected the occurrence of intermolecular charge–transfer dynamics between the AISQs and PCBM. The AISQ–et derivative was applied to the PD devices and showed sensitivity in the NIR region.

4.2 Introduction

The development of organic chromophores that enables the efficient conversion of light in the NIR region is of great attention devoted to the design and synthesis of various functional dyes such as porphyrin,¹⁻² phthalocyanine,³ perylene⁴⁻⁵ and SQs.⁶⁻⁷ Among these, USQ dyes have been successfully employed as sensitizers in optical data storage,⁸ two–photon absorption,⁹ fluorescent probes in bio labeling,¹⁰⁻¹¹ photodynamic therapy¹² and solar cells applications.¹³⁻¹⁴ However, in the BHJ–based and OPD devices using PCBM as an electron acceptor, the understanding of the charge carrier dynamics which is an important tool to enhance the efficiency and stability of the devices Though a large number of steady–state and time–resolved photophysical properties of SQs were widely reported¹⁵⁻²³ the intermolecular interaction dynamics of USQ derivatives with PCBM have not been investigated in detail. Indeed, the structure–property relationship of the sensitizers plays a significant role in designing suitable materials for optoelectronic devices. In this connection, Rana et al.¹⁷ investigated the charge carrier and polaron dynamics for the SQs and SQs:PC₇₁BM using ultrafast transient absorption spectroscopy resulting in the formation of polaron with a lifetime

of 550 ps leads to create the free electrons in the solar cell. Huang et al.²⁴ successfully fabricated BHJ solar cells by incorporating SQs in P₃HT:PC₆₁BM blend to improve the photon absorption range to NIR region and exciton harvesting. The femtosecond transient absorption studies revealed the highly efficient excitation energy from P₃HT to SQs occurring on a picosecond time scale by Förster resonance energy transfer (FRET). Their results opened a new paradigm for improving efficient polymer solar cells. Paterno et al.²⁵ reported novel indoline-based SQs, with dicyanovinylene core substituted and unsubstituted dyes. Their spectroscopic investigation suggested the deactivation pattern involving a dark state for the unsubstituted dyes and the lack of such a deactivation pathway in the core substituted dyes. These findings would be beneficial in minimizing the deactivation losses and thereby enhancing the efficiency of SQs-based optoelectronic devices. Here the USQ derivatives (**AISQs**) consisting of *N,N*-dimethyl aminoanthracene and *N*-alkylated indolium to [ethyl-(**AISQ-et**); hexyl-(**AISQ-hex**) and hexenyl-(**AISQ-hexen**)] were synthesized. The steady-state and time-resolved photophysical characterization of **AISQ** derivatives were carried out to understand the effect of solvents (toluene and ACN) on the excited state relaxation dynamics. The fluorescence spectra and lifetime measurements of **AISQs** with PCBM deduce the occurrence of intermolecular charge transfer via a dynamic quenching mechanism in the excited state deactivation.

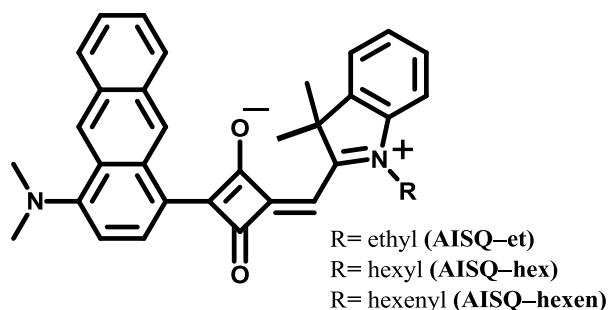
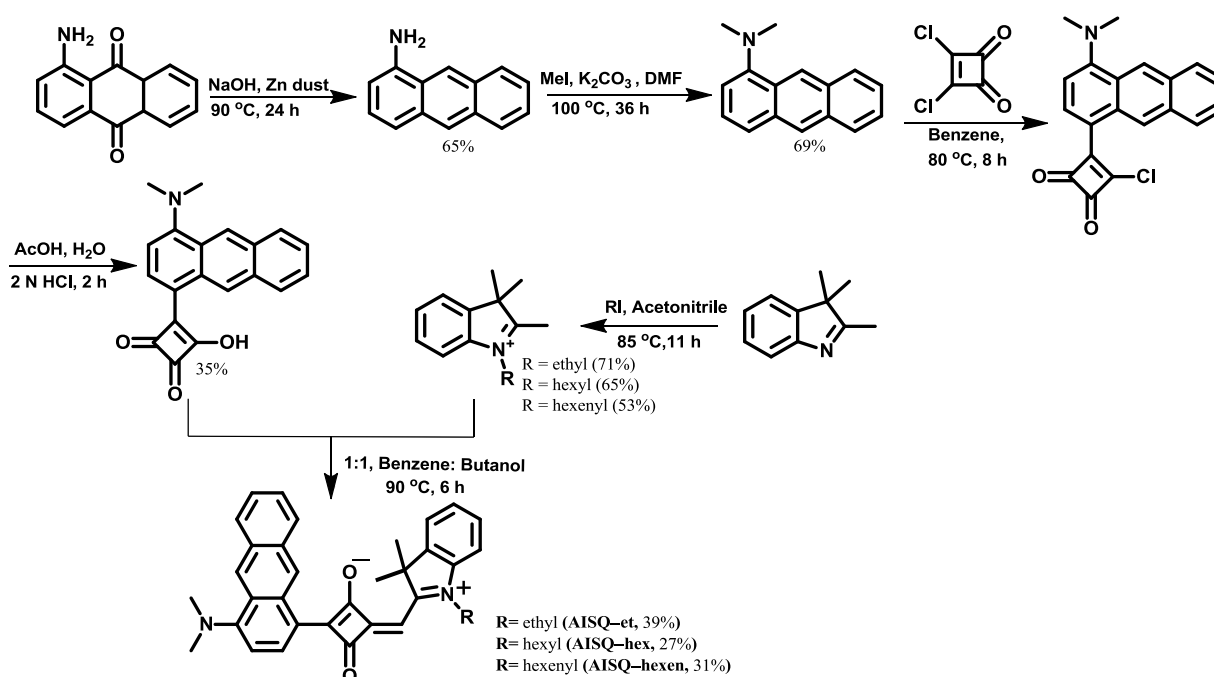


Figure 4.1 Chemical structure of **AISQ** derivatives.

4.3 Results and Discussion

4.3.1 Synthesis of AISQ Derivatives

The AISQ derivatives (**Figure 4.1**) were synthesized by modifying the previously reported procedures.²⁶⁻²⁸ The *N,N*-dimethyl aminoanthracene semisquaraine was obtained by reducing and methylation of 1-aminoanthroquinone and resulted *N,N*-dimethyl aminoanthracene treated with squarylium chloride. The indolium quaternization was generally performed with an excess alkylating agent in polar solvent. Then the alkyl and alkenylated indolium salt was refluxed with the *N,N*-dimethyl aminoanthracene semisquaraine in benzene: butanol azeotropic mixture (1:1), yielding the corresponding AISQ derivatives (**Scheme 4.1**). The structure of the compounds was characterized by NMR spectroscopy and HRMS.



Scheme 4.1 Synthetic Scheme of AISQ Derivatives.

4.3.2 Steady-State Photophysical Characterization

4.3.2.1 Solution state

The steady-state absorption and emission spectra of **AISQ-et**, **AISQ-hex** and **AISQ-hexen** were measured with an increase of solvent polarity and shown in **Figure 4.2–4.4** respectively. The **AISQ-et**, **AISQ-hex** and **AISQ-hexen** showed intense absorption maximum at ~ 676, 668 and 670 nm in toluene with the molar extinction coefficient of ~8.00, 9.05 and $7.50 \times 10^4 \text{ M}^{-1} \text{ cm}^{-1}$ respectively. The intense absorption is due to combined π - π^* transition with intramolecular charge transfer from *N,N*-dimethyl aminoanthracene and indolium donors to the central squaraine core.²⁹⁻³¹ The **AISQ** derivatives having such high extinction coefficient will be used as an effective sensitizer in the form of thinner photoactive film in the optoelectronic devices.³² Upon increasing the polarity of solvent (acetonitrile, ACN), the absorption maximum shifted to the blue region (~46 nm), hypsochromic shift, indicating more polarity of ground state compared to the excited state.³³ Upon increasing the alkyl chain length, the absorption maximum shifted to blue side (~8 nm) compared to **AISQ-et**. The fluorescence spectra of **AISQ-et**, **AISQ-hex** and **AISQ-hexen** in toluene showed a maximum at ~726, 732 and 734 nm with Stokes shift of ~1018, 1308 and 1301 cm^{-1} respectively and showed red shift with the increase of polarity of the solvent.

The fluorescence dynamics of **AISQ** derivatives were recorded in various solvents upon excitation at 670 nm and decay profiles are shown in **Figure 4.5**. The fluorescence lifetime (τ_f) of **AISQ-et**, **AISQ-hex** and **AISQ-hexen** in toluene was found to be around $\sim 2.14 \pm 0.25$, 2.07 ± 0.20 and 2.06 ± 0.25 ns respectively. With an increase of solvent polarity, it is decreased to $\sim 0.34 \pm 0.20$, 0.36 ± 0.20 and 0.58 ± 0.20 ns in acetonitrile. Such observations reveal the involvement of a non-radiative pathway sensitive to the electronic redistribution in the excited **AISQ** derivatives and/or formation of the solute-solvent complexes by shortening the

fluorescence lifetimes with an increase of solvent polarity.³⁴ The details of the absorption and emission maxima, Stokes shift, fluorescence lifetime and absolute quantum yield of AISQ-*et*, AISQ-*hex* and AISQ-*hexen* are given in Table 4.1–4.3 respectively. The radiative and non-radiative rate constants were also calculated from fluorescence quantum yield (Φ) and lifetime (τ_f) using the equations 1 provided in chapter 2.

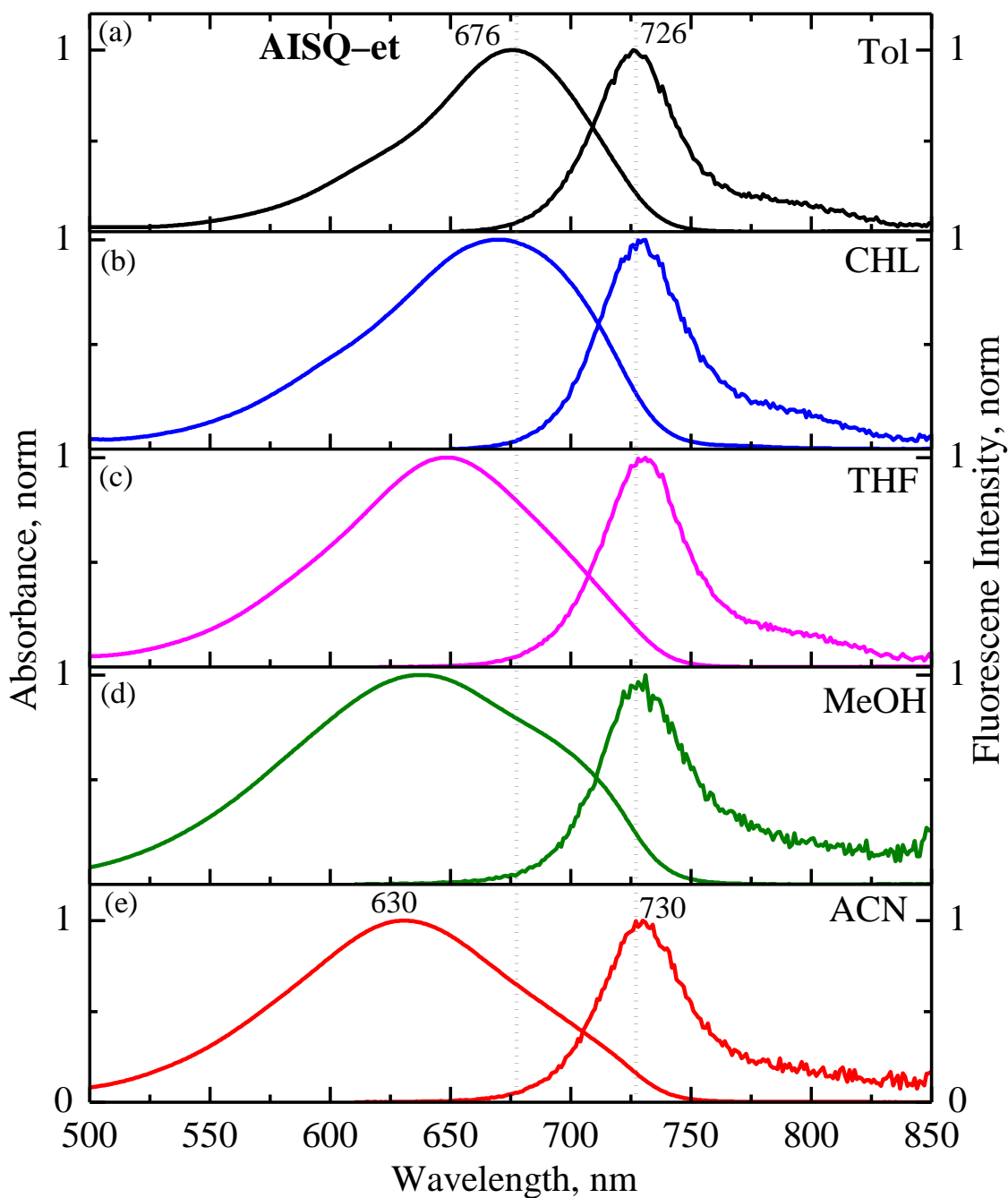


Figure 4.2 Steady-state absorption and emission spectra of AISQ-*et* in solvents of various polarities at room temperature.

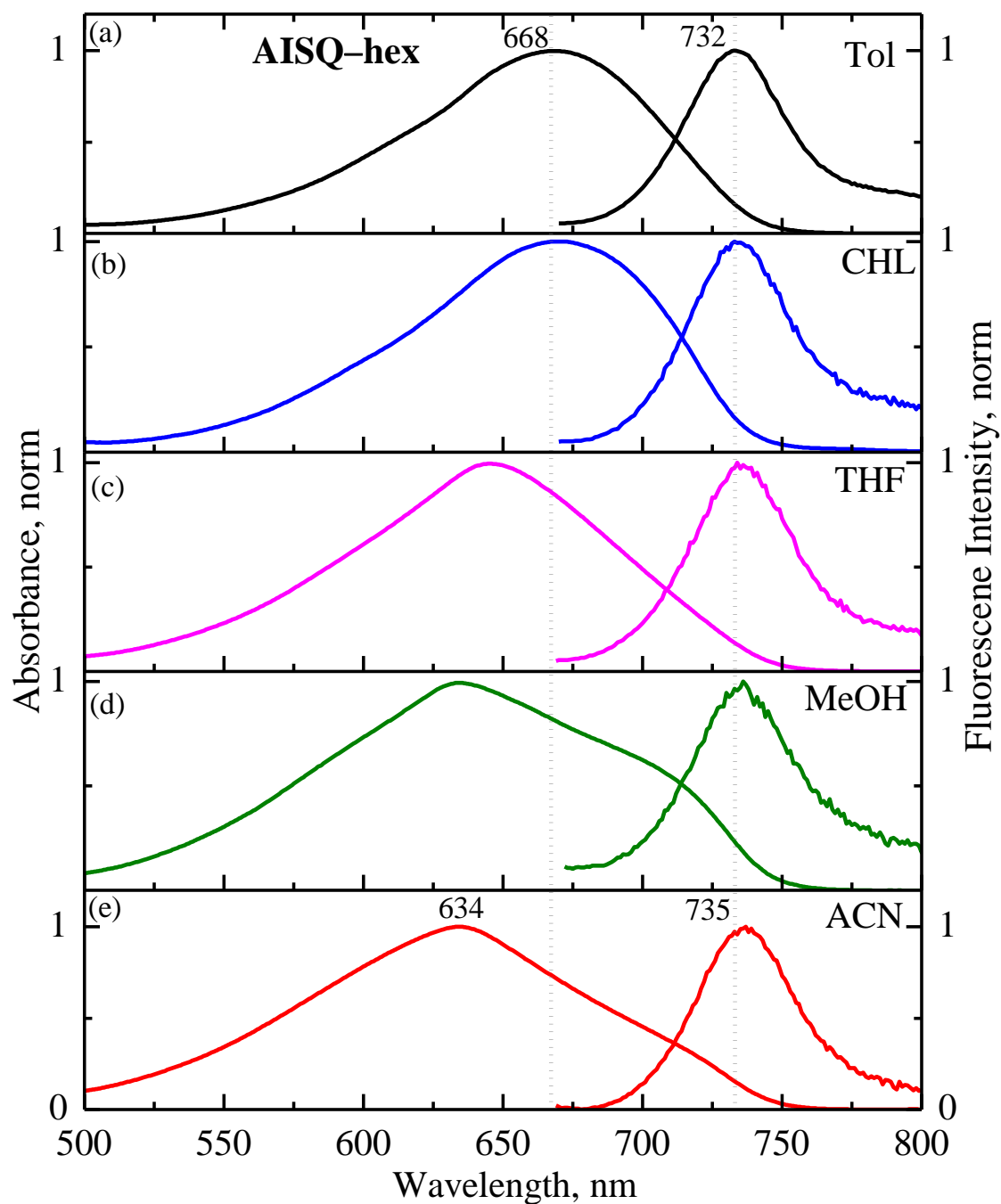


Figure 4.3 Steady-state absorption and emission spectra of **AISQ-hex** in solvents of various polarities at room temperature.

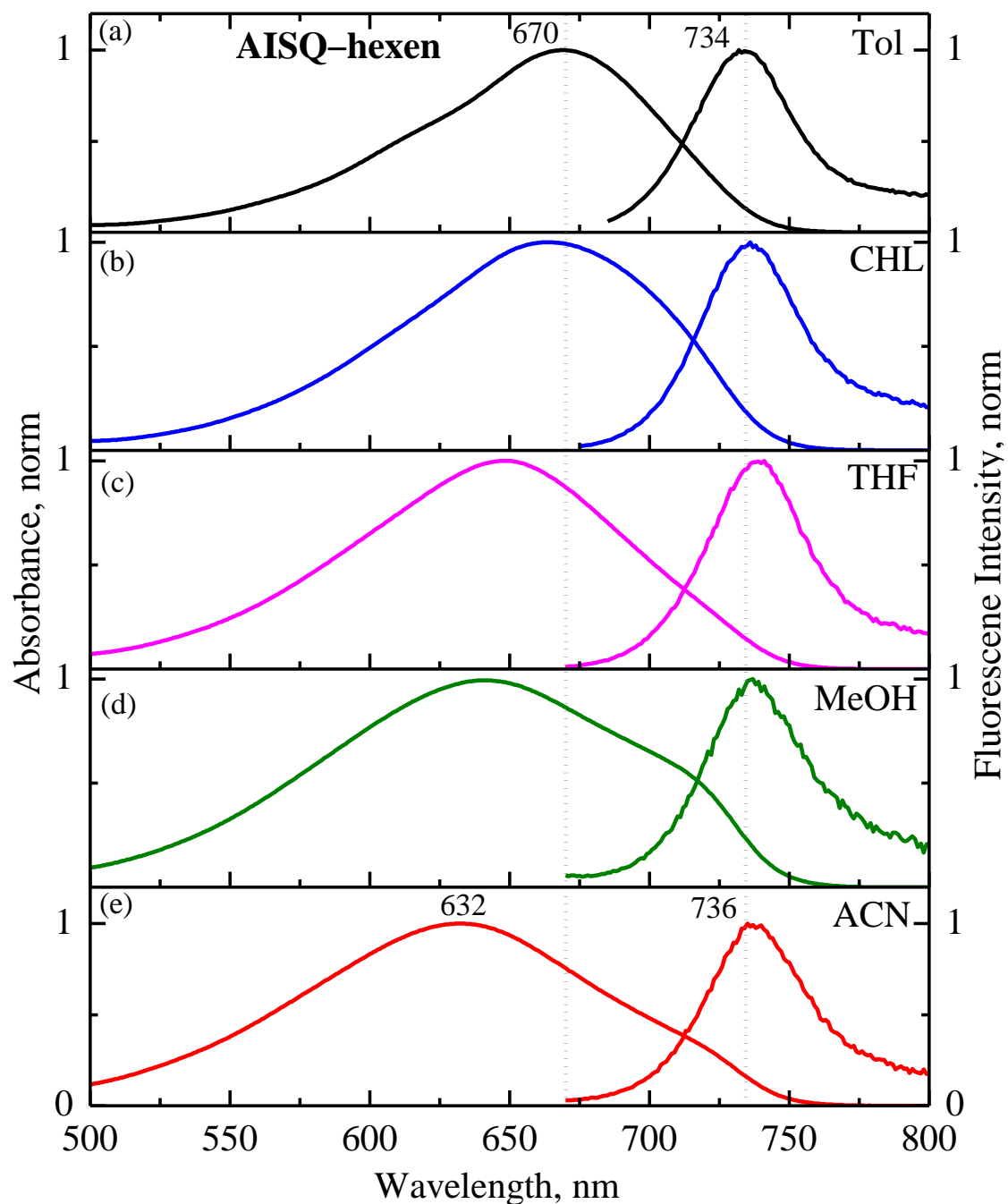


Figure 4.4 Steady-state absorption and emission spectra of AISQ-hexen in solvents of various polarities at room temperature.

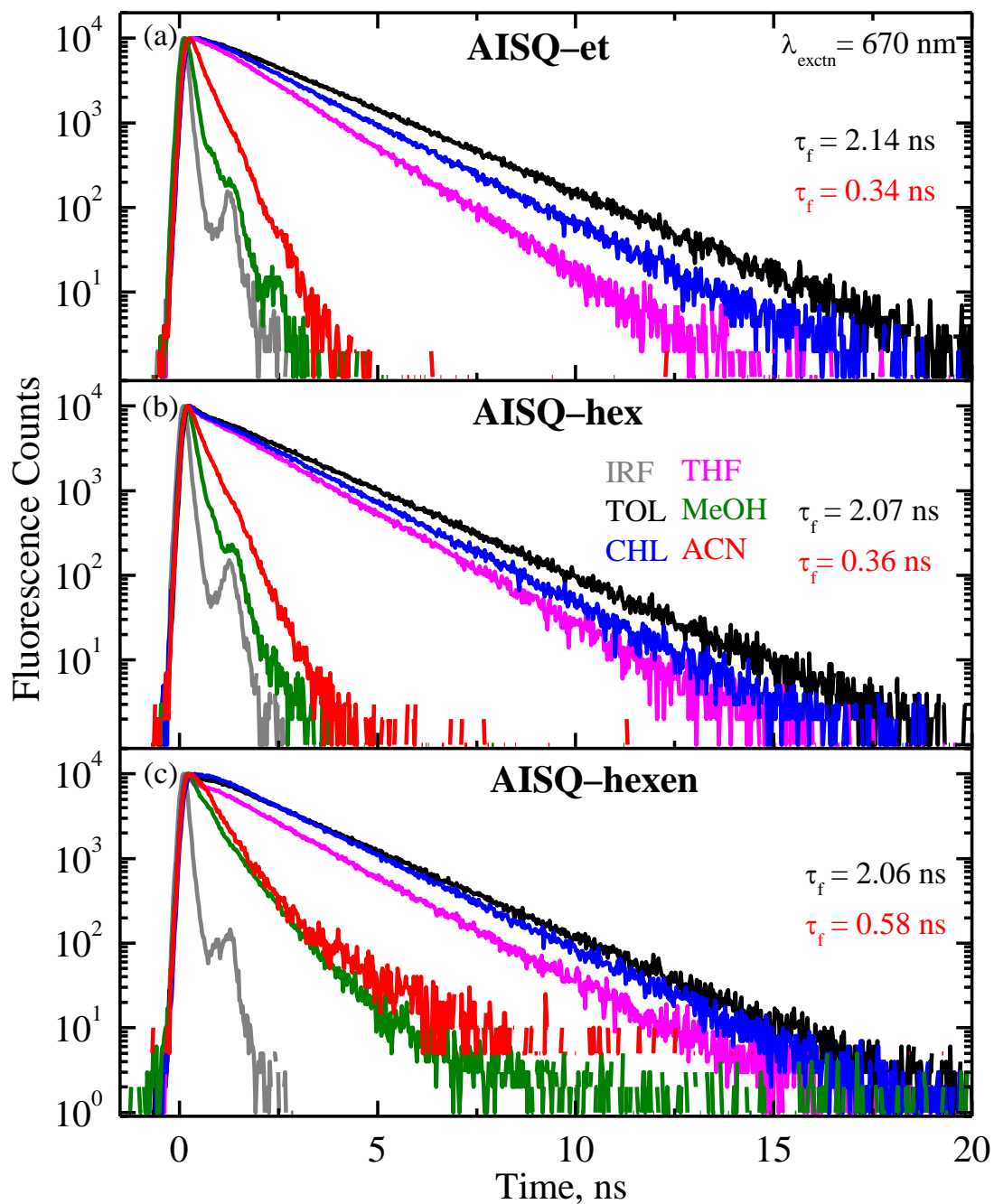


Figure 4.5 Fluorescence decay profiles of AISQ-et (a), AISQ-hex (b) and AISQ-hexen (c) in solvents of varying polarities obtained upon excitation at 670 nm.

Table 4.1 Absorption and Fluorescence Maxima, Lifetime and Quantum Yield and of AISQ-et in Various Solvents

Solvents	Absorption max, nm (λ_{\max})	Fluorescence max, nm (λ_{\max})	Stokes shift, cm^{-1} ($\Delta\nu$)	Fluorescence quantum yield ^a (Φ_f)	Fluorescence lifetime ^b , ns (τ_f)	Radiative constant, $\times 10^7 \text{ s}^{-1}$ (K_r)	Non-radiative constant, $\times 10^7 \text{ s}^{-1}$ (K_{nr})
Toluene	676	726	1018	0.28	2.14 ± 0.25	13.08	33.64
Chloroform	670	728	1189	0.20	1.82 ± 0.20	10.98	43.95
THF	648	730	1733	0.20	1.49 ± 0.15	13.42	53.69
MeOH	638	728	1937	0.01	0.12 ± 0.10	8.33	825
ACN	630	730	2174	0.02	0.34 ± 0.20	5.89	288

^aAbsolute fluorescence quantum yield attained by exciting at emission maximum using an integrating sphere. ^bFluorescence lifetime was obtained upon excitation at 670 nm and the χ^2 value of fluorescence kinetics fit is between 1.0 and 1.2.

Table 4.2 Absorption, Fluorescence Maxima and Lifetime of **AISQ-hex** in Various Solvents

Solvents	Absorption max, nm (λ_{\max})	Fluorescence max, nm (λ_{\max})	Stokes shift, cm^{-1} ($\Delta\nu$)	Fluorescence lifetime ^a , ns (τ_f)
Toluene	668	732	1308	2.07 ± 0.20
Chloroform	668	734	1346	1.62 ± 0.25
THF	646	735	1874	1.36 ± 0.20
MeOH	633	734	2173	0.25 ± 0.15
ACN	634	735	2167	0.36 ± 0.20

Table 4.3 Absorption, Fluorescence Maxima and Lifetime of **AISQ-hexen** in Various Solvents

Solvents	Absorption max, nm (λ_{\max})	Fluorescence max, nm (λ_{\max})	Stokes shift, cm^{-1} ($\Delta\nu$)	Fluorescence lifetime ^a , ns (τ_f)
Toluene	670	734	1301	2.06 ± 0.25
Chloroform	666	735	1409	1.95 ± 0.20
THF	649	739	1876	1.67 ± 0.25
MeOH	642	736	1989	0.35 ± 0.15
ACN	632	736	2235	0.58 ± 0.20

^aFluorescence lifetime was obtained upon excitation at 670 nm and the χ^2 value of fluorescence kinetics fit is between 1.0 and 1.2.

4.3.2.2 Film State

Figure 4.6 shows normalized absorption spectra of **AISQ** derivative in thin films recorded by drop-casting **AISQs** (1.5 mM) in chloroform. When compared to the neat solvent,

the absorption spectra in the thin film exhibited broad band ranging from 500–800 nm, indicating the formation of both H- and J-type aggregates by the strong intermolecular forces between the AISQ molecules.³⁵⁻³⁹ Indeed, such a broad range of absorption wavelength with a high molar absorptivity will be advantageous for light harvesting for optoelectronic devices.³²

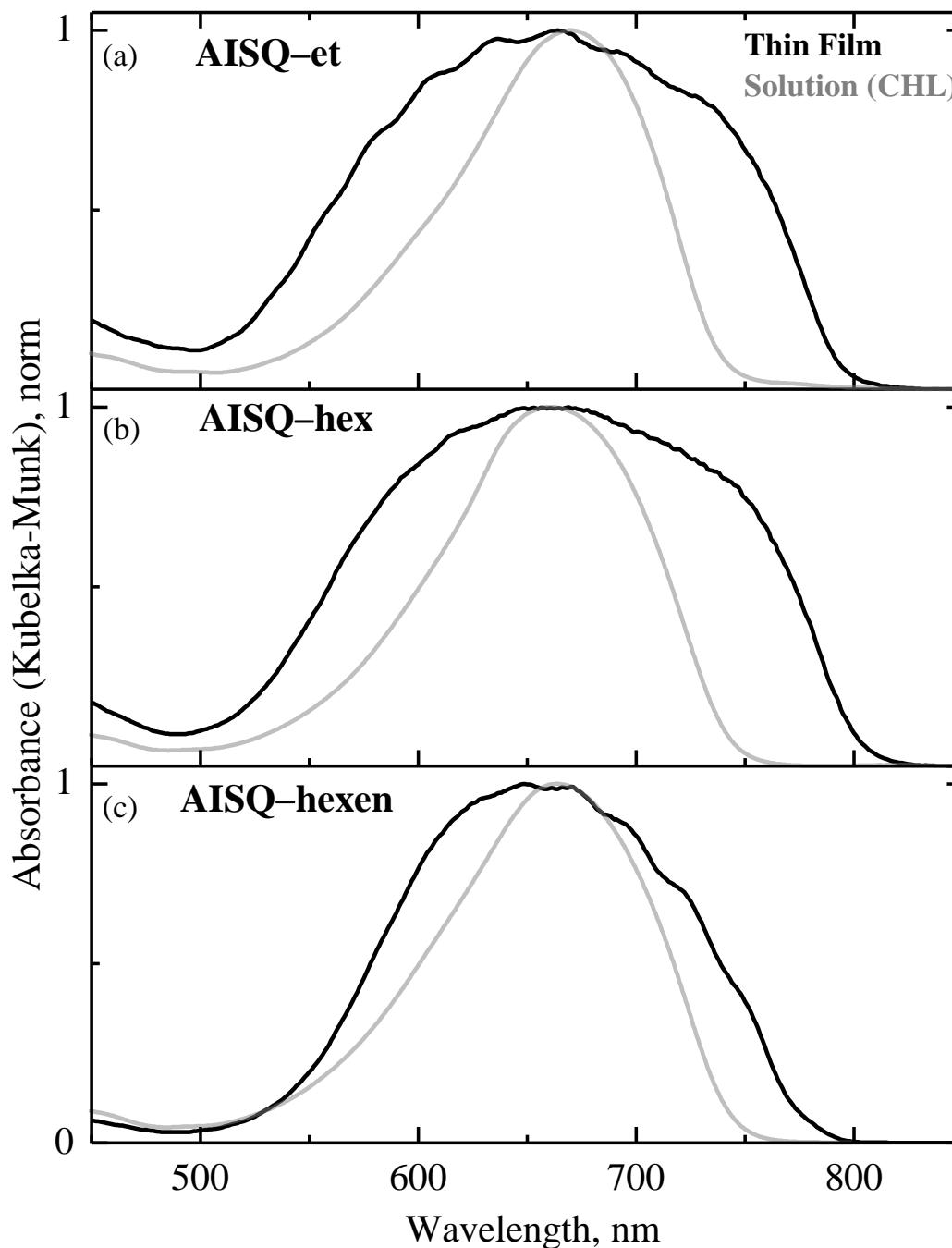


Figure 4.6 Normalized absorption spectra of AISQ-et (a), AISQ-hex (b) and AISQ-hexen (c) in a thin film and in chloroform solution.

4.3.2.3 Electrochemical Properties of AISQ Derivatives

Similarly, to the previous chapter the redox potentials of the **AISQ** derivatives were determined using cyclic voltammetry in acetonitrile using ferrocene as standard and the corresponding voltammograms are given in **Figure 4.7a**. The HOMO energy levels of **AISQ-et**, **AISQ-hex** and **AISQ-hexen** are found to be -4.82 , -4.80 and -4.84 eV respectively and the LUMO energy levels of **AISQ-et**, **AISQ-hex** and **AISQ-hexen** are found to be -3.16 , -3.05 and -3.19 eV respectively. It is interesting to note from the **Figure 4.7b** that the LUMO energy levels of all the derivatives are higher in energy compared to that of the PCBM (-3.7 eV) and simultaneously the HOMO energy level of the PCBM (-6.1 eV) is lower compared to that of **AISQ** derivatives, which is the important requirement of the sensitizer to be used in the BHJ-based optoelectronic devices for the efficient intermolecular charge-transfer in the excited state. Thus the energy levels of all the derivatives are suitable to act as donor materials in the BHJ-based OPD with PCBM as an acceptor. The electrochemical data of **AISQ** derivatives are summarised in **Table 4.4**.

4.3.2.4 Interaction of AISQs with PCBM

The absorption and fluorescence spectra of **AISQ-et**, **AISQ-hex** and **AISQ-hexen** with increased concentration of PCBM (1.5 to 13.5 mM) in toluene were measured. Though there were no notable changes in the absorption spectra of **AISQ** derivatives, the decrease of fluorescence intensity of all the **AISQ** derivatives upon the addition of PCBM were observed (**Figure 4.8**), reflecting the excited **AISQ** derivatives interacting with PCBM. Upon addition of PCBM, the fluorescence lifetime of **AISQ** derivatives was also measured by the excitation at 670 nm (left insets of **Figure 4.8**). In the presence of the PCBM (13.5 mM), the fluorescence lifetime is decreased from $\sim 2.14 \pm 0.25$, 2.07 ± 0.20 and 2.06 ± 0.20 ns to $\sim 1.49 \pm 0.25$,

1.54 ± 0.20 and 1.52 ± 0.20 ns for **AISQ-et**, **AISQ-hex** and **AISQ-hexen** respectively. The decrease in fluorescence intensity and lifetime deduces the occurrence of intermolecular charge-transfer from **AISQs** to PCBM.

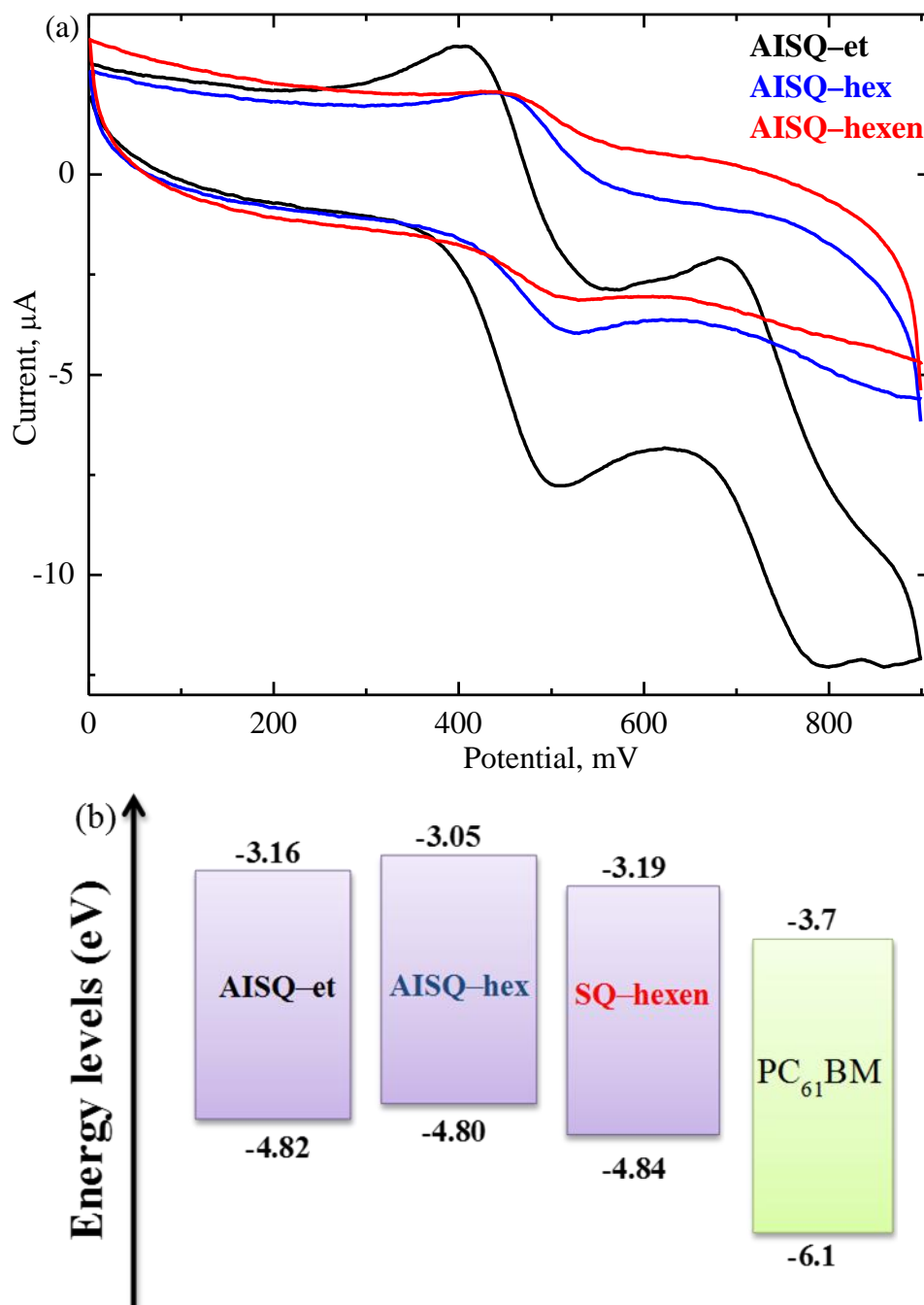


Figure 4.7 Cyclic voltammogram of **AISQ-et**, **AISQ-hex** and **AISQ-hexen** in ACN using tetrabutylammonium hexafluorophosphate as supporting electrolyte at a scanning rate of 50 mV/sec (a). HOMO and LUMO levels of **AISQ-et**, **AISQ-hex** and **AISQ-hexen** vs PCBM (b).

Table 4.4 Electrochemical data of **AISQ** derivatives from cyclic voltammetry in ACN

AISQs	λ_{00} , nm	E_{00} , eV	E_{ox} vs Ag/AgCl, V	HOMO, eV	LUMO, eV
AISQ–et	744	1.66	0.46	–4.82	–3.16
AISQ–hex	750	1.65	0.44	–4.80	–3.05
AISQ–hexen	750	1.65	0.48	–4.84	–3.19

The Stern–Volmer plot (right insets of **Figure 4.8**) for fluorescence quenching of **AISQs** with the increase of concentration of PCBM showed linear behaviour suggesting the occurrence of a dynamic quenching mechanism in the excited state deactivation. The k_q , ($k_q = K_{SV}/\tau_0$) and K_{SV} , ($\tau_0/\tau = 1 + K_{SV} \times [\text{PCBM}]$) were calculated and constants are provided in **Table 4.5**. Where τ_0 is the fluorescence lifetime of **AISQ** derivative in the absence of PCBM and τ_0/τ is the ratio of the fluorescence lifetime of **AISQs** in the absence and presence of PCBM. The k_q and K_{SV} for the **AISQ–et**, **AISQ–hex** and **AISQ–hexen** are found to be 14.71, 12.12, 12.67 ($\times 10^9 \text{ M}^{-1} \text{ s}^{-1}$) and 31.50, 25.10, 26.10 (M^{-1}) respectively. These constants are an order of magnitude larger⁴⁰ than that of normal diffusion controlled bimolecular reaction constant ($2 \times 10^9 \text{ M}^{-1} \text{ s}^{-1}$).⁴⁰ Overall, upon addition of PCBM, the quenching of fluorescence intensity and a lifetime of **AISQ** derivatives reveal the occurrence of the intermolecular charge–transfer from the **AISQs** to the PCBM.¹⁵

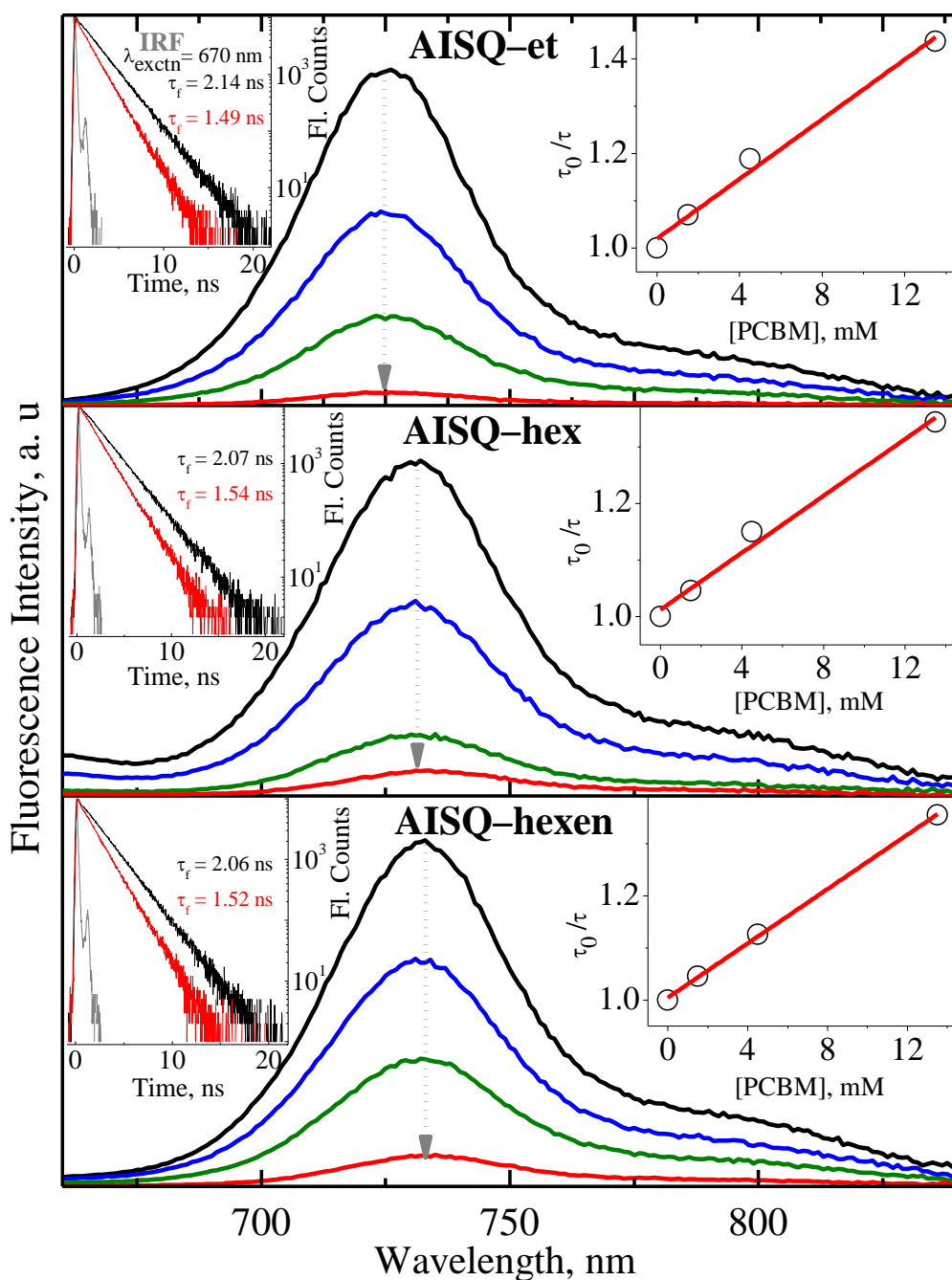


Figure 4.8 Fluorescence spectra of AISQ-*et* (a), AISQ-*hex* (b), AISQ-*hexen* (c) with different concentrations of PCBM in toluene 0 mM (black), 1.5 mM (blue), 4.5 mM (olive), 13.5 mM (red). Insets: fluorescence decay profiles recorded upon excitation at 670 nm (left) and plot of τ_0/τ versus [PCBM] (right).

Table 4.5 The Stern–Volmer quenching constant (K_{SV}) and bimolecular quenching rate constant (k_q) of AISQ derivatives

AISQs	K_{SV}, M^{-1}	τ_0, ns	τ, ns	$k_q, \times 10^9 M^{-1} s^{-1}$
AISQ–et	31.50	2.14 ± 0.25	1.49 ± 0.25	14.71
AISQ–hex	25.10	2.07 ± 0.20	1.54 ± 0.20	12.12
AISQ–hexen	26.10	2.06 ± 0.20	1.52 ± 0.20	12.67

4.4 Time-Resolved Photophysical Characterization

4.4.1 Femtosecond Transient Absorption Spectra of AISQ derivatives

Femtosecond time-resolved transient absorption spectra were measured in nonpolar (toluene) and polar (acetonitrile, ACN) solvents upon excitation at 600 nm using femtosecond pump-probe spectroscopy to understand the effect of solvent polarity on the excited state relaxation dynamics of AISQ derivatives. The transient absorption spectra of AISQ–et in toluene are shown in **Figure 4.9**, where panel a shows the spectral evolution starting from –50 fs to 10.70 ps. At the early time scale, it shows the broad positive band at ~496 nm and at the 200 fs two distinct negative absorption bands at around 627 and 710 nm were observed. The positive band at ~496 nm is attributed to the excited singlet state absorption (ESA, $S_n \leftarrow S_1$ transition) of the compound.⁴¹⁻⁴⁵ Though the evolution of GSB is not observed evidently due to the superimposing of SE, the evolution of SE was observed clearly at around 724 nm. In **Figure 4.9**, panel b shows the spectral evolution from 12.70 ps to 1.56 ns where the intensity of ESA, GSB and SE bands decreased with the increase of the delay time.

The transient absorption spectra of AISQ–et in ACN are shown in **Figure 4.10**, where panel a shows the spectral evolution starting from –50 fs to 10.30 ps. At early time scale, it shows the broad positive band at ~490 nm and after the time scale of 200 fs, a distinct negative

absorption bands at around 720 was formed. The positive band at 490 nm is due to the excited singlet state absorption (ESA, $S_n \leftarrow S_1$ transition). With an increase of delay time, at 10.30 ps the negative transient absorption band evolved to attain the steady-state emission maximum at 727 nm, corresponding to the SE. The evolution of GSB is not observed evidently due to the scattering of laser excitation and superimposing of SE. The panel b of **Figure 4.10** exhibits the transient absorption spectra recorded from 11.35 ps to 1.56 ns where the intensity of the ESA, GSB and SE bands decreased with increase of the delay time.

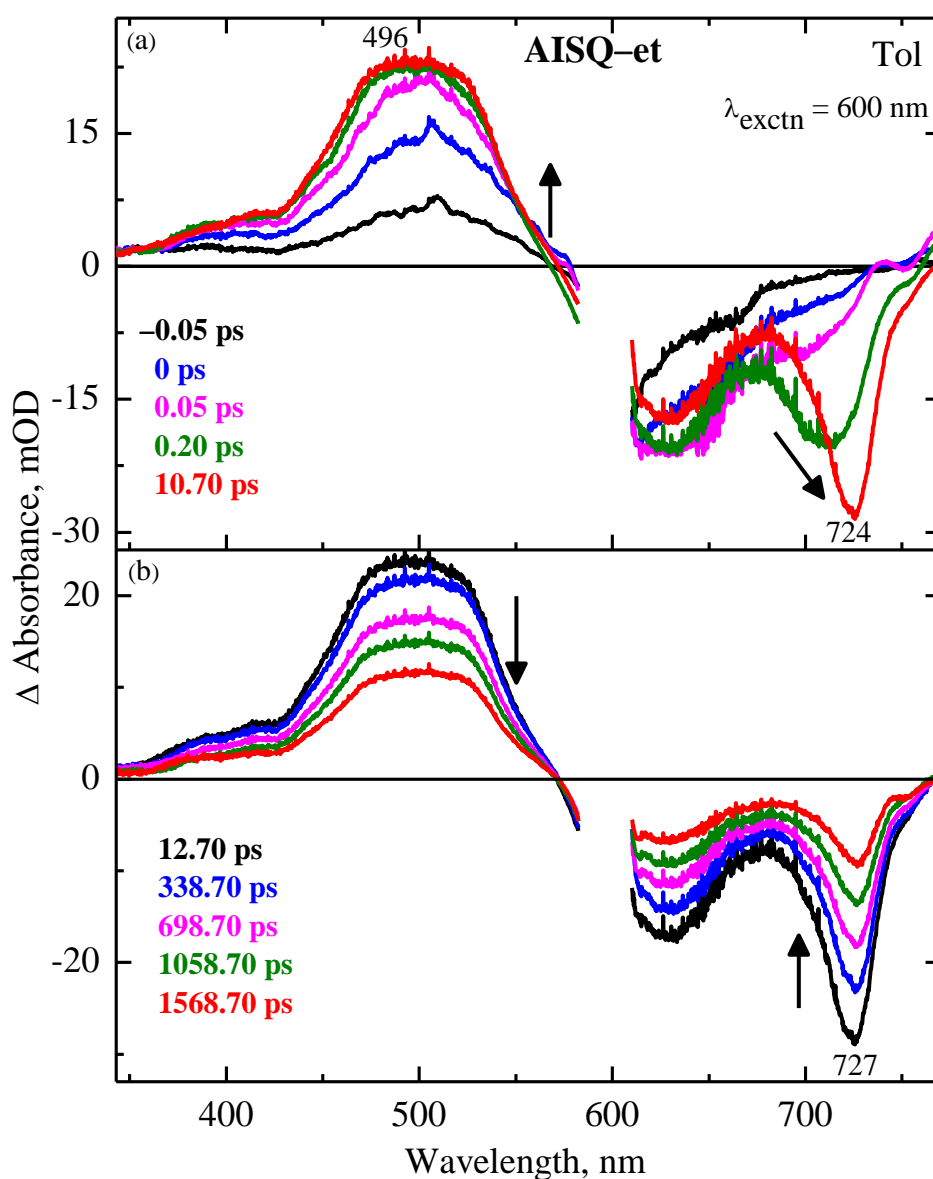


Figure 4.9 Femtosecond transient absorption spectra of AISQ-et in toluene upon excitation at 600 nm at different delay times.

The fs-TAS of AISQ-hex and AISQ-hexen derivatives in toluene and ACN are shown in **Figure 4.11–4.14**. The spectral behaviors of AISQ-hex, and AISQ-hexen in toluene and ACN are similar to that of AISQ-et in toluene and ACN respectively. Though the spectral features of ESA, SE and GSB of AISQ-et in toluene have resembled that of in ACN, the excited state relaxation dynamics are faster in ACN (**Figure 4.15**) when compared to that in toluene due to the change in the solvation dynamics.⁴⁶⁻⁴⁹

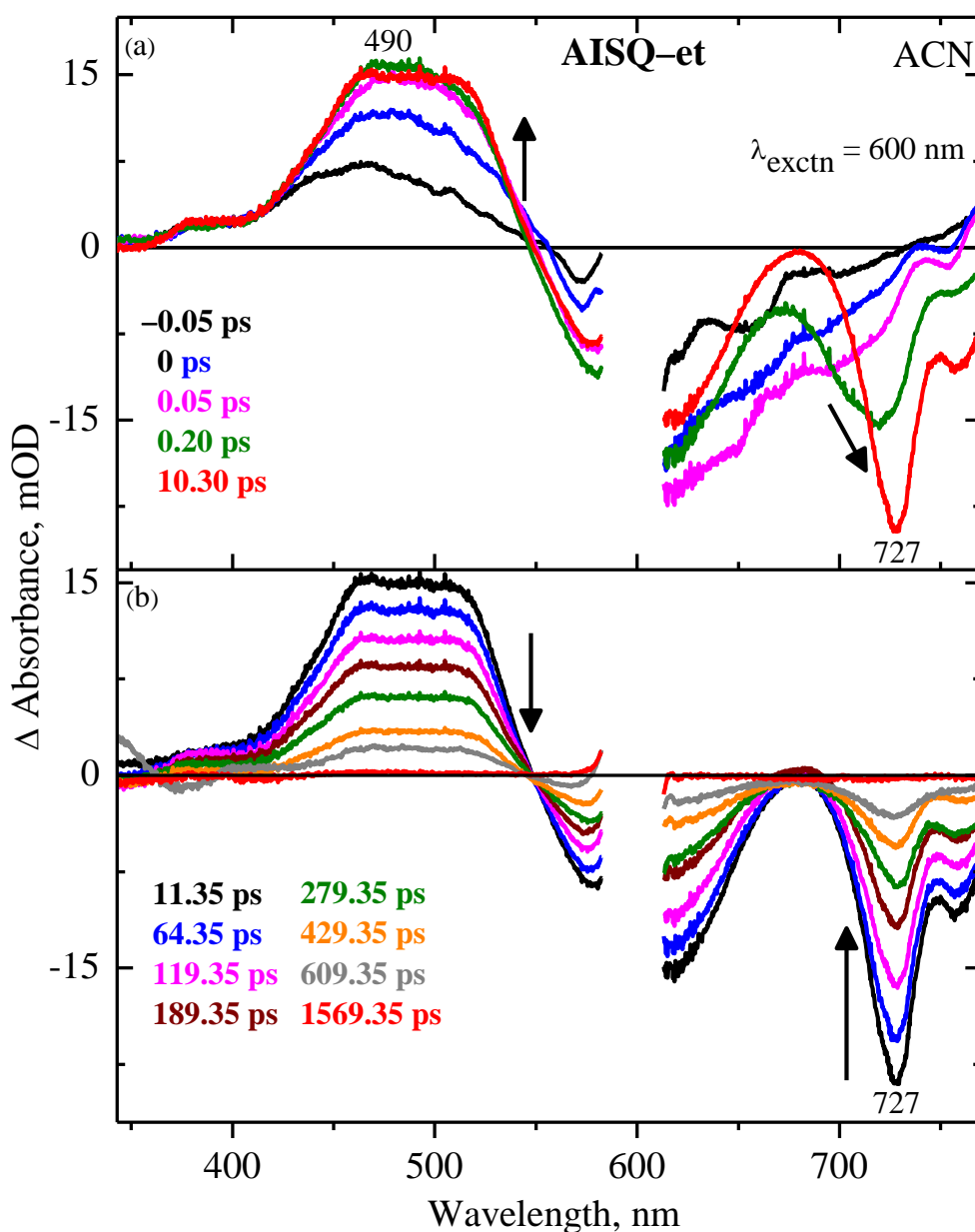


Figure 4.10 Femtosecond transient absorption spectra of AISQ-et in ACN upon excitation at 600 nm at different delay times.

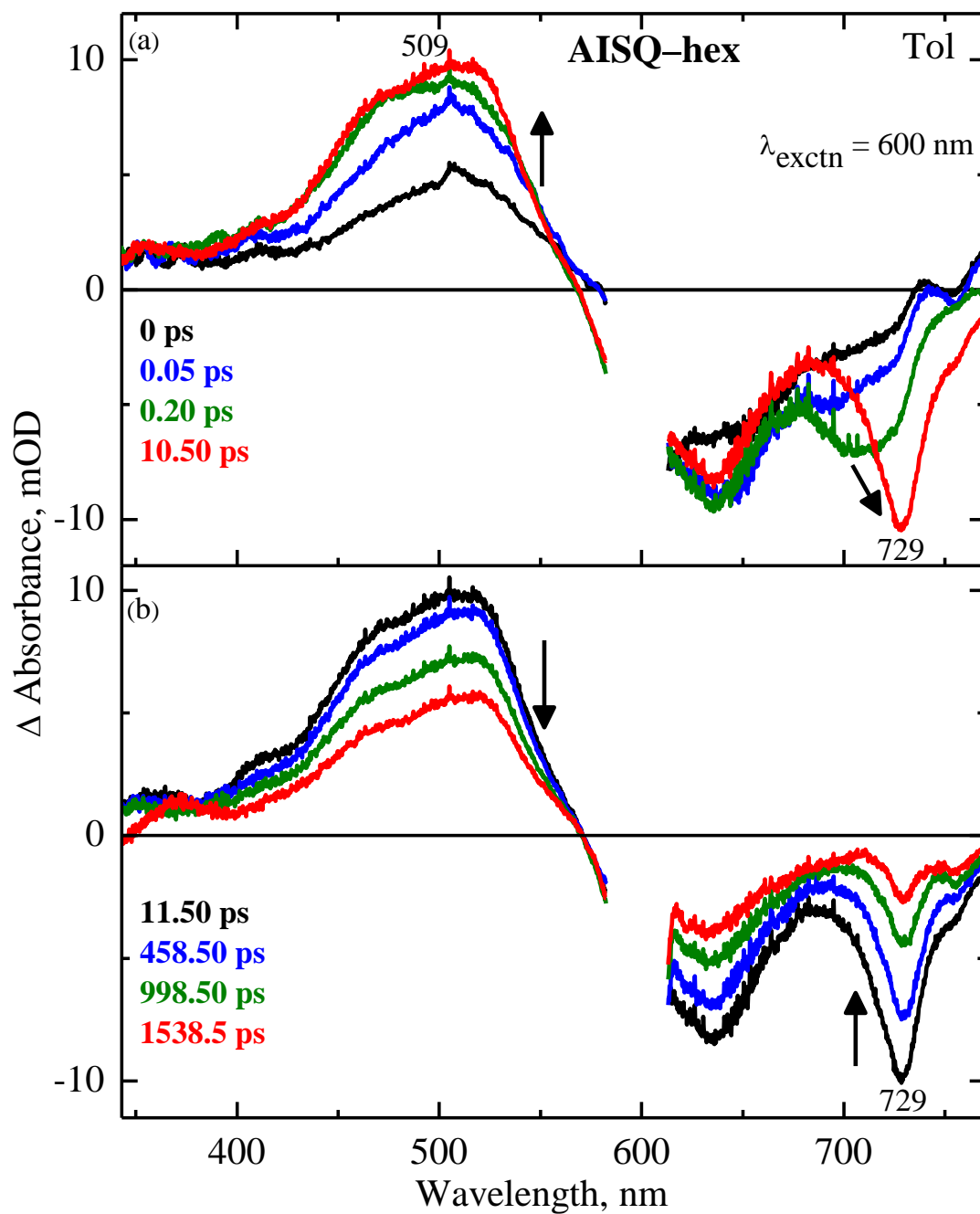


Figure 4.11 Femtosecond transient absorption spectra of AISQ-hex in toluene upon excitation at 600 nm at different delay times.

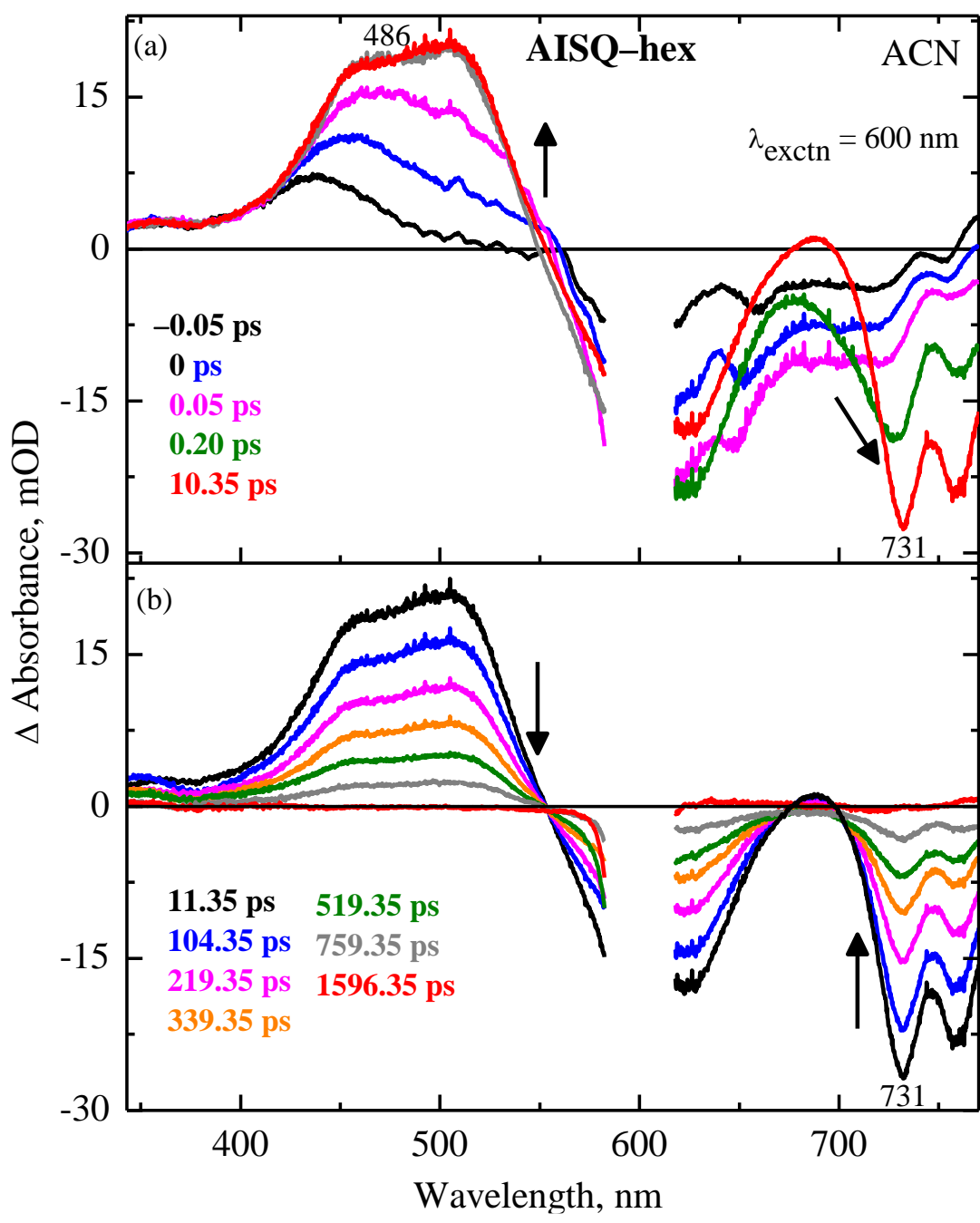


Figure 4.12 Femtosecond transient absorption spectra of AISQ-hex in ACN upon excitation at 600 nm at different delay times.

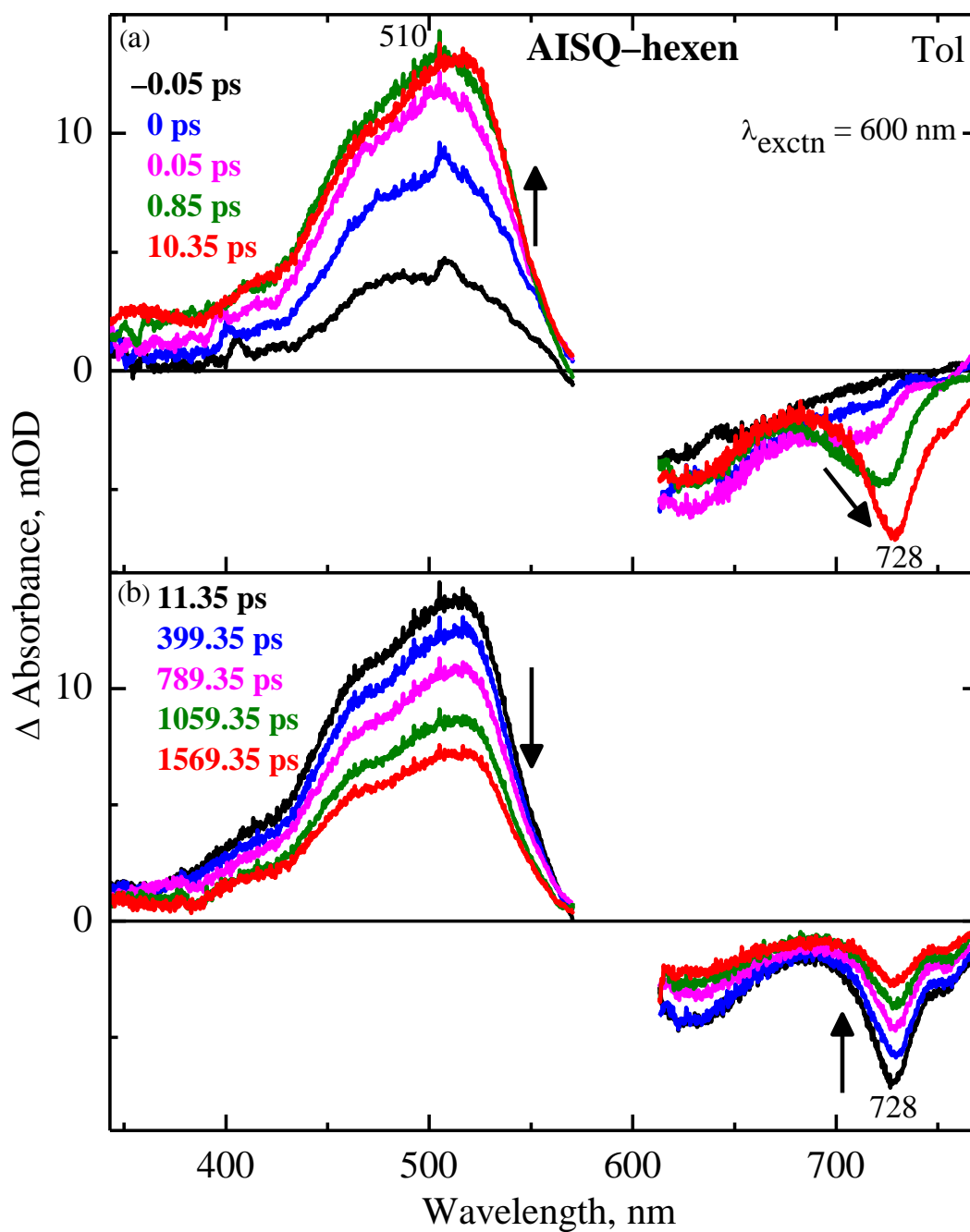


Figure 4.13 Femtosecond transient absorption spectra of AISQ-hexen in toluene upon excitation at 600 nm at different delay times.

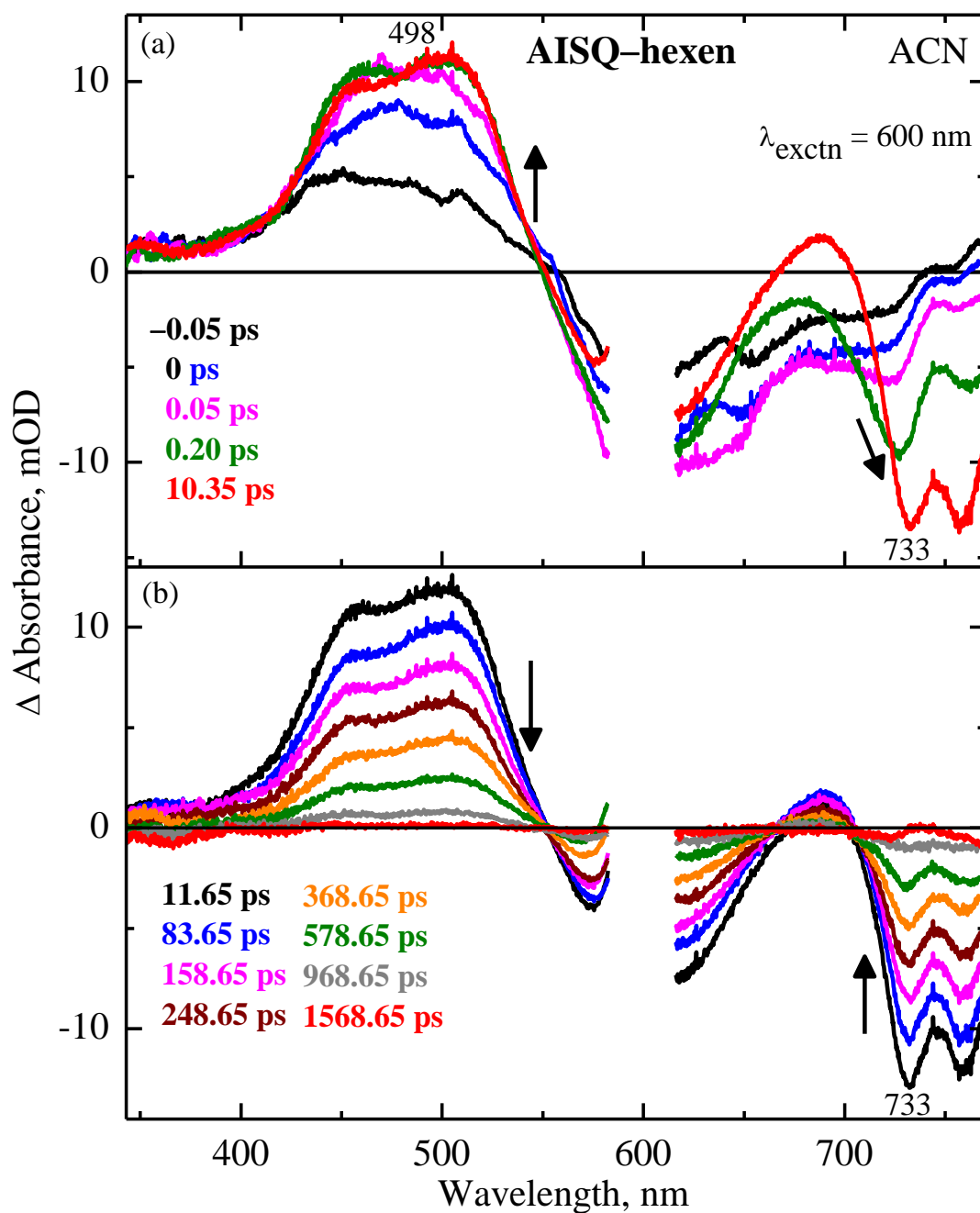


Figure 4.14 Femtosecond transient absorption spectra of AISQ-hexen in ACN upon excitation at 600 nm at different delay times.

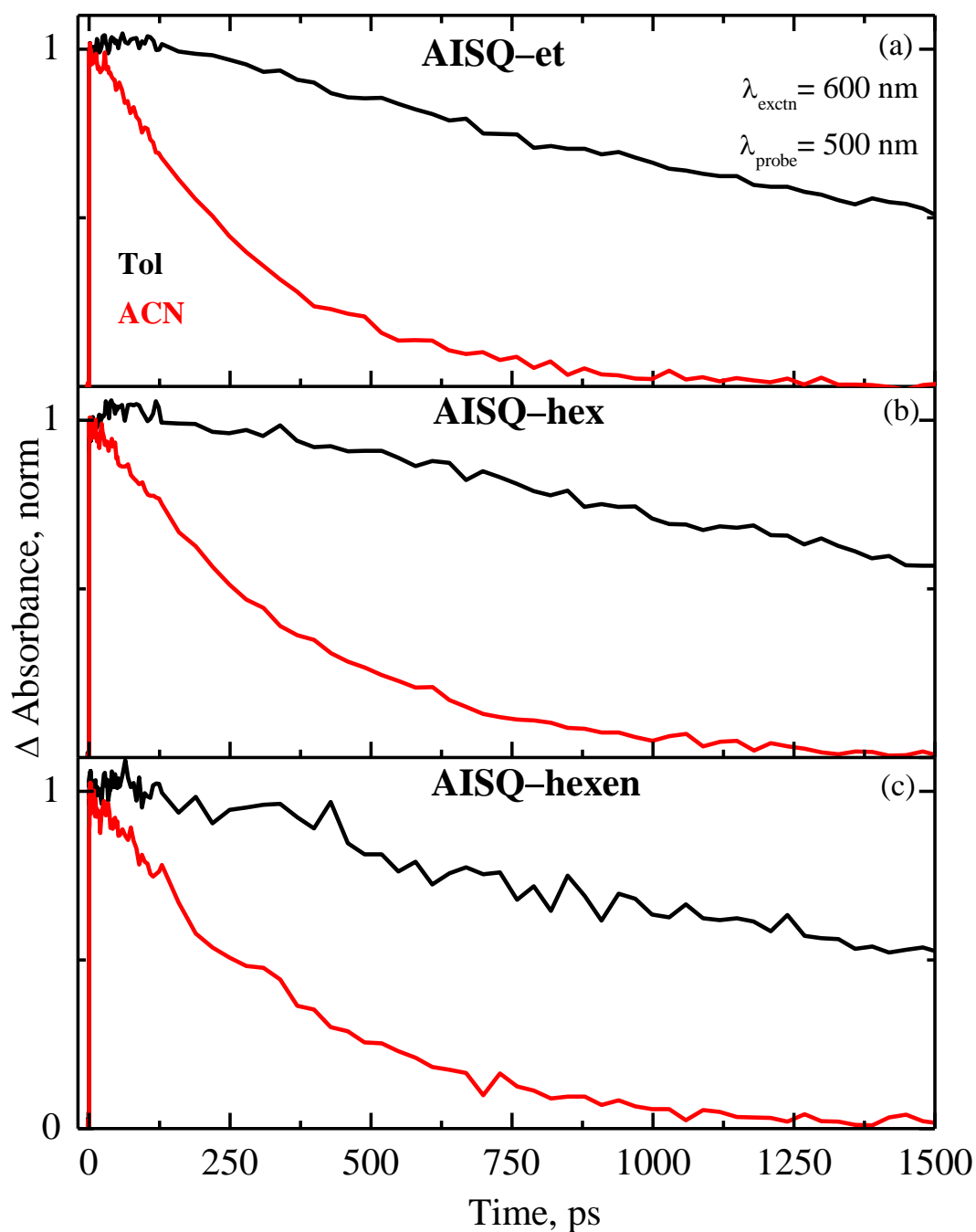


Figure 4.15 Femtosecond transient absorption decay of **AISQ-et** (a), **AISQ-hex** (b), and **AISQ-hexen** (c) in toluene and acetonitrile upon excitation at 600 nm.

4.4.2 Analysis of the Transient Absorption Spectra of AISQ Derivatives

The femtosecond transient absorption spectra were analyzed globally with the sequential model using Glotaran.⁵⁰ Three exponential components were optimally obtained to

describe the relaxation dynamics of **AISQ** derivatives in toluene and ACN. The resulted time constants are given in **Table 4.6** and the corresponding DADS are shown for comparison in **Figure 4.16–4.17**.

Table 4.6 Time Constants Attained from Global Analysis Using Glotaran⁵⁰ for **AISQs** upon Excitation at 600 nm

AISQs	ACN	Toluene
AISQ–et	$\tau_1 = 0.43 \pm 0.10$ ps	$\tau_1 = 2.19 \pm 0.20$ ps
	$\tau_2 = 40 \pm 1.00$ ps	$\tau_2 = 106.44 \pm 2.20$ ps
	$\tau_3 = 338.45 \pm 2.30$ ps	$\tau_3 = 2.14 \pm 0.10$ ns
AISQ–hex	$\tau_1 = 0.42 \pm 0.15$ ps	$\tau_1 = 2.46 \pm 0.25$ ps
	$\tau_2 = 30.90 \pm 1.00$ ps	$\tau_2 = 121.41 \pm 3.20$ ps
	$\tau_3 = 362.64 \pm 2.15$ ps	$\tau_3 = 2.19 \pm 0.10$ ns
AISQ–hexen	$\tau_1 = 0.44 \pm 0.12$ ps	$\tau_1 = 2.31 \pm 0.26$ ps
	$\tau_2 = 39.26 \pm 1.00$ ps	$\tau_2 = 112.50 \pm 1.20$ ps
	$\tau_3 = 579.55 \pm 3.20$ ps	$\tau_3 = 2 \pm 0.10$ ns

As there are no significant changes in the dynamic of **AISQ** derivatives by changing the alkyl and alkenyl substituents, the time constants obtained for **AISQ–et** is considered for discussion and those are $\tau_1 = 431$ fs, $\tau_2 = 39.98$ ps, and $\tau_3 = 338.45$ ps in ACN and $\tau_1 = 2.19$ ps, $\tau_2 = 106.44$ ps and $\tau_3 = 2.14$ ns in toluene. Based on the observation of dynamic redshift of SE (~710 nm) with an increase of delay time,⁵¹⁻⁵³ the fast component ($\tau_1 = 431$ fs in ACN and $\tau_1 = 2.19$ ps in toluene) obtained upon excitation at 600 nm corresponds to the solvation relaxation processes from Franck–Condon state to solvent stabilized local excited state. The

time constant $\tau_2 = 39.98$ and 106.44 ps for ACN and toluene respectively, could be attributed to the formation dark state resulting from the conformational changes of AISQ-et. This state enables the non-radiative deactivation to the ground state supporting the observation of a decrease of fluorescence quantum yield and lifetime in ACN (Table 4.1–4.3). Finally, the longer time constant τ_3 , obtained from the global analysis is consistent with the fluorescence lifetime obtained from the TCSPC in neat solvents (Table 4.1–4.3). Hence the time constant (0.33) 2.14 ns is attributed to the lifetime of the excited singlet state in ACN (toluene)

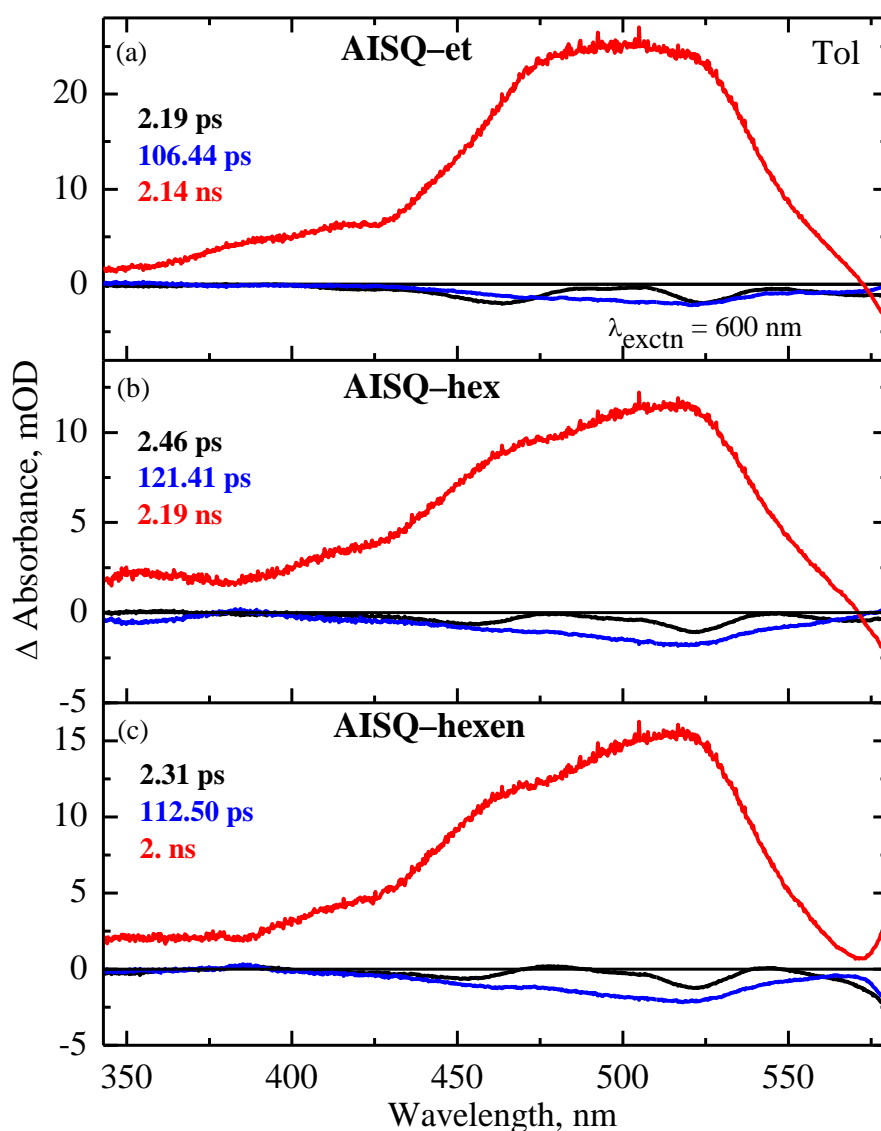


Figure 4.16 Decay associated difference spectra of AISQ-et (a), AISQ-hex (b), AISQ-hexen in toluene obtained by global analysis.

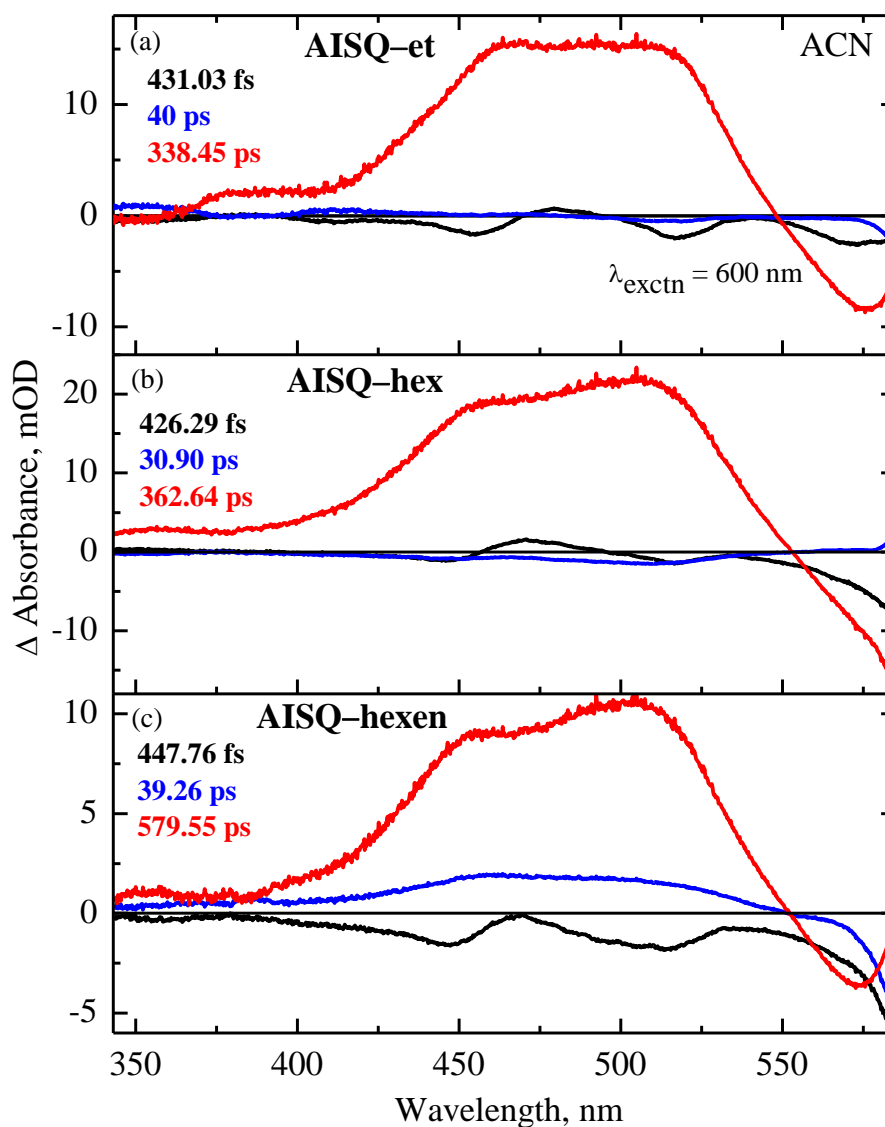


Figure 4.17 Decay associated difference spectra of AISQ-et (a), AISQ-hex (b), AISQ-hexen (c) in ACN obtained by global analysis.

4.5 Characterization of Photodetector

The BHJ-based OPDs were fabricated using AISQ-et as donor materials and its architecture and the corresponding energy level diagram are represented in Figure 4.18. In the device, molybdenum trioxide (MoO_3) and zinc oxide act as a hole and electron transporting layer respectively.

The results of preliminary characterization of the spectral response of the OPDs under unbiased conditions are shown in **Figure 4.19**. Interestingly, the devices showed sensitivity in the NIR region and needed further investigation.

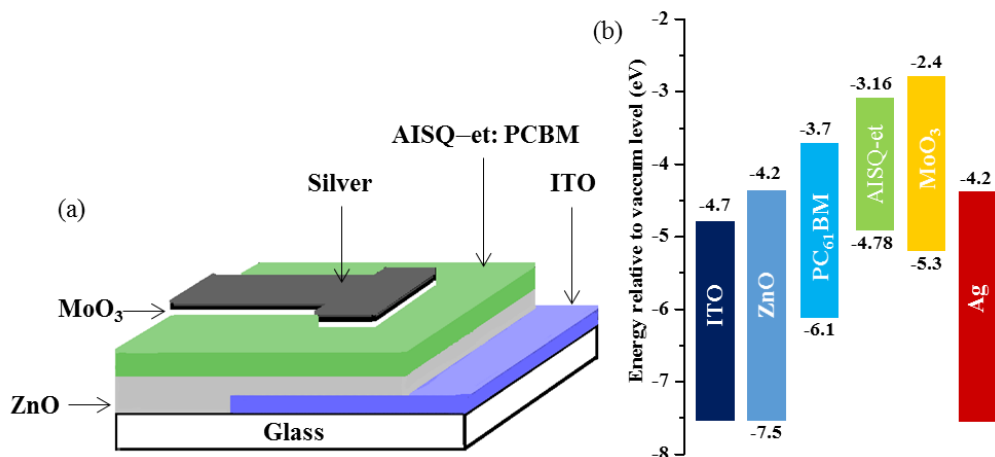


Figure 4.18 a) Fabricated OPD structure, b) band diagram for fabricated OPD.

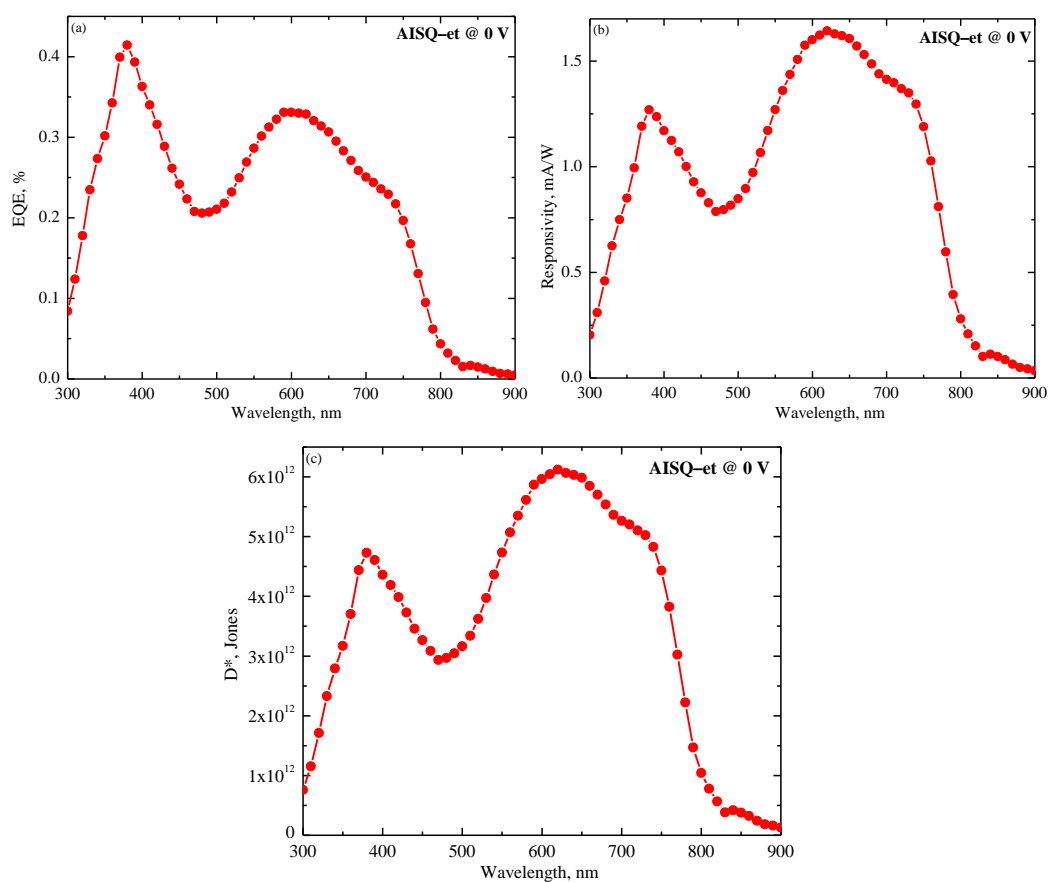


Figure 4.19 EQE (a), R (b) and D* (c) spectra of the devices using AISQ-et at short circuit condition.

4.6 Summary

Here the USQ derivatives comprising *N,N*-dimethyl aminoanthracene and various *N*-alkylated indolium (**AISQ**) were synthesized and their steady and excited state relaxation dynamics were investigated. The absorption spectra of the **AISQ** derivatives exhibited a strong absorption maximum at ~630–676 nm in toluene with a high extinction coefficient, $\sim 10^5 \text{ M}^{-1}\text{cm}^{-1}$. When compared to the neat solvents, the absorption spectra in thin film exhibits broad in nature covering a wide range of wavelength starting from 500–800 nm due to the formation of H- and J-type aggregates. Such a wide range of wavelengths with a high extinction coefficient will be significantly beneficial for optoelectronic devices. The energy levels of all the **AISQ** derivatives are suitably placed to act as donor materials in the BHJ-based OPD with PCBM as an acceptor. The quenching fluorescence intensity and lifetime upon the addition of PCBM reflects the occurrence of intermolecular charge transfer dynamics between the **AISQs** and PCBM. It is found that over all the transient absorption spectral features of all the **AISQ** derivatives in toluene appeared to be the same as in ACN. However, the excited state relaxation dynamics of **AISQ** derivatives in ACN are faster when compared to that in toluene due to the change in the solvation relaxation dynamics. The **AISQ** derivatives were applied into the PD devices and showed sensitivity in the NIR region.

4.7 Experimental Section

4.7.1 Materials and Methods

1 General Details: The reagents and chemicals used for synthesis were purchased from Merck, Sigma–Aldrich, and TCI. Dry solvents were prepared by following the reported procedures.⁵⁴ The material characterization techniques, steady–state measurements, electrochemical measurements, TCSPC measurements, femtosecond transient absorption

measurements details were provided in the experimental section of Chapter 2. The device fabrication and characterization details were provided in the experimental section of Chapter 3

4.8 Synthesis and Characterization of AISQ Derivatives

1. The synthetic procedure and characterization details of 1-Aminoanthracene, *N,N*-Dimethylantracene-1-amine and 3-(4-(dimethylamino) anthracen-1-yl)-4-hydroxycyclobut-3-ene-1, 2-dione were provided in the experimental section of Chapter 2.

2. General procedure for the quaternization reaction of 2,3,3-trimethylindoline

A mixture of 2,3,3-trimethylindoline (1 equivalent), and alkyl/alkenyl iodide (1.5 equivalent) was taken in a pressure tube. To this 4 ml of dry Acetonitrile was added and the mixture was heated at 80⁰ C for 15 Hrs. The solvent was removed under reduced pressure. The residue was washed several times with Diethyl ether to give the desired product.

2.1 Characterization details of 1-ethyl-2,3,3-trimethyl-3H-indol-1-ium.

¹H NMR (500 MHz, DMSO-*d*₆): δ 7.97-7.95 (d, 1H, *J* = 7.5 Hz), 7.85-7.62 (m, 3H), 4.51-4.46 (q, 2H), 2.82 (s, 3H), 1.53 (s, 6H), 1.46-1.43 (t, 3H); HRMS-EI: Calculated Molecular weight for C₁₃H₁₈N⁺ is 188.1434, Found=188.1440.

2.2 Characterization details of 1-hexyl-2,3,3-trimethyl-3H-indol-1-ium

¹H NMR (500 MHz, DMSO-*d*₆): δ 7.95-7.92 (d, 1H, *J* = 7.5 Hz), 7.83-6.99 (m, 3H), 4.37-4.33 (t, 2H), 2.81 (s, 3H), 1.50 (s, 6H), 1.46-1.43 (t, 3H), 1.33-1.27 (m, 4H), 1.20-0.97 (m, 2H), 0.90-0.87 (t, 3H); HRMS-EI: Calculated Molecular weight for C₁₇H₂₆N⁺ is 244.2060, Found=244.2069.

2.3 Characterization details of 1-(hex-5-en-1-yl)-2,3,3-trimethyl-3H-indol-1-ium

¹H NMR (500 MHz, DMSO-*d*₆): δ 7.9.8-7.96 (d, 1H, *J* = 7.5 Hz), 7.89-7.83 (m, 3H) 5.82-5.78 (m, 1H), 5.02-4.99 (d, 2H), 2.84 (s, 3H), 1.75-1.70 (m, 4H), 1.52 (s, 6H); HRMS-EI: Calculated Molecular weight for C₁₇H₂₄N⁺ is 242.1903, Found = 242.1890.

3 General procedure for the synthesis of AISQ–et, AISQ–hex and AISQ–hexen

A suspension of 3-(4-(dimethylamino) anthracen-1-yl)-4-hydroxycyclobut-3-ene-1,2-dione (1 equivalent), and the quaternized indolium salt (1 equivalent) was dissolved in a 1:1 benzene: butanol azeotropic mixture (30 ml), and refluxed at 90° C in a Dean–Stark apparatus for about 8 hrs. After the reaction, the mixture is allowed to cool to room temperature and the solvent is removed under reduced pressure. Then the residue was purified by column chromatography. (silica gel, hexane: ethyl acetate, 20:80), followed by recrystallization with chloroform.

3.1 Characterization details of AISQ–et [(Z)-2-((3-(4-(dimethylamino) anthracen-1-yl)-2-hydroxy-4-oxocyclobut-2-en-1-ylidene) methyl)-1-ethyl-3,3-dimethyl-3H-indol-1-ium]

¹H NMR (500 MHz, MeOD): δ 8.86-8.85 (d, 1H, $J = 8$ Hz), 8.76 (s, 1H), 8.15-8.14 (d, 1H, $J = 8$ Hz), 8.08-8.07 (d, 1H, $J = 8.5$ Hz), 7.66-7.65 (d, 1H, $J = 7.5$ Hz), 7.59-7.51 (m, 5H), 7.47-7.44 (dd, 1H, $J = 6.5$ Hz), 7.11-7.09 (d, 1H, $J = 8$ Hz), 6.49 (s, 1H), 4.51-4.46 (q, 2H), 3.17 (s, 6H), 1.90 (s, 6H), 1.56-1.53 (t, 3H); HRMS–EI: Calculated Molecular weight for C₃₃H₃₀N₂O₄ is 486.2307, Found=487.2374.

3.2 Characterization details of AISQ–hex [(E)-2-(4-(dimethylamino)anthracen-1-yl)-4-((1-hexyl-3,3-dimethyl-3H-indol-1-ium-2-yl)methylene)-3-oxocyclobut-1-en-1-olate]

¹H NMR (500 MHz, MeOD): δ 8.84-8.82 (d, 1H, $J = 8$ Hz), 8.71 (s, 1H), 8.19-8.16 (d, 1H, $J = 8$ Hz), 8.12-8.10 (d, 1H, $J = 8.5$ Hz), 7.62-7.61 (d, 1H, $J = 7.5$ Hz), 7.60-7.54 (m, 5H), 7.45-7.41 (dd, 1H, $J = 6.5$ Hz), 7.09-7.07 (d, 1H, $J = 8$ Hz), 6.51 (s, 1H), 4.01-3.97 (t, 2H), 3.15 (s, 6H), 1.93 (s, 6H), 1.29 (m, 6H), 1.17 (m, 2H), 0.81-0.78 (t, 3H); HRMS–EI: Calculated Molecular weight for C₃₇H₃₈N₂O₂ is 542.7098, Found= 543.3016.

3.3 Characterization details of AISQ–hexen [(E)-2-(4-(dimethylamino)anthracen-1-yl)-4-((1-(hex-5-en-1-yl)-3,3-dimethyl-3H-indol-1-ium-2-yl)methylene)-3-oxocyclobut-1-en-1-olate]

¹H NMR (500 MHz, MeOD): δ 8.88-8.87 (d, 1H, $J = 8$ Hz), 8.79 (s, 1H), 8.18-8.15 (d, 1H, $J = 8$ Hz), 8.10-8.08 (d, 1H, $J = 8.5$ Hz), 7.68-7.66 (d, 1H, $J = 7.5$ Hz), 7.60-7.56 (m, 5H), 7.49-7.47 (dd, 1H, $J = 6.5$ Hz), 7.10-7.08 (d, 1H, $J = 8$ Hz), 6.51 (s, 1H), 5.82 (m, 2H), 5.14 (t, 1H), 4.05-3.98 (t, 2H), 2.18-2.14 (m, 6H), 1.90 (s, 6H), 1.25 (m, 6H); HRMS–EI: Calculated Molecular weight for C₃₇H₃₆N₂O₂ is 540.2777, Found= 541.1341.

4.9 References

1. Wang, Q.; Campbell, W. M.; Bonfantani, E. E.; Jolley, K. W.; Officer, D. L.; Walsh, P. J.; Gordon, K.; Humphry-Baker, R.; Nazeeruddin, M. K.; Grätzel, M., Efficient Light Harvesting by Using Green Zn-Porphyrin-Sensitized Nanocrystalline TiO₂ Films. *J. Phys. Chem. A* **2005**, *109*, 15397-15409.
2. Tanaka, M.; Hayashi, S.; Eu, S.; Umeyama, T.; Matano, Y.; Imahori, H., Novel Unsymmetrically Π -Elongated Porphyrin for Dye-Sensitized TiO₂ Cells. *Chem. Commun.*, **2007**, 2069-2071.
3. Cid, J.-J.; Yum, J.-H.; Jang, S.-R.; Nazeeruddin, M. K.; Martínez-Ferrero, E.; Palomares, E.; Ko, J.; Grätzel, M.; Torres, T., Molecular Cosensitization for Efficient Panchromatic Dye-Sensitized Solar Cells. *Angew. Chem. Int. Ed.* **2007**, *46*, 8358-8362.
4. Shibano, Y.; Umeyama, T.; Matano, Y.; Imahori, H., Electron-Donating Perylene Tetracarboxylic Acids for Dye-Sensitized Solar Cells. *Org. Lett.* **2007**, *9*, 1971-1974.
5. Li, C., et al., An Improved Perylene Sensitizer for Solar Cell Applications. *ChemSusChem* **2008**, *1*, 615-618.
6. Kim, S.; Mor, G. K.; Paulose, M.; Varghese, O. K.; Baik, C.; Grimes, C. A., Molecular Design of near-Ir Harvesting Unsymmetrical Squaraine Dyes. *Langmuir* **2010**, *26*, 13486-13492.
7. He, J.; Jo, Y. J.; Sun, X.; Qiao, W.; Ok, J.; Kim, T.-i.; Li, Z. a., Squaraine Dyes for Photovoltaic and Biomedical Applications. *Adv. Funct. Mater.* **2021**, *31*, 2008201.
8. Corredor, C. C.; Huang, Z.-L.; Belfield, K. D., Two-Photon 3d Optical Data Storage Via Fluorescence Modulation of an Efficient Fluorene Dye by a Photochromic Diarylethene. *Adv. Mater.* **2006**, *18*, 2910-2914.
9. Sun, C.-L.; Lv, S.-K.; Liu, Y.-P.; Liao, Q.; Zhang, H.-L.; Fu, H.; Yao, J., Benzoindolic Squaraine Dyes with a Large Two-Photon Absorption Cross-Section. *J. Mater. Chem. C* **2017**, *5*, 1224-1230.
10. Chen, C.; Dong, H.; Chen, Y.; Guo, L.; Wang, Z.; Sun, J.-J.; Fu, N., Dual-Mode Unsymmetrical Squaraine-Based Sensor for Selective Detection of Hg²⁺ in Aqueous Media. *Org. Biomol. Chem.* **2011**, *9*, 8195-8201.
11. Butnarasu, C.; Barbero, N.; Barolo, C.; Visentin, S., Squaraine Dyes as Fluorescent Turn-on Sensors for the Detection of Porcine Gastric Mucin: A Spectroscopic and Kinetic Study. *J. Photochem. Photobiol. B, Biol.* **2020**, *205*, 111838.

12. Saneesh Babu, P. S., et al., Bis(3,5-Diiodo-2,4,6-Trihydroxyphenyl)Squaraine Photodynamic Therapy Disrupts Redox Homeostasis and Induce Mitochondria-Mediated Apoptosis in Human Breast Cancer Cells. *Sci. Rep.* **2017**, *7*, 42126.
13. Khopkar, S.; Shankarling, G., Synthesis, Photophysical Properties and Applications of Nir Absorbing Unsymmetrical Squaraines: A Review. *Dyes Pigm.* **2019**, *170*, 107645.
14. Yang, D.; Yang, Q.; Yang, L.; Luo, Q.; Huang, Y.; Lu, Z.; Zhao, S., Novel High Performance Asymmetrical Squaraines for Small Molecule Organic Solar Cells with a High Open Circuit Voltage of 1.12 V. *ChemComm* **2013**, *49*, 10465-10467.
15. Somashekharappa, G. M.; Govind, C.; Pulikodan, V.; Paul, M.; Namboothiry, M. A. G.; Das, S.; Karunakaran, V., Unsymmetrical Squaraine Dye-Based Organic Photodetector Exhibiting Enhanced near-Infrared Sensitivity. *J. Phys. Chem. C* **2020**, *124*, 21730-21739.
16. de Miguel, G.; Marchena, M.; Ziółek, M.; Pandey, S. S.; Hayase, S.; Douhal, A., Femto-to Millisecond Photophysical Characterization of Indole-Based Squaraines Adsorbed on TiO₂ Nanoparticle Thin Films. *J. Phys. Chem. C* **2012**, *116*, 12137-12148.
17. Rana, A.; Sharma, C.; Prabhu, D. D.; Kumar, M.; Karuvath, Y.; Das, S.; Chand, S.; Singh, R. K., Revealing Charge Carrier Dynamics in Squaraine:[6, 6]-Phenyl-C 71-Butyric Acid Methyl Ester Based Organic Solar Cells. *AIP Adv.* **2018**, *8*, 045302.
18. Singh, A. K.; Mele Kavungathodi, M. F.; Nithyanandhan, J., Alkyl-Group-Wrapped Unsymmetrical Squaraine Dyes for Dye-Sensitized Solar Cells: Branched Alkyl Chains Modulate the Aggregation of Dyes and Charge Recombination Processes. *ACS Appl. Energy Mater.* **2020**, *12*, 2555-2565.
19. Lambert, C.; Koch, F.; Völker, S. F.; Schmiedel, A.; Holzapfel, M.; Humeniuk, A.; Röhr, M. I. S.; Mitric, R.; Brixner, T., Energy Transfer between Squaraine Polymer Sections: From Helix to Zigzag and All the Way Back. *J. Am. Chem. Soc.* **2015**, *137*, 7851-7861.
20. Auerhammer, N.; Schmiedel, A.; Holzapfel, M.; Lambert, C., Exciton Coupling Enhancement in the Relaxed Excited State. *J. Phys. Chem. C* **2018**, *122*, 11720-11729.
21. Schreck, M. H.; Breitschwerdt, L.; Marciniak, H.; Holzapfel, M.; Schmidt, D.; Würthner, F.; Lambert, C., Fs-Ps Exciton Dynamics in a Stretched Tetraphenylsquaraine Polymer. *Phys. Chem. Chem. Phys.* **2019**, *21*, 15346-15355.
22. Marciniak, H.; Auerhammer, N.; Ricker, S.; Schmiedel, A.; Holzapfel, M.; Lambert, C., Reduction of the Fluorescence Transition Dipole Moment by Excitation Localization in a Vibronically Coupled Squaraine Dimer. *J. Phys. Chem. C* **2019**, *123*, 3426-3432.
23. Lambert, C.; Hoche, J.; Schreck, M. H.; Holzapfel, M.; Schmiedel, A.; Selby, J.; Turkin, A.; Mitric, R., Ultrafast Energy Transfer Dynamics in a Squaraine Heterotriad. *J. Phys. Chem. A* **2021**, *125*, 2504-2511.
24. Huang, J.-S.; Goh, T.; Li, X.; Sfeir, M. Y.; Bielinski, E. A.; Tomasulo, S.; Lee, M. L.; Hazari, N.; Taylor, A. D., Polymer Bulk Heterojunction Solar Cells Employing Förster Resonance Energy Transfer. *Nat. Photonics* **2013**, *7*, 479-485.
25. Paternò, G. M.; Barbero, N.; Galliano, S.; Barolo, C.; Lanzani, G.; Scotognella, F.; Borrelli, R., Excited State Photophysics of Squaraine Dyes for Photovoltaic Applications: An Alternative Deactivation Scenario. *J. Mater. Chem. C*, **2018**, *6*, 2778-2785.
26. Khan, R.; Ningombam, A.; Singh, K.; Singh, M., Stereoelectronic Effects in the Stereoselectivity of the Diels-Alder Reactions: Reactions of Aminoanthracenes with N-

- Phenylmaleimide. *J. Chem. Pharm. Res.* **2012**, *4*, 1532-1538.
27. Tatarets, A.; Fedyunyaeva, I.; Terpetschnig, E.; Patsenker, L., Synthesis of Novel Squaraine Dyes and Their Intermediates. *Dyes Pigm.* **2005**, *64*, 125-134.
28. Inoue, T.; Pandey, S. S.; Fujikawa, N.; Yamaguchi, Y.; Hayase, S., Synthesis and Characterization of Squaric Acid Based Nir Dyes for Their Application Towards Dye-Sensitized Solar Cells. *J. Photochem. Photobiol. A* **2010**, *213*, 23-29.
29. Yum, J.-H.; Walter, P.; Huber, S.; Rentsch, D.; Geiger, T.; Nüesch, F.; De Angelis, F.; Grätzel, M.; Nazeeruddin, M. K., Efficient Far Red Sensitization of Nanocrystalline TiO₂ Films by an Unsymmetrical Squaraine Dye. *J. Am. Chem. Soc.* **2007**, *129*, 10320-10321.
30. So, S.; Choi, H.; Kim, C.; Cho, N.; Ko, H. M.; Lee, J. K.; Ko, J., Novel Symmetric Squaraine Chromophore Containing Triphenylamine for Solution Processed Small Molecule Bulk Heterojunction Solar Cells. *Sol. Energy Mater. Sol. Cells* **2011**, *95*, 3433-3441.
31. Della Pelle, A. M.; Homnick, P. J.; Bae, Y.; Lahti, P. M.; Thayumanavan, S., Effect of Substituents on Optical Properties and Charge-Carrier Polarity of Squaraine Dyes. *J. Phys. Chem. C* **2014**, *118*, 1793-1799.
32. Chen, G.; Sasabe, H.; Igarashi, T.; Hong, Z.; Kido, J., Squaraine Dyes for Organic Photovoltaic Cells. *J. Mater. Chem. A* **2015**, *3*, 14517-14534.
33. Park, J., et al., Symmetric Vs. Asymmetric Squaraines as Photosensitisers in Mesoscopic Injection Solar Cells: A Structure–Property Relationship Study. *ChemComm* **2012**, *48*, 2782-2784.
34. Law, K. Y., Squaraine Chemistry: Effects of Structural Changes on the Absorption and Multiple Fluorescence Emission of Bis[4-(Dimethylamino)Phenyl]Squaraine and Its Derivatives. *J Phys Chem* **1987**, *91*, 5184-5193.
35. Alex, S.; Basheer, M. C.; Arun, K. T.; Ramaiah, D.; Das, S., Aggregation Properties of Heavy Atom Substituted Squaraine Dyes: Evidence for the Formation of J-Type Dimer Aggregates in Aprotic Solvents. *J. Phys. Chem. A* **2007**, *111*, 3226-3230.
36. Gsänger, M.; Kirchner, E.; Stolte, M.; Burschka, C.; Stepanenko, V.; Pflaum, J.; Würthner, F., High-Performance Organic Thin-Film Transistors of J-Stacked Squaraine Dyes. *J. Am. Chem. Soc.* **2014**, *136*, 2351-2362.
37. Pandey, S. S.; Inoue, T.; Fujikawa, N.; Yamaguchi, Y.; Hayase, S., Alkyl and Fluoro-Alkyl Substituted Squaraine Dyes: A Prospective Approach Towards Development of Novel Nir Sensitizers. *Thin Solid Films* **2010**, *519*, 1066.
38. Chen, H.; Farahat, M. S.; Law, K.-Y.; Whitten, D. G., Aggregation of Surfactant Squaraine Dyes in Aqueous Solution and Microheterogeneous Media: Correlation of Aggregation Behavior with Molecular Structure. *J. Am. Chem. Soc.* **1996**, *118*, 2584-2594.
39. Shafeekh, K. M.; Soumya, M. S.; Rahim, M. A.; Abraham, A.; Das, S., Synthesis and Characterization of near-Infrared Absorbing Water Soluble Squaraines and Study of Their Photodynamic Effects in D1a Live Cells. *Photochem. Photobiol.* **2014**, *90*, 585-595.
40. Kabatc, J.; Kostrzewska, K.; Kozak, M.; Balcerak, A., Visible Light Photoinitiating Systems Based on Squaraine Dye: Kinetic, Mechanistic and Laser Flash Photolysis Studies. *RSC Adv.* **2016**, *6*, 103851-103863.
41. Liu, T.; Bondar, M. V.; Belfield, K. D.; Anderson, D.; Masunov, A. E.; Hagan, D. J.;

- Stryland, E. W. V., Linear Photophysics and Femtosecond Nonlinear Spectroscopy of a Star-Shaped Squaraine Derivative with Efficient Two-Photon Absorption. *J. Phys. Chem. C* **2016**, *120*, 11099-11110.
42. Belfield, K. D.; Bondar, M. V.; Haniff, H. S.; Mikhailov, I. A.; Luchita, G.; Przhonska, O. V., Superfluorescent Squaraine with Efficient Two-Photon Absorption and High Photostability. *ChemPhysChem* **2013**, *14*, 3532-3542.
43. Webster, S., et al., Near-Unity Quantum Yields for Intersystem Crossing and Singlet Oxygen Generation in Polymethine-Like Molecules: Design and Experimental Realization. *J. Phys. Chem. Lett.* **2010**, *1*, 2354-2360.
44. Lambert, C.; Scherpf, T.; Ceymann, H.; Schmiedel, A.; Holzapfel, M., Coupled Oscillators for Tuning Fluorescence Properties of Squaraine Dyes. *J. Am. Chem. Soc.* **2015**, *137*, 3547-3557.
45. Chang, H.-J.; Bondar, M. V.; Liu, T.; Liu, X.; Singh, S.; Belfield, K. D.; Sheely, A.; Masunov, A. E.; Hagan, D. J.; Van Stryland, E. W., Electronic Nature of Neutral and Charged Two-Photon Absorbing Squaraines for Fluorescence Bioimaging Application. *ACS Omega* **2019**, *4*, 14669-14679.
46. Eom, I.; Joo, T., Polar Solvation Dynamics of Coumarin 153 by Ultrafast Time-Resolved Fluorescence. *J. Chem. Phys.* **2009**, *131*, 244507.
47. Martin, M. M.; Plaza, P.; Chagnenet-Barret, P.; Siemiarczuk, A., Uv Vis Subpicosecond Spectroscopy of 4-(9-Anthryl)-N,N -Dimethylaniline in Polar and Nonpolar Solvents: A Two-Dimensional View of the Photodynamic“. *J. Phys. Chem. A* **2002**, *106*, 2351-2358.
48. Mohammed, O. F.; Vauthey, E., Excited-State Dynamics of Nitroperylene in Solution: Solvent and Excitation Wavelength Dependence. *J. Phys. Chem. A* **2008**, *112*, 3823-3830.
49. Kuang, Z.; He, G.; Song, H.; Wang, X.; Hu, Z.; Sun, H.; Wan, Y.; Guo, Q.; Xia, A., Conformational Relaxation and Thermally Activated Delayed Fluorescence in Anthraquinone-Based Intramolecular Charge-Transfer Compound. *J. Phys. Chem. C* **2018**, *122*, 3727-3737.
50. Snellenburg, J.; Liptonok, S.; Seger, R.; Mullen, K.; Van Stokkum, I., Glotaran: A Java-Based Graphical User Interface for the R Package Timp. *J. Stat. Softw.* **2012**, *49*, 1-22.
51. Horng, M. L.; Gardecki, J. A.; Papazyan, A.; Maroncelli, M., Subpicosecond Measurements of Polar Solvation Dynamics: Coumarin 153 Revisited. *J Phys Chem* **1995**, *99*, 17311-17337.
52. Neelambra, A. U.; Govind, C.; Devassia, T. T.; Somashekharappa, G. M.; Karunakaran, V., Direct Evidence of Solvent Polarity Governing the Intramolecular Charge and Energy Transfer: Ultrafast Relaxation Dynamics of Push–Pull Fluorene Derivatives. *Phys. Chem. Chem. Phys.* **2019**, *21*, 11087-11102.
53. Zhu, H.; Li, M.; Hu, J.; Wang, X.; Jie, J.; Guo, Q.; Chen, C.; Xia, A., Ultrafast Investigation of Intramolecular Charge Transfer and Solvation Dynamics of Tetrahydro[5]-Helicene-Based Imide Derivatives. *Sci. Rep.* **2016**, *6*, 24313.
54. Armarego, W. L. F., Chapter 3 - Purification of Organic Chemicals. In *Purification of Laboratory Chemicals (Eighth Edition)*, Armarego, W. L. F., Ed. Butterworth-Heinemann: 2017; pp 95-634.

ABSTRACT

Name of the Student: **Mr. Guruprasad M. S.**

Registration No.: 10CC14A39004

Faculty of Study: Chemical Sciences

Year of Submission: 2022

AcSIR academic center/CSIR Lab: CSIR–National Institute for Interdisciplinary Science and Technology (CSIR–NIIST)

Name of the Supervisor: Dr. V. Karunakaran

Title of the thesis: **Aminoanthracene Appended Unsymmetrical Squaraine Derivatives: Synthesis and Ultrafast Time–Resolved Photophysical Characterization for NIR Photodetectors.**

The major objectives of the thesis are to design and synthesis of *N,N*-dimethyl amino anthracene based USQ derivatives by covalently linking the various aromatic donors such as pyrrole attached phenyl hydrazine, benzothiazolium and indolium moieties to obtain the spectral sensitivity of OPDs in the NIR regime. Since the ultrafast processes of photoinduced charge–transfer, charge carrier generation and their recombination control the efficiency of the devices, steady–state and excited–state relaxation dynamics of USQ derivatives with and without PCBM have been investigated using femtosecond pump–probe spectroscopy. Finally, all the USQ derivatives were applied to the optoelectronic devices. The details of the results of each chapter are provided below.

In **Chapter 1**, an overview of SQs dyes and their optical and electronic properties, fundamentals of OPDs and NIR sensitizers used in OPDs are discussed.

In **Chapter 2**, the USQ derivatives (**APSQs**) consisting of *N,N*-dimethyl aminoanthracene and pyrrole appended aryl hydrazine with various alkyl chain lengths [ethyl (**APSQ-et**), hexyl (**APSQ-hex**), and hexenyl (**APSQ-hexen**)] attached to the pyrrolic nitrogen were synthesized. The absorption spectra of the derivatives exhibited strong absorption maximum at around 760 nm with high extinction coefficient, $\sim 1.26 \times 10^5 \text{ M}^{-1} \text{ cm}^{-1}$. Femtosecond transient absorption and TCSPC measurements exhibited the quenching of time constants, reflecting the occurrence of intermolecular charge–transfer dynamics between the **APSQs** and PCBM. NIR–OPDs were fabricated using **APSQs** as electron donors in BHJ mode. The NIR–OPDs showed a broad–band response that extends to $\sim 950 \text{ nm}$. At a reverse bias of -1 V , the device with an **APSQ-et** exhibited a maximum shot-noise-limited specific detectivity of $\sim 6 \times 10^{11} \text{ cm Hz}^{1/2} \text{ W}^{-1}$ (Jones) at a working wavelength of 840 nm.

In **Chapter 3**, the USQ derivatives (**ABSQs**) comprising of *N,N*-dimethyl aminoanthracene and benzothiazole (**ABSQ-H**) halogenated with fluoride (**ABSQ-F**), chloride (**ABSQ-Cl**) and bromide (**ABSQ-Br**) were synthesized to understand the effect of halogen on the photophysical properties and intermolecular interaction dynamics with PCBM. Interestingly the **ABSQ-H** exhibited an intense absorption ($\epsilon \sim 6.72 \times 10^4 \text{ M}^{-1} \text{ cm}^{-1}$) spectra centered at $\sim 660 \text{ nm}$. Upon halogen substitution, a red shift in the absorption spectra with an increase of molar absorptivity was observed ($\epsilon \sim 8.59 \times 10^4 \text{ M}^{-1} \text{ cm}^{-1}$) which is beneficial for NIR light harvesting. Upon the addition of PCBM, the fluorescence intensity and dynamics of halogenated **ABSQs** were quenched and the formation of a squaraine radical cation was observed, reflecting the occurrence of intermolecular charge transfer between the **ABSQs** and PCBM. The **ABSQ-H** and **ABSQ-Cl** derivatives were applied to the OPD devices and showed sensitivity in the NIR region.

In **Chapter 4**, the USQ derivatives (**AISQs**) having of *N,N*-dimethyl aminoanthracene and various *N*-alkylated indolium [ethyl (**AISQ-et**), hexyl (**AISQ-hex**) and hexenyl (**AISQ-hexen**)] were synthesized. The absorption spectra of the **AISQs** exhibited intense absorption maximum at $\sim 676 \text{ nm}$ in toluene with high extinction coefficient, $\sim 8.0 \times 10^4 \text{ M}^{-1} \text{ cm}^{-1}$. When compared to the neat solvents, the absorption spectra in the thin film exhibited a broad in shape, covering a wide range of wavelength starting from 500–800 nm due to the formation of aggregations. The femtosecond transient absorption spectra of **AISQ** derivatives revealed that the polarity of solvent controlled the excited–state relaxation dynamics. The **AISQ-et** derivative was applied to the OPD devices and showed sensitivity in the NIR region.

List of the publications emanating from the thesis work

1. **Somashekharappa, G. M.**; Govind, C.; Pulikodan, V.; Paul, M.; Namboothiry, M. A. G.; Das, S.; Karunakaran, V., Unsymmetrical Squaraine Dye–Based Organic Photodetector Exhibiting Enhanced Near–Infrared Sensitivity. *J. Phys. Chem. C* **2020**, *124*, 21730-21739.
2. **Somashekharappa, G. M.**; Paul, M.; Govind, C.; Mathew, Ranimol.; Karunakaran, V., Ultrafast Intermolecular Interaction Dynamics between NIR–Absorbing Unsymmetrical Squaraines and PCBM: Effects of Halogen Substitution. *J. Phys. Chem. B* **2022**, *126*, 4509–4519.
3. **Somashekharappa, G. M.**; Paul, M.; Govind, C.; Karunakaran, V., Excited State Relaxation Dynamics of Indoline Appended Unsymmetrical Squaraine Dyes for Photodetector Applications: (To be submitted).

List of publications from other related works

1. Neelambra, A. U.; Govind, C.; Devassia, T. T.; **Somashekharappa, G. M.**; Karunakaran, V., Direct Evidence of Solvent Polarity Governing the Intramolecular Charge and Energy Transfer: Ultrafast Relaxation Dynamics of Push–Pull Fluorene Derivatives. *Phys. Chem. Chem. Phys.* **2019**, *21*, 11087-11102.

List of posters presented in conferences

1. **Somashekharappa, G. M.**; Govind, C.; Karunakaran, V.; and Das, S., Synthesis and Photophysical Characterization of Phenyl–Hydrazine Based Unsymmetrical Squaraine Derivatives, International Conference on Advanced Functional Materials (ICAFM–2019). CSIR–National Institute for Interdisciplinary Science and Technology, Thiruvananthapuram 695 019, Kerala, India, December, 9–10, **2019**.
2. **Somashekharappa, G. M.**; Govind, C.; Pulikodan, V.; Paul, M.; Namboothiry, M. A. G.; Das, S.; Karunakaran, V., Efficient Near–Infrared Organic Photodetector Based on Unsymmetrical Squaraine/PCBM Heterojunction, International Conference on Materials for the Millennium (MatCon–2021), Cochin University of Science and Technology (CUSAT), Kochi, Kerala, India, March15-19, **2021**.

Unsymmetrical Squaraine Dye-Based Organic Photodetector Exhibiting Enhanced Near-Infrared Sensitivity

Guruprasad M. Somashekarappa, Chinju Govind, Vijith Pulikodan, Megha Paul, Manoj A. G. Namboothiry,* Suresh Das,* and Venugopal Karunakaran*

Cite This: *J. Phys. Chem. C* 2020, 124, 21730–21739

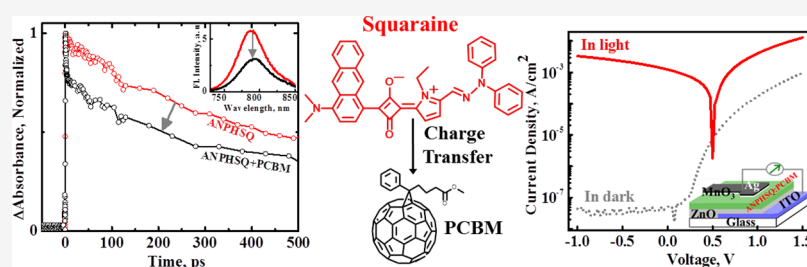
Read Online

ACCESS |

Metrics & More

Article Recommendations

Supporting Information



ABSTRACT: An unsymmetrical squaraine (SQ) derivative containing anthracene and phenyl hydrazine (ANPHSQ) units linked to the central SQ was synthesized and used as electron donors in bulk heterojunction photovoltaic mode organic photodetectors (OPD), containing PCBM as the electron acceptor. Although the ANPHSQ exhibited a strong narrow band in the near infrared peaking at ~ 760 nm in solution, the OPD constructed with this dye exhibited a broad spectral response extending to 950 nm. The enhanced sensitivity in the long wavelength region could be attributed to formation of ANPHSQ aggregates within the devices. A photocurrent of 1.3 mA/cm^2 , almost 3–5 orders of magnitude larger than the dark current ($\sim 50 \text{ nA/cm}^2$), was observed in the presence of light at -1 V bias condition. Devices showed an increase in external quantum efficiency from ~ 4 to $\sim 12\%$ as the bias varied from 0 to -1 V. At a reverse bias of -1 V, the device with a ANPHSQ exhibited a maximum shot-noise-limited specific detectivity of $6 \times 10^{11} \text{ cm Hz}^{1/2} \text{ W}^{-1}$ (Jones) @ 840 nm with an ultrafast photoresponse in the range of ~ 15 ns. The study of relaxation dynamics of the ANPHSQ excited state using femtosecond pump–probe spectroscopy and time-correlated single-photon counting indicated efficient charge transfer between the excited state of ANPHSQ and PCBM.

1. INTRODUCTION

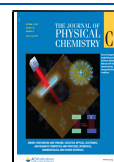
The detection of near-infrared (NIR) photons in the range of 700–1500 nm is important for the development of photodetectors, which are used for a variety of applications including *vivo* imaging,¹ biomedicine,^{2,3} therapeutic,^{4,5} optical communications,⁶ remote monitoring,^{7,8} and night vision.⁹ The potential of NIR imaging has however not been fully realized mainly because of the high cost of conventional inorganic semiconductor-based NIR photodetectors arising from difficulties involved in their fabrication and requirement of low-temperature operations. In view of this, there is a growing interest in the use of organic semiconductors which can be solution-processed onto large-area flexible surfaces using conventional printing technologies to provide affordable photodetectors. Although the use of several NIR dyes including cyanines,^{10–13} phthalocyanines,^{14,15} and porphyrins^{16,17} as organic semiconductors for the development of NIR organic photodetectors (OPDs)¹⁸ has been explored, several issues including low solubility, decreased stability with decrease in the band gap, and inability to form uniform films have remained as important issues that need to be addressed. Recently, there has been a growing interest in the use of a class

of ambipolar molecules, namely, symmetric SQ dyes. These dyes possess a unique electron donor–acceptor–donor molecular architecture, consisting of a central electron-deficient four-membered ring connected to two electron-donating chromophores. Such symmetric SQ's exhibit sharp and intense light absorption ($\epsilon > 200,000 \text{ M}^{-1} \text{ cm}^{-1}$), high emission yield ($\Phi \sim 0.8$) in the visible–NIR region,¹⁹ and large two photon absorption cross-sections ($\sim 10^4 \text{ GM}$).^{20,21} Binda et al. developed fast, air stable, and efficient NIR planar photodetector based on bulk heterojunction (BHJ) operating in air without encapsulation of devices, showing an external quantum efficiency (EQE) of 3.5% at 670 nm with response speed in the range of 240 ns. Recently, they reported an OPD using hydrazine-based symmetric SQ dyes with PCBM, exhibiting an EQE of 15% with detectivity and a dark current

Received: July 16, 2020

Revised: August 20, 2020

Published: September 10, 2020



of $3.4 \times 10^{12} \text{ Hz}^{0.5} \text{ cm/W}$ at 700 nm and 2 nA/cm^2 , respectively.²² Bellani et al.²³ developed a OPD using indole-based SQ derivative with PCBM showing the EQE of 12% at 590 nm, and charge transport properties of these devices in the dark were also characterized using admittance spectroscopy. Most of the OPDs based on SQ have utilized symmetrical squaraines, and their spectral window was limited to ~ 800 nm. Here, we report the design of an unsymmetrical SQ which can extend the spectral window of OPDs based on SQ to ~ 950 nm. Unsymmetrical squaraine dyes can be more versatile for optoelectronic applications in view of the tunability of their absorption and excited state properties easily brought about by varying the difference in the electron-donating ability of the peripheral substituents.²⁴ Moreover, in unsymmetrical SQ derivatives, the unidirectional flow of electron in the excited state can lead to improved charge separation, resulting in higher photocurrents, compared to the symmetrical derivatives.²⁵ In view of this, we have synthesized the unsymmetrical SQ dye (ANPHSQ) comprising of *N,N* dimethylated aminoanthracene and aryl hydrazine-appended pyrrole with the ethyl group attached to the pyrrolic nitrogen. This compound exhibited intense NIR absorption ($\epsilon \sim 10^5 \text{ M}^{-1} \text{ cm}^{-1}$) at 760 nm, and the optical band gap was estimated to be 1.52 eV which is ideal for designing fullerene-based BHJ optoelectronic devices. Photodetectors developed using the ANPHSQ sensitizer exhibited a high detectivity of $6 \times 10^{11} \text{ cm Hz}^{1/2} \text{ W}^{-1}$ (Jones) @ 840 nm with an ultrafast photoresponse in the range of ~ 15 ns.

The excited state relaxation dynamics of symmetric SQs,²⁶ SQ polymers,^{27,28} and SQ in optoelectronic devices²⁹ have been extensively studied in order to explore the relationship between efficiency of devices and charge carrier dynamics.^{30–32} With a view to understanding these aspects, we have also undertaken a detailed study of the photophysical properties including excited state dynamics of ANPHSQ and these aspects are also reported.

2. EXPERIMENTAL SECTION

2.1. General Details. The chemicals and reagents used for synthesis were purchased from Sigma-Aldrich, Merck, and TCI. Dry solvents were prepared by following the reported procedures.³³ ^1H NMR spectra were measured using Bruker AMX 500 MHz spectrometer using tetramethylsilane as the internal standard. High-resolution mass spectra of the compounds were recorded using the Thermo Scientific Exactive–liquid chromatography–mass spectrometry. The solvents used for the spectroscopic measurements were of high-performance liquid chromatography grade (Merck) and used as received.

2.2. Synthesis of Unsymmetrical Squaraine. The synthetic route and chemical structure of intermediates and the desired ANPHSQ derivative are shown in Scheme S1, and experimental details are provided in Supporting Information. The unsymmetrical ANPHSQ derivative was synthesized by modifying previously reported procedures.^{34–36} *N,N*-Dimethyl aminoanthracene semisquaraine was obtained by the reduction and methylation of 1-aminoanthraquinone, and resultant *N,N* dimethyl aminoanthracene reacted with squarylium chloride. The ethyl pyrrole-appended arylhydrazine was refluxed with the *N,N*-dimethyl aminoanthracene semisquaraine in benzene: butanol azeotropic mixture (1:1) yielding the ANPHSQ derivative. The structure of the compounds is characterized

by ^1H and ^{13}C NMR and high-resolution mass spectrometry, and spectral data are provided in Supporting Information.

2.3. Thin-Film Preparation. The thin film of ANPHSQ was prepared by the drop-casting method. A solution of ANPHSQ in chloroform with a concentration of 1.5 mM was used to prepare the thin film. The solution was dropped on the quartz window and allowed to dry for an hour in room temperature.

2.4. Steady-State Measurements. Absorption spectra were recorded using a Shimadzu UV-2600 UV–visible absorption spectrophotometer. Steady-state fluorescence experiments were performed with a Fluorolog-3 (Horiba) which was equipped with a 450 W Xe arc lamp. The fluorescence quantum yields in different solvents were measured by using the integrating sphere (Quanta- ϕ , Horiba) following a reported procedure.³⁷

2.5. Electrochemical Measurements. Cyclic voltammetry experiments were performed using a BAS CV-50W voltammetric analyzer with three electrode cell assemblies. Glassy carbon electrode, Ag/AgCl electrode, and platinum wire were used as working, reference, and counter electrodes, respectively. The measurements were carried out in DCM with tetrabutylammoniumhexafluorophosphate (TBAPF₆) as the supporting electrolyte at a scan rate of 50 mV s^{-1} . The ferrocene/ferrocenium (Fc/Fc⁺) redox couple was used as an external standard. All solutions for the electrochemical studies was degassed with argon before the measurements.

2.6. Time-Correlated Single-Photon Counting. Fluorescence decays were measured using a picosecond single-photon counting system (Horiba, DeltaFlex) with the 670 nm light-emitting diode (LED) as the excitation source and the picosecond photon detection module (PPD-850) as the detector. Time resolution of the TCSPC experimental setup is <200 ps with the 670 nm LED source. The fluorescence time constants are obtained by deconvoluting with the LED profile. The decay of the fluorescence intensity (I) with time (t) was fitted by single exponential function

$$I = Ae^{-t/\tau} \quad (1)$$

where τ and A are the fluorescence lifetime and its amplitude of the compound, respectively.

2.7. Femtosecond Transient Absorption Measurements. The instrument details for measuring the femtosecond transient absorption spectra have been discussed elsewhere.³⁸ It is a Ti:sapphire laser (MaiTai HP, Spectra Physics, USA) centered at 800 nm, having 80 MHz repetition rate with a pulse width of <100 fs. The amplified laser was split into two, and the high-energy beam was used as the pump (670 nm) for exciting the sample by using TOPAS (Prime, Light Conversion). The other part of the amplified beam (200 mW) focused on a 1 mm-thick CaF₂ plate to generate white light continuum (340–1000 nm) which further split into two beams (sample and reference probe beams). The sample cell (0.4 mm path length) was refreshed by rotating at a constant speed. Finally, the white light continuum was focused into a 100 μm optical fiber coupled to an imaging spectrometer after passing through the sample cell. The pump–probe spectrophotometer (ExciPro) setup was purchased from CDP Systems Corp, Russia. Normally transient absorption spectra were obtained by averaging about 2000 excitation pulses for each spectral delay. All the measurements were carried out at the magic angle (54.7°). All the transient absorption spectra obtained from the equipment is compensated for chirp of the

white light by determining the time zero using the coherent artefact observed in the solvent.³⁹ The absorbance of the solution used was ~ 0.5 OD in 1 mm path length, and the excitation energy was $\sim 2 \mu\text{J}$ for all the measurements. The effective time resolution of the ultrafast spectrometer is determined to be about ≤ 120 fs. The concentration of ANPHSQ derivatives used for transient absorption measurement was $\sim 40 \mu\text{M}$. The integrity of the sample is tested by measuring the absorption spectra of the sample before and after the experiments, and no significant changes were found in the absorption spectra.

2.8. Device Fabrication. Photodetectors were fabricated in the device architecture, glass/indium tin oxide (ITO)/zinc oxide (ZnO)/ANPHSQ:PCBM/molybdenum trioxide (MoO_3)/silver (Ag). ITO-coated glass plates were cleaned using detergent and deionized water. Further, the samples were ultrasonicated for 30 min each in acetone, isopropanol, and methanol, respectively. Just before making devices, the ITO glass plate was dried in a vacuum oven for 1 h. A 30 nm-thick ZnO films are spin-coated on ITO by using a ZnO nanoparticle solution, as mentioned previously.⁴⁰ The ANPHSQ:PCBM (1:6 ratio) blend in toluene (42 mg/mL) was spin-coated on top of ZnO to make a 100 nm-thin active layer film. A hole transporting layer of 10 nm MoO_3 and back contact Ag of 100 nm were deposited by thermal evaporation. A shadow mask was used for thermal evaporation to make an active area of 3×3 mm.

2.9. Device Characterization. Current–voltage (J – V) characteristics of OPD was recorded in dark and light using a Keithley 6430 source measuring unit (Tektronix USA). Oriol class 3A solar simulator of intensity $100 \text{ mW}/\text{cm}^2$ with AM 1.5 G filter was used as a light source for conducting light J – V measurements. EQE spectra of OPDs are measured using a lock in technique. In this method, the photocurrent is measured with respect to wavelength using a lock-in amplifier (Stanford Research SR830), which is locked at a nonharmonic light-chopping frequency. A Xenon lamp coupled with a monochromator and order sorting filters was used as the light source (250 W Xenon lamp). All the measurements were calibrated with a NREL-calibrated silicon solar cell. The specific detectivity was calculated without measuring the noise current. Even though the determination of noise current is essential for the accurate measurement of specific detectivities, it is not always performed because of its challenging experimental techniques. Instead, the dark current i_d is often assumed to be the dominant contribution to noise current.⁴¹ Hence, the specific detectivity [$D^*(\lambda)$] of the OPDs was calculated using by simplifying the shot-noise-limited specific detectivity equation as given below.⁴²

$$D^* = \frac{R(\lambda)\sqrt{AB}}{i_{\text{noise}}} = \frac{R(\lambda)\sqrt{A}}{\sqrt{2qi_d}} = \frac{R(\lambda)}{\sqrt{2qJ_d}} \quad (2)$$

where $R(\lambda)$, A , and B represent responsivity, area, and dark current density of the device, respectively. i_{noise} , i_d , and J_d represent the noise current, dark current, and dark current density, respectively, whereas q represents the charge of electron. Response time of the OPDs was measured using photovoltage and photocurrent transient measurements. A 532 nm picosecond pulsed laser (Ekspla Nd:YAG laser delivering pulses of duration 100 ps) was used as an excitation pulse with a repetition rate of 10 Hz. Transient signals were measured using 1 GHz, Tektronix MDO3104 oscilloscope. All the

measurements were performed under ambient condition without noticeable degradation of the devices.

3. RESULTS AND DISCUSSION

3.1. Steady-State Photophysical Characterization.

3.1.1. Solution State. The steady-state absorption and emission spectra of ANPHSQ were measured in solvents of varying polarities (Figures 1 and S1). Solutions of ANPHSQ in

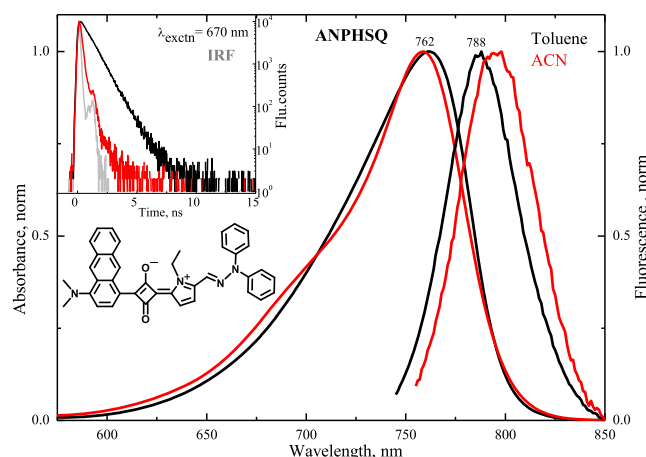


Figure 1. Steady-state absorption and emission spectra of ANPHSQ in toluene (black) and ACN (red) at room temperature. Inset shows the fluorescence decay profiles obtained by exciting at 670 nm.

toluene showed a sharp and intense absorption band in the NIR region with a maximum at around 762 nm ($\epsilon = 1.26 \times 10^5 \text{ M}^{-1} \text{ cm}^{-1}$). The absorption maximum of the derivative did not change significantly with increase in solvent polarity, indicating negligible solvent reorganization during the electronic transition.^{43,44} The fluorescence spectra of ANPHSQ in toluene exhibited a maximum at around 788 nm, indicating a Stokes shift of $\sim 430 \text{ cm}^{-1}$. The observation of similar spectral features in the absorption and emission spectra of ANPHSQ and small Stokes shift reflect the comparable molecular configurations in the ground and excited states. The fluorescence lifetime of ANPHSQ in various solvents was measured by exciting at 670 nm, and decay profiles in toluene and acetonitrile (ACN) are shown in the inset of Figure 1. The fluorescence lifetime of ANPHSQ in toluene was found to be around 0.83 ns, and with increase in solvent polarity, it decreased to 0.14 ns in ACN. The absolute fluorescence quantum yield of ANPHSQ also decreased with increase of the solvent polarity from 0.28 in toluene to 0.02 in ACN. The observation of decrease of fluorescence quantum yield and lifetime reveal the involvement of a nonradiative pathway sensitive to the electronic redistribution in the excited ANPHSQ derivative and/or formation of the solute–solvent complexes with increase of polarity.^{31,45} The details of the absorption and emission maxima, Stokes shift, fluorescence lifetime, and absolute quantum yield of ANPHSQ are summarized in Table 1. The radiative and nonradiative rate constants for ANPHSQ (Table 1) were calculated from the fluorescence quantum yield (Φ) and lifetime (τ_f) values using the following equation

$$K_r = \frac{\Phi}{\tau_f} \text{ and } K_{\text{nr}} = \frac{1}{\tau_f} - K_r \quad (3)$$

Table 1. Absorption and Fluorescence Maxima, Quantum Yield, and Lifetime of ANPHSQ in Different Solvents

solvents	absorption max, nm (λ_{max})	fluorescence max, nm (λ_{max})	stokes shift, cm^{-1} ($\Delta\nu$)	fluorescence quantum yield ^a (Φ_f)	fluorescence lifetime ^b , ns (τ)	radiative constant, $\times 10^7 \text{ s}^{-1}$ (K_r)	nonradiative constant, $\times 10^7 \text{ s}^{-1}$ (K_{nr})
toluene	762	788	433	28.79	0.83	34	85
chloroform	764	790	431	20.83	0.43	48	184
THF	766	790	397	20.87	0.56	37	141
MeOH	761	793	531	1.15	0.08	15	1412
ACN	758	798	661	2.75	0.15	19	695

^aAbsolute fluorescence quantum yield obtained upon excitation at 600 nm using an integrating sphere. ^bFluorescence lifetime was obtained upon excitation at 670 nm, and the χ^2 value of fluorescence kinetics fit is between 1.0 and 1.2.

where k_r and k_{nr} represent the radiative and nonradiative rate constants, respectively.

3.1.2. Film State. Figure 2 shows normalized absorption spectra of the ANPHSQ derivative in films formed by drop-

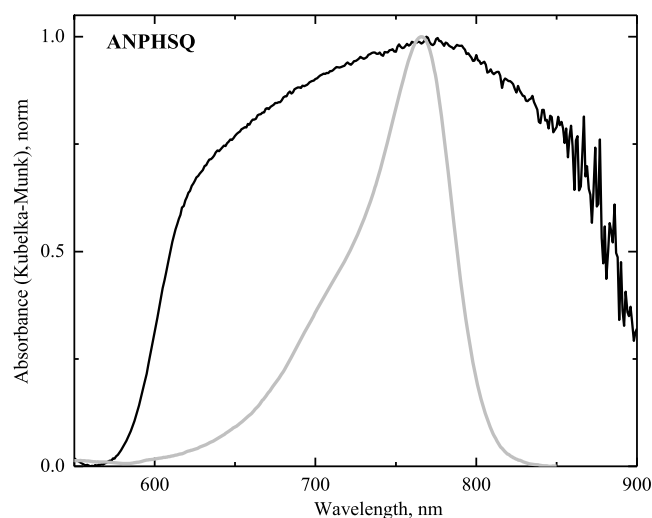


Figure 2. Absorption spectra of ANPHSQ in the thin film (black) and chloroform solution (gray) normalized at 766 nm.

casting a solution of the compound (1.5 mM) in chloroform. The absorption spectra of the film exhibited a broad band ranging from 600–900 nm, indicating the formation of both H- and J-type aggregates.^{46–50} by the strong intermolecular forces between the ANPHSQ molecules. Such a wide range of wavelengths with a high extinction coefficient will be significantly beneficial for light harvesting.⁵¹ It is to be noted that as the absorption spectra of ANPHSQ in the thin film is broad in nature and its emission intensity quenches drastically (Figure S2) due to the formation of various degrees of aggregates, it would be difficult to distinguish the effect of solvent in the thin film made from the solution of ANPHSQ dissolved in different solvents.

3.2. Electrochemical Properties. Cyclic voltammetry of a 1 mM solution of ANPHSQ in ACN was measured using ferrocene as the standard, and the voltammograms obtained are shown in Figure S3a. The highest occupied molecular orbital (HOMO) and lowest unoccupied molecular orbital (LUMO) energy levels of the ANPHSQ derivative in eV can be obtained from the following equations

$$\begin{aligned} \text{HOMO(ANPHSQ)} \\ = -[4.8 - E_{\text{ox}}(\text{Fc}/\text{Fc}^+ \text{ vs Ag}/\text{AgCl}) \\ + E_{\text{ox}}(\text{ANPHSQ vs Ag}/\text{AgCl})] \end{aligned} \quad (4)$$

$$\text{LUMO(ANPHSQ)} = E_{\text{HOMO}} + E_{00} \quad (5)$$

where $E_{00} = 1242/\lambda_{\text{onset}}$. The HOMO and LUMO energy levels of the ANPHSQ derivative are found to be around -4.79 and -3.26 eV, respectively. The LUMO energy level of the derivative was higher compared to that of the PCBM (-3.7 eV), and the HOMO energy level of the PCBM (-6.1 eV) was also lower compared to that of the ANPHSQ derivative. Thus, the energy levels of the derivative is suitable for it to act as a donor material in the BHJ-based photodetector with PCBM as an acceptor.

3.3. Interaction with PCBM. The absorption and fluorescence spectra of ANPHSQ upon addition of PCBM (4.5–13.5 mM) in toluene were measured. With increase of concentration of PCBM, there were no significant changes in the absorption spectra of ANPHSQ derivative, whereas the fluorescence intensity of the ANPHSQ derivative decreased significantly (Figure 3), indicating the possibility of excited

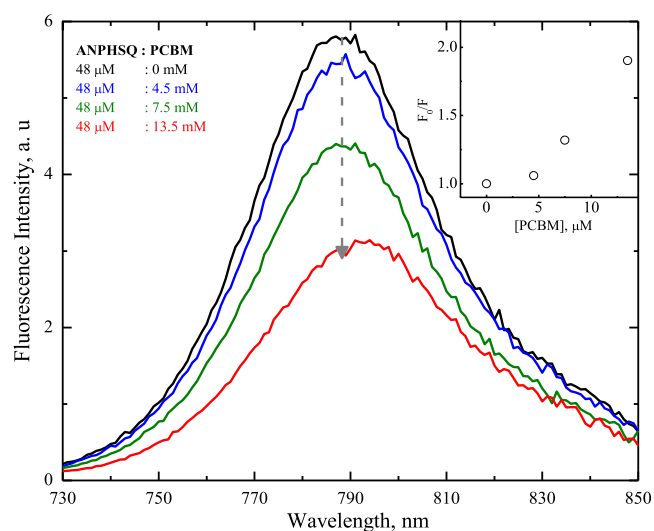


Figure 3. Fluorescence spectra of ANPHSQ containing PCBM in toluene. The inset shows the plot of F_0/F vs $[\text{PCBM}]$.

state interactions between ANPHSQ and PCBM. The Stern–Volmer plot (inset, Figure 3) for fluorescence quenching of ANPHSQ with increase of concentration of PCBM showed a nonlinear behavior (positive deviation), suggesting the occurrence of both the static and dynamic quenching mechanism in the excited state deactivation. The fluorescence lifetime of ANPHSQ derivative in the presence of PCBM was measured by exciting the solution at 670 nm. In the presence of PCBM (13.5 mM), the fluorescence lifetime decreased from 750 to 660 ps, reflecting the occurrence of dynamic (diffusion controlled) quenching in the excited state. The bimolecular

quenching rate constant (K_q) obtained from the relationship, $K_q = K_{SV}/\tau_0$, was $5.11 \times 10^{11} \text{ M}^{-1} \text{ s}^{-1}$, where τ_0 is the fluorescence lifetime of the ANPHSQ derivative in the absence of PCBM. The Stern–Volmer quenching constant (K_{SV}) obtained from the equation $F_0/F = 1 + K_{SV} \times [\text{PCBM}]$ was $42.4 \times 10^3 \text{ M}^{-1}$. The decrease of fluorescence intensity and lifetime of ANPHSQ upon addition of PCBM can be attributed to the charge transfer from the excited state of ANPHSQ to PCBM.

3.4. Time-Resolved Photophysical Characterization.

3.4.1. Femtosecond Transient Absorption Spectra of ANPHSQ. Femtosecond time-resolved transient absorption spectra were measured in nonpolar (toluene) and polar (ACN) solvents upon excitation at 670 nm using femtosecond pump–probe spectroscopy in order to understand the effect of solvent polarity on the excited state relaxation dynamics of the excited state of ANPHSQ. Transient absorption spectra of ANPHSQ in toluene covering the wavelength range of ~ 345 –585 nm are shown in Figure 4. In Figure 4, panel a shows the spectral evolution of ANPHSQ recorded from 900 fs to 1.47 ns. At the early time scales, two transient absorption bands centered at around 421 and 525 nm are observed. As the decay profile of the peaks at ~ 421 and 525 nm is found to be the

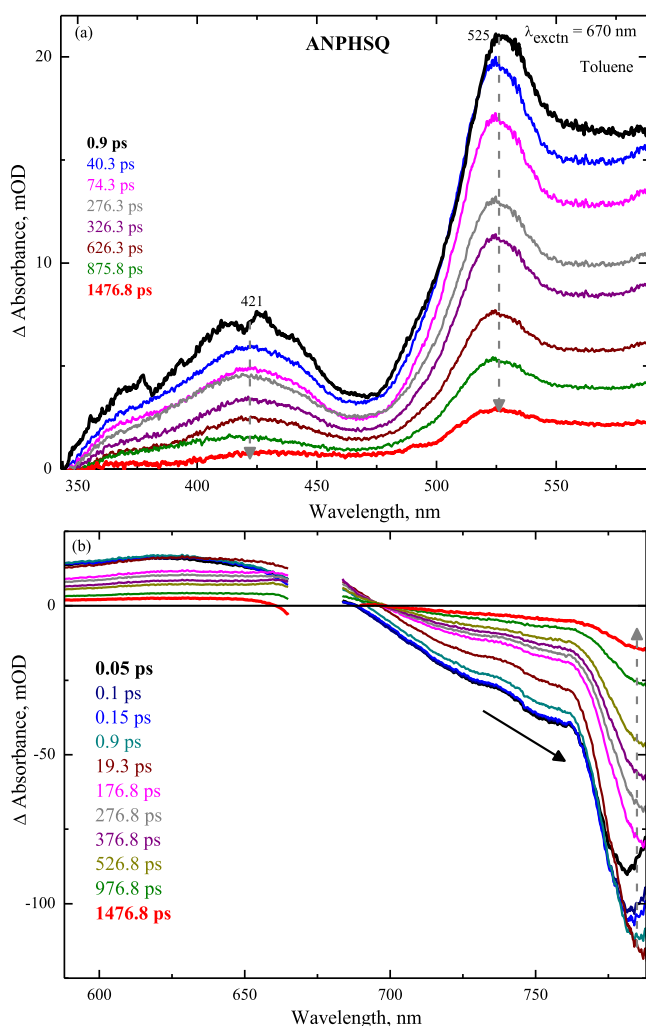


Figure 4. Femtosecond transient absorption spectra of ANPHSQ in toluene upon excitation at 670 nm in the shorter (a) and longer (b) wavelength regions at different delay times.

same, the positive bands are attributed to the excited singlet state absorption of the molecule ($S_n \leftarrow S_1$ transition). The transient absorption spectra in the longer wavelength region (~ 585 –788 nm, Figure 4b) indicating the negative transient absorption peak at ~ 788 nm which coincided with the steady-state emission maximum attributed to stimulated emission. Similar results were obtained for the transient absorption spectra of ANPHSQ in ACN on excitation at 670 nm (Figure S4). However, the excited state relaxation dynamics of the ANPHSQ derivative are faster in ACN when compared to toluene (Figure S5a) because of the change in the solvation relaxation processes.^{52–54}

The dynamics of photogenerated charge separation between the excited state of ANPHSQ and PCBM was investigated by measuring the transient absorption spectra of ANPHSQ and PCBM mixture upon excitation at 670 nm. The transient absorption spectral features of the mixture (Figure S6) are found to be the same when compared to the ANPHSQ alone in toluene. However, the decay profile of ANPHSQ with the PCBM mixture probed at 525 and 760 nm in toluene (Figure S5b,c) indicated significant reduction in lifetime when compared to that of ANPHSQ alone.

The femtosecond transient absorption spectra were analyzed using GLOTARAN⁵⁵ by global analysis, and three exponential components were optimally obtained to completely describe the excited relaxation dynamics. The resultant time constants are given in Table 2, and the corresponding decay associated spectra are shown in Figure S7 in Supporting Information. The fast component ($\tau_1 = 412$ fs in ACN and $\tau_1 = 2.5$ ps in toluene) can be assigned to the solvation relaxation processes from the Franck–Condon state to the solvent-stabilized local excited state^{56,57} based on the observation of the redshift of stimulated emission (~ 763 nm) and blueshift of excited state absorption (~ 525 nm) with increasing time. The time constant τ_2 , 10.78 and 114.8 ps, for ACN and toluene respectively, could be attributed to the dark state, resulting from the conformational changes of ANPHSQ, as result of a charge transfer stabilization in the polar solvent. This state facilitates the nonradiative deactivation to the ground state supporting the observation of decrease of fluorescence quantum yield and lifetime in ACN (Table 1). Finally, the longer time constant τ_3 resulted from the global analysis is consistent with the fluorescence lifetime obtained from the TCSPC in neat solvents (Table 1). Hence, the time constant of 122 (747) ps is attributed to the lifetime of excited singlet state of ANPHSQ in ACN (toluene). Interestingly, upon addition of PCBM, the transient absorption measurements exhibited the quenching of all the time constants especially τ_3 consistent with the quenching of fluorescence dynamics observed in the TCSPC. Such decrease of time constants further supports the occurrence of the charge transfer between ANPHSQ and PCBM.

3.5. Characterization of the Photodetector. The favorable charge transfer properties of ANPHSQ in the presence of PCBM was explored to make OPDs. OPDs were fabricated using ANPHSQ as sensitizers, and its device structure and the corresponding energy level diagram are depicted in Figure 5a,b respectively. The ratio between the ANPHSQ and PCBM was optimized to balance exciton dissociation and free carrier transport across the OPDs. The current density versus voltage (J – V) characteristics of the OPDs are shown in Figure 5c. The asymmetric J – V characteristics are attributed to the different hole-tunneling

Table 2. Time Constants Obtained by Global Analysis Using GLOTARAN⁵⁵ for the ANPHSQ Derivative Upon Excitation at 670 nm

sample	ACN	Toluene	
		−PCBM	+PCBM
ANPHSQ	$\tau_1 = 0.41 \pm 0.10$ ps	$\tau_1 = 2.53 \pm 0.20$ ps	$\tau_1 = 1.50 \pm 0.20$ ps
	$\tau_2 = 10.78 \pm 0.50$ ps	$\tau_2 = 114.81 \pm 2.20$ ps	$\tau_2 = 62.52 \pm 1.20$ ps
	$\tau_3 = 122.20 \pm 2.30$ ps	$\tau_3 = 747.84 \pm 6.20$ ps	$\tau_3 = 625.05 \pm 5.20$ ps

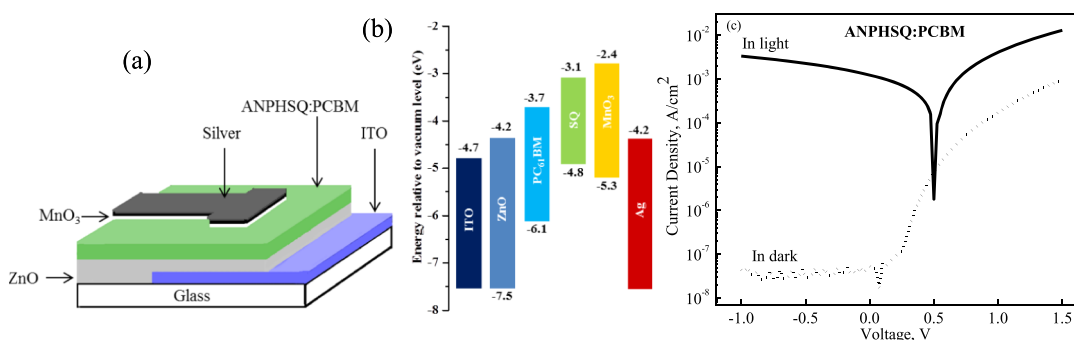


Figure 5. (a) Fabricated OPD structure, (b) band diagram for fabricated OPD, and (c) J – V characteristics in dark and light in semi-logarithmic.

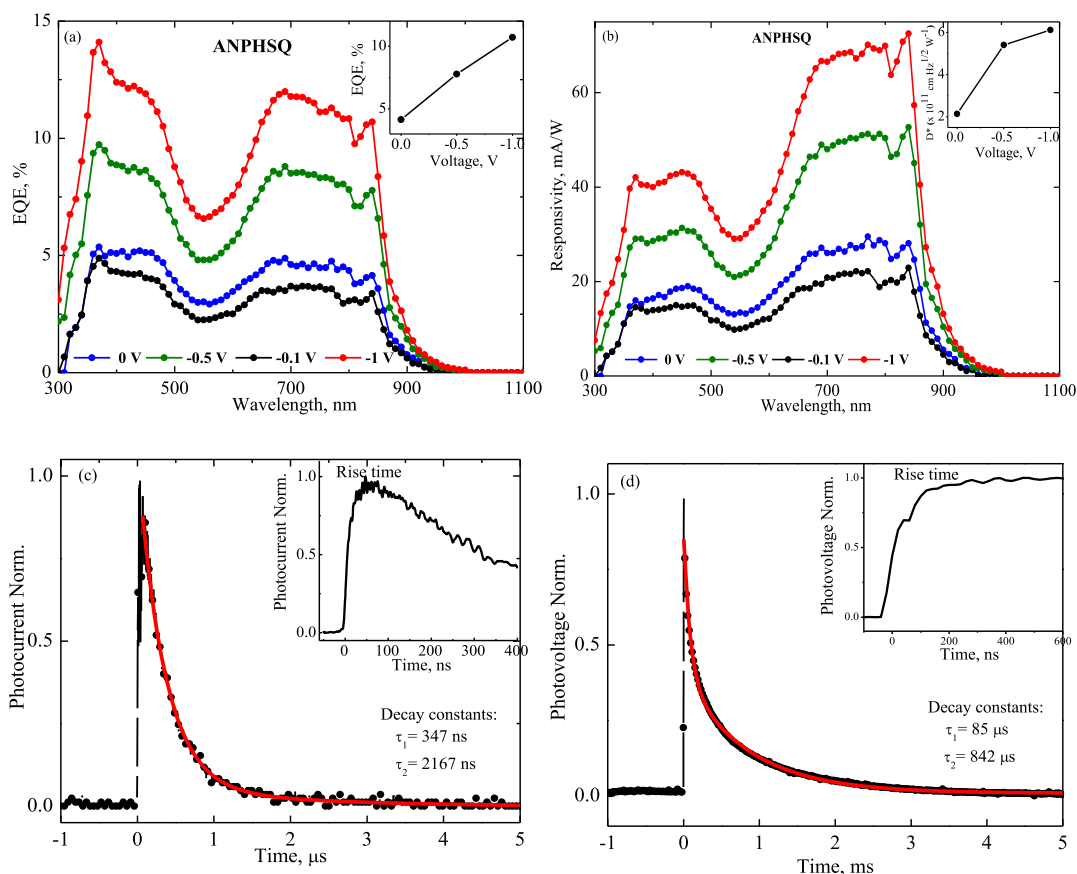


Figure 6. EQE spectra (a) and spectral responsivity (b) of devices using ANPHSQ:PCBM at different bias conditions. Insets of (a,b) show EQE and specific detectivity of devices at negative bias voltage at 532 nm, respectively. TPC (c) and photovoltage decay (d) and their rise time responses (insets) of OPD detectors.

injection barriers at the electrode/active layer interface. The hole-tunneling injection from the silver (Ag) electrode is easier than that from the ITO electrode. Hence, the dark current in the reverse bias is much lesser than in the forward bias. The light current densities of the OPDs are markedly increased under white light illumination compared to dark current. A

current value of 1.3 mA/cm^2 is observed in the presence of light, which is almost 3–5 orders of magnitude larger than the dark current ($\sim 50 \text{ nA/cm}^2$) at -1 V bias condition (with respect to ITO) of the OPD. In the presence of light, current shows a gradual increase with increase of the reverse bias. This

can be attributed to enhanced charge extraction and decrease of nongeminate losses in the presence of high electric field.⁵⁸

The spectral response of the OPDs under different bias conditions is shown in Figure 6a. The EQE spectrum follows the absorption spectra of the blend, showing the features of both PCBM and ANPHSQ. EQE in the wavelength (λ) range 300 nm < λ < 500 nm is attributed to the PCBM and that in the λ range 600 nm < λ < 950 nm is attributed to ANPHSQ. It is to be noted that the cause of the dip is due to the low absorbance of the ANPHSQ and PCBM mixture at around 550 nm. The photocurrent is due to efficient photogenerated exciton dissociation at the ANPHSQ/PCBM interface and its transfer to the external circuit through the interface layers. It is observed that the EQE values increase with the increasing reverse bias voltages. Devices showed an EQE increase from ~4% at short circuit condition to ~12% at -1 V in the NIR region, with the peak EQE at ~840 nm. Field-dependent dissociation of bound electron–hole pairs, the increased hole-transport velocity in the active layer with increasing electric field, and increased hole-tunneling injection can be the reason for such an increase in EQE.⁵⁹

Figure 6b shows the responsivity curve of the OPDs, which clearly shows a broad spectral range response extending to $\lambda \sim 950$ nm. The spectral profile of responsivity peaks around 700 and 840 nm. The responsivity is 25 and 70 mA/W for unbiased and biased (-1 V) devices, respectively (Figure 6b) at $\lambda \sim 840$ nm. The responsivity of the OPD is greatly enhanced with an increase in reverse bias, consistent with the increase in photocurrent with reverse bias. The combination of reduced dark current and enhanced EQE led to a dramatically improved shot-noise-limited specific detectivity (D^*) in the NIR region. At a reverse bias of -1 V, the device with an ANPHSQ exhibited a maximum D^* of 6×10^{11} cm Hz^{1/2} W⁻¹ (Jones) at a working wavelength of 840 nm (Figure 6b inset). It is worth noting that D^* monotonically increases as the reverse bias increases for all the devices.

Transient photovoltage (TPV) and transient photocurrent (TPC) measurements are an established technique for probing the charge carrier dynamics of photodetector devices.

The TPC signal is used to reveal the charge extraction dynamics, whereas the TPV signal is a good measure of the charge carrier density in the OPD. A combination of TPC and TPV studies shows insight into the recombination rate of the photogenerated charge.⁶⁰ Figure 6c,d shows the TPC and TPV for the ANPHSQ devices under 532 nm laser light pulses. A double exponential equation as shown below is used to fit the light OFF decay transient curve to determine the decay time constants.

$$y = A_1 e^{(-x/t_1)} + A_2 e^{(-x/t_2)} + y_0 \quad (6)$$

The response envelope of both the TPC and TPV transients is similar. However, the TPC decay time is typically 2–3 order of magnitude faster than the TPV time. The difference can be due to the (i) TPV signal is measured at approximately open circuit, so the decay primarily represents the charge recombination dynamics and the (ii) TPC signal is measured close to short circuit, so the signal decay predominantly represents the charge extraction (which occurs on a faster timescale).⁶¹ All the transient measurements are done in short-circuit condition. The devices display a fast pulse response with short rise times and longer fall times. From the insets of Figure 6c,d, it is clear that both the current and the voltages are rising

within few nanoseconds. Hence, the OPDs in the photovoltaic mode shows an ultrafast response in the range of ~15 ns.

4. CONCLUSIONS

The unsymmetrical SQ derivative (ANPHSQ) possessing anthracene and phenyl hydrazine as donor moieties was synthesized, and their steady-state and excited state relaxation dynamics were investigated. The absorption spectra of the ANPHSQ derivative exhibited strong absorption maximum at around 760 nm with a high extinction coefficient, $\sim 1.26 \times 10^5$ M⁻¹ cm⁻¹. Femtosecond transient absorption and TCSPC measurements revealed the quenching of time constants reflecting the occurrence of charge transfer dynamics between the ANPHSQ and PCBM. OPDs were fabricated using asymmetric ANPHSQ working in the photovoltaic mode. The OPDs showed a broad spectral response extending to $\lambda \sim 950$ nm. A photocurrent value of 1.3 mA/cm² is observed in the presence of light, which is almost 3–5 orders of magnitude larger than the dark current (~ 50 nA/cm²) at -1 V bias condition of the OPD. Devices showed an EQE increase from ~4% at short circuit condition to ~12% at -1 V in the NIR region, with the peak EQE at ~840 nm. At a reverse bias of -1 V, the device with an ANPHSQ exhibited a maximum shot-noise-limited specific detectivity of 6×10^{11} cm Hz^{1/2} W⁻¹ (Jones) at a working wavelength of 840 nm. The OPDs show an ultrafast photoresponse in the range of ~15 ns. To best of our knowledge, these will be the first OPDs with unsymmetrical SQ dyes showing ultrafast high detectivity in the NIR range of 760 nm.

■ ASSOCIATED CONTENT

Supporting Information

The Supporting Information is available free of charge at <https://pubs.acs.org/doi/10.1021/acs.jpcc.0c06497>.

Synthetic procedure, steady-state absorption and emission spectra in solvents of various polarities, cyclic voltammogram, HOMO and LUMO levels with respect to PCBM, femtosecond transient absorption spectra and dynamics in ACN and with PCBM upon 670 nm excitation, decay-associated spectra in ACN and toluene, and electrochemical data (PDF)

■ AUTHOR INFORMATION

Corresponding Authors

Manoj A. G. Namboothiry – School of Physics, Indian Institute of Science Education and Research Thiruvananthapuram, Thiruvananthapuram, Kerala 695551, India; orcid.org/0000-0002-7805-1962; Phone: 091-471- 2778081; Email: manoj@iisertvm.ac.in

Suresh Das – School of Chemistry, Indian Institute of Science Education and Research Thiruvananthapuram, Thiruvananthapuram, Kerala 695551, India; orcid.org/0000-0002-8903-7285; Phone: 091-471- 2543557; Email: sureshdas55@gmail.com

Venugopal Karunakaran – Photosciences and Photonics Section, Chemical Sciences and Technology Division, CSIR-National Institute for Interdisciplinary Science and Technology, Thiruvananthapuram, Kerala 695 019, India; Academy of Scientific and Innovative Research (AcSIR), Ghaziabad 201002, India; orcid.org/0000-0001-8482-0900; Phone: 091-471-2515240; Email: k.venugopal@niist.res.in

Authors

Guruprasad M. Somashekharappa – Photosciences and Photonics Section, Chemical Sciences and Technology Division, CSIR-National Institute for Interdisciplinary Science and Technology, Thiruvananthapuram, Kerala 695 019, India; Academy of Scientific and Innovative Research (AcSIR), Ghaziabad 201002, India

Chinju Govind – Photosciences and Photonics Section, Chemical Sciences and Technology Division, CSIR-National Institute for Interdisciplinary Science and Technology, Thiruvananthapuram, Kerala 695 019, India; Academy of Scientific and Innovative Research (AcSIR), Ghaziabad 201002, India; orcid.org/0000-0002-7751-4873

Vijith Pulikodan – School of Physics, Indian Institute of Science Education and Research Thiruvananthapuram, Thiruvananthapuram, Kerala 695551, India

Megha Paul – Photosciences and Photonics Section, Chemical Sciences and Technology Division, CSIR-National Institute for Interdisciplinary Science and Technology, Thiruvananthapuram, Kerala 695 019, India; Academy of Scientific and Innovative Research (AcSIR), Ghaziabad 201002, India

Complete contact information is available at:
<https://pubs.acs.org/10.1021/acs.jpcc.0c06497>

Notes

The authors declare no competing financial interest.

ACKNOWLEDGMENTS

G.M.S., C.G., V.K.P., and M.P. thank CSIR and UGC for research fellowships. M.A.G.N. acknowledges the Solar Energy Research Initiative [DST, Government of India Grant reference number: DST/TMD/SERI/S15(G)]. V.K. acknowledges Department of Biotechnology (DBT), Government of India (BT/PR24173/BRB/10/1604/2017), for the financial support.

REFERENCES

- (1) Umezawa, K.; Citterio, D.; Suzuki, K. Water-Soluble Nir Fluorescent Probes Based on Squaraine and Their Application for Protein Labeling. *Anal. Sci.* **2008**, *24*, 213–217.
- (2) Wojciechowski, J. R.; Shriver-Lake, L. C.; Yamaguchi, M. Y.; Füreder, E.; Pieler, R.; Schamesberger, M.; Winder, C.; Prall, H. J.; Sonnleitner, M.; Ligler, F. S. Organic Photodiodes for Biosensor Miniaturization. *Anal. Chem.* **2009**, *81*, 3455–3461.
- (3) Pais, A.; Banerjee, A.; Klotzkin, D.; Papautsky, I. High-Sensitivity, Disposable Lab-on-a-Chip with Thin-Film Organic Electronics for Fluorescence Detection. *Lab Chip* **2008**, *8*, 794–800.
- (4) Avirah, R. R.; Jayaram, D. T.; Adarsh, N.; Ramaiah, D. Squaraine Dyes in Pdt: From Basic Design to in Vivo Demonstration. *Org. Biomol. Chem.* **2012**, *10*, 911–920.
- (5) Beverina, L.; Crippa, M.; Landenna, M.; Ruffo, R.; Salice, P.; Silvestri, F.; Versari, S.; Villa, A.; Ciaffoni, L.; Collini, E.; et al. Assessment of Water-Soluble Π -Extended Squaraines as One- and Two-Photon Singlet Oxygen Photosensitizers: Design, Synthesis, and Characterization. *J. Am. Chem. Soc.* **2008**, *130*, 1894–1902.
- (6) Clark, J.; Lanzani, G. Organic Photonics for Communications. *Nat. Photonics* **2010**, *4*, 438–446.
- (7) Aragoni, M. C.; Arca, M.; Caironi, M.; Denotti, C.; Devillanova, F. A.; Grigiotti, E.; Isaia, F.; Laschi, F.; Lippolis, V.; Natali, D.; et al. Monoreduced [M(R,R'Timdt)₂]–Dithiolenes (M = Ni, Pd, Pt; R,R'Timdt = Disubstituted Imidazolidine-2,4,5-Trithione): Solid State Photoconducting Properties in the Third Optical Fiber Window. *Chem. Commun.* **2004**, 1882–1883.
- (8) Kobayashi, A.; Sasa, M.; Suzuki, W.; Fujiwara, E.; Tanaka, H.; Tokumoto, M.; Okano, Y.; Fujiwara, H.; Kobayashi, H. Infrared

Electronic Absorption in a Single-Component Molecular Metal. *J. Am. Chem. Soc.* **2004**, *126*, 426–427.

(9) Strassel, K.; Kaiser, A.; Jenatsch, S.; Véron, A. C.; Anantharaman, S. B.; Hack, E.; Diethelm, M.; Nüesch, F.; Aderne, R.; Legnani, C.; et al. Squaraine Dye for a Visibly Transparent All-Organic Optical Upconversion Device with Sensitivity at 1000 Nm. *ACS Appl. Mater. Interfaces* **2018**, *10*, 11063–11069.

(10) Figueras, E.; Martins, A.; Borbély, A.; Le Joncour, V.; Cordella, P.; Perego, R.; Modena, D.; Pagani, P.; Esposito, S.; Auciello, G.; et al. Octreotide Conjugates for Tumor Targeting and Imaging. *Pharmaceutics* **2019**, *11*, 220.

(11) Li, P.; Liu, Y.; Liu, W.; Li, G.; Tang, Q.; Zhang, Q.; Leng, F.; Sheng, F.; Hu, C.; Lai, W.; et al. Ir-783 Inhibits Breast Cancer Cell Proliferation and Migration by Inducing Mitochondrial Fission. *Int. J. Oncol.* **2019**, *55*, 415–424.

(12) Duan, L.; Wang, L.; Zhang, C.; Yu, L.; Guo, F.; Sun, Z.; Xu, Y.; Yan, F. Role of near-Infrared Heptamethine Cyanine Dye Ir-783 in Diagnosis of Cervical Cancer and Its Mechanism. *Int. J. Clin. Exp. Pathol.* **2019**, *12*, 2353–2362.

(13) Henary, M.; Paranjpe, S.; Owens, E. A. Synthesis and Applications of Benzothiazole Containing Cyanine Dyes. *Heterocycl. Commun.* **2013**, *19*, 1.

(14) Abrahamse, H.; Houreld, N. N. Genetic Aberrations Associated with Photodynamic Therapy in Colorectal Cancer Cells. *Int. J. Mol. Sci.* **2019**, *20*, 3254.

(15) Zink-Lorre, N.; Font-Sanchis, E.; Seetharaman, S.; Karr, P. A.; Sastre-Santos, Á.; D'Souza, F.; Fernández-Lázaro, F. Directly Linked Zinc Phthalocyanine–Peryleneimide Dyads and a Triad for Ultrafast Charge Separation. *Chem.—Eur. J.* **2019**, *25*, 10123–10132.

(16) Zenkevich, E.; Sagun, E.; Knyukshto, V.; Shulga, A.; Mironov, A.; Efremova, O.; Bonnett, R.; Songca, S. P.; Kassem, M. Photophysical and Photochemical Properties of Potential Porphyrin and Chlorin Photosensitizers for Pdt. *J. Photochem. Photobiol. B Biol.* **1996**, *33*, 171–180.

(17) Finlay, J. C.; Conover, D. L.; Hull, E. L.; Foster, T. H. Porphyrin Bleaching and Pdt-Induced Spectral Changes Are Irradiance Dependent in Ala-Sensitized Normal Rat Skin in Vivo. *J. Photochem. Photobiol.* **2001**, *73*, 54–63.

(18) Li, Q.; Guo, Y.; Liu, Y. Exploration of near-Infrared Organic Photodetectors. *Chem. Mater.* **2019**, *31*, 6359–6379.

(19) Law, K. Y.; Bailey, F. C. Squaraine Chemistry. Synthesis, Characterization, and Optical Properties of a Class of Novel Unsymmetrical Squaraines: [4-(Dimethylamino)Phenyl](4'-Methoxyphenyl)Squaraine and Its Derivatives. *J. Org. Chem.* **1992**, *57*, 3278–3286.

(20) Sun, C.-L.; Lv, S.-K.; Liu, Y.-P.; Liao, Q.; Zhang, H.-L.; Fu, H.; Yao, J. Benzoindolic Squaraine Dyes with a Large Two-Photon Absorption Cross-Section. *J. Mater. Chem. C* **2017**, *5*, 1224–1230.

(21) Ahn, H.-Y.; Yao, S.; Wang, X.; Belfield, K. D. Near-Infrared-Emitting Squaraine Dyes with High 2pa Cross-Sections for Multi-photon Fluorescence Imaging. *ACS Appl. Mater. Interfaces* **2012**, *4*, 2847–2854.

(22) Binda, M.; Iacchetti, A.; Natali, D.; Beverina, L.; Sassi, M.; Sampietro, M. High Detectivity Squaraine-Based near Infrared Photodetector with Na/Cm2 Dark Current. *Appl. Phys. Lett.* **2011**, *98*, 073303.

(23) Bellani, S.; Iacchetti, A.; Porro, M.; Beverina, L.; Antognazza, M. R.; Natali, D. Charge Transport Characterization in a Squaraine-Based Photodetector by Means of Admittance Spectroscopy. *Org. Electron.* **2015**, *22*, 56–61.

(24) Khopkar, S.; Shankarling, G. Synthesis, Photophysical Properties and Applications of Nir Absorbing Unsymmetrical Squaraines: A Review. *Dyes Pigm.* **2019**, *170*, 107645.

(25) Alex, S.; Santhosh, U.; Das, S. Dye Sensitization of Nanocrystalline TiO₂: Enhanced Efficiency of Unsymmetrical Versus Symmetrical Squaraine Dyes. *J. Photochem. Photobiol., A* **2005**, *172*, 63–71.

- (26) Lambert, C.; Scherpf, T.; Ceymann, H.; Schmiedel, A.; Holzapfel, M. Coupled Oscillators for Tuning Fluorescence Properties of Squaraine Dyes. *J. Am. Chem. Soc.* **2015**, *137*, 3547–3557.
- (27) Schreck, M. H.; Breitschwerdt, L.; Marciniak, H.; Holzapfel, M.; Schmidt, D.; Würthner, F.; Lambert, C. Fs–Ps Exciton Dynamics in a Stretched Tetraphenylsquaraine Polymer. *Phys. Chem. Chem. Phys.* **2019**, *21*, 15346–15355.
- (28) Lambert, C.; Koch, F.; Völker, S. F.; Schmiedel, A.; Holzapfel, M.; Humeniuk, A.; Röhr, M. I. S.; Mitric, R.; Brixner, T. Energy Transfer between Squaraine Polymer Sections: From Helix to Zigzag and All the Way Back. *J. Am. Chem. Soc.* **2015**, *137*, 7851–7861.
- (29) Goh, T.; Huang, J.-S.; Bielinski, E.; Thompson, B.; Tomasulo, S.; Lee, M.; Sfeir, M.; Hazari, N.; Taylor, A. Coevaporated Bisquaraine Inverted Solar Cells: Enhancement Due to Energy Transfer and Open Circuit Voltage Control. *ACS Photonics* **2015**, *2*, 86.
- (30) de Miguel, G.; Marchena, M.; Cohen, B.; Pandey, S. S.; Hayase, S.; Douhal, A. Relating the Photodynamics of Squaraine-Based Dye-Sensitized Solar Cells to the Molecular Structure of the Sensitizers and to the Presence of Additives. *J. Phys. Chem. C* **2012**, *116*, 22157–22168.
- (31) de Miguel, G.; Marchena, M.; Zitnan, M.; Pandey, S. S.; Hayase, S.; Douhal, A. Femto to Millisecond Observations of Indole-Based Squaraine Molecules Photodynamics in Solution. *Phys. Chem. Chem. Phys.* **2012**, *14*, 1796–1805.
- (32) Marchena, M. J.; de Miguel, G.; Cohen, B.; Organero, J. A.; Pandey, S.; Hayase, S.; Douhal, A. Real-Time Photodynamics of Squaraine-Based Dye-Sensitized Solar Cells with Iodide and Cobalt Electrolytes. *J. Phys. Chem. C* **2013**, *117*, 11906–11919.
- (33) Armarego, W. L. F.; Chai, C. Purification of Organic Chemicals. In *Purification of Laboratory Chemicals*, 7th ed; Armarego, W. L. F., Chai, C., Eds.; Butterworth-Heinemann: Boston, 2013; Chapter 4, pp 103–554.
- (34) Khan, R.; Ningombam, A.; Singh, K.; Singh, M. Stereoelectronic Effects in the Stereoselectivity of the Diels-Alder Reactions: Reactions of Aminoanthracenes with N-Phenylmaleimide. *J. Chem. Pharm. Res.* **2012**, *4*, 1532–1538.
- (35) Tatars, A.; Fedyunyaeva, I.; Terpetschnig, E.; Patsenker, L. Synthesis of Novel Squaraine Dyes and Their Intermediates. *Dyes Pigm.* **2005**, *64*, 125–134.
- (36) Bagnis, D.; Beverina, L.; Huang, H.; Silvestri, F.; Yao, Y.; Yan, H.; Pagani, G. A.; Marks, T. J.; Facchetti, A. Marked Alkyl- Vs Alkenyl-Substituent Effects on Squaraine Dye Solid-State Structure, Carrier Mobility, and Bulk-Heterojunction Solar Cell Efficiency. *J. Am. Chem. Soc.* **2010**, *132*, 4074–4075.
- (37) Pålsson, L.-O.; Monkman, A. P. Measurements of Solid-State Photoluminescence Quantum Yields of Films Using a Fluorimeter. *Adv. Mater.* **2002**, *14*, 757–758.
- (38) Govind, C.; Karunakaran, V. Ultrafast Relaxation Dynamics of Photoexcited Heme Model Compounds: Observation of Multiple Electronic Spin States and Vibrational Cooling. *J. Phys. Chem. B* **2017**, *121*, 3111–3120.
- (39) Megerle, U.; Pugliesi, I.; Schriever, C.; Sailer, C. F.; Riedle, E. Sub-50 fs Broadband Absorption Spectroscopy with Tunable Excitation: Putting the Analysis of Ultrafast Molecular Dynamics on solid Ground. *Appl. Phys. B* **2009**, *96*, 215–231.
- (40) Mohan, M.; Nandal, V.; Paramadam, S.; Reddy, K. P.; Ramkumar, S.; Agarwal, S.; Gopinath, C. S.; Nair, P. R.; Nambhoorthy, M. A. G. Efficient Organic Photovoltaics with Improved Charge Extraction and High Short-Circuit Current. *J. Phys. Chem. C* **2017**, *121*, 5523–5530.
- (41) Simone, G.; Dyson, M. J.; Meskers, S. C. J.; Janssen, R. A. J.; Gelinck, G. H. Organic Photodetectors and Their Application in Large Area and Flexible Image Sensors: The Role of Dark Current. *Adv. Funct. Mater.* **2020**, *30*, 1904205.
- (42) Zhang, H.; Jenatsch, S.; De Jonghe, J.; Nüesch, F.; Steim, R.; Véron, A. C.; Hany, R. Transparent Organic Photodetector Using a near-Infrared Absorbing Cyanine Dye. *Sci. Rep.* **2015**, *5*, 9439.
- (43) Bigelow, R. W.; Freund, H.-J. An Mndo and Cndo(S + Des Ci) Study on the Structural and Electronic Properties of a Model Squaraine Dye and Related Cyanine. *Chem. Phys.* **1986**, *107*, 159–174.
- (44) Beverina, L.; Salice, P. Squaraine Compounds: Tailored Design and Synthesis Towards a Variety of Material Science Applications. *Eur. J. Org. Chem.* **2010**, *2010*, 1207–1225.
- (45) Law, K. Y. Squaraine Chemistry: Effects of Structural Changes on the Absorption and Multiple Fluorescence Emission of Bis[4-(Dimethylamino)Phenyl]Squaraine and Its Derivatives. *J. Phys. Chem.* **1987**, *91*, 5184–5193.
- (46) Alex, S.; Basheer, M. C.; Arun, K. T.; Ramaiah, D.; Das, S. Aggregation Properties of Heavy Atom Substituted Squaraine Dyes: Evidence for the Formation of J-Type Dimer Aggregates in Aprotic Solvents. *J. Phys. Chem. A* **2007**, *111*, 3226–3230.
- (47) Gsänger, M.; Kirchner, E.; Stolte, M.; Burschka, C.; Stepanenko, V.; Pflaum, J.; Würthner, F. High-Performance Organic Thin-Film Transistors of J-Stacked Squaraine Dyes. *J. Am. Chem. Soc.* **2014**, *136*, 2351–2362.
- (48) Pandey, S. S.; Inoue, T.; Fujikawa, N.; Yamaguchi, Y.; Hayase, S. Alkyl and Fluoro-Alkyl Substituted Squaraine Dyes: A Prospective Approach Towards Development of Novel NIR Sensitizers. *Thin Solid Films* **2010**, *519*, 1066–1071.
- (49) Chen, H.; Farahat, M. S.; Law, K.-Y.; Whitten, D. G. Aggregation of Surfactant Squaraine Dyes in Aqueous Solution and Microheterogeneous Media: Correlation of Aggregation Behavior with Molecular Structure. *J. Am. Chem. Soc.* **1996**, *118*, 2584–2594.
- (50) Shafeekh, K. M.; Soumya, M. S.; Rahim, M. A.; Abraham, A.; Das, S. Synthesis and Characterization of near-Infrared Absorbing Water Soluble Squaraines and Study of Their Photodynamic Effects in Dla Live Cells. *Photochem. Photobiol.* **2014**, *90*, 585–595.
- (51) Chen, G.; Sasabe, H.; Igarashi, T.; Hong, Z.; Kido, J. Squaraine Dyes for Organic Photovoltaic Cells. *J. Mater. Chem. A* **2015**, *3*, 14517–14534.
- (52) Horng, M. L.; Gardecki, J. A.; Papazyan, A.; Maroncelli, M. Subpicosecond Measurements of Polar Solvation Dynamics: Coumarin 153 Revisited. *J. Phys. Chem.* **1995**, *99*, 17311–17337.
- (53) Pal, S. K.; Peon, J.; Bagchi, B.; Zewail, A. H. Biological Water: Femtosecond Dynamics of Macromolecular Hydration. *J. Phys. Chem. B* **2002**, *106*, 12376–12395.
- (54) Zhu, H.; Li, M.; Hu, J.; Wang, X.; Jie, J.; Guo, Q.; Chen, C.; Xia, A. Ultrafast Investigation of Intramolecular Charge Transfer and Solvation Dynamics of Tetrahydro[5]-Helicene-Based Imide Derivatives. *Sci. Rep.* **2016**, *6*, 24313.
- (55) Snellenburg, J. J.; Laptinok, S.; Seger, R.; Mullen, K. M.; van Stokkum, I. H. M. Glotaran: A Java-Based Graphical User Interface for the R Package. *J. Stat. Software* **2012**, *49*, 22.
- (56) Zhu, H. *Ultrafast Investigation of Intramolecular Charge Transfer and Solvation Dynamics of Tetrahydro[5]-Helicene-Based Imide Derivatives*; Nature Publishing Group, 2016.
- (57) Karunakaran, V.; Das, S. Direct Observation of Cascade of Photoinduced Ultrafast Intramolecular Charge Transfer Dynamics in Diphenyl Acetylene Derivatives: Via Solvation and Intramolecular Relaxation. *J. Phys. Chem. B* **2016**, *120*, 7016–7023.
- (58) Hahn, T.; Tscheuschner, S.; Kahle, F.-J.; Reichenberger, M.; Athanopoulos, S.; Saller, C.; Bazan, G. C.; Nguyen, T.-Q.; Strohrriegel, P.; Bäessler, H.; et al. Monomolecular and Bimolecular Recombination of Electron–Hole Pairs at the Interface of a Bilayer Organic Solar Cell. *Adv. Funct. Mater.* **2017**, *27*, 1604906.
- (59) Miao, J.; Zhang, F.; Du, M.; Wang, W.; Fang, Y. Photo-multiplication Type Narrowband Organic Photodetectors Working at Forward and Reverse Bias. *Phys. Chem. Chem. Phys.* **2017**, *19*, 14424–14430.
- (60) Shuttle, C. G.; O'Regan, B.; Ballantyne, A. M.; Nelson, J.; Bradley, D. D. C.; de Mello, J.; Durrant, J. R. Experimental Determination of the Rate Law for Charge Carrier Decay in a Polythiophene: Fullerene Solar Cell. *Appl. Phys. Lett.* **2008**, *92*, 093311.

(61) Wood, S.; O'Connor, D.; Jones, C. W.; Claverley, J. D.; Blakesley, J. C.; Giusca, C.; Castro, F. A. Transient Photocurrent and Photovoltage Mapping for Characterisation of Defects in Organic Photovoltaics. *Sol. Energy Mater. Sol. Cells* **2017**, *161*, 89–95.

Ultrafast Intermolecular Interaction Dynamics between NIR-Absorbing Unsymmetrical Squaraines and PCBM: Effects of Halogen Substitution

Guruprasad M. Somashekharappa, Megha Paul, Chinju Govind, Ranimol Mathew, and Venugopal Karunakaran*



Cite This: *J. Phys. Chem. B* 2022, 126, 4509–4519



Read Online

ACCESS |



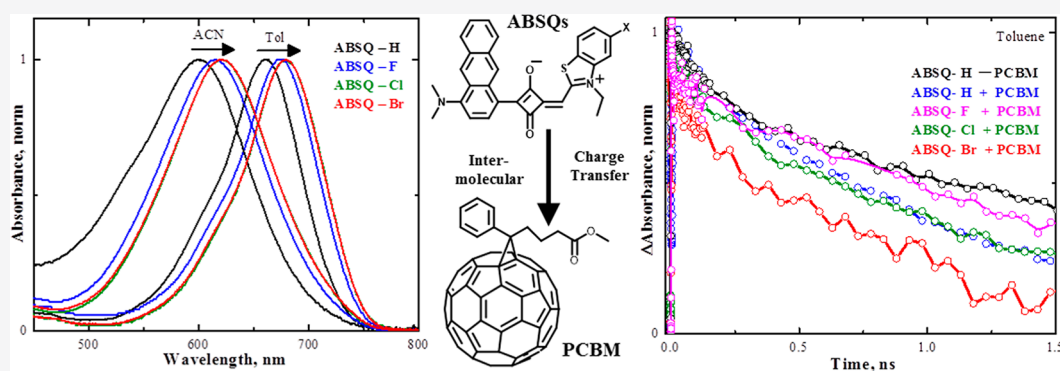
Metrics & More



Article Recommendations



Supporting Information



ABSTRACT: Among near-infrared (NIR) dyes, squaraine derivatives are applied as efficient sensitizers in optoelectronic and biomedical devices due to their simple synthesis, intense absorption, and emission and exceptional photochemical stability. The fundamental understanding of the structure–property relationships of sensitizers provides the insight to increase the efficiency of such devices. Here, unsymmetrical squaraine derivatives (ABSQs) with donor–acceptor–donor (D–A–D') architectures having *N,N*-dimethyl amino anthracene and benzothiazole (ABSQ-H) halogenated with fluoride (ABSQ-F), chloride (ABSQ-Cl), and bromide (ABSQ-Br) were synthesized to understand the effect of halogen on the photophysical properties and intermolecular interaction dynamics with phenyl- C_{61} -butyric acid methyl ester (PCBM), which is used widely as an electron acceptor in bulk heterojunction-based devices. Interestingly, ABSQ-H exhibited intense absorption ($\epsilon \sim 6.72 \times 10^4 \text{ M}^{-1} \text{ cm}^{-1}$) spectra centered at $\sim 660 \text{ nm}$. Upon halogen substitution, a bathochromic shift in the absorption spectra with an increase of molar absorptivity was observed ($\epsilon \sim 8.59 \times 10^4 \text{ M}^{-1} \text{ cm}^{-1}$), which is beneficial for NIR light harvesting. The femtosecond transient absorption spectra of ABSQs revealed that the polarity of the solvent controlled the excited-state relaxation dynamics. Upon addition of PCBM, the fluorescence intensity and dynamics of halogenated ABSQs were quenched, and the formation of a squaraine radical cation was observed, reflecting the occurrence of intermolecular charge-transfer dynamics between ABSQs and PCBM. Thus, the observation of a bathochromic shift with intense absorption and an efficient intermolecular interaction with PCBM upon halogenation of ABSQs provide a design strategy for the development of unsymmetrical squaraine derivatives for bulk heterojunction-based optoelectronic devices.

INTRODUCTION

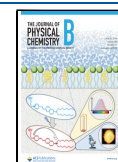
Near-infrared (NIR) dyes are significantly used as sensitizers in various optoelectronic applications^{1,2} due to their efficient optical properties with high sensitivity in the range of 700–1500 nm. Among the various NIR dyes, the squaraine derivatives possessing an electron–acceptor–donor architecture have been widely applied in organic photovoltaic cells,^{3–6} optical data storage,⁷ two-photon absorption,⁸ fluorescent labels,^{9,10} and photodynamic therapy¹¹ due to their strong absorption ($\epsilon > 10^5 \text{ M}^{-1} \text{ cm}^{-1}$) and high fluorescence ($\Phi = 0.8$) in the region of visible to NIR and ease of synthesis with exceptional photostability.¹² The optical and electrical proper-

ties of the symmetrical squaraines dyes can be easily modified by changing the electron-donating capability of aromatic or heterocyclic peripheral substituents. However, unsymmetrical squaraines emerged as versatile sensitizers^{13–15} due to the unidirectional flow of electrons in the excited states upon

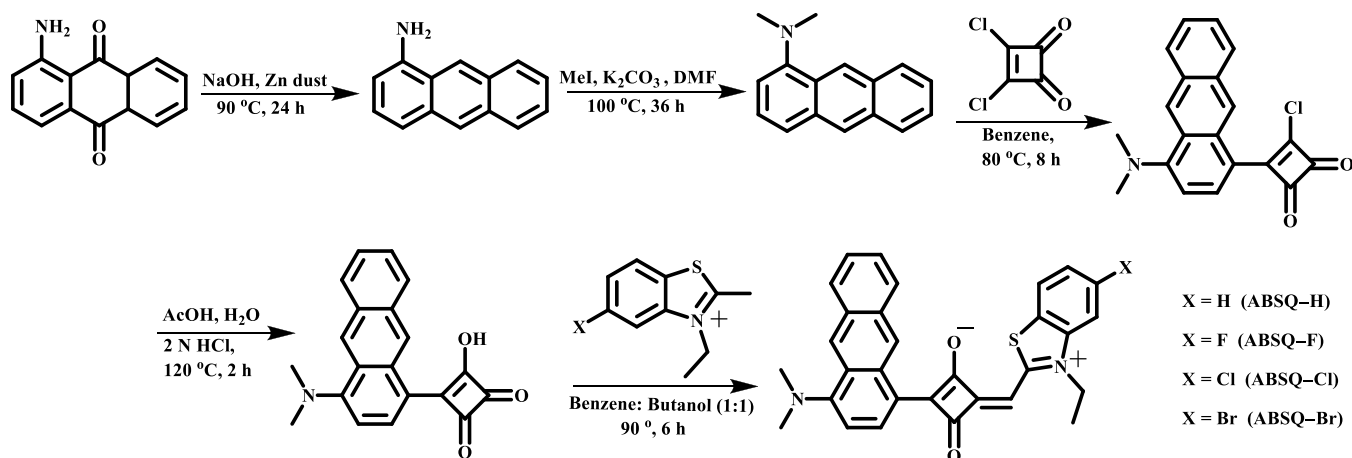
Received: December 24, 2021

Revised: May 21, 2022

Published: June 9, 2022



Scheme 1. Synthetic Scheme of ABSQ Derivatives



excitation, yielding enhanced charge separation and leading to higher photocurrents, compared to the symmetrical derivatives.^{16,17} Indeed, the unsymmetrical squaraines have been widely used in various optoelectronic^{18–21} and biomedical devices.⁴ However, in the bulk heterojunction-based photovoltaic and photodetector devices using phenyl-*C*₆₁-butyric acid methyl ester (PCBM, an electron acceptor), the ultrafast processes of photoinduced charge transfer, charge carrier generation, and their recombination control the efficiency of the devices. Though a large number of steady-state and time-resolved photophysical properties of squaraine derivatives were widely reported,^{22–30} the intermolecular interaction dynamics of unsymmetrical squaraine derivatives with PCBM have not been investigated in detail.

Here, a series of unsymmetrical squaraine derivatives (ABSQs) having the D–A–D' architecture comprising *N,N*-dimethylated amino anthracene and benzothiazole (ABSQ-H) halogenated with fluoride (ABSQ-F), chloride (ABSQ-Cl), and bromide (ABSQ-Br) were synthesized (Scheme 1). The steady-state and time-resolved photophysical characterization of ABSQ derivatives and with PCBM were carried out to understand the effect of halogen on the photophysical properties and intermolecular interaction dynamics with PCBM to improve the efficiency of the devices. It is found that upon halogenation of ABSQs, the absorption spectra showed a bathochromic shift with an increase of molar absorptivity and firm interaction with the PCBM.

EXPERIMENTAL SECTION

General. The reagents and chemicals used for synthesis were procured from TCI, Sigma-Aldrich, and Merck. Dry solvents were made by following the literature studies.³¹ ¹H NMR spectra were recorded using a Bruker AMX 500 MHz spectrometer with tetramethylsilane as the internal standard. The Thermo Scientific Exactive-LC–MS by the electrospray ionization method with ions given in *m/z* using an Orbitrap analyzer was used to record the high-resolution mass spectra of the derivatives. The spectroscopic measurements were made by using the solvents of HPLC grade (Merck) and used as received.

Preparation of Thin Films. A drop casting method was followed to prepare the thin films of ABSQ derivatives. ABSQ derivatives in chloroform (1.5 mM) were used to make thin

films. The above solution was dropped on the thin quartz window, which was dried for 1 h at 25 °C.

Steady-State Photophysical Measurements. Steady-state absorption spectra were recorded using a UV-2600 (Shimadzu) UV–vis absorption spectrophotometer. The fluorescence spectra were recorded with a Fluorolog-3 (HORIBA) having a 450 W Xe arc lamp. The fluorescence quantum yields were recorded using the integrating sphere (Quanta-φ, HORIBA).³²

Electrochemical Measurements. The BAS CV-50W voltammetric analyzer with three-electrode cell assemblies was used to perform cyclic voltammetry. The Ag/AgCl electrode, glassy carbon electrode, and platinum wire were used as the reference, working, and counter electrodes respectively. Measurements were performed in 1 mM ABSQ solution in ACN using tetrabutylammonium hexafluorophosphate (TBAPF₆, supporting electrolyte) with a scan rate of 50 mV s⁻¹. The ferrocene/ferrocenium (Fc/Fc⁺) redox couple was used as the external standard.

Time-Correlated Single-Photon Counting Spectrometer. The fluorescence lifetime was recorded upon excitation at 670 nm (LED) using a picosecond single-photon counting system (HORIBA, DeltaFlex) with a PPD-850 detector. The instrument response function (IRF) of time-correlated single-photon counting (TCSPC) is found to be <200 ps. The fluorescence time constants are attained by deconvoluting with the profile of LED source. Single exponential function was used to fit the decay of the fluorescence intensity (*I*) with time (*t*)

$$I = A e^{-t/\tau} \quad (1)$$

where *A* and τ are the amplitude and lifetime of the derivative, respectively.

Femtosecond Pump-Probe Spectrometer. The details of the femtosecond pump-probe spectrometer were provided elsewhere.³³ The seed laser is the Ti:sapphire laser (MaiTai HP, Spectra Physics, USA) having a center wavelength of 800 nm with a pulse width of <100 fs and a repetition rate of 80 MHz. The amplified laser was divided into two and the beam with high energy was used for exciting the compounds (670 nm) using TOPAS (prime, light conversion). The other portion (200 mW) of the amplified beam was focused on a CaF₂ plate (1 mm) to obtain a white light continuum (340–1000 nm) that further divided into two beams (reference and sample probe beams). The sample (0.4 mm thickness) was

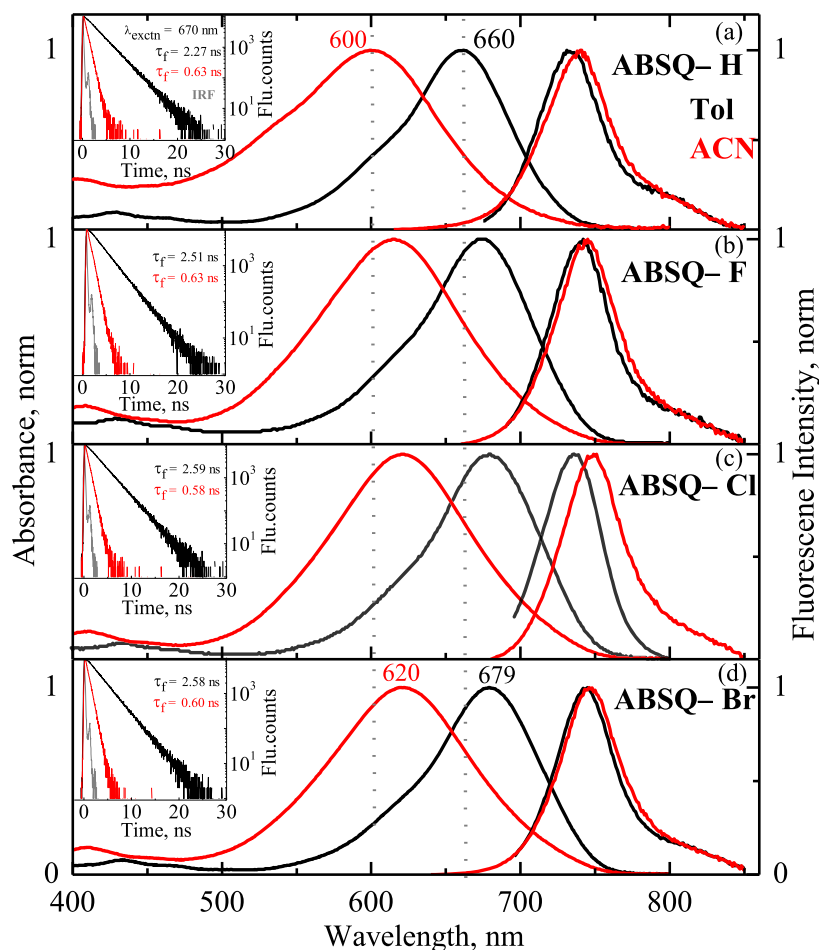


Figure 1. Absorption and emission spectra of ABSQ-H (a), ABSQ-F (b), ABSQ-Cl (c), and ABSQ-Br (d) in ACN (red) and toluene (black) at room temperature. The emission spectra were obtained upon excitation at the corresponding absorption maximum of the derivatives. The inset shows the fluorescence decay profiles obtained upon excitation at 670 nm.

refreshed by spinning at a constant speed. After passing through the sample, the white light continuum was focused into an optical fiber (100 μm) attached to the imaging spectrometer. The spectrophotometer setup is ExciPro, CDP Systems Corp, Russia. The transient absorption spectra were recorded at a magic angle (54.7°) by averaging about 2000 excitation pulses for each delay time. All the transient absorption spectra are corrected for chirp of the white light by estimating the time zero with the coherent artifact found in the solvent.³⁴ The laser fluence used for all the transient absorption measurements is $\sim 3 \mu\text{J}/\text{cm}^2$. The IRF of the ultrafast spectrometer is found to be about ≤ 120 fs. The stability of the sample is checked by recording the absorption spectra of the sample (before and after the measurements) and observed to have no substantial differences in the absorption spectra. The concentration of ABSQ derivatives was $\sim 80 \mu\text{M}$ for femtosecond transient absorption measurements.

RESULTS AND DISCUSSION

Synthesis of ABSQ Derivatives. The synthetic scheme and the chemical structure of the intermediates and ABSQ derivatives are provided in Scheme 1. The unsymmetrical ABSQ derivatives were synthesized by altering the reported procedures.^{35–37} *N,N*-Dimethyl aminoanthracene semisquaraine was synthesized by reducing and methylating 1-aminoanthraquinone, and the obtained *N,N*-dimethyl aminoanthra-

cene was added with squarylium chloride. The halogenated *N*-ethyl benzothiazolium salt was refluxed with the *N,N*-dimethyl aminoanthracene semisquaraine in a butanol:benzene azeotropic mixture (1:1) yielding the ABSQ derivatives.²⁷ The structure of each compound is analyzed by ^1H and ^{13}C NMR and HRMS, and spectral data are given in the Supporting Information.

Stationary Photophysical Characterization. In Solution. The absorption and emission spectra of ABSQ derivatives with the increase of solvent polarity were recorded and are shown in Figures 1 and S1–S4 in the Supporting Information. ABSQ-H, ABSQ-F, ABSQ-Cl, and ABSQ-Br exhibited an intense absorption maximum at ~ 660 , 674, 678, and 679 nm in toluene with a molar extinction coefficient of ~ 6.72 , 7.15, 8.59, and $7.96 \times 10^4 \text{ M}^{-1} \text{ cm}^{-1}$, respectively, due to the combined $\pi-\pi^*$ transition with intramolecular charge transfer from *N,N*-dimethyl anthracene and benzothiazolium donors to the central squaraine core.^{38–40} Interestingly, it is found that upon substitution of halogen, the absorption maximum shifted to the red region (~ 19 nm) compared to ABSQ-H consistent with the literature.⁴¹ Upon increasing the polarity of the solvent (acetonitrile, ACN), the absorption maximum of ABSQ derivatives shifted to the blue region (~ 60 nm), negative solvatochromism, indicating that the ground state is more stabilized compared to the excited state.⁴²

Table 1. Absorption and Fluorescence Maxima, Lifetime, and Quantum Yield of ABSQ-H in Various Solvents

solvents	absorption max, nm (λ_{max})	fluorescence max, nm (λ_{max})	Stokes shift, cm^{-1} ($\Delta\nu$)	fluorescence quantum yield ^a (Φ_f)	fluorescence lifetime ^b , ns (τ)	radiative constant, $\times 10^7 \text{ s}^{-1}$ (K_r)	non-radiative constant, $\times 10^7 \text{ s}^{-1}$ (K_{nr})
toluene	660	733	1509	0.46	2.27 \pm 0.20	20.26	23
chloroform	651	737	1792	0.44	2.48 \pm 0.25	17.74	22
tetrahydrofuran	629	736	2311	0.32	2.06 \pm 0.25	15.53	33
MeOH	599	735	3089	0.06	0.23 \pm 0.20	27.39	407
ACN	600	740	3153	0.14	0.63 \pm 0.20	22.22	136

^aAbsolute fluorescence quantum yield attained by exciting at emission maximum using an integrating sphere. ^bFluorescence lifetime was attained upon excitation at 670 nm ($\chi^2 = 1.0\text{--}1.2$).

The fluorescence spectra of ABSQ-H, ABSQ-F, ABSQ-Cl, and ABSQ-Br in toluene exhibited maximum at around 733, 741, 736, and 743 nm, respectively, and showed a bathochromic shift with an increase in the polarity of the solvent (Figure 1). When compared to other derivatives, there is a significant red shift of the emission spectra of ABSQ-Cl in ACN compared to toluene, reflecting the stabilization of excited state of ABSQ-Cl in a highly polar solvent.

The fluorescence dynamics of ABSQ derivatives were measured (Figure S5) upon excitation at 670 nm, and the corresponding decay profiles in toluene and ACN are provided for comparison in the inset of Figure 1. The fluorescence lifetime (τ_f) of ABSQ-H in toluene was obtained as $\sim 2.27 \pm 0.20$ ns, and with the increase of solvent polarity, it was decreased to 0.63 ± 0.20 ns in ACN. Though there are no significant changes in the fluorescence lifetime upon halogenation in toluene, a difference of ~ 0.32 ns in the fluorescence lifetime in the order of ABSQ-H (2.27 ns) < ABSQ-F (2.51 ns) < ABSQ-Cl (2.59 ns) \approx ABSQ-Br (2.58 ns) was observed. The absolute fluorescence quantum yield (Φ) of ABSQ-H in toluene was found to be ~ 0.46 , which was reduced to 0.14 in ACN. Such a similar trend was also observed for other derivatives, revealing the contribution of a non-radiative decay sensitive to the electronic redistribution in the excited ABSQs and/or the formation of the solute–solvent complexes upon increase of polarity.^{13,27} The photophysical characterization data of the absorption and emission maxima, Stokes shift, absolute quantum yield, and fluorescence lifetime of ABSQ-H, ABSQ-F, ABSQ-Cl, and ABSQ-Br are provided in Tables 1 and S1–S3, respectively. The radiative (K_r) and non-radiative (K_{nr}) rate constants were also determined from the fluorescence quantum yield (Φ) and lifetime (τ_f) using the following equations

$$K_r = \frac{\Phi}{\tau_f} \text{ and } K_{\text{nr}} = \frac{1}{\tau_f} - K_r \quad (2)$$

Film State. The absorption spectra of ABSQ derivatives were recorded in the film state by drop-casting 1.5 mM ABSQs in chloroform and are shown in Figure 2. The absorption spectra in the film state showed a broad band covering a wide range of $\sim 475\text{--}775$ nm with a maximum at around 550–570 nm. When compared to the solution state, the appearance of absorption maximum at ~ 560 nm showed a broad band in nature and shifted to the blue region by ~ 100 nm, suggesting the formation of H-aggregates by the intermolecular $\pi\text{--}\pi$ interaction³⁹ in the thin film. Indeed, such a broad range of absorption wavelengths with a high molar absorptivity will be advantageous for light harvesting for optoelectronic devices.¹²

Electrochemical Characterization. In order to obtain the highest occupied molecular orbital (HOMO) and the lowest

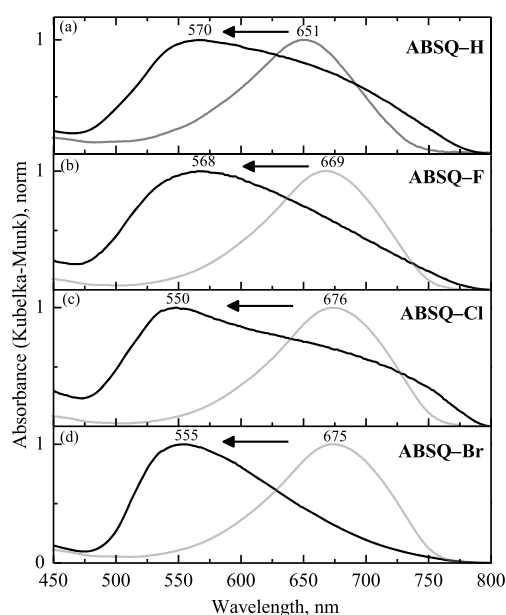


Figure 2. Normalized absorption spectra of ABSQ-H (a), ABSQ-F (b), ABSQ-Cl (c), and ABSQ-Br (d) in a thin film (black) and chloroform solution (gray).

unoccupied molecular orbital (LUMO) energy levels of the ABSQ derivatives, cyclic voltammetry was performed using ferrocene as the standard, and the results are shown in Figure S6a. The HOMO and LUMO energy levels were calculated using the following equations and are provided in Figure S6b along with PCBM.

$$\begin{aligned} \text{HOMO (ABSQs)} \\ = -[4.8 - E_{\text{ox}}(\text{Fc}/\text{Fc}^+ \text{ vs Ag}/\text{AgCl}) + E_{\text{ox}} \\ \text{(ABSQs vs Ag}/\text{AgCl})] \end{aligned} \quad (3)$$

$$\text{LUMO (ABSQs)} = E_{\text{HOMO}} + E_{00} \quad (4)$$

where $E_{00} = 1242/\lambda_{\text{onset}}$.

The HOMO and LUMO energy levels of ABSQ-H were found to be -4.78 and -3.04 eV, respectively. Though there are no significant changes in the HOMO energy levels of ABSQ derivatives, there is a remarkable reduction of LUMO energy levels and thus leading to the decrease of energy of band gap of ABSQ derivatives upon substitution of halogen. Interestingly, the HOMO and LUMO energy levels of ABSQ derivatives are higher than those of the PCBM, which is the important requirement of the sensitizer to be used in the bulk heterojunction-based optoelectronic devices with efficient intermolecular charge transfer in the excited state. Hence,

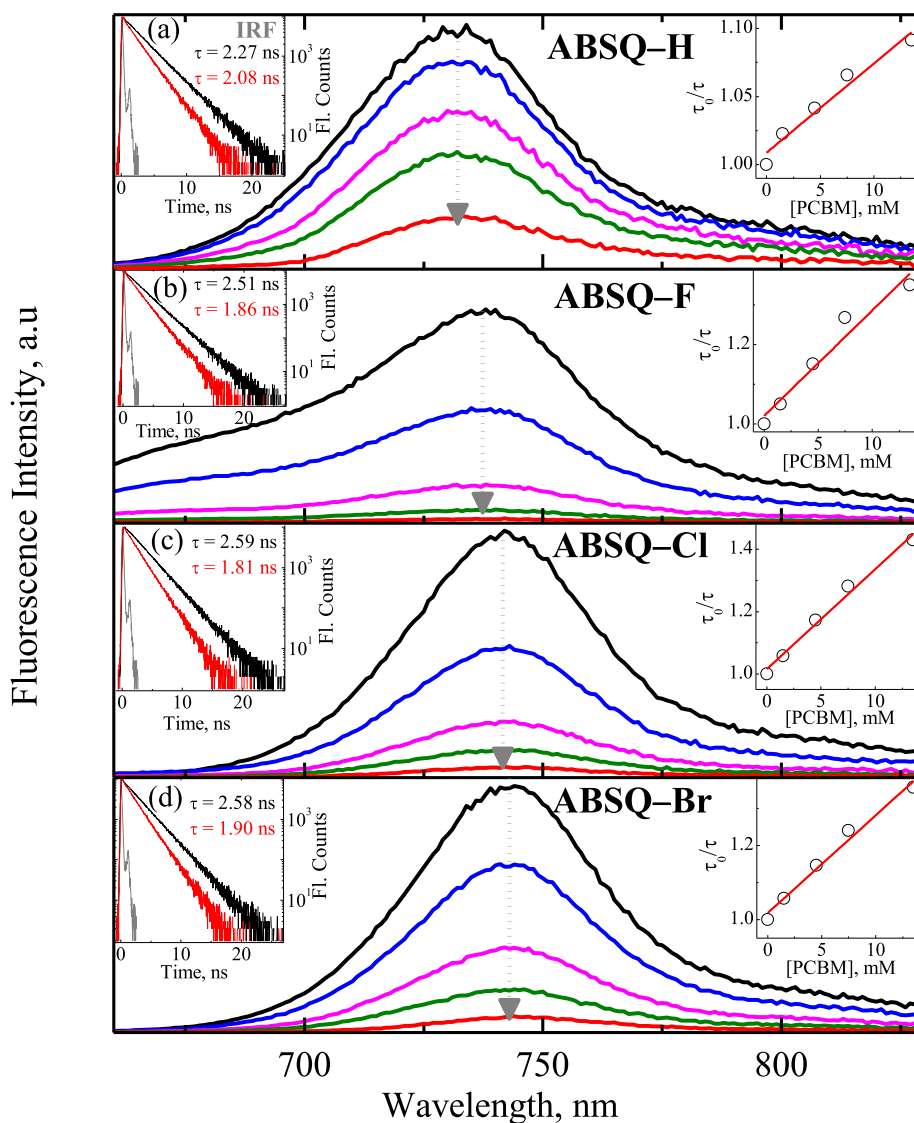


Figure 3. Fluorescence spectra of ABSQ-H (a), ABSQ-F (b), ABSQ-Cl (c), and ABSQ-Br (d) with different concentrations of PCBM in toluene 0 mM (black), 1.5 mM (blue), 4.5 mM (magenta), 7.5 mM (olive), and 13.5 mM (red). Insets: fluorescence decay profiles obtained upon excitation at 670 nm (left) and plot of τ_0/τ vs [PCBM] (right).

these ABSQ derivatives are highly suitable for the optoelectronic devices.

Interaction with PCBM. The absorption and fluorescence spectra of ABSQ-H, ABSQ-F, ABSQ-Cl, and ABSQ-Br with an increase of the concentration of PCBM (1.5 to 13.5 mM) in toluene were recorded. Though there were no significant changes in the absorption spectra of ABSQ derivatives, the decrease of fluorescence intensity of all the ABSQ derivatives upon addition of PCBM was observed (Figure 3), reflecting the excited ABSQ derivatives interacting with PCBM. Upon addition of PCBM, the fluorescence lifetime of ABSQ derivatives was also measured by the excitation at 670 nm (left insets of Figure 3). The fluorescence lifetime of ABSQ-H, ABSQ-F, ABSQ-Cl, and ABSQ-Br upon addition of PCBM (13.5 mM) was decreased from 2.27, 2.51, 2.59, and 2.58 ns to 2.08, 1.86, 1.81, and 1.90 ns, respectively, suggesting the occurrence of dynamic quenching (diffusion controlled) in the excited state. It is important to note that the magnitude of quenching of fluorescence lifetime is higher in the halogenated derivatives (780 ps, ABSQ-Cl) compared to the non-

halogenated derivative (330 ps, ABSQ-H) upon addition of PCBM. However, ABSQ-F showed complete quenching of fluorescence intensity compared to other derivatives, whereas ABSQ-Cl showed fast decay time compared to other derivatives. Such an observation of difference in the photophysical properties could be due to the resultant of competition between the electron-withdrawing (electronegativity) and electron-donating (mesomeric effect) characteristics of halogens in nature.⁴¹

The bimolecular quenching rate constant, K_q ($K_q = K_{SV}/\tau_0$), and the Stern–Volmer quenching constant, K_{SV} ($\tau_0/\tau = 1 + K_{SV} \times [\text{PCBM}]$), were calculated, and the constants are provided in Table S4, where τ_0 and τ are the fluorescence lifetimes of ABSQ derivatives in the absence and presence of PCBM. The K_q and K_{SV} values for ABSQ-H are found to be $2.88 \times 10^9 \text{ M}^{-1} \text{ s}^{-1}$ and 6.54 M^{-1} , respectively. These constants are increased upon halogen substitution (ABSQ-Cl $1.24 \times 10^{10} \text{ M}^{-1} \text{ s}^{-1}$ and 32.10 M^{-1}), suggesting the occurrence of a strong interaction between the halogenated ABSQs and PCBM compared to that of ABSQ-H with PCBM.

It is to be noted that the K_q value of the halogen-substituted ABSQ derivatives is an order of magnitude larger⁴³ than that of a normal diffusion-controlled bimolecular reaction constant ($2 \times 10^9 \text{ M}^{-1} \text{ s}^{-1}$). Overall upon addition of PCBM, the quenching of fluorescence intensity and the lifetime of ABSQ derivatives reveal the occurrence of the intermolecular charge transfer between ABSQs and PCBM²⁷ and consistent with their electrochemical data (Table S5).

Time-Resolved Photophysical Characterization. Femtosecond Transient Absorption Spectra. In order to explore the influence of solvent polarity on the excited-state relaxation dynamics of the ABSQ derivatives, the femtosecond time-resolved transient absorption spectra were recorded in ACN and toluene upon excitation at 670 nm using femtosecond pump-probe spectroscopy. The transient absorption spectra of ABSQ-H in ACN are shown in Figure 4, where panel a shows

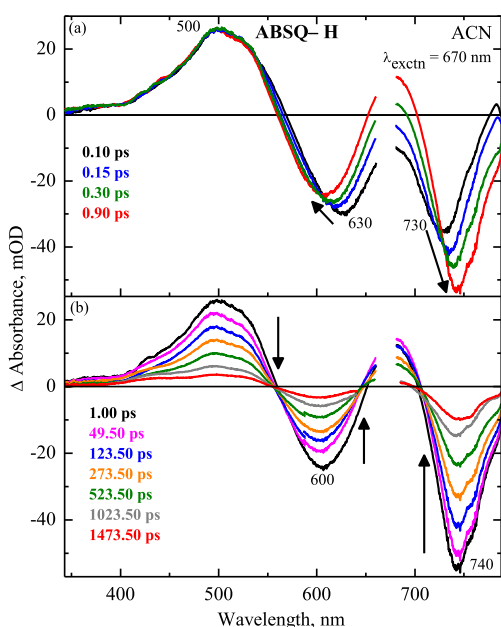


Figure 4. Femtosecond transient absorption spectra of ABSQ-H in ACN at different delay times upon excitation at 670 nm.

the spectral evolution starting from 0.1 to 0.9 ps. At an early time scale of 100 fs, it shows the broad positive band at ~ 500 nm and two negative absorption bands at around 630 and 730 nm. The positive band at ~ 500 nm is due to the excited singlet-state absorption (ESA, $S_n \leftarrow S_1$ transition) of the compound.^{30,44–47} With the increase of delay time, at 900 fs, the negative band at 630 nm shifted to the blue region (600 nm) consistent with the ground-state bleaching (GSB) of the absorption spectra of ABSQ-H, whereas the negative absorption band at 730 nm evolved to attain the steady-state emission maximum at 740 nm, corresponding to the stimulated emission (SE). In addition, a formation of peak at around 680 nm was observed. Panel b of Figure 4 exhibits the transient absorption spectra recorded from 1 ps to 1.47 ns where the intensity of the ESA, GSB, and SE bands decreased with the increase of the delay time.

The femtosecond transient absorption spectra of ABSQ-H in toluene are shown at a representative delay time in Figure 5. The spectral evolution at early time scales shown in panel a of Figure 5 exhibited dominant ESA at around 516 nm. Though the evolution of GSB is not observed evidently due to the

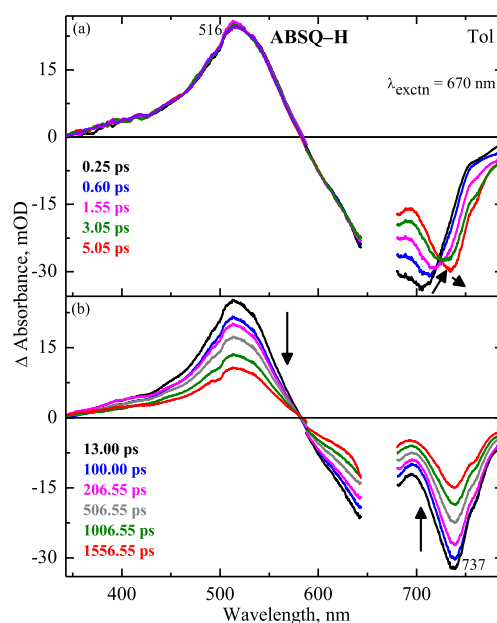


Figure 5. Femtosecond transient absorption spectra of ABSQ-H in toluene upon excitation at 670 nm at different delay times.

scattering of laser excitation at 670 nm and superimposing of SE spectra, the evolution of SE was observed clearly at around 730 nm. In Figure 5, panel b shows the spectral evolution from 13.0 ps to 1.55 ns where the intensity of ESA, GSB, and SE bands decreased with the increase of the delay time. Though the spectral features of ESA, SE, and GSB of ABSQ-H in toluene are resembled to that in ACN, the excited-state relaxation dynamics are slower in toluene when compared to that in ACN (Figure 6) due to the change in the solvation dynamics.^{48–52} The femtosecond transient absorption spectra of other ABSQ derivatives in ACN and toluene are provided in

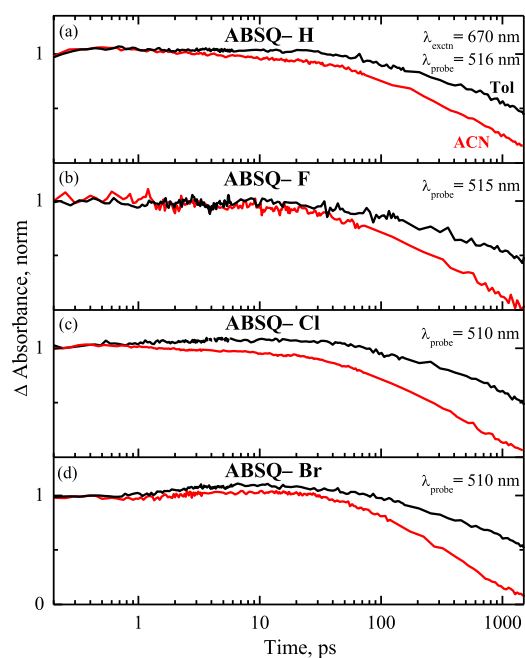


Figure 6. Femtosecond transient absorption decay of ABSQ-H (a), ABSQ-F (b), ABSQ-Cl (c), and ABSQ-Br (d) in toluene and acetonitrile upon excitation at 670 nm.

the Supporting Information (Figures S7–S12). The spectral behaviors of ABSQ-F, ABSQ-Cl, and ABSQ-Br in ACN and toluene are observed to be similar to that of ABSQ-H in ACN and toluene, respectively.

Importantly, to understand the intermolecular interaction dynamics between ABSQs and PCBM, the transient absorption spectra of ABSQs with PCBM in toluene were recorded by exciting at 670 nm and are provided in the Supporting Information as Figures S13–S20. Since an excitation wavelength of 670 nm is used to measure the transient absorption spectra of ABSQs upon addition of PCBM, where PCBM has a negligible absorbance and ABSQ derivatives have a high extinction coefficient ($\sim 7.5 \times 10^4 \text{ M}^{-1} \text{ cm}^{-1}$), there will be a negligible signal contribution arising from PCBM alone in the probe range of wavelength. When compared to ABSQ-H, the transient absorption spectra showed narrow absorption spectra at early dynamics (~ 500 fs) upon addition of PCBM (Figure S13). With the increase of delay time, the transient absorption spectrum became broader, and the increase of positive absorption in the red region at ~ 710 nm was observed at longer time delay. The appearance of positive transient absorption at around 710 nm is attributed to the formation of a radical cation of squaraine derivatives and consistent with the literature.^{25,53,54} Similarly, for other derivatives, changes in the spectral width of transient absorption spectra were observed upon addition of PCBM. These observations could reflect the effect of intermolecular interaction between ABSQs and PCBM. It is to be noted that the concentration of PCBM was 13.5 mM, having high absorbance in the region of < 390 nm. Since all the probe beam below 390 nm was completely absorbed by PCBM, we could not observe any changes in the optical density in this region. In addition, there is an artifact raised at ~ 433 nm due to the strong and narrow absorption of PCBM. The excited-state relaxation dynamics probed at the excited-state absorption maximum were quenched upon addition of PCBM (Figure 7) as observed in the fluorescence dynamics (Figure 3).

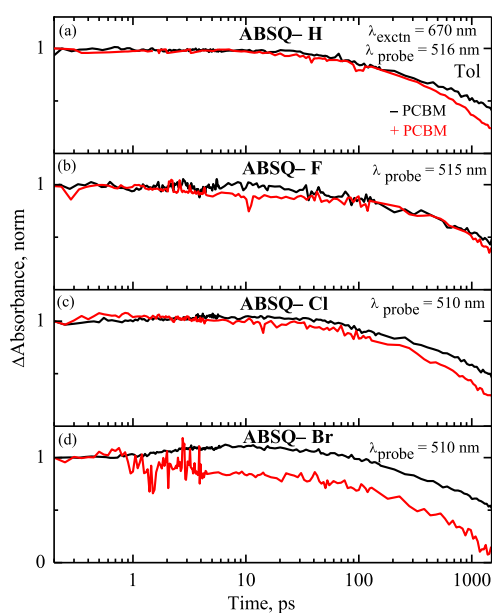


Figure 7. Femtosecond transient absorption decay of ABSQ-H (a), ABSQ-F (b), ABSQ-Cl (c), and ABSQ-Br (d) with and without PCBM in toluene upon excitation at 670 nm.

Nevertheless, only a small change between the transient absorption decay of ABSQ-F with and without PCBM was observed, in spite of significant quenching in the fluorescence data. This could be due to the resultant of competition between the electron-withdrawing (electronegativity) and electron-donating (+ mesomeric effect) characteristics of fluoride in nature.⁴¹

Analysis of the Transient Absorption Spectra. The femtosecond transient absorption spectra were analyzed globally with the sequential model using Glotaran.⁵⁵ Three exponential time constants were ideally determined to completely describe the excited-state relaxation dynamics of ABSQ derivatives in ACN and toluene as well as with PCBM in toluene. The obtained time constants are provided in Table 2, and the corresponding decay-associated difference spectra (DADS) are shown for comparison in the Supporting Information (Figures S21–S24). The DADS exhibited the amplitude of a particular decay time constant as a function of the corresponding wavelength and reflecting the common features of transient absorption spectra.

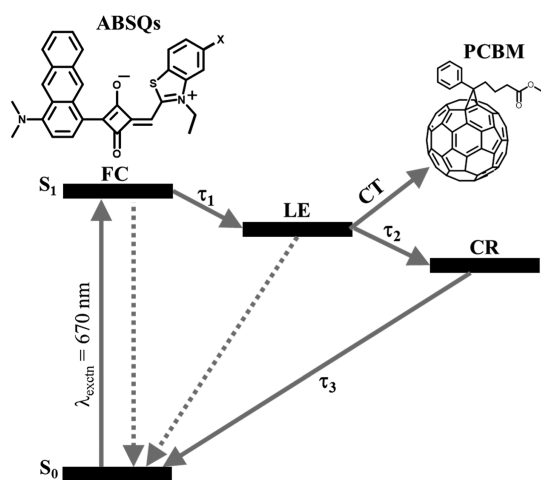
ABSQ-H is considered at first for the discussion of time constants attained from the global analysis. The fast component [$\tau_1 = 445$ fs (2.22 ps) in ACN (toluene)] is attributed to the solvation dynamics from the Franck–Condon state to the local excited state (solvent stabilized) based on the appearance of a dynamic red shift of SE with the increase of delay time.^{52,56,57} The time constant τ_2 , 33.23 ps (167.04 ps) for ACN (toluene), might be due to the formation of the dark state arising from the conformational changes of ABSQ-H. This state enables the non-radiative deactivation to the ground state, supporting the appearance of reduction of fluorescence lifetime and quantum yield in ACN (Tables 1 and S1–S3). Last, the longer time constant τ_3 obtained from the global analysis is equivalent with the fluorescence lifetime attained from the TCSPC in neat solvent (Tables 1 and S1–S3). Hence, a time constant of 0.63 (2.50) ns is assigned to the lifetime of the excited singlet state of ABSQ-H in ACN (toluene). A similar excited-state relaxation pathway is plausible to occur for other halogenated ABSQ derivatives. Thus, based on the spectral observations and kinetic analysis, the excited-state relaxation dynamics of the ABSQs are proposed in Scheme 2 upon ultrafast laser excitation.

Interestingly, the analysis of transient absorption measurements of all the derivatives upon addition of PCBM showed the quenching of all time constants (Table 2). For example, the time constants of ABSQ-H were decreased from $\tau_1 = 2.22$ ps, $\tau_2 = 167.04$ ps, and $\tau_3 = 2.50$ ns to $\tau_1 = 1.81$ ps, $\tau_2 = 76.92$ ps, and $\tau_3 = 2.07$ ns upon addition of PCBM. Importantly, the decrease of τ_3 for all the derivatives is consistent with the reduction of fluorescence dynamics observed in the TCSPC. Such a decrease of all the time constants supports the occurrence of the intermolecular charge transfer between ABSQs and PCBM.⁵⁸ The occurrence of the charge-transfer dynamics is further confirmed by the formation of radical cations of squaraine derivatives exhibiting positive transient absorption at around 710 nm, consistent with the literature,^{25,53,54} upon addition of PCBM at a longer time delay (Figure S14). However, the transient absorption spectra showing the anion radical of PCBM in the NIR region^{59,60} would be advantageous to support the occurrence of the intermolecular charge-transfer process in the mixture.

Further, to shed more light on the charge-transfer dynamics, global target analysis has been carried out to extract the time

Table 2. Time Constants Attained from Global Analysis Using Glotaran⁵⁵ for ABSQ Derivatives upon Excitation at 670 nm

derivatives	ACN	toluene	
		– PCBM	+ PCBM
ABSQ-H	$\tau_1 = 0.44 \pm 0.12$ ps	$\tau_1 = 2.22 \pm 0.12$ ps	$\tau_1 = 1.81 \pm 0.12$ ps
	$\tau_2 = 33.23 \pm 1.20$ ps	$\tau_2 = 167.04 \pm 5.5$ ps	$\tau_2 = 76.92 \pm 2.5$ ps
	$\tau_3 = 632 \pm 10$ ps	$\tau_3 = 2.50 \pm 0.25$ ns	$\tau_3 = 2.07 \pm 0.15$ ns
ABSQ-F	$\tau_1 = 0.43 \pm 0.12$ ps	$\tau_1 = 2.31 \pm 0.12$ ps	$\tau_1 = 1.89 \pm 0.12$ ps
	$\tau_2 = 41.84 \pm 1.50$ ps	$\tau_2 = 151.51 \pm 4.50$ ps	$\tau_2 = 83.34 \pm 2.35$ ps
	$\tau_3 = 629 \pm 10$ ps	$\tau_3 = 2.41 \pm 0.15$ ns	$\tau_3 = 1.96 \pm 0.10$ ns
ABSQ-Cl	$\tau_1 = 0.45 \pm 0.12$ ps	$\tau_1 = 2.25 \pm 0.15$ ps	$\tau_1 = 1.15 \pm 0.12$ ps
	$\tau_2 = 35.07 \pm 1.35$ ps	$\tau_2 = 139.95 \pm 3.25$ ps	$\tau_2 = 85.85 \pm 3.25$ ps
	$\tau_3 = 577 \pm 5$ ps	$\tau_3 = 2.62 \pm 0.10$ ns	$\tau_3 = 1.85 \pm 0.15$ ns
ABSQ-Br	$\tau_1 = 0.42 \pm 0.12$ ps	$\tau_1 = 2.39 \pm 0.15$ ps	$\tau_1 = 1.18 \pm 0.12$ ps
	$\tau_2 = 17.60 \pm 0.82$ ps	$\tau_2 = 134.90 \pm 3.15$ ps	$\tau_2 = 91.19 \pm 4.05$ ps
	$\tau_3 = 616 \pm 10$ ps	$\tau_3 = 2.60 \pm 0.10$ ns	$\tau_3 = 1.97 \pm 0.15$ ns

Scheme 2. Proposed Excited-State Relaxation Dynamics of ABSQ Derivatives upon Ultrafast Excitation^a

^aFC—Franck–Condon state, LE—local excited state, CR—conformationally relaxed state, and CT—charge transfer.

constant of charge transfer and spectral signatures of each excited species. The species-associated spectra of ABSQ derivatives upon addition of PCBM are provided in Figures S25–S28 in the Supporting Information. The rate constant of a particular process can be obtained from the fraction of population conversion from one state to another divided by the associated time constant of the state.^{61–64} The relative fraction of population is tested by multiplying the amplitude of each of the kinetic traces with the corresponding species-associated spectrum and summing the result, leading to the observed transient absorption spectra within the experimental noise.^{61–65} Thus, based on the target analysis, the charge transfer proposed to occur from the solvent-stabilized local excited state with the relative population of ~89% and the time constants of charge transfer from ABSQ-H, ABSQ-F, ABSQ-Cl, and ABSQ-Br to PCBM were found to be 86.43, 93.72, 96.52, and 102.56 ps, respectively.

Thus, upon halogenation of ABSQs, the bathochromic shift with the increase of molar absorptivity, high bimolecular quenching constant, and efficient intermolecular charge transfer with PCBM were observed. These effects could be due to the transfer of electron density from the halogen substituents to the benzothiazole moiety core, which increases with the increase of polarizability of the halogen substituents.

This is consistent with the report of Würthner et al.⁴¹ that a bathochromic shift of absorption with the increase of the molar absorptivity and enhancement of the fluorescence quantum yield were observed from fluorine over chlorine and bromine to iodine-substituted NIR squaraine derivatives.

CONCLUSIONS

The unsymmetrical squaraine derivatives having *N,N*-dimethylated anthracene and benzothiazole (ABSQ-H) halogenated with fluoride (ABSQ-F), chloride (ABSQ-Cl), and bromide (ABSQ-Br) were synthesized to understand the effect of halogen on the intermolecular interaction dynamics between the ABSQ derivatives and PCBM. Interestingly, ABSQ-H exhibited intense absorption ($\epsilon \sim 10^4 \text{ M}^{-1} \text{ cm}^{-1}$) in the NIR region with maxima centered at ~660 nm. Upon halogen substitution, a bathochromic shift in the absorption spectra with an increase of molar absorptivity was observed. The excited-state relaxation dynamics of ABSQ derivatives in acetonitrile are faster when compared to that in toluene due to the change in the solvation relaxation dynamics. The quenching of fluorescence intensity and lifetime of ABSQs and the formation of squaraine radical cation upon addition of PCBM revealed the occurrence of intermolecular charge transfer between ABSQs and PCBM. These results will help for the development of efficient unsymmetrical squaraine derivatives for optoelectronic devices.

ASSOCIATED CONTENT

Supporting Information

The Supporting Information is available free of charge at <https://pubs.acs.org/doi/10.1021/acs.jpcc.1c10840>.

Synthetic procedures, stationary absorption and emission spectra in solvents of various polarities, fluorescence lifetime in various solvents, femtosecond transient absorption spectra in toluene and ACN and also with PCBM upon excitation at 670 nm, decay-associated spectra in ACN and toluene and with PCBM, cyclic voltammogram, HOMO and LUMO levels with respect to PCBM, Stern–Volmer quenching constant (K_{SV}), bimolecular quenching rate constant (K_q), and electrochemical data of ABSQ derivatives (PDF)

AUTHOR INFORMATION

Corresponding Author

Venugopal Karunakaran – Photosciences and Photonics Section, Chemical Sciences and Technology Division, CSIR-National Institute for Interdisciplinary Science and Technology, Thiruvananthapuram 695 019 Kerala, India; Academy of Scientific and Innovative Research (AcSIR), Ghaziabad 201002, India; orcid.org/0000-0001-8482-0900; Phone: 091-471-2515240; Email: k.venugopal@niist.res.in

Authors

Guruprasad M. Somashekarappa – Photosciences and Photonics Section, Chemical Sciences and Technology Division, CSIR-National Institute for Interdisciplinary Science and Technology, Thiruvananthapuram 695 019 Kerala, India; Academy of Scientific and Innovative Research (AcSIR), Ghaziabad 201002, India

Megha Paul – Photosciences and Photonics Section, Chemical Sciences and Technology Division, CSIR-National Institute for Interdisciplinary Science and Technology, Thiruvananthapuram 695 019 Kerala, India; Academy of Scientific and Innovative Research (AcSIR), Ghaziabad 201002, India

Chinju Govind – Photosciences and Photonics Section, Chemical Sciences and Technology Division, CSIR-National Institute for Interdisciplinary Science and Technology, Thiruvananthapuram 695 019 Kerala, India; Academy of Scientific and Innovative Research (AcSIR), Ghaziabad 201002, India; orcid.org/0000-0002-7751-4873

Ranimol Mathew – Photosciences and Photonics Section, Chemical Sciences and Technology Division, CSIR-National Institute for Interdisciplinary Science and Technology, Thiruvananthapuram 695 019 Kerala, India; Academy of Scientific and Innovative Research (AcSIR), Ghaziabad 201002, India

Complete contact information is available at:
<https://pubs.acs.org/10.1021/acs.jpccb.1c10840>

Notes

The authors declare no competing financial interest.

ACKNOWLEDGMENTS

G.M.S. thanks CSIR, New Delhi, for his research fellowship. M.P. and C.G. thank UGC, New Delhi, for their research fellowship. V.K. gratefully acknowledges DBT (BT/PR24173/BRB/10/1604/2017), Government of India, and the CSIR project (MLP 0061) under energy and energy devices theme for financial support. We thank Dr. Suresh Das for a discussion.

REFERENCES

- (1) Aumaitre, C.; Rodriguez-Seco, C.; Jover, J.; Bardagot, O.; Caffy, F.; Kervella, Y.; López, N.; Palomares, E.; Demadrille, R. Visible and near-Infrared Organic Photosensitizers Comprising Isoindigo Derivatives as Chromophores: Synthesis, Optoelectronic Properties and Factors Limiting Their Efficiency in Dye Solar Cells. *J. Mater. Chem. A* **2018**, *6*, 10074–10084.
- (2) Sharma, V.; Kovida, K.; Sahoo, D.; Varghese, N.; Mohanta, K.; Koner, A. L. Synthesis and Photovoltaic Application of Nir-Emitting Perylene-Monoimide Dyes with Large Stokes-Shift. *RSC Adv.* **2019**, *9*, 30448–30452.
- (3) Chen, Y.; Zhu, W.; Wu, J.; Huang, Y.; Facchetti, A.; Marks, T. J. Recent Advances in Squaraine Dyes for Bulk-Heterojunction Organic Solar Cells. *Org. Photonics Photovoltaics* **2019**, *6*, 1–16.
- (4) He, J.; Jo, Y. J.; Sun, X.; Qiao, W.; Ok, J.; Kim, T. i.; Li, Z. a. Squaraine Dyes for Photovoltaic and Biomedical Applications. *Adv. Funct. Mater.* **2021**, *31*, 2008201.
- (5) Kublitski, J.; Fischer, A.; Xing, S.; Baisinger, L.; Bittrich, E.; Spoltore, D.; Benduhn, J.; Vandewal, K.; Leo, K. Enhancing Sub-Bandgap External Quantum Efficiency by Photomultiplication for Narrowband Organic near-Infrared Photodetectors. *Nat. Commun.* **2021**, *12*, 4259.
- (6) Goh, T.; Huang, J.-S.; Bielinski, E. A.; Thompson, B. A.; Tomasulo, S.; Lee, M. L.; Sfeir, M. Y.; Hazari, N.; Taylor, A. D. Coevaporated Bisquaraine Inverted Solar Cells: Enhancement Due to Energy Transfer and Open Circuit Voltage Control. *ACS Photonics* **2015**, *2*, 86–95.
- (7) Corredor, C. C.; Huang, Z.-L.; Belfield, K. D. Two-Photon 3d Optical Data Storage Via Fluorescence Modulation of an Efficient Fluorene Dye by a Photochromic Diarylethene. *Adv. Mater.* **2006**, *18*, 2910–2914.
- (8) Sun, C.-L.; Lv, S.-K.; Liu, Y.-P.; Liao, Q.; Zhang, H.-L.; Fu, H.; Yao, J. Benzoidolic Squaraine Dyes with a Large Two-Photon Absorption Cross-Section. *J. Mater. Chem. C* **2017**, *5*, 1224–1230.
- (9) Chen, C.; Dong, H.; Chen, Y.; Guo, L.; Wang, Z.; Sun, J.-J.; Fu, N. Dual-Mode Unsymmetrical Squaraine-Based Sensor for Selective Detection of Hg²⁺ in Aqueous Media. *Org. Biomol. Chem.* **2011**, *9*, 8195–8201.
- (10) Butnarusu, C.; Barbero, N.; Barolo, C.; Visentin, S. Squaraine Dyes as Fluorescent Turn-on Sensors for the Detection of Porcine Gastric Mucin: A Spectroscopic and Kinetic Study. *J. Photochem. Photobiol., B* **2020**, *205*, 111838.
- (11) Saneesh Babu, P. S.; Manu, P. M.; Dhanya, T. J.; Tapas, P.; Meera, R. N.; Surendran, A.; Aneesh, K. A.; Vadakkancheril, S. J.; Ramaiah, D.; Nair, S. A.; et al. Bis(3,5-Diiodo-2,4,6-Trihydroxyphenyl)Squaraine Photodynamic Therapy Disrupts Redox Homeostasis and Induce Mitochondria-Mediated Apoptosis in Human Breast Cancer Cells. *Sci. Rep.* **2017**, *7*, 42126.
- (12) Chen, G.; Sasabe, H.; Igarashi, T.; Hong, Z.; Kido, J. Squaraine Dyes for Organic Photovoltaic Cells. *J. Mater. Chem. A* **2015**, *3*, 14517–14534.
- (13) Law, K. Y. Squaraine Chemistry: Effects of Structural Changes on the Absorption and Multiple Fluorescence Emission of Bis[4-(Dimethylamino)Phenyl]Squaraine and Its Derivatives. *J. Phys. Chem.* **1987**, *91*, 5184–5193.
- (14) Khopkar, S.; Shankarling, G. Synthesis, Photophysical Properties and Applications of Nir Absorbing Unsymmetrical Squaraines: A Review. *Dyes Pigm.* **2019**, *170*, 107645.
- (15) Yang, D.; Yang, Q.; Yang, L.; Luo, Q.; Huang, Y.; Lu, Z.; Zhao, S. Novel High Performance Asymmetrical Squaraines for Small Molecule Organic Solar Cells with a High Open Circuit Voltage of 1.12 V. *Chem. Commun.* **2013**, *49*, 10465–10467.
- (16) Alex, S.; Santhosh, U.; Das, S. Dye Sensitization of Nanocrystalline TiO₂: Enhanced Efficiency of Unsymmetrical Versus Symmetrical Squaraine Dyes. *J. Photochem. Photobiol., A* **2005**, *172*, 63–71.
- (17) Kim, S.; Mor, G. K.; Paulose, M.; Varghese, O. K.; Baik, C.; Grimes, C. A. Molecular Design of near-Ir Harvesting Unsymmetrical Squaraine Dyes. *Langmuir* **2010**, *26*, 13486–13492.
- (18) Maeda, T.; Nguyen, T. V.; Kuwano, Y.; Chen, X.; Miyayama, K.; Nakazumi, H.; Yagi, S.; Soman, S.; Ajayaghosh, A. Intramolecular Exciton-Coupled Squaraine Dyes for Dye-Sensitized Solar Cells. *J. Phys. Chem. C* **2018**, *122*, 21745–21754.
- (19) Singh, A. K.; Maibam, A.; Javaregowda, B. H.; Bisht, R.; Kudlu, A.; Krishnamurthy, S.; Krishnamoorthy, K.; Nithyanandhan, J. Unsymmetrical Squaraine Dyes for Dye-Sensitized Solar Cells: Position of the Anchoring Group Controls the Orientation and Self-Assembly of Sensitizers on the TiO₂ Surface and Modulates Its Flat Band Potential. *J. Phys. Chem. C* **2020**, *124*, 18436–18451.

- (20) Singh, A. K.; Veetil, A. N.; Nithyanandhan, J. D—*a*—*D* Based Complementary Unsymmetrical Squaraine Dyes for Co-Sensitized Solar Cells: Enhanced Photocurrent Generation and Suppressed Charge Recombination Processes by Controlled Aggregation. *ACS Appl. Energy Mater.* **2021**, *4*, 3182–3193.
- (21) Rao, G. H.; Rana, P. J. S.; Islam, A.; Singh, S. P. Synthesis of Multichromophoric Asymmetrical Squaraine Sensitizer Via C–H Arylation for See-through Photovoltaic. *ACS Appl. Energy Mater.* **2018**, *1*, 4786–4793.
- (22) Lambert, C.; Hoche, J.; Schreck, M. H.; Holzapfel, M.; Schmiedel, A.; Selby, J.; Turkin, A.; Mitric, R. Ultrafast Energy Transfer Dynamics in a Squaraine Heterotriad. *J. Phys. Chem. A* **2021**, *125*, 2504–2511.
- (23) Schreck, M. H.; Breitschwerdt, L.; Marciniak, H.; Holzapfel, M.; Schmidt, D.; Würthner, F.; Lambert, C. Fs–Ps Exciton Dynamics in a Stretched Tetraphenylsquaraine Polymer. *Phys. Chem. Chem. Phys.* **2019**, *21*, 15346–15355.
- (24) Kim, J. H.; Liess, A.; Stolte, M.; Krause, A. M.; Stepanenko, V.; Zhong, C.; Bialas, D.; Spano, F.; Würthner, F. An Efficient Narrowband near-Infrared at 1040 nm Organic Photodetector Realized by Intermolecular Charge Transfer Mediated Coupling Based on a Squaraine Dye. *Adv. Mater.* **2021**, *33*, 2100582.
- (25) de Miguel, G.; Marchena, M.; Ziólek, M.; Pandey, S. S.; Hayase, S.; Douhal, A. Femto- to Millisecond Photophysical Characterization of Indole-Based Squaraines Adsorbed on TiO₂ Nanoparticle Thin Films. *J. Phys. Chem. C* **2012**, *116*, 12137–12148.
- (26) Rana, A.; Sharma, C.; Prabhu, D. D.; Kumar, M.; Karuvath, Y.; Das, S.; Chand, S.; Singh, R. K. Revealing Charge Carrier Dynamics in Squaraine:[6, 6]-Phenyl-C 71-Butyric Acid Methyl Ester Based Organic Solar Cells. *AIP Adv.* **2018**, *8*, 045302.
- (27) Somashekharappa, G. M.; Govind, C.; Pulikodan, V.; Paul, M.; Namboothiry, M. A. G.; Das, S.; Karunakaran, V. Unsymmetrical Squaraine Dye-Based Organic Photodetector Exhibiting Enhanced near-Infrared Sensitivity. *J. Phys. Chem. C* **2020**, *124*, 21730–21739.
- (28) Thomas, K. G.; Thomas, K. J.; Das, S.; George, M. V.; Liu, D.; Kamat, P. V. Photochemistry of Squaraine Dyes. Part 10.—Excited-State Properties and Photosensitization Behaviour of an Ir Sensitive Cationic Squaraine Dye. *J. Chem. Soc., Faraday Trans.* **1996**, *92*, 4913–4916.
- (29) Ajayaghosh, A. Chemistry of Squaraine-Derived Materials: Near-Ir Dyes, Low Band Gap Systems, and Cation Sensors. *Acc. Chem. Res.* **2005**, *38*, 449–459.
- (30) Chang, H.-J.; Bondar, M. V.; Liu, T.; Liu, X.; Singh, S.; Belfield, K. D.; Sheely, A.; Masunov, A. E.; Hagan, D. J.; Van Stryland, E. W. Electronic Nature of Neutral and Charged Two-Photon Absorbing Squaraines for Fluorescence Bioimaging Application. *ACS Omega* **2019**, *4*, 14669–14679.
- (31) Armarego, W. L. F. Chapter 3—Purification of Organic Chemicals. In *Purification of Laboratory Chemicals (Eighth Edition)*; Armarego, W. L. F., Ed.; Butterworth-Heinemann, 2017; pp 95–634.
- (32) Pålsson, L.-O.; Monkman, A. P. Measurements of Solid-State Photoluminescence Quantum Yields of Films Using a Fluorimeter. *Adv. Mater.* **2002**, *14*, 757–758.
- (33) Paul, S.; Govind, C.; Karunakaran, V. Planarity and Length of the Bridge Control Rate and Efficiency of Intramolecular Singlet Fission in Pentacene Dimers. *J. Phys. Chem. B* **2021**, *125*, 231–239.
- (34) Megerle, U.; Pugliese, I.; Schriever, C.; Sailer, C. F.; Riedle, E. Sub-50 fs Broadband Absorption Spectroscopy with Tunable Excitation: Putting the Analysis of Ultrafast Molecular Dynamics on solid Ground. *Appl. Phys. B* **2009**, *96*, 215–231.
- (35) Khan, R.; Ningombam, A.; Singh, K. B.; Singh, M. D. Stereoelectronic Effects in the Stereoselectivity of the Diels-Alder Reactions: Reactions of Aminoanthracenes with N-Phenylmaleimide. *J. Chem. Pharm. Res.* **2012**, *4*, 1532–1538.
- (36) Tatarts, A.; Fedunyaeva, I.; Terpetschnig, E.; Patsenker, L. Synthesis of Novel Squaraine Dyes and Their Intermediates. *Dyes Pigm.* **2005**, *64*, 125–134.
- (37) Inoue, T.; Pandey, S. S.; Fujikawa, N.; Yamaguchi, Y.; Hayase, S. Synthesis and Characterization of Squaric Acid Based Nir Dyes for Their Application Towards Dye-Sensitized Solar Cells. *J. Photochem. Photobiol., A* **2010**, *213*, 23–29.
- (38) Yum, J.-H.; Walter, P.; Huber, S.; Rentsch, D.; Geiger, T.; Nüesch, F.; De Angelis, F.; Grätzel, M.; Nazeeruddin, M. K. Efficient Far Red Sensitization of Nanocrystalline TiO₂ Films by an Unsymmetrical Squaraine Dye. *J. Am. Chem. Soc.* **2007**, *129*, 10320–10321.
- (39) So, S.; Choi, H.; Kim, C.; Cho, N.; Ko, H. M.; Lee, J. K.; Ko, J. Novel Symmetric Squaraine Chromophore Containing Triphenylamine for Solution Processed Small Molecule Bulk Heterojunction Solar Cells. *Sol. Energy Mater. Sol. Cells* **2011**, *95*, 3433–3441.
- (40) Della Pelle, A. M.; Homnick, P. J.; Bae, Y.; Lahti, P. M.; Thayumanavan, S. Effect of Substituents on Optical Properties and Charge-Carrier Polarity of Squaraine Dyes. *J. Phys. Chem. C* **2014**, *118*, 1793–1799.
- (41) Mayerhöffer, U.; Fimmel, B.; Würthner, F. Bright near-Infrared Fluorophores Based on Squaraines by Unexpected Halogen Effects. *Angew. Chem., Int. Ed.* **2012**, *51*, 164–167.
- (42) Park, J.; Barolo, C.; Sauvage, F.; Barbero, N.; Benzi, C.; Quagliotto, P.; Coluccia, S.; Di Censo, D.; Grätzel, M.; Nazeeruddin, M. K.; et al. Symmetric Vs. Asymmetric Squaraines as Photosensitisers in Mesoscopic Injection Solar Cells: A Structure–Property Relationship Study. *Chem. Commun.* **2012**, *48*, 2782–2784.
- (43) Kabatc, J.; Kostrzewska, K.; Kozak, M.; Balcerak, A. Visible Light Photoinitiating Systems Based on Squaraine Dye: Kinetic, Mechanistic and Laser Flash Photolysis Studies. *RSC Adv.* **2016**, *6*, 103851–103863.
- (44) Liu, T.; Bondar, M. V.; Belfield, K. D.; Anderson, D.; Masunov, A. E.; Hagan, D. J.; Stryland, E. W. V. Linear Photophysics and Femtosecond Nonlinear Spectroscopy of a Star-Shaped Squaraine Derivative with Efficient Two-Photon Absorption. *J. Phys. Chem. C* **2016**, *120*, 11099–11110.
- (45) Belfield, K. D.; Bondar, M. V.; Haniff, H. S.; Mikhailov, I. A.; Luchita, G.; Przhonska, O. V. Superfluorescent Squaraine with Efficient Two-Photon Absorption and High Photostability. *ChemPhysChem* **2013**, *14*, 3532–3542.
- (46) Webster, S.; Peceli, D.; Hu, H.; Padilha, L. A.; Przhonska, O. V.; Masunov, A. E.; Gerasov, A. O.; Kachkovski, A. D.; Slominsky, Y. L.; Tolmachev, A. I.; et al. Near-Unity Quantum Yields for Intersystem Crossing and Singlet Oxygen Generation in Polymethine-Like Molecules: Design and Experimental Realization. *J. Phys. Chem. Lett.* **2010**, *1*, 2354–2360.
- (47) Lambert, C.; Scherpf, T.; Ceymann, H.; Schmiedel, A.; Holzapfel, M. Coupled Oscillators for Tuning Fluorescence Properties of Squaraine Dyes. *J. Am. Chem. Soc.* **2015**, *137*, 3547–3557.
- (48) Martin, M. M.; Plaza, P.; Changenet-Barret, P.; Siemiarczuk, A. UV–vis Subpicosecond Spectroscopy of 4-(9-Anthryl)-N,N'-dimethylaniline in Polar and Nonpolar Solvents: A Two-Dimensional View of the Photodynamics. *J. Phys. Chem. A* **2002**, *106*, 2351–2358.
- (49) Mohammed, O. F.; Vauthey, E. Excited-State Dynamics of Nitroperylene in Solution: Solvent and Excitation Wavelength Dependence. *J. Phys. Chem. A* **2008**, *112*, 3823–3830.
- (50) Eom, I.; Joo, T. Polar Solvation Dynamics of Coumarin 153 by Ultrafast Time-Resolved Fluorescence. *J. Chem. Phys.* **2009**, *131*, 244507.
- (51) Kuang, Z.; He, G.; Song, H.; Wang, X.; Hu, Z.; Sun, H.; Wan, Y.; Guo, Q.; Xia, A. Conformational Relaxation and Thermally Activated Delayed Fluorescence in Anthraquinone-Based Intramolecular Charge-Transfer Compound. *J. Phys. Chem. C* **2018**, *122*, 3727–3737.
- (52) Horng, M. L.; Gardecki, J. A.; Papazyan, A.; Maroncelli, M. Subpicosecond Measurements of Polar Solvation Dynamics: Coumarin 153 Revisited. *J. Phys. Chem.* **1995**, *99*, 17311–17337.
- (53) Sauve, G.; Kamat, P. V.; Thomas, K. G.; Thomas, K. J.; Das, S.; George, M. V. Photochemistry of Squaraine Dyes: Excited Triplet State and Redox Properties of Crown Ether Squaraines. *J. Phys. Chem.* **1996**, *100*, 2117–2124.
- (54) Marchena, M. J.; de Miguel, G.; Cohen, B.; Organero, J. A.; Pandey, S.; Hayase, S.; Douhal, A. Real-Time Photodynamics of

Squaraine-Based Dye-Sensitized Solar Cells with Iodide and Cobalt Electrolytes. *J. Phys. Chem. C* **2013**, *117*, 11906–11919.

(55) Snellenburg, J. J.; Laptienok, S.; Seger, R.; Mullen, K. M.; Van Stokkum, I. H. M. Glotaran: A Java-Based Graphical User Interface for the R Package Timp. *J. Stat. Software* **2012**, *49*, 1–22.

(56) Neelambra, A. U.; Govind, C.; Devassia, T. T.; Somashekharappa, G. M.; Karunakaran, V. Direct Evidence of Solvent Polarity Governing the Intramolecular Charge and Energy Transfer: Ultrafast Relaxation Dynamics of Push–Pull Fluorene Derivatives. *Phys. Chem. Chem. Phys.* **2019**, *21*, 11087–11102.

(57) Zhu, H.; Li, M.; Hu, J.; Wang, X.; Jie, J.; Guo, Q.; Chen, C.; Xia, A. Ultrafast Investigation of Intramolecular Charge Transfer and Solvation Dynamics of Tetrahydro[5]-Helicene-Based Imide Derivatives. *Sci. Rep.* **2016**, *6*, 24313.

(58) Lee, S.; Lee, M.; An, J.; Ahme, H.; Im, C. Exciton Dynamics of P3ht:Pcbm Blend Films with Different Polymer Regioregularities Using Transient Absorption Spectroscopy. *Mol. Cryst. Liq. Cryst.* **2013**, *578*, 68–72.

(59) Guldi, D. M.; Prato, M. Excited-State Properties of C60 Fullerene Derivatives. *Acc. Chem. Res.* **2000**, *33*, 695–703.

(60) Yamamoto, S.; Guo, J.; Ohkita, H.; Ito, S. Formation of Methanofullerene Cation in Bulk Heterojunction Polymer Solar Cells Studied by Transient Absorption Spectroscopy. *Adv. Funct. Mater.* **2008**, *18*, 2555–2562.

(61) Williams, R. M.; Vãn Anh, N.; van Stokkum, I. H. M. Triplet Formation by Charge Recombination in Thin Film Blends of Perylene Red and Pyrene: Developing a Target Model for the Photophysics of Organic Photovoltaic Materials. *J. Phys. Chem. B* **2013**, *117*, 11239–11248.

(62) Ghosh, A.; Ghosh, S.; Ghosh, G.; Jana, B.; Patra, A. Revealing Complex Relaxation Processes of Collapsed Conjugated Polymer Nanoparticles in the Presence of Different Shapes of Gold Nanoparticles Using Global and Target Analysis. *J. Phys. Chem. C* **2020**, *124*, 26165–26173.

(63) Lee, D.; Lee, J.; Sin, D. H.; Han, S. G.; Lee, H.; Choi, W.; Kim, H.; Noh, J.; Mun, J.; Sung, W.; et al. Intrachain Delocalization Effect of Charge Carriers on the Charge-Transfer State Dynamics in Organic Solar Cells. *J. Phys. Chem. C* **2022**, *126*, 3171–3179.

(64) van Stokkum, I. H. M.; Beekman, L. M. P.; Jones, M. R.; van Brederode, M. E.; van Grondelle, R. Primary Electron Transfer Kinetics in Membrane-Bound Rhodospirillum Rubrum Reaction Centers: A Global and Target Analysis. *Biochemistry* **1997**, *36*, 11360–11368.

(65) Karunakaran, V.; Pérez Lustres, J. L.; Zhao, L.; Ernsting, N. P.; Seitz, O. Large Dynamic Stokes Shift of DNA Intercalation Dye Thiazole Orange Has Contribution from a High-Frequency Mode. *J. Am. Chem. Soc.* **2006**, *128*, 2954–2962.

Recommended by ACS

Squaraine Dyes: Molecular Design for Different Applications and Remaining Challenges

Kristina Ilina, Maged Henary, *et al.*

JULY 31, 2019
BIOCONJUGATE CHEMISTRY

READ 

Amphiphilic Indoline-Based Unsymmetrical Squaraine Dyes for Dye-Sensitized Solar Cells: Modulating the Dye-TiO₂/Electrolyte Interface for Nonaqueous and...

Ambarish Kumar Singh and Jayaraj Nithyanandhan

NOVEMBER 30, 2021
ACS APPLIED ENERGY MATERIALS

READ 

π -Extended cis-Configured Unsymmetrical Squaraine Dyes for Dye-Sensitized Solar Cells: Panchromatic Response

Vellimalai Punitharasu, Jayaraj Nithyanandhan, *et al.*

NOVEMBER 08, 2019
ACS APPLIED ENERGY MATERIALS

READ 

Systematic Molecular Engineering of a Series of Aniline-Based Squaraine Dyes and Their Structure-Related Properties

Taihong Liu, Kevin D. Belfield, *et al.*

JANUARY 25, 2018
THE JOURNAL OF PHYSICAL CHEMISTRY C

READ 

Get More Suggestions >